Computational and Experimental Modelling of the Crushing of Prepared Sugar Cane

Thesis submitted by

Arasu Kannapiran

B.E., University of Madras, India

M.Tech., Indian Institute of Technology, Madras, India

in September 2003

for the degree of Doctor of Philosophy

in the School of Engineering (Mechanical Engineering)

James Cook University of North Queensland

STATEMENT OF ACCESS

I, the undersigned, the author of this thesis, understand that James Cook University of North Queensland will make it available for use within the University Library and, by microfilm or other means, allow access to users in other approved libraries. All users consulting this thesis will have to sign the following statement:

> *In consulting this thesis I agree not to copy or closely paraphrase it in whole or in part without the written consent of the author; and to make proper public written acknowledgement for any assistance that I have obtained from it.*

Beyond this, I do not wish to place any restriction on access to this thesis.

____________________________ Date ________________

(**Arasu Kannapiran**)

ABSTRACT

This thesis presents the investigation and application of porous media mechanics and elasto-plastic constitutive theory for the crushing of prepared sugar cane using finite element simulation. This research specifically investigates the experiments carried out on C. R. Murry Advanced Experimental Milling Facility using cane that has also passed through a series of basic tests to characterise its properties for the computational models. For isotropic plastic material behaviour, constitutive models that represent yielding under hydrostatic pressures are applied. The constitutive behaviour of the solid skeleton, and the plastic strain hardening response are derived from a series of slow speed confined uniaxial compression experiments. The liquid flow within fibrous solid matrix of prepared cane is modelled by applying Darcy's law, and the coefficient of permeability therefore was determined experimentally.

The finite element technique applied to the crushing process, couple the elasto-plastic constitutive theory for the solid fibre and the Darcy's liquid flow theory for the liquid juice in conjunction with the frictional relation between the roller and blanket material. The material law has been coded initially into a two-dimensional plane strain computer model.

Series of experiments on two-roll mill was conducted. The two-dimensional plane strain model predicted the roll load in agreement with experimental values, however failed to capture the tangential component of compression and the torque values were 50% lower than the experimental values. However, numerical prediction of a flat roll surface matched well in roll load and torque with experimental values as the stress levels associated with grooves are absent. The rolls were then modelled with grooves in three-dimension. The three-dimensional model captured high and low compression regions in groove tip and base respectively. The roll loads as well as roll torques matched well with experimental values.

STATEMENT ON SOURCES

I declare that this thesis is my own work and has not been submitted in any form for another degree or diploma at any university or other institution of tertiary education. Information derived from the published or unpublished work of others has been acknowledged in the text and a list of references is given.

______________________________ Date _______________

(**Arasu Kannapiran**)

ACKNOWLEDGEMENTS

The author wishes to thank gratefully the following people for their valuable contributions to the present study:

Associate Professor Jeffrey Loughran, for his encouragement and invaluable guidance throughout the research project as a supervisor.

Sugar Research Development Council (SRDC) of Australia, for financial support and encouragement throughout the project.

Dr. Clayton Adam, QUT for his valuable notes and discussions on the important aspects of this research.

Dr. Kai Duan, UWA for the useful discussions during initial stage of computation.

Mr. Geoff Kent, Dr. Christopher Downing and Mr. Neil McKenzie of Sugar Research Institute (SRI), Mackay for the useful discussions during initial experimental stage.

Mr. David Kauppila and Mr. Paul Britton of Mechanical engineering, and Mr. Gordon McNealy, Mr. Warren O'Donnel and Mr. Stuart Petersen of School of Engineering for all their technical assistance during grooved and flat roll mill experiments.

Contents

Chapter

Appendix

Tables

Table

Figures

Figure

List of symbols

α	Contact angle
α_a	Angle of contact between feed chute and rolls
α, β, γ, J	Geometrical coefficients in elliptic equation
β	Material's angle of friction
ϵ	Total strain vector
ϵ^e	Elastic strain
ϵ^p	Plastic strain
ϵ_s^p	Plastic shear strain
$\epsilon_v^p, \epsilon_v^{pl}$	Plastic volumetric strains
ϵ^t	Total strain
ϵ_h	Horizontal strain
ϵ_s	Shear strain
ϵ_s^e	Elastic shear strain
ϵ_{vn}	Volumetric strain at C= 1
ϵ_v, ϵ_p	Volumetric strain
ϵ_v^e	Elastic volumetric strain
ϵ_v^p	Plastic volumetric strain
$\epsilon_x, \epsilon_y, \epsilon_z$	Strains in x, y, z directions, respectively
η, μ	Dynamic viscosity
Γ	Slope of the specific volume at p'= 0
γ_f	Unit weight of fluid
$\gamma_{xy}, \gamma_{yz}, \gamma_{zx}$	Shear strains

κ	Slope of Swelling Recompression Line (SRL)
λ	Slope of Normal Compression Line (NCL)
μ	Friction factor
ν	Poisson's ratio
ϕ	Angle at neutral plane
ϕ	Angle of internal friction
ϕ	Slope in the τ/σ plane
ϕ'_{crit}	Soil friction angle
ρ	Density of solid-fluid mixture
ρ_c	Density of cane
ρ_f	Density of fibre
ρ_j	Density of juice
ρ_l	Density of liquid
ρ_{ng}	No gas density
ρ_s	Density of solid
σ'	Normal effective stress
σ	Total normal stress
$\sigma_1, \sigma_2, \sigma_3$	Principle stresses
σ_{av}	Average stress
σ_e	Effective stress
σ_e	von Mises equivalent stress
σ_h	Horizontal stress
σ_n	Normal stress
σ'_v	Normal effective stress
$\sigma_x, \sigma_y, \sigma_z$	Normal stresses
σ_Y	Yield stress
σ_z	Vertical stress

τ, τ_f	Shear stresses
τ_{max}	Maximum shear stress
$\tau_{xy}, \tau_{yz}, \tau_{zx}$	Shear stresses
θ	Angular position in mill measured from axial plane
θ_1, θ_2	Angular positions for roll arc surface
υ	Specific volume
υ_f	Final specific volume
υ_o	Initial specific volume
ξ, η	Computational domain coordinates

$1, 2, 3$	Spatial coordinate directions
A	Cross sectional area
A_p	Cross sectional area of test cell
A_s	Specific surface area
A_v	Cross sectional area of voids
$\hat{a}$	Treatment number
b	Length
C	Compression ratio
C_θ	Compression ratio as a function of angular position
C_c	Slope in the $e/\ln\sigma'$ plane, Corrected compression ratio
C_i	Initial compression ratio
C_o	Reference or mill compression ratio
c	Contact clearance
D	Roll diameter
d	Groove depth
d	Material cohesion
E	Extraction fraction

E, E'	Young's modulus
e	Void ratio
e_o	Initial void ratio
F	Force
F_c	Compaction
F_r	Filling ratio
F_r	Radial force
F_t	Tangential force
F_v	Vertical force
f	Fibre ratio
f_o	Reference fibre ratio
G, G'	Shear modulus
G_α	Grooving angle
g	Gravitational constant
h	Height of specimen
h	Pressure head
h_θ	Height as a function of θ
h_θ	Total height between the rolls
h_f	Height of feed chute
h_{ng}	No gas height
h_o	Blanket height
h_o	Initial height of specimen
$h_{s\theta}$	Height of solid material
i	Gradient or head loss
J_1, J_2	First and second stress invariants
K	Permeability
K	Re-absorption factor

K, K'	Bulk modulus
K_e	Effective permeability
K_o	Coefficient of lateral pressure
K_s, K_l	Bulk moduli of solid and liquid phases
k	Coefficient of permeability
k	Darcy coefficient matrix of permeability
L, l	Lengths
l_b	Cane blanket length
M	Slope of the q/p' plane
m_f	Mass of fibre
N	Torque-load number
n	Porosity
$\bar{P}$	Global liquid pressure
P	Pore pressure
P, Q	Mesh control functions
P_a	Pressure in the axial direction, psi
P_b	Yield locus
P_l	Liquid pore pressure
P_t	Total fluid pressure
p	Mean stress
p	Pressure, Contact pressure
p'	Mean normal effective stress
p_t^e	Elastic tensile stress
p_m	Mean load per unit area
p_o	Initial pressure
p_t	Tensile stress
p'_y	Yield stress

Q	Volume flow rate
q	Deviator stress
q'	Effective shear stress
$\dot{q}$	Crushing rate
R	Residual error
R	Roll separating force
S	Platen speed, Roll surface speed
S	Speed of piston
S_f	Feed velocity
S_l	Degree of liquid saturation
S_o	Set opening
S_r	Relative rubbing speed
T	Roll torque
T_{tot}	Total torque
T_x, T_y	Traction forces in x and y direction
t	Deviatoric stress measure
t	Thickness
t	time
$\ddot{u}$	Solid phase acceleration
$\dot{\bar{u}}$	Global velocity vector for the solid
u	Displacement for the solid
u	Pore pressure
u_x, u_y	Displacements in x and y direction
V	Average velocity of liquid
V	Total volume or sample volume
V_b	Volume of bagasse
V_c	Volume of cane

V_f	Volume of fibre
V_j	Volume of juice
V_{ng}	No gas volume
V_{ref}	Reference volume
V_s	Volume of solid
V_v	Volume of voids
V_w	Volume of liquid
$\dot{V}_b$	Volume rate of bagasse
$\dot{V}_e$	Escribed volume rate of juice
$\dot{V}_f$	Volume rate of fibre
$\dot{V}_{je}$	Volume rate of juice
$\dot{V}_j$	Total volume rate of juice
$\dot{V}_{ng}$	No void volume rate of juice
v	Superficial velocity
v	Velocity
v_v	Seepage velocity
v_x, v_y	Velocities in x and y direction
v_y	Vertical compression speed
w	Uncertainty
w	Weighting function
$\dot{w}$	Liquid velocity vector
$w_{\mathrm{d}h}$	Uncertainty in differential head
w_{av}	Uncertainty in vertical stress
w_A	Uncertainty in area
w_c	Uncertainty in compression ratio
w_d	Work opening at delivery nip
w_f	Work opening at feed nip

w_h	Uncertainty in height of specimen
w_k	Uncertainty in permeability
w_l	Uncertainty in length
w_{ng}	Uncertainty in no gas height
w_o	Work opening
w_Q	Uncertainty in flow rate
w_{F_v}	Uncertainty in vertical force
x, y, z	Spatial coordinate directions

Chapter 1

Introduction

The sugar cane plant is a grass of the genus *Saccharum* and has a rich source of sucrose containing up to 15% by mass. Australia produces approximately 4.5% of the world's sugar, and the annual export earning from Australian sugar industry is around $1.5 billion. Most of the production occurs in Queensland. Extraction of sugar from the sugar cane stalk is essentially a multistage separation process. Expression of juice from the cane is carried out in the initial stages of the raw sugar production process. The juice extracted from the cane stalk is concentrated to syrup, prior to the production of raw sugar by crystallization. A brief account of various stages involved in the raw sugar production process is given in the next section.

1.1 Sugar production processes

Harvested cane stalks in the form of billets are transported to the mills mostly by rail. On arrival at the mill, the billets are comminuted by heavy-duty swing hammer shredders, converting billets into a mass of finely chopped fibres, thereby exposing their sweet juices. Industries use two methods to extract juice from the prepared cane on a large scale. The first method is by milling or crushing and consists of rolling prepared cane between sets of counter-rotating rollers with light maceration between units. The second method is by a diffusion process, which involves saturation of prepared cane in a large tank of hot water with counter current washing. High residence time and elevated liquid temperature provide favourable conditions for working dissolved sugar from the skeleton matrix where the sugar solution is again collected for further processing. In both methods, the material must still pass through a final dewatering mill to remove as much liquid as possible from the saturated exit blanket. Rolling the prepared cane between sets of counter-rotating rollers is the more traditional method, and this process is repeated several times down a series of mills to ensure that most of the moisture is removed. The dry fibre ($\simeq$ 47-52% moisture) discharged from the last mill is called bagasse and is the main source of fuel for boilers.

The resultant mixed juice from the extraction process contains water, sucrose and other impurities. The juice is heated with lime solution to neutralize the acids, which then forms a precipitate. The clear juice is then pumped to evaporators arranged in series. Steam from the boilers is sent to the first evaporator and the resultant vapour from it is used to boil the juice in the next vessel and so on. In this process about 85% of the water is evaporated, concentrating the juice solids from about 12% to 65%.

Crystallisation of sugar is accomplished by further evaporation of water under controlled conditions, in vacuum pans. At this stage, seed crystals in the form of a slurry are added as nuclei which grow into larger sugar crystals. After discharging from the vacuum pans it passes through crystallisers which are large open vessels under the action of stirring to exhaust more sugar from the mother liquid known as massecuite.

The sugar crystals from the mother liquid are separated by a centrifuge process using a perforated basket lined with a metallic screen that acts as a filter. The raw sugar is discharged and then passes through a drier before being dispatched. The dry sugar thus produced is transported to bulk storage terminals for export and refining to white sugar and other generic products.

1.2 Australian sugar industry

Sugar is Australia's second largest export crop- second only to wheat. The Australian sugar industry produces raw and refined sugar from sugar cane, for use in both

Australia and overseas. Unlike most sugar-producing countries, Australia exports majority of the sugar it produces. Around 85 per cent of the raw sugar produced here is exported.

Australia's sugar industry is based along Australia's east coast from northern Queensland to northern New South Wales, and in Ord river region of Western Australia. The thriving sugar cane farming and sugar industry is largely due to favourable tropical climate, high rainfall and highly mechanised processing techniques.

Over 545,000 hectares are devoted to growing cane in Australia. There are 7,200 cane growers and 30 raw sugar mills. The industry generates more than 40,000 jobs, directly and indirectly. In 1997 season Australia produced 5.74 Million tonnes (Mt) of raw sugar from 41 Mt of sugar cane harvested. Most of the cane production in Queensland is transported to the mills through 4100 km narrow gauge rail network.

1.3 Mill rollers

As this thesis presents the research investigation on the mechanics of sugar cane crushing between rollers, a brief description of rollers are explained in this section. The mill rollers are circumferentially grooved. The grooved rollers break up the bagasse more completely, and thus facilitate the extraction of the juice by the following mills. The section of grooves normally forms a V-shaped grooves with a groove angle. The compression of fibre against the walls of the V-shaped groove gives the gripping action, while the bottom of the groove is not so highly compacted, the drainage of juice results. Sharp groove angle $\sim$(30-35°) give more surface, and this is useful for a better drainage, however groove angle of $\sim 45°$ is also practicable and has been used in sugar mills.

The preferred roll grooving geometry is however not well defined and industrial practice varies significantly. The grooves of two rollers of a mill, for example, are arranged in such a way that the teeth of the top roller mesh with the grooves of the bottom roll as shown in Fig. 1.1. Each milling unit commonly contains six cylindrical

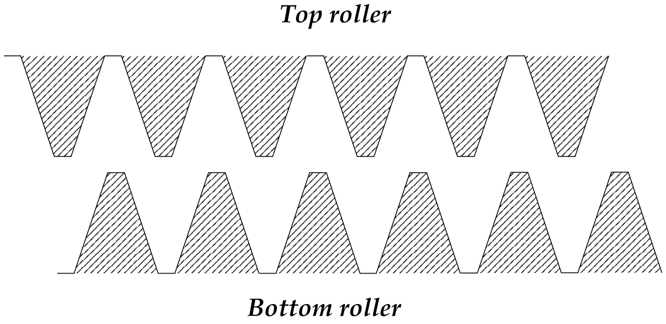

Figure 1.1: Circumferential grooving.

rolls and associated chutes and plates to enable continuous feeding of the material between each set of rolls. Figure 1.2 shows a schematic representation of a six-roll crushing unit.

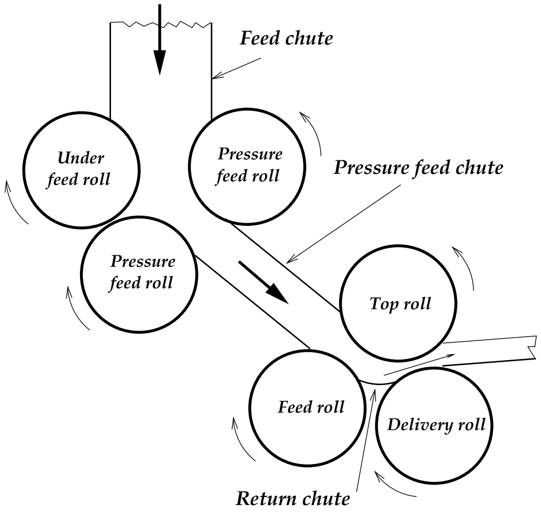

Figure 1.2: Schematic diagram of a six-roll crushing unit.

The current technology defining six-roll milling units evolved largely to increase the crushing rate. Rolling mill technology is largely empirical and has generally evolved with minimal use of advanced analysis for an optimised performance. However, increased research into milling took place in recent years with a motivation of optimising the process itself, rather than increasing the crushing rate itself. In this regard, computational and experimental porous media mechanics has been applied to crushing with a view to an improved understanding of the governing principles.

1.4 Specific objectives of current investigation

While empirical models have served the sugar industries well, they are limited in their use because they are based on limited physics. The fundamental mechanics involved in extraction of juice from sugar cane through crushing is a complex phenomenon that has been studied extensively through experimentation and more recently through coupled mathematical models. In a competitive market, factories strive for improved extraction, rate and reduction in whole-of-life costs. Hence, it is evident that a more thorough understanding of governing mechanisms, particularly those that dominate the boundary region between the bagasse and the grooved surfaces is required. In addition, improved computational models are required to enable the mathematical models to be solved. It is hypothesised that the existing numerical models oversimplify the complex three-dimensional grooving geometry, and while this does not appear to greatly affect roll load, it has a major effect on roll torque. Roll torque is dependent on the local shear stress at the groove/bagasse interface and this cannot be estimated correctly without a three- dimensional model. A further limitation of the existing models involves excessive element distortion at large strain. This can be overcome by mapping the current solution to a revised mesh. In view of the above scenario, the current investigation concentrates specifically on the following areas.

(1) To investigate and determine elasto-plastic constitutive behaviour of the fibrous solid matrix of ruptured cane, from quasi-static confined uniaxial compression experiments.

(2) To investigate and determine experimentally the permeability response which represents juice flow behaviour within the fibrous solid matrix of prepared cane.

(3) Application of the constitutive models for the fibrous solid and liquid flow, and to perform finite element numerical simulation of the crushing process between a pair of rolls.

(4) To conduct two roll mill experiments, and to validate numerical models against experimental data.

(5) Application and improvement of rezoning techniques to multiroll systems.

(6) Application of validated model through a realistic three-dimensional model.

Chapter 2

Literature review and the theory of sugar cane crushing

2.1 Nature of prepared sugar cane

Well grown sugar cane stalks stand as high as 3-4 m in length, and the diameter varies from 20-50 mm. The stalk of cane may be divided into a strong outer peripheral region or rind and an inner soft pith section. At intervals along the stalk are the nodes, similar to bamboo. The rind is a relatively thin external layer of the stalk. By virtue of its high fibre content, rind is the strongest portion of the plant and gives the stalk much of its characteristic strength and rigidity.

Figure 2.1: Portion of inter node transverse section (Sockhill, 1958).

Each individual fibre consist of conducting vessels or tubes called "vascular bundles", which serve to bring soil moisture and plant nutrients to the leaves and return the synthesised sugars for storage to the pith cells. The vascular bundles extend throughout the length of the stalk. Figure 2.1 illustrates the general structure of a segment of a cane stalk in which can be seen the distribution of vascular bundles in the pith and rind section.

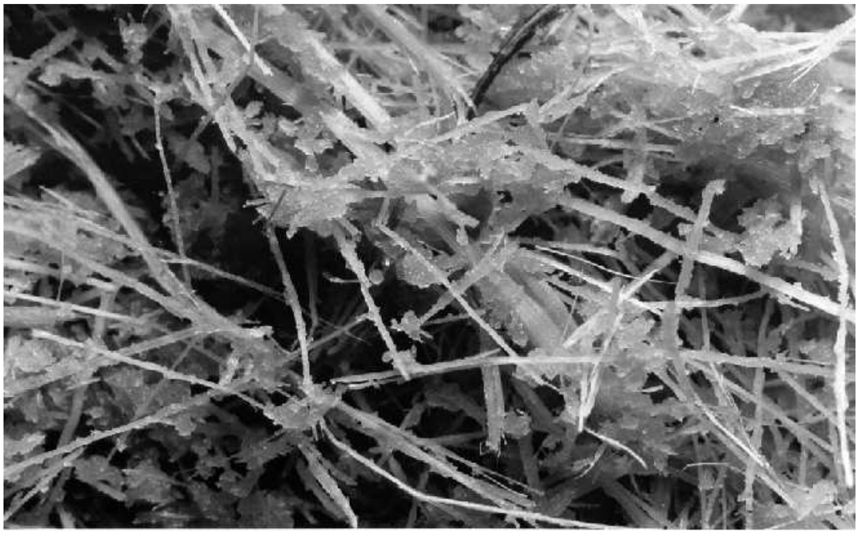

Figure 2.2: Prepared cane.

The sugar cane as such is resistive to applied load depending on the the degree of compaction, high levels of comminution are necessary to attain good extraction performance. At the mills, the cane billets are progressively fragmented between rows of rapidly rotating heavy swing hammers and a stationary grid bar. The shredding process ruptures most of the juice cells, and releases the fibrovascular bundles and the pith cells. The resulting prepared cane consist of solid, liquid and gas with solid content within the range 10-18% by mass. Figure 2.2 shows a macroscopic view of typical "prepared cane".

2.2 Early research (1900-1950)

In simple terms cane consists of solid-fibre, liquid-juice and gas. Ignoring the gas phase, milling is basically a material separation process, in this case separation of juice from the fibre. The separation of juice is carried out in a milling tandem, by successive application of pressure as the cane passes between a pair of rolls. The main factors which determine the efficiencies of juice separation are, degree of cell rupture, effective pressure, drainage, physical properties of fibre, and number of squeezes.

During the beginning of the 20th century Noël Deerr pioneered and consolidated many of the basic principles of sugar technology, by applying scientific techniques through factory observations (Payne, 1983). His works established the foundation for the present day milling theory, that the major factor is the volume occupied by the fibre when compressed between mill rolls. During 1928-31, Deerr presented his well known Algebraic Theory of Extraction of Juice by Milling in the International Sugar Journal. Egeter and others in Java about 1928, carried out extensive milling investigations and made some progress towards a better understanding of the crushing process. Since the juice is removed from the fibrous cane material by the application of pressure, the use of a pressure-volume relationship was considered to be the basics for the early research. Evolution in sugar mill crushing equipment took place in an effort to improve extraction performance. Roll speeds and diameters have been increased to improve the capacity. Juice grooves were installed to provide better drainage. Countless combinations of roll geometry, precompressing rolls, feed chutes, and other mechanical aids have been tried to improve the feedability. These attempts were made with little fundamental knowledge of the mechanics of juice flow or of the forces involved. For decades, the technology of rolling a fibrous material has relied exclusively on the use of empirical models, and trial and error experience.

2.3 Fundamental properties of prepared sugar cane (1950-1990)

Between 1950 and 1990 a number of advances in experimental and theoretical understanding of crushing mechanics was achieved by researchers at the University of Queensland (UQ) and at the Sugar Research Institute (SRI) in Mackay. This work was generally carried out by postgraduate students (Braddock, 1963; Bullock, 1957; Cullen, 1965; Holt, 1963; Munro, 1964; Murry, 1960a; Russell, 1968; Solomon, 1968). The early research programme carried out by Bullock was concerned with fundamental investigations of the mechanics of crushing. For this reason, a two-roll experimental rig was designed and constructed for crushing cane at UQ. Together with the experimental milling investigations, a programme to investigate the physical properties of sugar cane and bagasse from an engineering point of view was also commenced.

Bullock (1957) introduced the concept of compression ratio (C) as the ratio of no-gas volume of cane (V_{ng}) before compression, to the volume of cane (V) at the particular location under investigation. This fundamental definition is defined mathematically as,

$$C = \frac{V_{ng}}{V} \tag{2.1}$$

Besides compression ratio, the compaction and filling ratio have also been used in sugar industries. Compaction (F_c) is the ratio of mass of fibre (m_f) to the volume of cane (V_c), and the filling ratio (F_r) is the ratio between volume of fibre (V_f) and volume of cane. They are mathematically defined as,

$$F_c = \frac{m_f}{V_c} \tag{2.2}$$

$$F_r = \frac{V_f}{V_c} \tag{2.3}$$

The density of dry fibre has been quoted as 1.2-1.4 gm/cm^3 (Hugot, 1986), however its value under different pressures, was estimated from the following relation (Pidduck, 1955)

$$\rho_f = 1.512 + 1.61X10^{-6}P_a \tag{2.4}$$

where P_a is pressure in axial direction in psi, while the density of fibre ρ_f is expressed in g/cm^3. The density of fibre as 1530 kg/m^3 has been used since 1960. The bulk density of cane based on fibre content and the juice density is found as follows. As the volume of cane V_c is comprised of fibre volume and juice volume,

$$V_c = V_f + V_j \tag{2.5}$$

Here V refers to the volume and the suffix c, f and j refers to cane, fibre, and juice respectively. Expressing the cane, fibre and juice volumes in terms of their respective densities, Eq. (2.5) becomes,

$$\frac{1}{\rho_c} = f\frac{1}{\rho_f} + \ (1-f)\frac{1}{\rho_j} \tag{2.6a}$$

$$\text{or } \rho_c = \left[\frac{f}{\rho_f} + \ (1-f)\frac{1}{\rho_j}\right]^{-1} \tag{2.6b}$$

where f is the fibre ratio, and ρ is density.

2.3.1 Treatment number

Cane that had undergone high levels of comminution gives a better milling performance, hence an appropriate indicator of comminution is also a measure to predict the milling performance. This was dealt through a new measurement, termed *"treatment number"* (Loughran, 1990) which is statistically independent of fibre content. This new measurement for assessing the preparation level of prepared cane was based on pre-compressor experimental results. The treatment number, â, is expressed as,

$$\hat{a} = \tfrac{1}{C} - 6.3f \tag{2.7}$$

where C is the compression ratio at 50 kPa in the pre-compressor, and f is the fibre content expressed as a fraction. A treatment number of 0.4 corresponds to finely prepared cane, and treatment number of 1.1 would represent coarsely prepared cane.

2.3.2 Theoretical juice extraction

In estimating the efficiency of a milling process, an expression for the theoretical juice extraction as a function of compression ratio was derived, based on simple volumetric theory of extraction. The blanket of prepared cane entering a mill unit consists of juice and fibre. Assuming the material leaving the mill moves at the same speed as the roll surface, the volume of material leaving the mill in unit time is given by the escribed volume of the mill rolls and it is denoted as $\dot{V}_e$. If $\dot{V}_{ng}$ is the no-void volume rate of material entering, since both fibre and juice are almost incompressible, the reduction in the volume rate of juice extracted $\dot{V}_{je}$ is,

$$\dot{V}_{je} = \dot{V}_{ng} - \dot{V}_e \tag{2.8}$$

The total volume rate of juice entering the mill in unit time is given by,

$$\dot{V}_j = \dot{V}_{ng} - \dot{V}_f \tag{2.9}$$

where $\dot{V}_f$ is the volume rate of fibre. The extraction fraction E is given by

$$E = \frac{\dot{V}_{je}}{\dot{V}_j} = \frac{(\dot{V}_{ng} - \dot{V}_e)}{(\dot{V}_{ng} - \dot{V}_f)} = \frac{1 - \frac{\dot{V}_e}{\dot{V}_{ng}}}{1 - \frac{\dot{V}_f}{\dot{V}_{ng}}} \tag{2.10}$$

The term $\dot{V}_{ng}/\dot{V}_e$ is the ratio of no gas volume $\dot{V}_{ng}$ to escribed volume rate $\dot{V}_e$, and is the nip compression ratio of the mill. Expressing the volume rates $\dot{V}_f$ and $\dot{V}_{ng}$ in terms of fibre and no-gas densities respectively, the theoretical extraction becomes,

$$E = \frac{1 - \frac{1}{C}}{1 - f\frac{\rho_{ng}}{\rho_f}} \tag{2.11}$$

2.3.3 Reabsorption in sugar mills

Experiments shows that the actual extractions realized in a mill, fall below the ideal Eq. (2.11). Egeter (1928) was the first to observe that in a mill when the speed of the mills becomes high enough, the cane material moved forward at a speed exceeding that of the rolls. When this occurs, the volume of bagasse leaving a mill is greater than the volume escribed by the rolls. This reduces the extraction performance of a mill. Hence, to account for this, it is postulated that, at least some of the material is moving faster than the rolls in the axial plane. In this case

$$\dot{V}_{je} = \dot{V}_{ng} - \dot{V}_b \tag{2.12}$$

where $\dot{V}_b$ is the volume rate of bagasse leaving the mill. Equation (2.10) becomes

$$E = \frac{1 - \frac{\dot{V}_b}{\dot{V}_{ng}}}{1 - \frac{\dot{V}_f}{\dot{V}_{ng}}} \tag{2.13}$$

and re-expressing Eq. (2.11) to incorporate this new concept, we have

$$E = \frac{1 - \frac{1}{C}\frac{\dot{V}_b}{\dot{V}_e}}{1 - f\frac{\rho_{ng}}{\rho_f}} \tag{2.14}$$

Murry (1960a) noted that this phenomenon is similar to inline steel rolling, and the term $\dot{V}_b/\dot{V}_e$ has been used as the “reabsorption factor” in sugar industries. It is denoted by K, and the equation governing the mill extraction is,

$$E = \frac{1}{1 - f\frac{\rho_{ng}}{\rho_f}}(1 - \tfrac{K}{C}) \tag{2.15}$$

The bagasse, leaving the mill, has the capacity to re-absorb a portion of the juice as it passes the axial, plane of the rollers. Thus a large portion of benefit just obtained is lost and much of the power expended is wasted. No method has been found to remedy this inherent disadvantage of milling. However, over the years several possible mechanisms have been reported to describe this phenomenon (Bullock, 1957; Holt, 1963; Murry, 1960a; Solomon, 1968). Egeter concluded that the most plausible explanation was that juice on the feed side of the nip must squirt forward through the compressed cane mat at the nip at a speed faster than the average speed of the mat relative to the mill frame. Bullock (1957) carried out experiments on a two-roll mill and assessed the reabsorption quantitatively. Further study on the behaviour of the coefficient of friction of prepared cane on grooved surface led to the conclusion of forward slipping of the compressed fibre mat through the nip, at speeds greater than the roll speed. Bullock quantified the reabsorption by the influencing mechanical quantities such as compression ratio, degree of preparation, roll surface speed by an empirical relation. Cullen's Master's thesis (Cullen, 1965) summarizes the following reasons for the reabsorption to occur in a mill.

(1) By free juice passing through the interstices of the blanket at a speed greater than that of the blanket.

(2) By free juice, passing along the boundary surfaces between rollers and blanket.

(3) By extrusion of the whole blanket through the work opening.

(4) By a combination of two or more of the above.

(5) By movement of the juice forward along the bottom of the grooves not completely filled with bagasse.

(6) By internal shear of the material.

The work of Bullock, Crawford and Holt (Bullock, 1957; Crawford, 1959; Holt, 1963) however indicated that there is a strong possibility of a shear failure or extrusion of bagasse under pressure that is of the same order as those existing during milling. Hence, Cullen (1965) performed direct shear tests and determined the limiting and dynamic coefficient of friction on steel over varying conditions of speed, groove, and cane preparation. He further indicated that the failure of a bagasse sample could occur by shear rather than slip on the roll surfaces. Murry obtained experimental values of reabsorption factor as a function of compression ratio, over a wide range of conditions in the experimental mill. Loughran (1990) proposed a model for reabsorption factor on the experimental two-roll data of Murry based on his treatment number that is independent of fibre content,

$$K = 1.128 - 0.0904C - 0.437S - 0.496\hat{a} + 0.31C\hat{a} + 0.56CS \tag{2.16}$$

where C = compression ratio.

S = roll surface speed (m/s).

$\hat{a}$ = treatment number.

2.4 Fundamental theory of crushing mechanics

Roll load and torque are fundamentally important parameters in assessing the strength and life time of rollers and to estimate the energy required in achieving the crushing rate. Attempts have been made, without great success to estimate load and torque from hydraulic press tests (Bullock, 1957; Hugot, 1986; Jenkins, 1956; Murry, 1960a). Murry (1960a) suggested that these attempts have failed because of two reasons. The first is that the reabsorption phenomenon has not been taken into account. The second reason is that the flow pattern of juice in the mill is basically different from that in a compression test. From considerations of the basic mechanics of the forces on the mill, and juice flow in the mill and in a compression test, it is possible to predict a pressure distribution during crushing, and hence the roll load and torque requirements, from the results of dynamic compression tests and a knowledge of a reabsorption factor.

2.4.1 Early mill experiments

Murry and Holt (Holt, 1963; Murry, 1960a) constructed a special test cell of width the same as a two-roll experimental mill, and length approximately simulating the effective arc of contact for the mill. Cane was compressed uniaxially between grooved platens identical to that used in a mill, to simulate milling conditions. A one-dimensional model for juice expression in a press and an experimental two-roll mill were developed.

Good agreement between roll loads and torques as predicted for the mill, from hydraulic press tests were obtained. The success of the Murry and Holt models based on that special test cells, enabled an equivalent dynamic permeability to be calculated as a function of compression. The Murry and Holt models however cannot be applied to rolls of larger diameter without investigating in new test cell of the required geometry due to scale effects.

The mill experiments at the University of Queensland have shown that the whole process of juice extraction and power compressions are highly complicated. Many factors such as cane preparation, roll speed, work opening, crushing rate, roll load, juice grooves and roll diameter affect the results. A quantitative analysis has shown the various interactions which exists between these factors. Murry and Holt (1967) report from dimensional analysis, the milling quantities likely to influence roll load and torque. Four dimensional groups were identified from six independent quantities. The dimensional analysis indicates that the compression ratio, preparation (represented by ratio of bulk density to no-void density of cane) and the work opening to diameter ratio (w_o/D) ought to influence roll load and torque. Further, the load and torque equations suggest that they are proportional to crushing rate (Q_C) times the surface speed of roll (S). The experimental evidence (Murry, 1960a; Russell, 1968) agrees with this in part. Roll load increases with compression ratio, decreases with fineness of preparation and increases with diameter. Roll load and torque decrease slightly as surface speed increases, however it conflicts with the dimensional analysis, since the dimensional analysis does not account for the reabsorption phenomenon.

2.4.2 Two-roll mill geometry

The investigation at UQ's two-roll mill during 1960's was carried out under controlled laboratory conditions, together with the physical properties of cane from an engineering point of view. This has led to a better understanding of the basics of milling theory, than from factory investigations where the fundamentals were hindered by the presence of numerous uncontrolled variables. The flow pattern of the juice in the mill was ascertained from permeability considerations. The permeability decreases rapidly as the compression ratio increases, and hence the juice flow in a mill at the minimum opening is markedly affected.

The juice flow can be considered to be in two parts- that juice which will finally be in the bagasse called "fixed juice", and that juice which will be extracted is "free juice" (Murry, 1960b). Material entering the mill, therefore will be comprised of volume of fibre, volume of fixed juice and the volume of free juice. At steady state, the volume entering the shaded wedge in Fig. 2.3 must be equal to the volume leaving. This ideology indicates that all the free juice will be expressed in the early parts of compression. It is reasonable to say that no juice which is to be extracted need enter the mouth of the mill. Hence a pool of "stationary" juice under pressure, is formed in the shaded wedge of Fig. 2.3 and the pressure in this juice serves to push the free juice out at some section near the mouth of the mill.

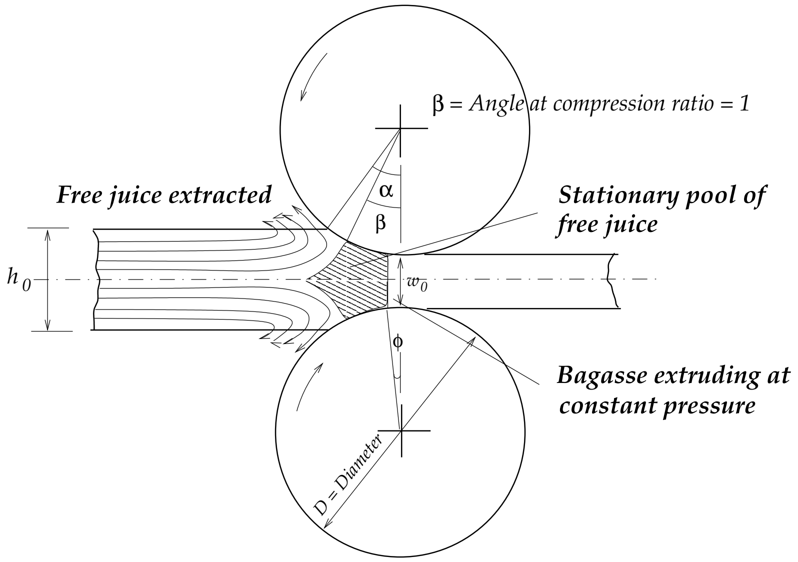

Figure 2.3: Juice flow.

As the volume is reduced when the material moves in, the no void volume of the solid material is reached and from here on the system is one of essentially constant mass, and no further juice is expressed. Using this postulate of constant mass, the basic governing equations were set (Murry, 1960a).

Considering a pair of rollers as shown in Fig. 2.3, the mill compression ratio at the minimum work opening (w_o) is expressed in terms of no gas height (h_{ng}) and the contact angle α as

$$C = \frac{h_{ng} \cos \alpha}{w_o} \tag{2.17}$$

The contact angle α is a matter of mill geometry is expressed as

$$\alpha = \cos^{-1} \left(1 + \frac{w_o}{D} - \frac{h_o}{D} \right) \tag{2.18}$$

The general expression for work opening is

$$w_o = \text{set opening} + \text{ one groove depth} \tag{2.19}$$

For the grooved rolls, when the grooves are mesh, the set opening or the tip to tip distance is negative in the above expression. The compression ratio C_θ as a function of angle θ may be expressed as

$$C_\theta = \frac{C_o \frac{w_o}{D}}{\left(1 + \frac{w_o}{D} - \cos \theta\right) \cos \theta} \tag{2.20}$$

where C_o is the compression ratio of the mill.

2.4.3 Determination of roll load and roll torque

Experiments show that the pressure required to compress dry fibre from finely prepared cane is fairly small (Murry, 1960a) and therefore, the major pressures in the mill are probably due to the juice flow. On this basis, for a simplified two-roll system shown in Fig. 2.3, it has been assumed that Darcy's law (see Section 2.5.1) for flow of liquid through porous media holds for the material under consideration. Hence the flow of liquid through porous media may be represented by an equation of the form,

$$Q = \frac{AK}{\eta}\frac{\mathrm{d}p}{\mathrm{d}l} \tag{2.21}$$

where Q = volume flow rate of liquid.

A = total cross-sectional area available for flow.

η = dynamic viscosity of liquid.

$\frac{\mathrm{d}p}{\mathrm{d}l}$ = pressure gradient in the direction of flow.

K = constant characteristic of the medium termed "permeability".

If the mean superficial velocity of juice $S_j = Q/A$, relative to the roll surface speed S, the differential pressure can be shown to be

$$\mathrm{d}p = \frac{S\eta D}{2}\frac{1}{K}\frac{h_\theta - h_{s\theta}}{h_\theta}\, cos^2\theta \; \mathrm{d}\theta \tag{2.22}$$

where h_θ = total height between the rolls.

$h_{s\theta}$= height of the solid material.

The variation of total height (h_θ) between the rolls is a matter of mill geometry, and it is expressed as,

$$h_\theta = D\left(1 + \frac{w_o}{D} - cos\theta\right) \tag{2.23}$$

Murry (1960a) has also postulated a vertical plane at $\theta = \phi$, the position of the neutral plane at which reabsorption may be considered to start. The neutral plane is determined by the following relation,

$$cos\phi = \frac{1}{2}\left(1 + \frac{w_o}{D}\right) + \left[\frac{1}{4}\left(1 + \frac{w_o}{D}\right)^2 - K\frac{w_o}{D}\right]^{\frac{1}{2}} \tag{2.24}$$

Experiments have given the permeability as a function of compression ratio C, of the cane. It can be shown that the determined values of permeability can be expressed in terms of a power function of the form (Murry and Holt, 1967)

$$K = aC^{-b} \tag{2.25}$$

where a, and b are constants depend on the degree of fineness of preparation of the cane.

Figure 2.4: Pressure distribution (Holt, 1963).

The shape of the pressure distribution was investigated (Murry, 1960a) by solving the Eq. (2.22) over the contact surface of the roll. A typical form of pressure distribution is shown in Fig. 2.4. In general, it appears that the theories developed for the prediction of a pressure distribution gave practical results.

On the postulate that the main loads on the roll surface are due to the fluid pressure through the fibrous material, it is possible to develop the relationship for the separating force between the rolls. Considering the forces on an element of roll surface (Fig. 2.5), the radial force F_r due to the pressure of the bagasse is

$$F_r = p\frac{D}{2}\,\mathrm{d}\theta \tag{2.26}$$

where D is the diameter of the roll. The tangential force F_t required to move the cane into the mill is

$$F_t = \mu p \frac{D}{2}\, \mathrm{d}\theta \tag{2.27}$$

where μ is the friction factor, which is the ratio of tangential force to the radial force.

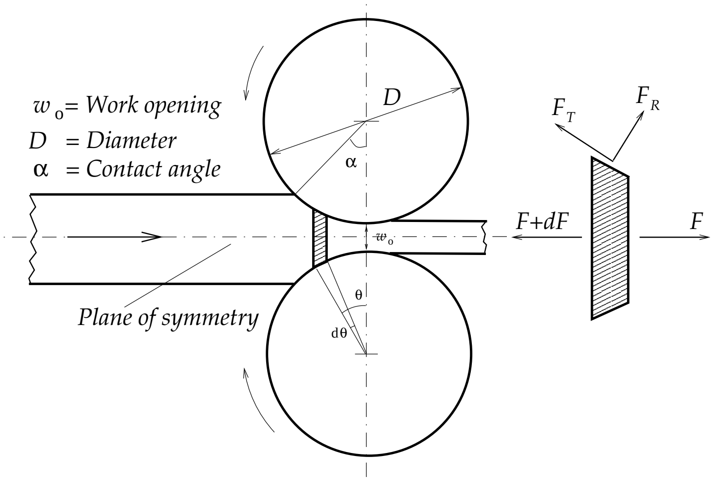

Figure 2.5: Forces on roll surface.

Resolving the component of roll load along the centre of the rolls, the element separating force dr, per unit length is,

$$\begin{aligned} \mathrm{d}r &= F_r\, cos\theta + F_t\, sin\theta \\ &= \frac{D}{2} p\,(cos\theta + \mu\, sin\theta)\, \mathrm{d}\theta \end{aligned} \tag{2.28}$$

Or, the total separating force R, for a roller with Length L is

$$R = \frac{LD}{2} \int p\,(cos\theta + \mu\, sin\theta)\, \mathrm{d}\theta \tag{2.29}$$

The element of roll torque, dt on unit length of the roll is

$$\begin{aligned} \mathrm{d}t &= \frac{D}{2} F_t \\ &= \frac{D^2}{4} \mu p\, \mathrm{d}\theta \end{aligned} \tag{2.30}$$

or the total torque on one roll, T, is given by

$$T = \frac{LD^2}{4} \int \mu p \, \mathrm{d}\theta \tag{2.31}$$

The integral for Eq. (2.29) and Eq. (2.31) is taken from the position at which cane contacts the roll to the position where the bagasse leaves the rolls. In order to solve the equation for load and roll torque it is necessary to know both μ and p as a function of θ. Murry (1960a) set $\mu = \tan\theta$ for $\theta \geq \phi$, and he has utilized the pressure variation as a function of θ from Eq. (2.22). The roll load and torque predicted from the pressure distribution correspond fairly close to those encountered with the experimental two-roll mill. This approach gives a fast and fairly accurate estimate of the load and power requirements for a two-roll mill (Holt, 1963).

Russell (1968) developed a mathematical equation to estimate the total roll load per unit length on a pair of rolls for any feed or delivery nip along the milling train. No account of the roll load as a function of roll speed was considered, and the load proportionality factor only represents an average material fineness at a particular mill. Murry and Holt (1967) recognized this fact and suggested an empirical model, where the roll load was a function of nip compression ratio and bulk density as measured with a precompressor apparatus. This model suffered from the fact that bulk density alone is not a good measure of preparation as it is compounded by the level of the fibre in the cane. A new empirical model of roll load that incorporates the treatment number was built, using data collected at UQ over 30 years ago (Loughran, 1990). The model also includes diameter (D) and roll surface speed (S), but was specific to cane mills and cannot be applied to bagasse mills. The roll load equation using experimental two-roll mill data (Bullock, 1957; Murry, 1960a) is estimated in the following form,

$$R = 647 - 2611D - 1330S + 722DC + 3385DS + 1006D\hat{a} - 818DCS\hat{a} \tag{2.32}$$

where $R =$ roll load (kN/m).

$D =$ roll diameter (m).

$S =$ roll surface speed (m/s).

$C =$ compression ratio.

$\hat{a} =$ treatment number.

Although the empirical relations for load, torque and extraction performance based on experiments are used in milling practices, the effects of roll diameter, cane preparation, cane varieties, fibre content and scale effects of experimental mills are not adequately considered in the emprical models. Due to the semi-empirical nature of the technology, extrapolation of predictions to very large diameter, novel roll arrangements is questionable as it requires a basic understanding of the kinematics and dynamics of juice flow through bagasse (Loughran and Murry, 1988). The need to increase rate and reduce cost has resulted in increased research into the governing principles of the crushing process over recent years.

2.5 Prepared cane as a deformable porous media

Sugar cane, being a biological material, does not exhibit the well known stress-strain characteristics of the common engineering materials. This is due to its composition of fibrovascular bundles and other cellular material. The primary constituents of prepared cane are insoluble and soluble solids. The insoluble solid is about 8-18% percent of stalk mass composed of fibrovascular bundles, storage cell walls, and rind. The soluble solid is composed of sugar (sucrose, glucose and fructose) and dissolved impurities. Water constitutes 73-76% by mass of the cane stalk. A proportion of the water is loosely chemically attached to the insoluble solid material which is about 25-30% of the fibre mass. The sugar cane juice consists of water and soluble solids. The percentage distribution of these different component phases for a given mass is illustrated in Fig. 2.6. For all practical purposes, the insoluble solid components are collectively referred as *fibre* in this thesis.

On a macroscopic scale, prepared cane be considered as saturated and unsaturated porous medium with a combination of solid fibres and voids. The term *voids* is assumed to encompass both the volume of liquid juice and the volume of entrapped air. Hence, a total prepared cane mass will be assumed to be composed of solid fibre, liquid juice, and air. For convenience, the mass is separated into these three basic components, as illustrated in Fig. 2.6. When the prepared cane is subject to stress, it deforms.

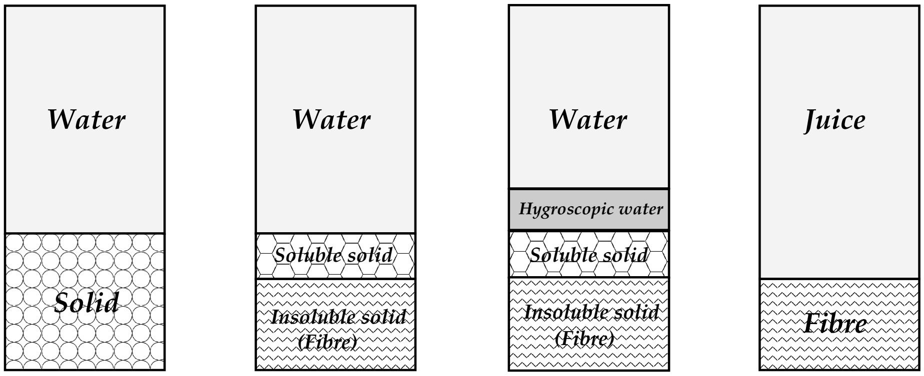

Figure 2.6: Constituents of sugar cane.

While the volume of solid and liquid in a given mass remains constant, the gaseous or the air phase volume is subject to change very easily. The ratio of the volume of juice or liquid (V_w) to the volume of voids (V_v) expresses the degree of saturation and it may be written as

$$S = \frac{V_w}{V_v} \tag{2.33}$$

From Eq. (2.33), one notes that the degree of saturation varies from S = 0 for a completely dry fibre, to S = 1 for saturation, where the void consists of only liquid. The other property which describes the closeness of packing of the solid fibres is described by the *specific volume* v, and it is expressed as,

$$\text{Specific volume, } v = \frac{V}{V_s} \tag{2.34}$$

where V_s = volume of solid.

Sometimes, the *void ratio*, e of the prepared cane mass is used instead of specific volume, where

$$\text{Void ratio, } e = \frac{V_v}{V_s} \tag{2.35}$$

Since $V = V_v + V_s$, the relationship between specific volume and void ratio may be written as

$$v = 1 + e \tag{2.36}$$

Another way of expressing the void ratio is through the *porosity* n

$$\text{Porosity, } n = \frac{\text{Volume of voids}}{\text{Total volume}} = \frac{V_v}{V} \tag{2.37}$$

The porous material model illustrated in Fig. 2.7 shows the volume dimensions.

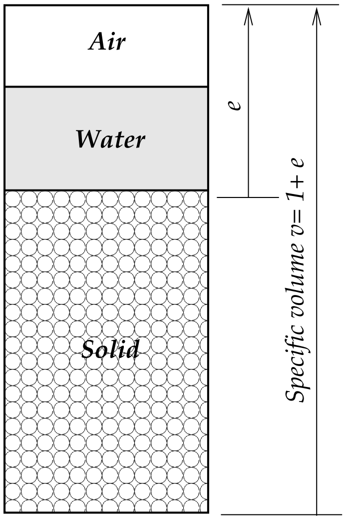

Figure 2.7: Unit volume soil model.

2.5.1 Darcy's law

Flow phenomenon in porous media was first studied by Darcy in 1856. Darcy demonstrated experimentally, that the rate of flow of water through a soil is proportional to the hydraulic gradient i.

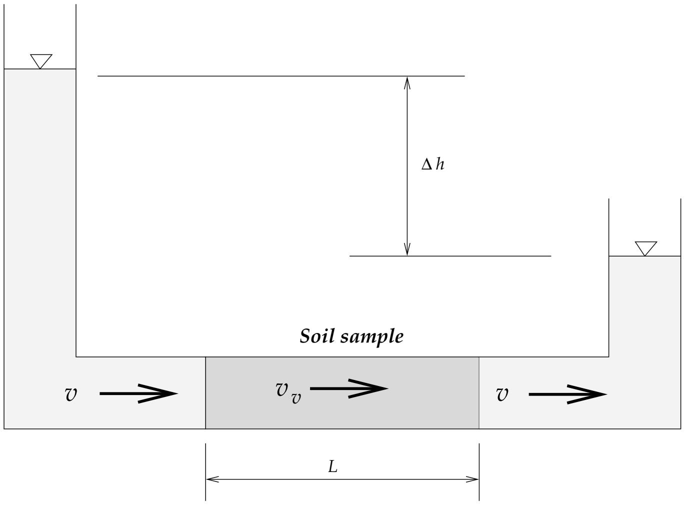

Figure 2.8: Flow through soil.

Referring to Fig. 2.8 and assuming laminar flow, Darcy's law may be written as

$$Q = kiA \tag{2.38}$$

$$\text{or } Q = k\frac{\Delta h}{L}A \tag{2.39}$$

where Q = volume rate of flow.

k = coefficient of permeability.

i = gradient or head loss between two given points = $h_1 - h_2/L$.

A = total cross-sectional area of tube.

Δh = difference in heads at the two ends of soil sample.

L = length of sample.

The velocity of water through the soil voids, or *seepage velocity* v_v is different from the tube velocity v, since the cross-sectional area of the voids A_v is much smaller than the tube area, A. For continuity of flow, the quantity of flow Q must be the same throughout the system. Hence,

$$Q = Av = A_v v_v \tag{2.40}$$

from which

$$v_v = \left(\frac{A}{A_v}\right) v = \left(\frac{AL}{A_v L}\right) v = \left(\frac{V}{V_v}\right) v \tag{2.41}$$

$$\text{or } v_v = \frac{1}{n} v \tag{2.42}$$

$$\text{or } v = n v_v \tag{2.43}$$

where V = total volume of mass.

V_v = volume of voids.

n = porosity (ratio).

From Eq. (2.38), $Q/A = v = ki$. Hence, substituting in Eq. (2.42)

$$v_v = \frac{ki}{n} \tag{2.44}$$

Values for the coefficient of permeability k for porous materials depend largely on the grain size or more particularly on the size of void spaces through which the seepage takes place. We note that the common unit for the coefficient of permeability is that of velocity. The k of a soil or porous material is a constant of proportionality between the tube velocity v and the hydraulic gradient i. However, the value of k may vary quite greatly for a given porous material with the direction of flow, pore size, degree of saturation etc.

Pore fluid flow within the fibrous solid matrix of prepared sugar cane may be modelled by applying Darcy's law, where the pore fluid phase is assumed continuous and homogeneous over a representative elementary volume of material. In reality, the formation of "dead end" pores at higher compression levels causes discontinuity of the liquid phase, however this behaviour is reflected in the rapid decrease of permeability with decreasing void ratio (Adam, 1997).

2.5.2 Effective stress

The compression of prepared cane and the associated expression of juice is seen as a flow through deformable porous medium problem. The force applied to the sample of prepared cane subjected to a compression test is resisted by both pore fluid (juice and air) pressure and the fibrous skeleton. Lambe and Whitman (1969) suggested that the amount of compression that has occurred at any time is related to both the applied load and the amount of stress transmitted at the particle contacts, i.e. difference between the applied stress and the pore pressure. This difference is called the "effective stress".

The importance of pore pressure is the first major step towards the understanding the stress at the fibrous skeleton. The definition of effective stress was first formulated by Terzaghi (1943) while studying the behaviour of porous soils. The pore spaces in a soil are interconnected and pressure may therefore be transmitted through the pore fluid between two points in the soil, and for the water to flow through the soil, a pressure differential must exist.

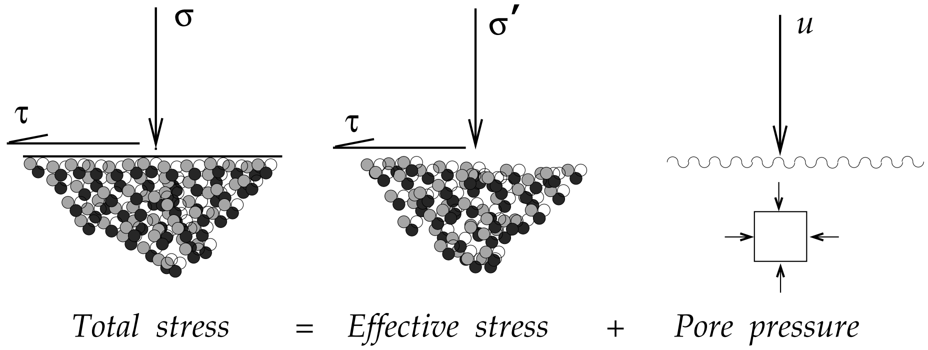

Figure 2.9: The principle of effective stress.

When an external stress is applied to a saturated soil mass, the immediate effect is an increase in the pore pressure. This produces a tendency for the pore water to flow away through adjoining voids, with the result that the pore pressure decreases as the applied stress is transferred to the granules. The main effect of pore pressure is to reduce the contact forces between soil particles, by “pushing apart” the particles. This means that, at steady state, the total stresses within the body of soil are transferred through fluid pressure in the pores, and partly through the solid grains (Fig. 2.9). Loads transferred by the solid grain are transferred between the grain via their point of contact. The deformation and failure of soil are related only to the inter particle forces, which are most conveniently described in terms of an “effective” stress, which is the summation over unit area of the components of inter particle forces normal to any plane under consideration.

Algebraically the definition of effective stress for a saturated porous material is given by

$$\sigma' = \sigma - u \tag{2.45}$$

where σ is the total normal stress on some plane at a point within the soil, u is the pore pressure at the point, and σ' is the corresponding normal effective stress on the plane. It is this stress component that is effective in controlling both volume change deformation and the shear strength of the soil. Fluid cannot resist shear stresses so that the shear stress on a plane is not affected by pore pressure. It may be noted that the effective normal stresses cannot be measured directly, as they are a cumulative effect of a large number of local highly stressed contact between grains. They are determined only as the difference between the total stress and the pressure.

Loads transferred by the solid phase are transferred between the particles via their points of contact. Since both normal stress and shear stresses are transmitted across the fibrous contacts, it is convenient to express the stress as the load divided by a more “identifiable” area. The “identifiable” area is at the contact points between solid particles, and an irregular line as shown in Fig. 2.10 which passes tangentially through the contact interfaces between particles. Thus the effective stress can be regarded as the contact forces between soil particles averaged over the whole area of the soil. The validity of the effective stress with regard to saturated prepared cane lies in the assumption of the point of contact between the solid particles.

Figure 2.10: Contact area in soil (Lambe and Whitman, 1969).

2.6 Continuum approach

Prepared sugar cane is unsaturated and becomes saturated under light loading. Juice extraction, in practice takes place when it is fed between multi-roller crushing units. Hence, the compression of cane is a "flow through deformable porous media" problem. The problem is complex, as there are interactions between juice pressure, fibre stress and the loading rate. Cane variety, possible inclusion of dirt and other foreign matters, and varying degrees of comminution are other compounding parameters. The prepared cane is considered to be a saturated and unsaturated porous medium composed of a solid skeleton separated by space or voids which are filled with liquid or gas or both.

The gaseous component may have little or no influence on the rolling process. The solid phase is assumed to be distributed throughout the porous medium in such a way that it is present inside each representative unit volume. It is assumed that this unit volume in the porous material can be considered large when compared to the pores but still small as compared to the overall extent of the domain. On a macroscopic scale, it is assumed that the prepared cane acts as a porous medium, is continuous with fluid and solid phases forming an overlapping region (Zhao, 1993).

2.6.1 Theory of stresses

The customary mathematical treatment of stress requires that the body be continuous. This however gives rise to some concern when dealing with fibrous material like prepared cane. The effect of confined pressure on the fibres, for example is to draw them into a denser, more stable arrangement normal to the applied pressure. Fortunately, the continuity limitation is not important, because the calculated stress represent average values involving a great number of individual fibres, and these values are compared with similar average values of strength which are obtained from standardized tests of the material.

Force intensity (force per unit area) or called stress, is a useful term to compare with the strength properties of the materials. For a material, which is a continuous media, where the scale of interest is macroscopic rather than microscopic, the mathematical concept of local stress at a point is obtained as the limit.

The stress when acts normal to the areas concerned, is known as *normal stress.* Normal stresses can be either tensile (as in Fig. 2.11) with the force acting out of the area to which it is applied, or compressive, with the force acting into the area. The normal stresses shown in Fig. 2.11 are uniaxial, in that they act in one direction only, the direction along the length of the bar.

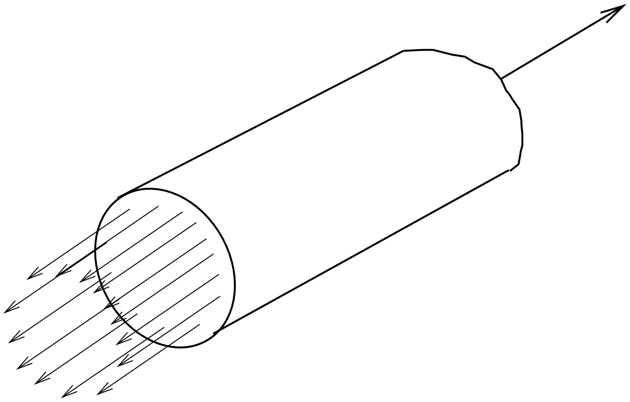

Figure 2.11: Normal tensile load.

More common are the biaxial and triaxial states illustrated in Fig. 2.12, where the stresses act in two and three mutually perpendicular directions respectively. When the cross sectional area of a block of material is subject to a distribution of forces which are parallel, rather than normal to the area concerned, such forces are referred to as *shear forces*. For a continuum, the local shear stress τ at a point may be defined as

$$\tau = \lim_{\delta A \to 0} \frac{\delta F}{\delta A} \tag{2.46}$$

where δF is the magnitude of the force acting over a small element of area δA.

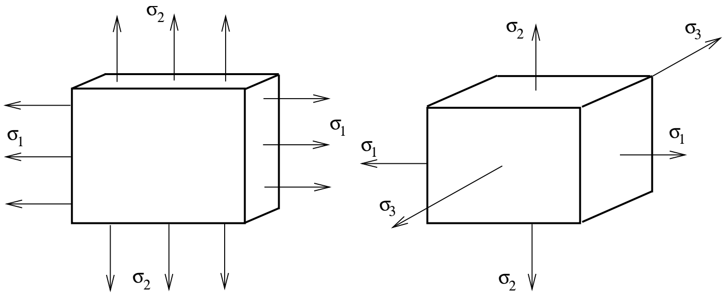

Figure 2.12: Multidimensional forces.

Except in simple cases, the planes on which the maximum normal and shear stresses act for complex stress states cannot be determined by inspection. In general, the overall stress state is determined first, and then maximum stress values are derived from the information. The state of stress at a point can normally be determined by computing the stresses acting on certain conveniently oriented planes passing through the point of interest. Stresses acting on any other planes can then be determined by means of simple, analytical methods. Hence knowledge of stresses on any three mutually perpendicular planes passing through a point is sufficient to define the state of stress at that point.

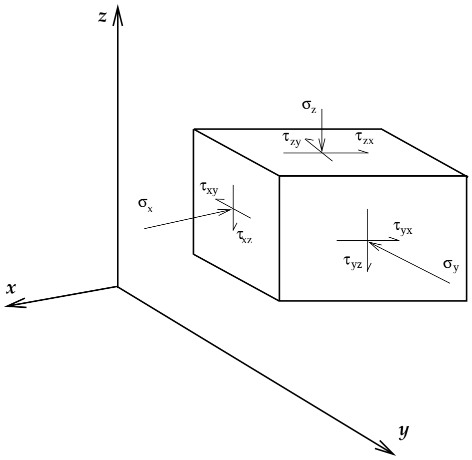

Figure 2.13: Triaxial elemental stresses.

It is convenient to consider the three mutually perpendicular planes as faces of a cube of infinitesimal size, which surrounds the point at which the stress state is to be determined. This cube or rectangular prism is called a stress element. Figure 2.13 shows a conventional representation of a stress element of a larger continuous body with reference to a rectangular coordinate system.

Forces are transmitted across each of the six faces of the element, and they can be conveniently described in terms of the stress tensor σ_{ij}.

$$\sigma_{ij} = \begin{pmatrix} \sigma_{xx} & \sigma_{xy} & \sigma_{xz} \\ \sigma_{yx} & \sigma_{yy} & \sigma_{yz} \\ \sigma_{zx} & \sigma_{zy} & \sigma_{zz} \end{pmatrix} \tag{2.47}$$

$$= \begin{pmatrix} \sigma_{x} & \tau_{xy} & \tau_{xz} \\ \tau_{yx} & \sigma_{y} & \tau_{yz} \\ \tau_{zx} & \tau_{zy} & \sigma_{z} \end{pmatrix} \tag{2.48}$$

Each component of the stress represents a force acting in a specific coordinate direction on a unit area oriented in a particular way. Thus σ_{xy} is the stress in the positive x direction acting on a unit area whose outward normal is in the positive y direction. The term σ_{xx}, σ_{yy} and σ_{zz} are normal stresses, and the rest are shear stresses. Although Fig. 2.13 shows the general state of three-dimensional stress to involve nine stress components, only six of these components are independent. By momentum equilibrium, the three equal pairs of shear stresses,

$$\tau_{xy} = \tau_{yx}; \quad \tau_{xz} = \tau_{zx}; \quad \tau_{yz} = \tau_{zy} \tag{2.49}$$

Similar to stress tensor σ_{ij}, nine components of the strain tensor are designated by ϵ_{ij}.

When the tensor represents the state of stress at a point, there always exists a set of mutually perpendicular planes on which only normal stresses act. These planes of zero shear stress are called principal planes, the direction of their outer normals are called principal directions, and the stresses acting on these planes are *principal stresses.* It should also be emphasized that there are maximum and minimum shear stresses in the planes considered. Relationships exist for directions and magnitudes of maximum shear stresses, and for normal stresses on planes of maximum shearing stresses (Shigley, 1963).

2.6.2 Stress invariants

In a stressed body the components of stresses are $\sigma_x, \sigma_y, \sigma_z, \tau_{xy}, \tau_{yz}$ and τ_{zx}. Stresses acting on any other set of axes (e.g., a, b, c in Fig. 2.14) can also be determined by means of simple analytical methods. Stress invariants are functions of stress components which are independent of the axis system chosen. For example,

$$p = \frac{\sigma_x + \sigma_y + \sigma_z}{3} = \frac{\sigma_a + \sigma_b + \sigma_c}{3} \tag{2.50}$$

is a stress invariant. The stress invariant p in terms of the principal stress is written as

$$p = \frac{\sigma_1 + \sigma_2 + \sigma_3}{3} \tag{2.51}$$

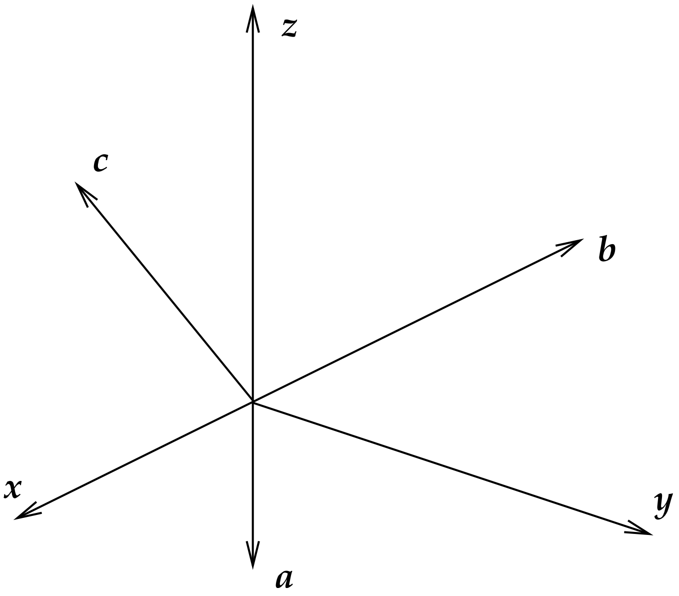

Figure 2.14: Planes of stresses.

Another stress invariant is q where

$$q = \sqrt{\frac{(\sigma_x - \sigma_y)^2 + (\sigma_y - \sigma_z)^2 + (\sigma_z - \sigma_x)^2}{2}} \tag{2.52}$$

The stress invariants p and q provide indication of the normal and shear stresses respectively and they are known as mean stress and deviator stress in soil mechanics. They may be used together with void ratio e, to define stress states and to plot the stress paths. It may be noted that the principal stresses σ_1, σ_2 and σ_3 are also stress invariants.

2.6.3 Concept of strain and of state of strain

Any physical body subjected to stress, deforms under the action of the applied load. Strain is the direction and intensity of the deformation at any given point with respect to a specific plane passing through that point. Thus, for every stress component or invariant there is a "corresponding" strain component.

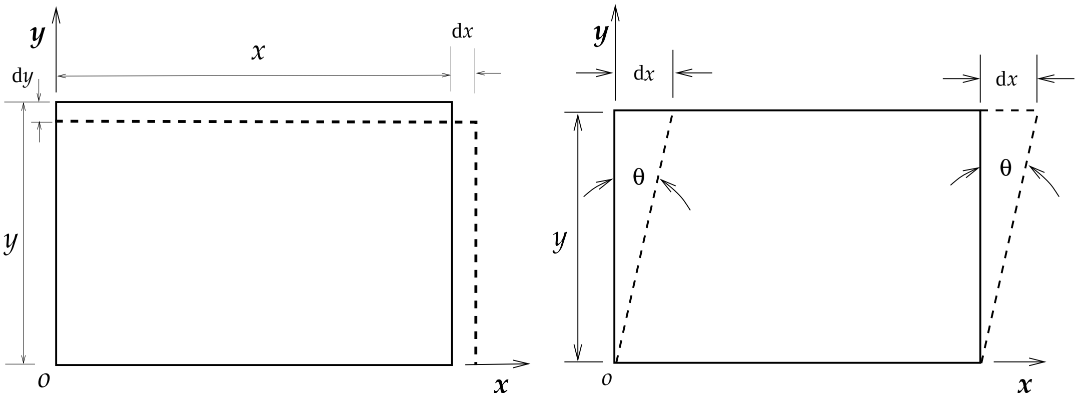

(a) Element subjected to normal strain **(b)** Element subjected to shear strain

Figure 2.15: Normal and shear strains.

For convenience, strains are always resolved into normal components ϵ and shear components γ. With reference to Fig. 2.15(a), normal strains in the x-direction may be defined as

$$\epsilon_x = \lim_{x \to 0} \frac{\mathrm{d}x}{x} \tag{2.53}$$

With reference to Fig. 2.15(b), shear strains may be defined as

$$\gamma_{yx} = \lim_{y \to 0} \frac{\mathrm{d}x}{y} = tan\theta \approx \theta \tag{2.54}$$

where angle θ represents the deviation from an initial right angle. The subscript notation and sign convention for strain corresponds to that used with stresses. For infinitesimal strains, the state of strain is written as tensor, say ϵ_{ij} analogous to Eq. (2.48) for stresses.

$$\epsilon_{ij} = \begin{pmatrix} \epsilon_x & \frac{1}{2}\gamma_{xy} & \frac{1}{2}\gamma_{xz} \\ \frac{1}{2}\gamma_{yx} & \epsilon_y & \frac{1}{2}\gamma_{yz} \\ \frac{1}{2}\gamma_{zx} & \frac{1}{2}\gamma_{zy} & \epsilon_z \end{pmatrix} \tag{2.55}$$

It may be helpful in appreciating the physical significance of the fact that τ is analogous with $\gamma/2$ rather than with γ itself. Here it is seen that each side of an element changes in slope by an angle $\gamma/2$ when subjected to pure shear. Having observed the correspondence between strain Eq. (2.55) and stress Eq. (2.48), it is evident that maximum and minimum principal strains exist for strain. In other words for strain states, principal strains, planes, and directions exist in a manner directly analogous to those for stresses.

2.6.4 Plane stress and plane strain

Two possible special cases are of extreme practical importance are the *plane stress* and *plane strain*. The plane stress case is for

$$\sigma_z = \tau_{xz} = \tau_{yz} = 0 \tag{2.56}$$

An example of this type of stress distribution is, a body of the one where dimension is very small compared to the other two and when it is loaded by forces lying in the plane of symmetry of the body, i.e. a thin plate with loads in its middle plane.

For the plane strain case, the definition

$$\epsilon_z = \gamma_{xz} = \gamma_{yz} = 0 \tag{2.57}$$

and also the body force in the Z direction must be zero. As example of this type of strain distribution is a thick body subject to lateral loads. In the regions some distance from each of the two ends strain at any section in the direction of the axis (Z-axis) is prevented by the action of adjacent material. In both types of problems the shear stresses and strains in the Z direction are assumed to be zero.

2.7 Theory of elasticity

2.7.1 Generalized Hooke's law

For many engineering applications, the assumption of small strain, leads to a relatively simple equation linking stress and strain. For example in uniaxial tension, the relationship between stress and strain in the elastic region can be expressed by Hooke's law as

$$\sigma = E\epsilon \tag{2.58}$$

where E is slope of the stress-strain curve in the linear region (Young's modulus). When the specimen is subjected to axial stress, then not only does it increase in length, but also its cross section becomes smaller. The ratio between lateral and axial strain, like Young's modulus is an elastic property termed *Poisson's ratio* ν. We should note that a state of uniaxial stress such as shown in Fig. 2.11 gives rise to a triaxial state of strain. If we now consider a triaxial state of stress such as shown in Fig. 2.12, we must also expect to create a triaxial state of strain. Therefore if all the stresses act, the resulting total strain in the coordinate directions is expressed by the principle of superposition as

$$\begin{pmatrix} \epsilon x \\ \epsilon y \\ \epsilon z \\ \gamma_{xy} \\ \gamma_{yz} \\ \gamma_{zx} \end{pmatrix} = \begin{bmatrix} \frac{1}{E} & -\frac{\nu}{E} & -\frac{\nu}{E} & 0 & 0 & 0 \\ -\frac{\nu}{E} & \frac{1}{E} & -\frac{\nu}{E} & 0 & 0 & 0 \\ -\frac{\nu}{E} & -\frac{\nu}{E} & \frac{1}{E} & 0 & 0 & 0 \\ 0 & 0 & 0 & \frac{1}{G} & 0 & 0 \\ 0 & 0 & 0 & 0 & \frac{1}{G} & 0 \\ 0 & 0 & 0 & 0 & 0 & \frac{1}{G} \end{bmatrix} \begin{pmatrix} \sigma_x \\ \sigma_y \\ \sigma_z \\ \tau_{xy} \\ \tau_{yz} \\ \tau_{zx} \end{pmatrix} \tag{2.59}$$

where $G = \frac{E}{2(1+\nu)}$ is the elastic shear modulus. This set of equations are often referred as *generalized Hooke's law.* These equations may be solved to obtain stress components as functions of strain. Analyses based upon the theory of elasticity give much more detailed and more precise information about the state of stress, strain, and deformation at any point within the body than a more simplified one dimensional approach. However, they are valid only for the materials that are stressed within the elastic limits.

2.8 Plasticity

In the elastic range, the strains are linearly related to the stresses by Hooke's law. Hence, the theory of elasticity allows the calculation of stress and strain in a loaded body when the body is linear and elastic. For example with the stress-strain curve in the tension test as shown in Fig. 2.16, the linear portion of the curve extends up to the point A. It is in this range that the linear theory of elasticity, using Hooke's law is valid.

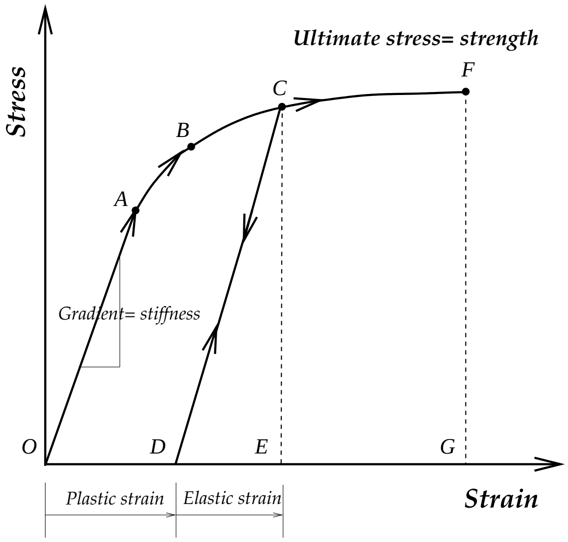

Figure 2.16: Stress-strain curve typical to metals.

In the elastic range the strains are uniquely determined by the stress, i.e. for a given stress we can compute the strains directly using Hooke's law (Eq. (2.58)) without any regard to how the stress state was attained. Beyond the elastic limit point, permanent deformation, called *plastic deformation* takes place, and strain increases at a greater rate. In the plastic range, the relations will generally be non-linear and the strains are in general not uniquely determined by the stress, rather they depend on the history of loading or how the stress state was reached. As the plastic strains are path dependent, it becomes necessary, in general, to complete the differential or increments of plastic strain throughout the loading history and then obtain the total strains by integration or summation.

Up to point B, the behaviour of the specimen is regarded as being elastic in which unloading is reversible. Beyond point B, unloading is not reversible. This is called the *yield point* of the material. The specimen is plastic beyond the point B. When the specimen is loaded up to point C, and then unloaded, the path CD is followed. OD represents the permanent strain which remains after unloading. Reloading the material from point D results in the line DC being followed until the point C is reached which is the new yield point of the material. The process of raising the yield point is often linked to either the plastic strain or mechanical work that is done on the material. This behaviour is known as *work hardening* or *strain hardening.*

The total strain ϵ^t at the new yield point C is made up of the plastic strain OD (ϵ^p) and an elastic strain DE (ϵ^e). The elastic strain ϵ^e is completely recovered on unloading. This relationship is written as

$$\epsilon^t = \epsilon^p + \epsilon^e \tag{2.60}$$

Further loading follows a continuation of the original stress-strain curve. When the load reaches the maximum value at F, the material fails.

2.9 Approach to modelling

2.9.1 Yield criteria

From the above discussion of simple tension, it was shown that there exits a yield point at which the material will begin to deform plastically. In this case the stress is uniaxial and this point can readily be determined. However, when several stresses are acting at a point in different directions, what combination of these stresses will cause yielding? The criterion governing which combination of multiaxial stresses cause yielding is the *yield criterion.* Hence the first step of any plastic flow analysis is to decide on a yield criterion. The next step is to decide how to describe the behaviour of the material after yielding has started.

Ductile materials for example, in uniaxial tension can exhibit large amount of plastic deformation before final failure. The failure surface occurs not along the plane at right angle to the axis of the specimen but along a series of small planes inclined typically at about 45^o to the axis. This suggests that yielding and failure are due to shear stresses causing slipping of the ductile material along oblique planes. On the other hand, brittle materials exhibit little or no plastic deformation before failure occurs, and fracture along planes normal to the applied load. For a complex state of stress, one may like to compare the severity of the combined effect of the several stress components with that of a simple stress state, usually simple tension. Some commonly known yield criteria are discussed in the following section briefly, and are most conveniently expressed in terms of principal stresses or stress invariants.

2.9.2 Maximum shear stress (Tresca) criterion

This criterion is based on the idea (after Henri Tresca, 1814-1885) that a ductile material will yield under a general state of stress when the absolute maximum shear stress is equal to the absolute maximum shear stress at the yield point in a simple tension test. In a state of simple uniaxial tension with an applied stress of σ, the absolute maximum shear stress is $\sigma/2$. Consequently, the maximum shear stress yield criterion can be expressed as

$$\tau_{max} = \frac{\sigma_Y}{2} \tag{2.61}$$

In a state of plane stress with principal stresses σ_1, and σ_2, the absolute maximum is given by

$$\tau_{max} = \left|\frac{\sigma_1 - \sigma_2}{2}\right| \text{ or } \left|\frac{\sigma_1}{2}\right| \text{ or } \left|\frac{\sigma_2}{2}\right| \tag{2.62}$$

Therefore, if σ_1 and σ_2 are of opposite signs

$$\sigma_1\sigma_2 < 0 \quad \text{and} \quad |\sigma_1 - \sigma_2| = \sigma_Y \tag{2.63}$$

and if they are of same sign

$$\sigma_1\sigma_2 > 0 \quad \text{and} \quad |\sigma_1| = \sigma_Y \quad \text{or} \quad |\sigma_2| = \sigma_Y \tag{2.64}$$

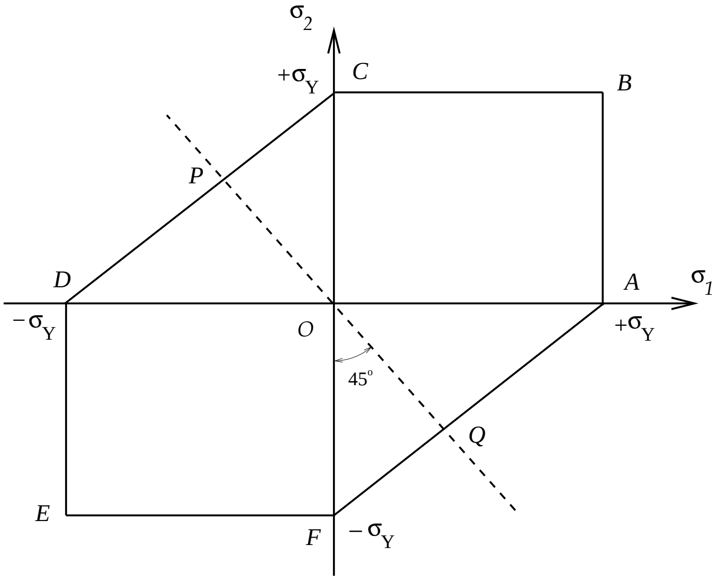

Figure 2.17: Tresca yield surface.

These relationships are shown schematically in Fig. 2.17. The closed hexagon $ABCDEF$ is known as the yield locus. In other words, if a two dimensional state of stress has principal stresses which when plotted define a point within the hexagon, the material has not yielded. If it is outside, yielding has occurred.

2.9.3 Shear strain energy (von Mises) criterion

It was postulated by von Mises, that yielding for ductile materials was not a simple tension or compression phenomenon at all but, rather it was related somehow to the angular distortion of the stressed element. It is employed to define only the beginning of yield, based on the root mean square of maximum shear stress, thereby taking into account the shear stresses on planes at right angles to that of the absolute maximum. The maximum shear stresses associated with each of the three principal planes in a three-dimensional state of stress, namely are $\frac{\sigma_1-\sigma_2}{2}$, $\frac{\sigma_2-\sigma_3}{2}$ and $\frac{\sigma_1-\sigma_3}{2}$

Using the above equation, the root mean square maximum shear stress for a complex three-dimensional state of stress is

$$\tau_m = \sqrt{\frac{1}{3}\left[\left(\frac{\sigma_1-\sigma_2}{2}\right)^2+\left(\frac{\sigma_2-\sigma_3}{2}\right)^2+\left(\frac{\sigma_3-\sigma_1}{2}\right)^2\right]} \tag{2.65}$$

In a simple uniaxial tension, with $\sigma_1 = \sigma_Y, \sigma_2 = 0$ and $\sigma_3 = 0$, this becomes

$$\tau'_m = \frac{\sigma_Y}{\sqrt{6}} \tag{2.66}$$

and we obtain the yield criterion by equating τ_m and $\tau'_m$to give

$$(\sigma_1-\sigma_2)^2+(\sigma_2-\sigma_3)^2+(\sigma_3-\sigma_1)^2 = 2\sigma_Y^2 \tag{2.67}$$

Under plane stress condition, with $\sigma_3 = 0$, this becomes

$$\sigma_1^2+\sigma_2^2-\sigma_1\sigma_2 = \sigma_Y^2 \tag{2.68}$$

Another way of expressing the same result is to define a *von Mises equivalent stress* σ_e (also referred as *effective stress*) as

$$\sigma_e = \sqrt{(\sigma_1^2+\sigma_2^2-\sigma_1\sigma_2)} \tag{2.69}$$

and take yielding to occur when this normal stress is equal to the measured yield stress in simple tension. In other words, the equivalent stress is the stress in uniaxial tension which is equivalent to the complex state of stress according to the von Mises criterion of yielding.

If we plot the curve defined by Eq. (2.68) with axes of σ_1 and σ_2, we obtain Fig. 2.18. The shape of the yield locus is an ellipse, with the major and minor axes along the biaxial tension/compression line TT and pure shear line SS, respectively.

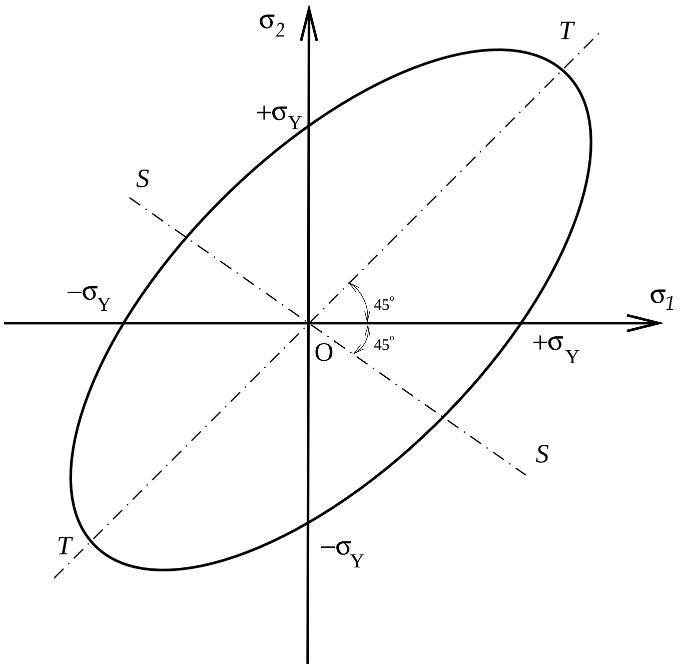

Figure 2.18: von Mises yield surface.

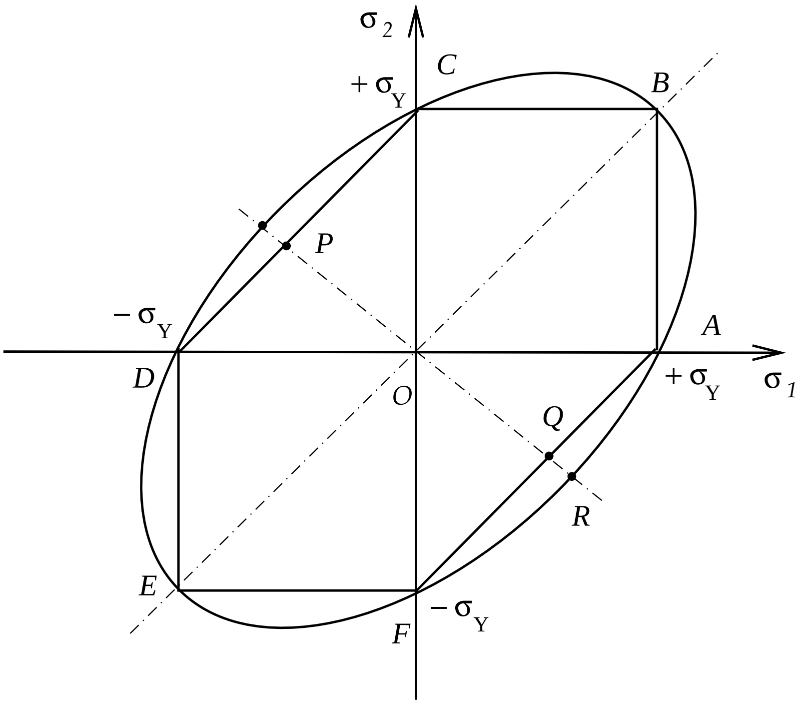

Figure 2.19: Tresca and von Mises yield surfaces.

Figure 2.19 shows Tresca and von Mises yield loci, and the Tresca locus either lies within or just touches the von Mises locus, so that it tends to predict the onset of yielding at stress levels somewhat below the actual ones. It is instructive to extend the plotting of yield criteria to three-dimensional states of stress.

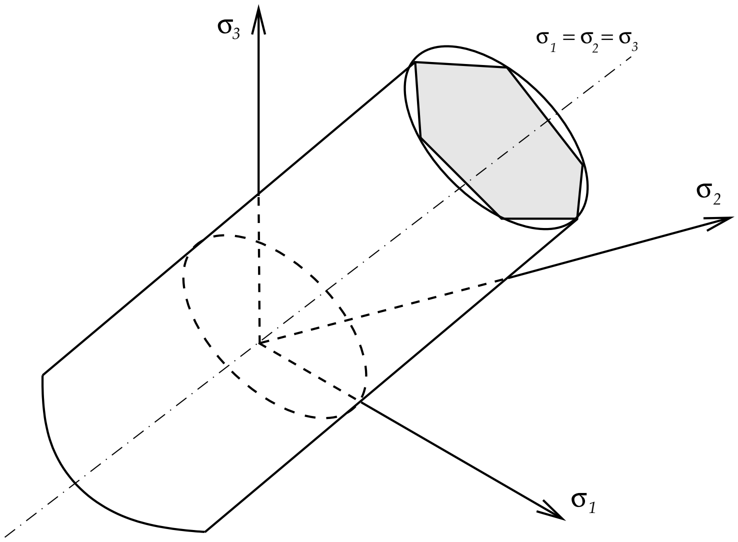

Figure 2.20: Three-dimensional yield shape.

Figure 2.20 does this for Tresca and von Mises, the two dimensional loci becomes three-dimensional yield surfaces or envelopes. An envelope represents the interface between elastic states of stress inside and plastic outside, according to the particular criterion of yielding. The von Mises envelope is a circular cylinder with its geometric axis lying along the line $\sigma_1 = \sigma_2 = \sigma_3$ of equal principal stresses, which is equally inclined to the three principal stress axes. The Tresca surface has the same geometric axes but has a cross section in the form of a regular hexagon just touching the von Mises cylinder at six positions around its circumference. The axis $\sigma_1 = \sigma_2 = \sigma_3$ is of particular interest, where according to both criteria yielding never occurs, irrespective of the magnitude of stresses. This is because with three equal principal stresses there are no shear stresses, and therefore no ductile yielding.

2.9.4 Mohr-Coulomb yield surface

The Tresca and von Mises yield theories are useful for metals where yielding is essentially independent of hydrostatic stress. However, for soils and prepared cane materials where compressive yield is usually dependent on the value of hydrostatic stress, these theories are not appropriate. Mohr extended the maximum shear stress theory by assuming that the critical shear stress is not necessarily equal to the maximum shear stress but depends also on the normal stress acting on the shear plane.

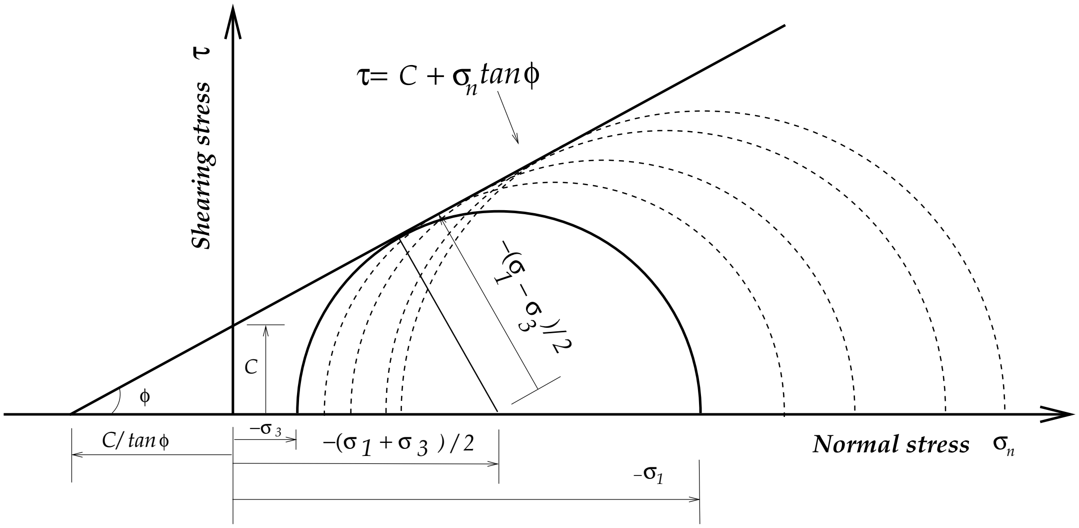

Figure 2.21: Mohr-Coulomb failure envelope.

Mohr's theory of failure involves the construction of an envelope to all possible circles of stress, i.e. Mohr circle containing normal and shear stresses that can be drawn for a particular problem. These envelopes are represented by a straight line, and are based on the assumption that the soil confirms to the Coulomb failure criterion which states that there is a linear relationship between the shear stress τ at failure and the normal stress σ_n (Fig. 2.21)

$$\tau = c + \sigma_n \ tan\phi \tag{2.70}$$

where c = apparent cohesion.

ϕ = angle of internal friction.

An alternative form of this failure theory can be expressed as a linear relation between q and p (from Eqs (2.50) and (2.52)). The slope of the line is M, as expressed below.

$$q = Mp \tag{2.71}$$

From Fig. 2.21, it may be deduced that

$$sin\phi = \frac{\frac{1}{2}(\sigma_1 - \sigma_3)}{\frac{C}{tan\phi} + \frac{(\sigma_1+\sigma_3)}{2}} \tag{2.72}$$

or, by rearranging

$$(\sigma_1 - \sigma_3) = (\sigma_1 + \sigma_3)\ sin\phi + 2c\ cos\phi \tag{2.73}$$

where σ_1 and σ_3 are the major and minor principal stresses at failure.

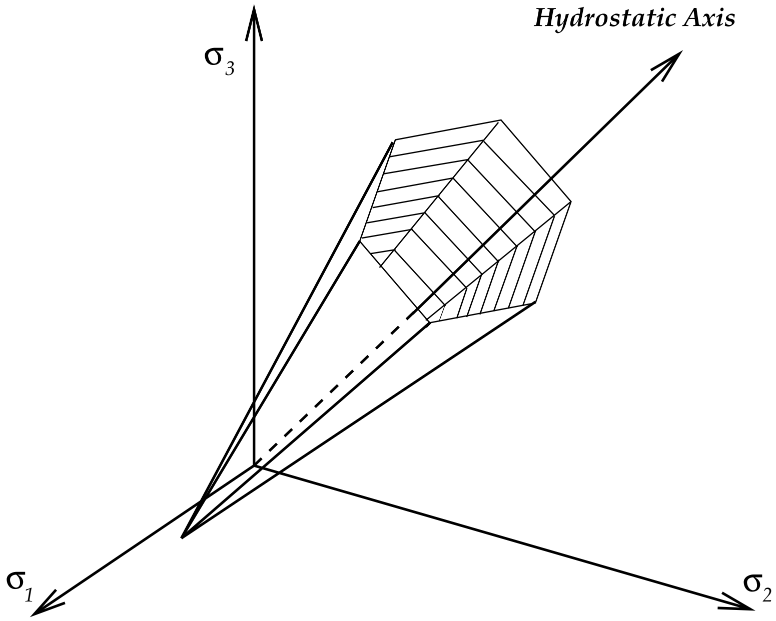

Figure 2.22: Mohr-Coulomb failure criterion in stress space.

The complete generality of the true behaviour in stress space is shown as an irregular hexagonal pyramid (Fig. 2.22). The surface of this pyramid is known as the yield surface. If a material conforms to this theory, then the material will be yielding if its stress state lies on the surface. When the stress states lies inside the yield surface, it will be elastic. Stress states outside the yield surface are impossible, by definition. It is evident, from the shape of the yield surface, as the hydrostatic stress increases, a larger deviation from the hydrostatic stress axis is required to cause yield.

2.9.5 The Drucker-Prager yield surface

The Mohr-Coulomb criterion represents an incomplete picture of the yielding of porous materials like soils. In practice, soils show evidence of volumetric yielding under isotropic stress changes where Mohr-Coulomb suggest elastic behaviour. Further, if one follows the normal approach of calculating plastic strain when yielding, then prediction of expansive volumetric strains are unrealistic (Britto and Gunn, 1987). Drucker and Prager believed it might be useful to “round off” the Mohr-Coulomb yield surface to give the conical surface for soils as shown in Fig. 2.23.

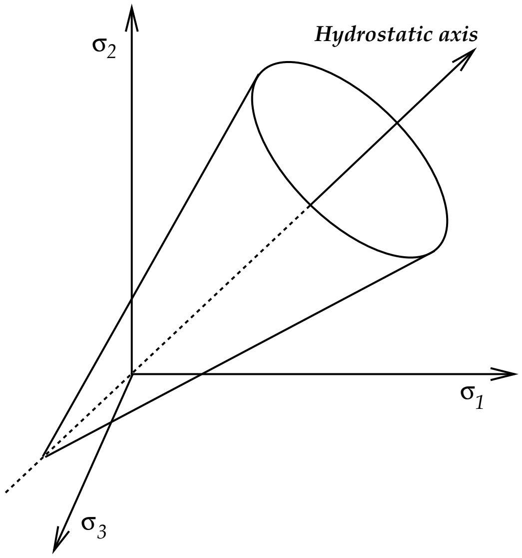

Figure 2.23: The Drucker-Prager yield surface.

Drucker and Prager (1952) developed a constitutive model which includes the effect of all three principal stresses. Their yield criterion was expressed as

$$f = \sqrt{J_{2D}} - \alpha J_1 - \kappa = 0 \tag{2.74}$$

Where α and κ are positive material parameters. J_1 is the first material invariant of the stress tensor, and J_{2D} is the second invariant of the deviatoric stress tensor which are defined in terms of principal stress as

$$J_1 = \sigma_1 + \sigma_2 + \sigma_3 \tag{2.75}$$

$$J_{2D} = \frac{1}{6}\left[(\sigma_1 - \sigma_2)^2 + (\sigma_2 - \sigma_3)^2 + (\sigma_3 - \sigma_1)^2\right] \tag{2.76}$$

The J_{2D} stress tensor can be related to Mises stress q as

$$\sqrt{J_{2D}} = \frac{q}{\sqrt{3}} \tag{2.77}$$

The yield criterion from Eq. (2.74) plots as a straight line on a graph of J_{2D} Vs J_1 as shown in Fig. 2.24.

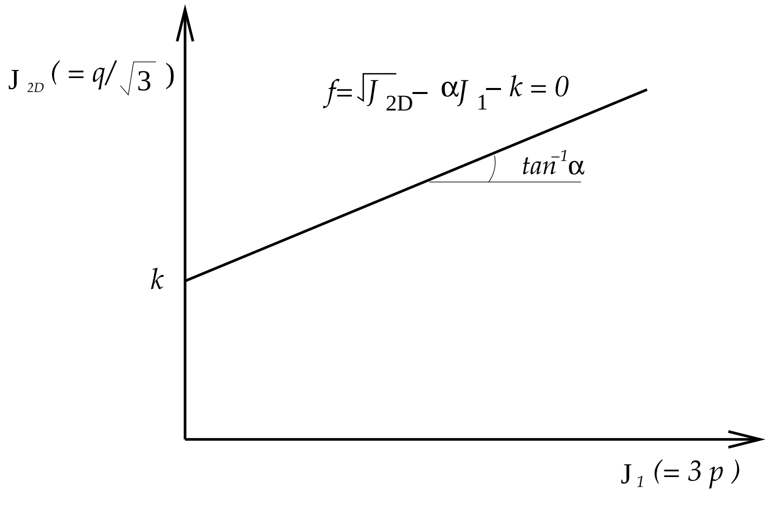

Figure 2.24: The Drucker-Prager yield criterion.

2.9.6 Cap models

Drucker-Prager's proposal of "rounding-off" the Mohr-Coulomb yield surface for soils was mainly derived from some metal plasticity calculations, where von Mises is more convenient than Tresca. However, Drucker-Prager yield surface has all the drawbacks of Mohr-Coulomb yield surface and gives a worse fit to the data of soil failure (Britto and Gunn, 1987). Cap models were developed to allow constitutive relation to simulate a material yielding under the action of hydrostatic stress. These models are characterized by a fixed plastic surface which defines the shear strength of the material and a work hardening cap to model yielding under hydrostatic compression. The modified Drucker-Prager/Cap plasticity models in ABAQUS for example were developed to exhibit pressure dependent yield relevant for soil related materials.

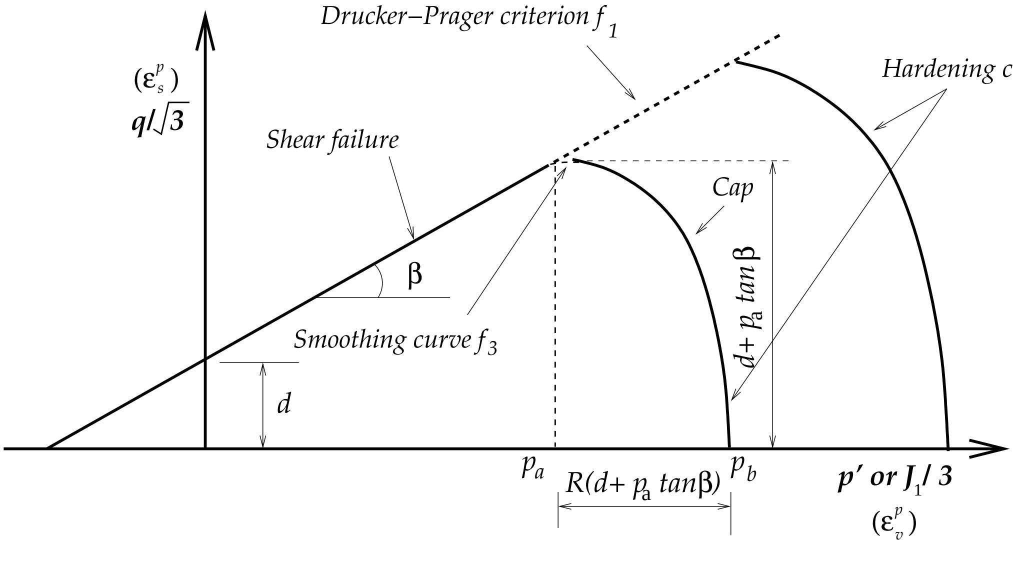

Figure 2.25: Modified Drucker-Prager/cap model: yield surfaces.

The capped Drucker models consist of a Drucker-Prager yield surface, as already defined by Eq. (2.74) with a superimposed hardening cap, which is another separately defined yield surface (f_2) that encloses the previously open end as shown in Fig. 2.25. The shape of the hardening cap is usually approximated by a circular or elliptical arc and is also normally assumed to have a horizontal tangent at the intersection with the limiting Drucker-Prager yield surface. The cap serves two main purposes. Firstly, it bounds the yield surface in hydrostatic compression, thus providing an inelastic hardening to represent plastic compaction. Secondly it helps to control volume dilatancy when the material yields in shear by providing softening as a function of the inelastic volume increase. As the material is subjected to increasing values of mean normal effective stress (p'), the hardening cap expands as shown in Fig. 2.25.

An associated flow rule is normally assumed for this model in which, the plastic potential function has the same shape as the yield function. This is represented graphically by overlaying the plastic volumetric strain axis (ϵ_v^p), along the p' axis and the plastic shear strain axis (ϵ_s^p) along the q axis as shown in Fig. 2.25. Consequently, if the material yields by reaching the yield surface f_1, then it will dilate and undergo strain softening, where by it will become weaker as it expands in volume. Alternatively, if the stress state causes the material to yield by reaching the hardening cap, then the incremental plastic strain vector will be normal to the yield surface f_2 and the material will strain harden. To overcome the discontinuity where the yield surface f_1 and f_2 meet, a smoothing curve f_3 can be specified which is tangent to both f_1 and f_2.

In three dimensional stress space, the Drucker-Prager yield surface plots as a right circular cone with its axis along the hydrostatic axis and the hardening cap plot as hemispherical or ellipsoid domes that enclose the open end of the cone.

2.10 Critical state theory

The critical state theory discussed here for soils is considered to be applicable to prepared cane, as in general, prepared cane is a multiphase material containing solid fibrous material and liquid juice and air. When sheared, a soil will eventually reach a critical void ratio, at which continued deformation can take place without further change in volume or stress. This condition, at which unlimited shear strain can be applied without further changes in specific volume, shear stress and normal effective stress, is known as *critical state.* The critical state concept was originally recognized by Casagrande in 1936, and was developed considerably by Roscoe et al. (1958) during late 1950's and '60s.

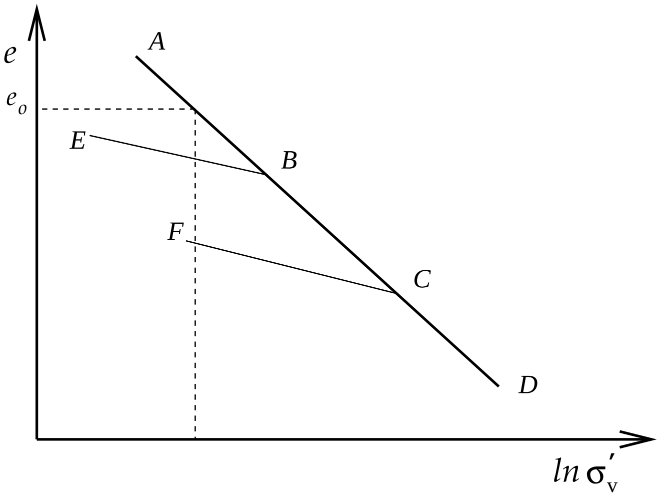

Figure 2.26: Void ratio Vs $\ln \sigma'_v$ relationship for one-dimensional compression.

If a soil is subjected to one-dimensional compression (and swelling) tests, then the paths in void ratio e, and effective normal stress σ'_v is obtained as shown in Fig. 2.26. When the soil is loaded for the first time to stress levels greater than it has previously experienced, the void ratio is found to reduce approximately linearly with the logarithm of σ'_v. Such a soil is said to be normally consolidated, and the line joining successive points representing such states ($ABCD$) in Fig. 2.26 is known as the "virgin compression" (or "consolidation") line. If the soil element is unloaded, it increases in volume again but at a very much lower rate as shown by typical "swelling line" BE and CF. A soil represented by a state such as E or F is said to be *over consolidated.* On reloading, the soil returns along the swelling line before continuing down the virgin compression line, along the path such as FCD. The mean effective normal stress in the case of one dimensional loading may be written as

$$p = \frac{(1 + 2K_o)\,\sigma'_v}{3} \tag{2.78}$$

where K_o is the ratio of horizontal to vertical stress and is approximately constant for one-dimensional loading. The effective maximum shear stress q' may be expressed as

$$q' = (1 - K_o)\,\sigma'_v > 0 \tag{2.79}$$

This indicates, one-dimensional consolidation involves shear as well as volumetric distortion.

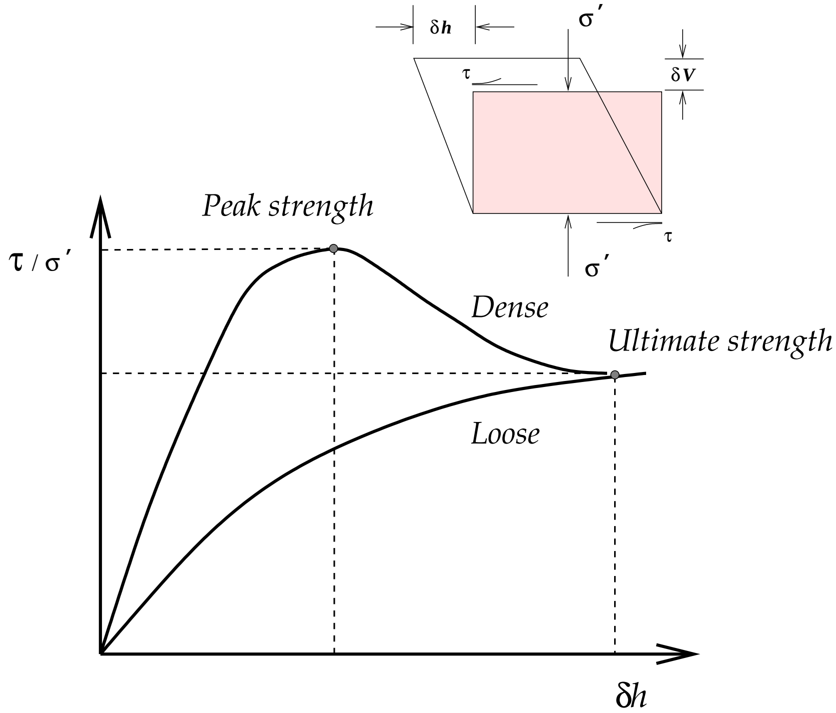

Figure 2.27: Drained peak and ultimate strength.

The shear strength of soil as measured in tests depends mainly on the state of the soil at start. In hard or soft soils, the stress-strain curve ultimately flattens out at the ultimate or critical value (Fig. 2.27). After the ultimate (critical) strength is reached, the volume remains constant while shearing continues. The soil is now in the critical state and the volume is the *critical volume.*

In the critical state there is a unique relationship between the shear stress τ_f, the normal stress σ' and the volume (or void ratio e). A series of tests on the same soil will produce a critical strength envelope that is a straight line, referred to as the critical state line (CSL). The critical state is, however, three dimensional, having also a volume or void ratio axis (Fig. 2.28).

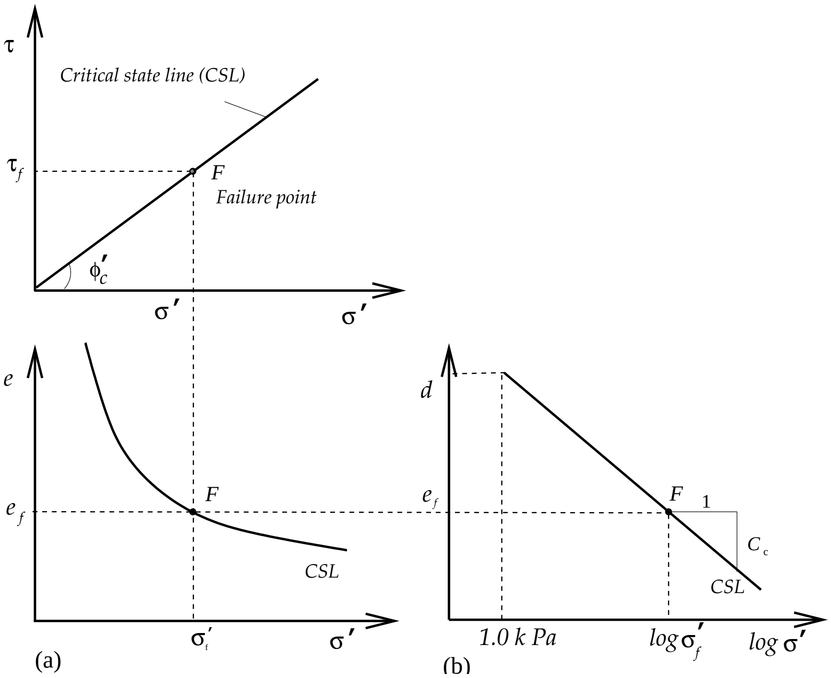

Figure 2.28: Critical strength.

Figure 2.28(a) shows elevation of CSL drawn from $\tau : \sigma'$ and $e : \sigma'$ axes respectively. When $\log \sigma'$ axis is used, the CSL elevation is a straight line. It may be noted that for direct shear tests the axial parameters are (τ, σ', e) while for triaxial tests they are (q, p', v).

The relevant expressions for direct shear are

$$\tau_f = \sigma'_f \; tan\phi' \tag{2.80}$$

$$e_f = e_\Gamma - C_c \; \ln \sigma' \tag{2.81}$$

where ϕ' = slope of the CSL in τ / σ' plane.

$e_\Gamma =$ the void ratio at σ'=1.0 kPa.

C_c= slope of the CSL in the $e/\ln\sigma'$ plane.

For triaxial tests

$$q = Mp' \tag{2.82}$$

$$v_f = \Gamma - \lambda\ \ln p' \tag{2.83}$$

where M= slope of the CSL in the q/p' plane.

$\Gamma =$ specific volume at p'=1.0 kPa.

$\lambda =$ slope of the CSL in the $v/\ln p'$ plane.

The critical strength is the only unique measure of the strength of a soil. Other measures, e.g. undrained strength or peak strength, depend on the initial state of the soil and is therefore not constant. As the soil is compressed its shear strength increases. The volume change behaviour and strength of soil are related. In the Mohr-Coulomb failure theory, volume changes are ignored, and thus it is difficult to model soil behaviour accurately for over consolidated and undrained soil. And yet, however, there is a unique relationship between applied stress, shear strength and volume- and this occurs at the critical state.

2.10.1 Cam-clay critical state model

The critical state theory provides a unified model of soil behaviour in which stress and volume states are interrelated. For soils, the concept was first proposed in 1958 by Roscoe, Schofield and Wroth (1958) incorporating yield, known as Cam clay. Further work followed, mainly in the University Engineering Department at Cambridge during 1960s and '70s (Atkinson, 1993; Schofield and Wroth, 1968). It is proposed that soil will yield, and reach its critical state strength, at a critical specific volume and shear stress.

It is well known that a material yields when its stress-strain behaviour changes from being purely elastic to partly plastic. The failure however is not synonymous with yield. Metals such as mild steel which undergo ductile failure continue to deform under static load, in contrast with brittle materials which fail by fracture, with sudden loss of all their load-carrying ability. For soils, the onset of a critical state at which deformation continues at constant stress ratio and volume represents the failure of the material. It is therefore important to be able to predict combinations of q and p' (or shear and normal effective stresses), which will cause failure, as well as yield, at which rates of deformation may be expected to increase significantly.

At the critical state, the soil continues to deform at constant stress ratio q/p' and constant specific volume. The line joining critical states referred to as the critical state line or CSL has equations

$$q = Mp' \tag{2.84}$$

$$\text{and } v = \Gamma - \lambda \ \ln p' \tag{2.85}$$

where M, Γ, and λ are parameters whose values depend on the soil type, and are determined from triaxial tests. Figure 2.29 shows the CSL in q, p' and p', v plots of what in reality is a single line in three-dimensional q, p', v space. The critical state line represents the final state of soil samples in triaxial tests where it is possible to continue to shear the sample with no change in imposed stresses or volume of the soil. Hence, at the critical state,

$$\frac{\delta v}{\delta \epsilon} = 0 \ ; \ \ \frac{\delta q}{\delta \epsilon} = 0 \ ; \ \ \frac{\delta p'}{\delta \epsilon} = 0 \tag{2.86}$$

The critical state line is parallel to the isotropic normal compression line (NCL) in $v, \ln p$ space. The critical state line shown in Fig. 2.29 is exactly analogous to that from standard shear box tests. The deviator stress q is a measure of the shear stress acting on the soil, which was characterized in the shear box test by the shear stress τ on the central horizontal plane. The average effective stress p' is analogous to that effective stress σ' on the central horizontal plane of the shear box. The critical state

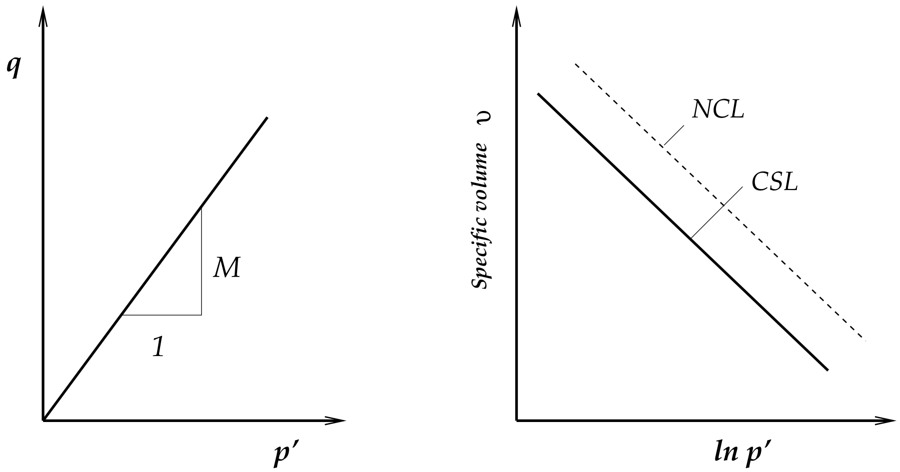

Figure 2.29: Triaxial compression and extension tests in q, p' and v, $\ln p'$ space.

parameter M is a measure of the ratio of shear to normal effective stress at failure, and is therefore related to the soil friction angle ϕ'_{crit}. The relation between M and ϕ'_{crit} for triaxial compression is (Powrie, 1997).

$$M = \frac{6\,\sin\phi'_{crit}}{3 - \sin\phi'_{crit}} \tag{2.87}$$

2.10.2 Yielding of Cam-clay

The significant difference between soil and metals is that with soils the elasto-plastic behaviour is associated with volumetric strain. The mathematical description of the yield surface considers the effect of shearing a sample. Equations (2.84) and (2.85) can be combined to give

$$\frac{q}{Mp'} + \left(\frac{\lambda}{\lambda - \kappa}\right)\ln p' - \left(\frac{\Gamma - v}{\lambda - \kappa}\right) = 1 \tag{2.88}$$

This defines a surface in $p'vq$ space known as *Stable State Boundary Surface* (SSBS) shown as an isometric view in Fig. 2.30. The surface meets the $v : p'$ plane along the isotropic normal compression line where $q = 0$, and $v = N - \lambda\ \ln p'$. A yield curve is the intersection of an elastic wall given by $v = v_\kappa - \kappa\ \ln p'$ with the SSBS. At the critical state line the specific volume is v_c and the mean stress is p'_c as shown in

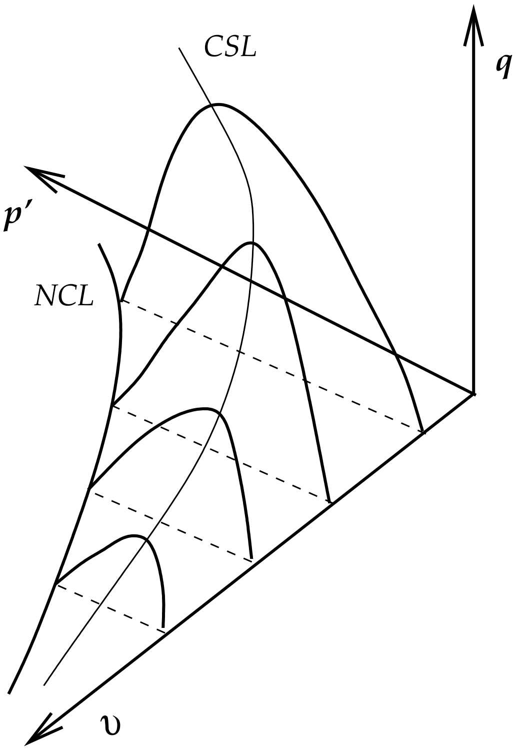

Figure 2.30: State boundary surface for Cam clay.

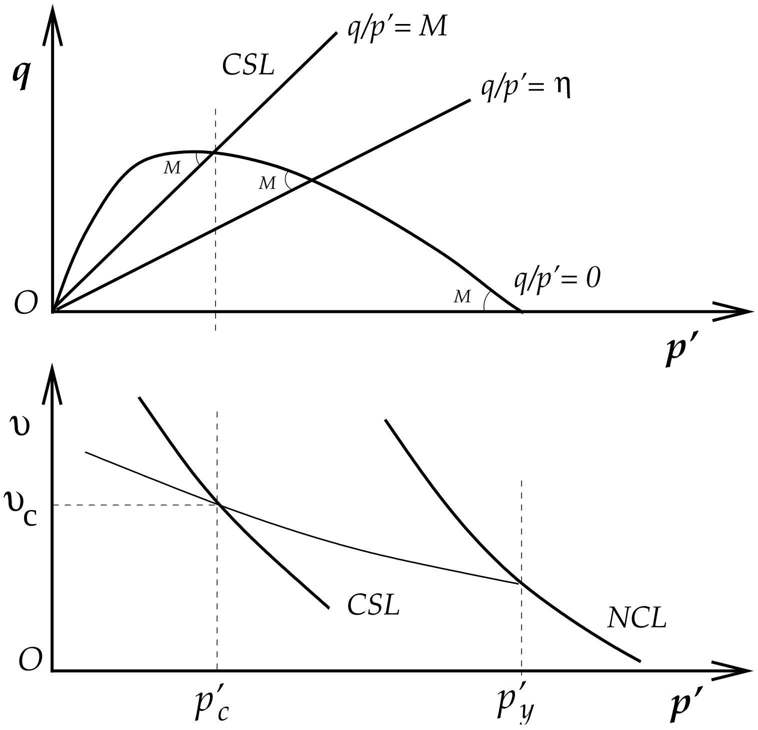

Figure 2.31: Yield curve for Cam-clay.

Fig. 2.31, where

$$v_c = v_k - \kappa \ \ln p'_c = \Gamma - \lambda \ \ln p'_c \tag{2.89}$$

Eliminating v and v_κ, the equation for the yield curve in the $p'q$ plane is shown in Fig. 2.31, i.e.

$$\frac{q}{Mp'} + \ln\left(\frac{p'}{p_c}\right) = 1 \tag{2.90}$$

From Eq. (2.90), with $q = 0$, the yield stress p'_y is related to critical state stress p'_c, on the same yield curve by

$$\frac{p'_y}{p'_c} = \exp(1) = 2.72 \tag{2.91}$$

Equation 2.91 represents the outer limit of the possible stress states for any given value of p'. Inside the yield locus, the material behaves elastically, but on the yield locus, the material is yielding. The material cannot experience stress states outside the yield surface without first undergoing a change in plastic strain, in which case the material strain hardens or strain softens and the yield locus grows or shrinks.

If the material stress state reaches the yield locus at a point to the right of the critical point C as shown in Fig. 2.32, then the material will strain harden, its volume will reduce, and the yield surface will grow. This process will continue until the stress state reaches a critical point on a larger yield surface. Now the material is in a critical state and will continue to undergo increasing shear strain at a constant volume and constant stress, and the material is considered to have failed. If the material stress state reaches the yield locus at a point to the left of the critical point then the material will strain soften, its volume will increase and the yield surface will shrink. The material will continue to strain soften until it attains critical state i.e. the stress state reaches a critical point on a smaller yield surface. Associate flow rule assumes the plastic potential function has the same shape as the yield function. Mathematically it is expressed as the product of slope of the yield surface and plastic strain increment as shown in Fig. 2.32, i.e.

$$\frac{\mathrm{d}q}{\mathrm{d}p'}.\frac{\mathrm{d}\epsilon_s^p}{\mathrm{d}\epsilon_v^p} = -1 \tag{2.92}$$

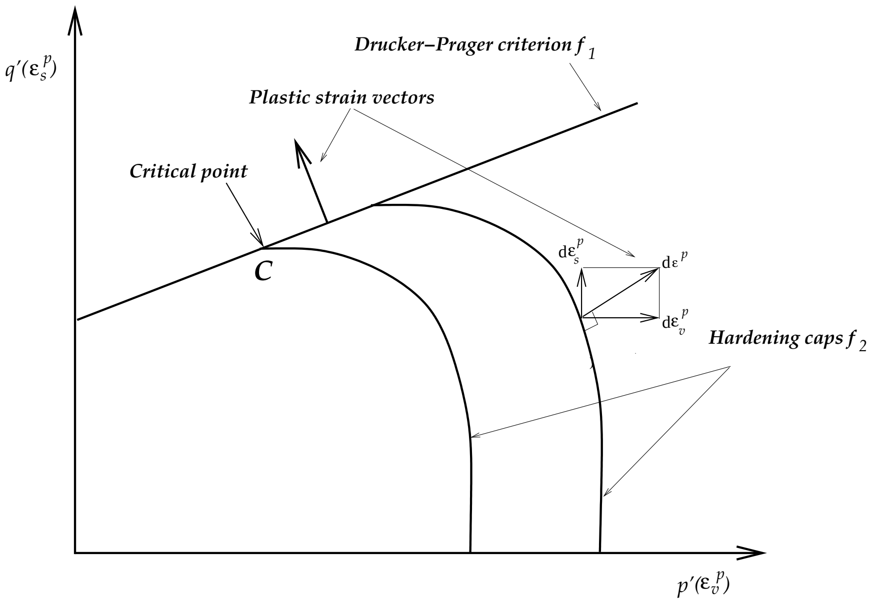

Figure 2.32: The Cam clay yield locus and the flow rule.

By applying physical balance laws describing equilibrium of stress and continuity of volumetric strain with liquid flow to infinitesimally small elements of the material, it is possible to obtain a system of partial differential equations to describe a physical situation. The system of partial differential equations describes the relationship between total and effective stress, excess pore pressure, strain, seepage velocity etc. The finite element method can be used to solve a particular boundary value problem with known loads and drainage boundary conditions that act on a finite volume of material or domain.

2.11 Governing equations and finite element solution to porous media mechanics

Zhao's doctoral thesis (Zhao, 1993) describes the mathematical theory of governing equations for the coupled problem of saturated and unsaturated flow in deforming porous media. This theory was applied for the first time to the rolling and compression of prepared cane, by treating as a fully coupled unsaturated-saturated two phase flow problems (Owen et al., 1994). The extracts of the derived governing partial differential equations, boundary and initial conditions and other parameters involved are briefly discussed (from De Souza Neta et al. (1997); Owen et al. (1995); Zhao (1993)) in the following sections.

2.11.1 Overall equilibrium equations

The overall equilibrium equations for partially saturated porous medium is

$$\mathrm{L}^T\sigma + \rho g = \rho\ddot{u} + \rho_l n S_l \frac{\mathrm{D}}{\mathrm{D}t}\left(\frac{\dot{w}}{nS_l}\right) \tag{2.93}$$

where L is the differential operator given by

$$\mathrm{L} = \begin{vmatrix} \frac{\delta}{\delta x} & 0 & 0 \\ 0 & \frac{\delta}{\delta y} & 0 \\ 0 & 0 & \frac{\delta}{\delta z} \\ \frac{\delta}{\delta y} & \frac{\delta}{\delta x} & 0 \\ 0 & \frac{\delta}{\delta z} & \frac{\delta}{\delta y} \\ \frac{\delta}{\delta z} & 0 & \frac{\delta}{\delta x} \end{vmatrix} \tag{2.94}$$

and σ is the total stress vector, g the gravitational acceleration, u and $\ddot{u}$ are the displacement and acceleration vectors of the solid phase respectively, n the porosity of porous medium, S_l the degree of liquid saturation, ρ the density of solid-fluid mixture, ρ_l the density of liquid and $\dot{w}$ the velocity of liquid. It is reasonable to neglect the weight of gas. Therefore we have

$$\rho = \rho_s\,(1-n) + \rho_l n S_l \tag{2.95}$$

where, ρ_s is the density of the solid.

2.11.2 Equilibrium equation of liquid

The equilibrium equation of the liquid phase is the generalized Darcy's law

$$k^{-1}\dot{w} = -\nabla\rho_l + \rho_l\left(g - \ddot{u} - \frac{\mathrm{D}}{\mathrm{D}t}\left(\frac{\dot{w}}{nS_l}\right)\right) \tag{2.96}$$

where k is the Darcy coefficient matrix of permeability. For the isotropic case k can be replaced by a single value of K. In the case of rolling of prepared cane, K may be expressed as a function of compression ratio or volumetric strain.

2.11.3 Liquid flow continuity equation

The liquid flow continuity equation is given by applying the mass conservation principles

$$-\nabla^T\dot{w} = \left(\frac{n}{K_l}S_l + S_l^2\frac{\alpha - n}{K_s}\right)\dot{P}_l + S_l\alpha\, m^T\dot{\epsilon} \tag{2.97}$$

where, $\nabla^T = \left[\frac{\delta}{\delta x}, \frac{\delta}{\delta y}, \frac{\delta}{\delta z}\right]$ and $m^T = [1,1,1,0,0,0]$.

The terms K_s and K_l are the bulk moduli of the solid and liquid phases respectively. P_l is the liquid pore pressure, ϵ the total strain vector and α a coefficient of the porous medium.

2.11.4 Stress, pressure, displacement and strain

For a saturated porous media, the relationship between total stress σ, effective stress σ_e and liquid pressure P_l is written as

$$\sigma = \sigma_e - mP_l \tag{2.98}$$

The general incremental constitutive relation is introduced as

$$\mathrm{d}\sigma_e = \mathrm{D}_T\left(\mathrm{d}\epsilon - \mathrm{d}\epsilon_p\right) \tag{2.99}$$

where the tangent matrix D_T is dependent on the level of the effective stress and also, if strain effects are considered, on the total strain of the skeleton. The volumetric strain ϵ_p, caused by uniform compression of solid grains and can be written as

$$\mathrm{d}\epsilon_p = -\frac{m\,\mathrm{d}P_t}{3K_s} \tag{2.100}$$

where, P_t is the sum of liquid and gas pressure of an unsaturated porous media. Following substitutions into Eq. (2.99),

$$\mathrm{d}\sigma_e = \mathrm{D}_T\left(\mathrm{d}\epsilon + \frac{m\,\mathrm{d}P_t}{3K_s}\right) \tag{2.101}$$

The strain displacement relation for the solid skeleton can be written in incremental form as

$$\mathrm{d}\epsilon = \mathrm{L}_t\,\mathrm{d}u \tag{2.102}$$

For the case of small strain analysis, L_t is the same differential operator defined in Eq. (2.94), but for large deformation analysis, rotational terms must be included (Owen and Hinton, 1980).

2.11.5 The finite element transient solution

The governing Eqs. (2.93) to (2.102) except for simple geometry and linear or near linear, are difficult to solve analytically for general two and three-dimensional cases, especially for the rolling process of two- phase material behaviour. The finite element method has been widely used in geomechanics to solve these equations. Zhao (1993) presented a transient finite element solution procedure, which discretizes (spatial and temporal) these governing equations, and solves them using “weak formulation”. The weak form is a weighted-integral statement of a differential equation and includes the natural boundary conditions of the problem.

2.11.5.1 Boundary and initial conditions

Boundary conditions for the solid phase

On the boundaries of the rolled material, two sets of boundary conditions are given. They are

$$T = 0 \quad \text{and} \quad \dot{u} = 0 \tag{2.103}$$

where T and $\dot{u}$ are the vectors of the boundary traction and velocity.

The physical contact between the grooved surface and rolled material is assumed rough, hence a no-slip boundary condition was given to the solid on the contact arc. This is expressed as

$$\dot{u}_x = S\cos\alpha, \quad \dot{u}_y = S\sin\alpha \tag{2.104}$$

where S is the tangent velocity of the roll surface.

Boundary conditions for the liquid phase

On the contact arc, for the liquid phase, porous boundary is used because the rolled material actually does not fill up the grooves during the rolling process. Hence $P = 0$ gives a condition of very little or no resistance to liquid flow at the roll surface.

On the symmetric axis (Fig. 2.5), no liquid can flow through the boundary, hence an impermeable boundary condition $\frac{\delta P}{\delta n} = 0$ is given. This condition may be given to the roll surface for a well prepared cane, because the rolled material may nearly fill up the grooves.

Initial conditions for the solid and liquid phases

Initial conditions at $t = 0$ is prescribed for the solid and liquid phases. For the solid phase, prescribed initial conditions are, the displacement and velocity and for the liquid, an initial pore pressure is assigned.

2.11.6 Spatial discretization of governing equations

A standard procedure of the finite element solution by weighted residual method was applied (Zhao, 1993) for the solution of the equations. The governing equations were spatially discretized.

$$\int B^T\sigma''\,\mathrm{d}\Omega - Q\bar{P} + M\ddot{u} = f^u \tag{2.105}$$

$$H\bar{P} + Q^T\dot{\bar{u}} + S\dot{\bar{P}} = f^p \tag{2.106}$$

In the above $B \;= LN_{\dot{u}}$

$Q \;= \int_\Omega B^T m\alpha S_l N_P\,\mathrm{d}\Omega$

$H \;= \int_\Omega (\nabla N_P)^T\,k\,\nabla N_P\,\mathrm{d}\Omega$

$S \;= \int_\Omega N_P^T\frac{1}{Q}N_P\,\mathrm{d}\Omega$

$f^u = \int_\Omega N_{\dot{u}}^T\left[\rho_s\,(1-n) + \rho_l n S_l\right]g\;\;\mathrm{d}\Omega + \int_{\delta\Omega_t} N_{\dot{u}}^T\bar{t}\,\mathrm{d}S$

$f^P = \int_\Omega (\nabla N_P)^T\,k\rho_l g\,\mathrm{d}\Omega - \int_{\delta\Omega_f} \nabla N_P^T\dot{\bar{\omega}}^T n\,\mathrm{d}S$

$\frac{1}{Q} \;= \frac{n}{K_l}S_l + S_l^2\frac{\alpha-n}{K_s}$

where $N_{\dot{u}}$ and N_P are the global shape functions for the velocity of the solid skeleton and liquid pressure respectively. $\dot{\bar{u}}$ and $\bar{P}$ are the global velocity vector for the solid matrix and global liquid pressure vector at element nodes respectively. In the analysis of rolling of two-phase materials, the solid velocity $\dot{u}$ and pore pressure $\bar{p}$ were taken as primary variables, and the liquid velocity $\dot{w}$ can be easily obtained by secondary calculation.

2.11.6.1 Time domain discretization

The spatially discretized coupled governing Eqs. (2.105) and (2.106) are first order ordinary differential equations in time because quasi-static condition has been used. To obtain the numerical solution of these equations with a general non-linear constitutive law, some step-by-step time integration method must be used (Owen et al., 1995).

For quasi-static condition, reduced rank scheme is derived, however if quasi-static condition is not considered but $\ddot{u} >> \ddot{w}$ is taken into account (therefore $\ddot{w}= 0$), in which full Newmark scheme is used (Zhao, 1993). For the present quasi-static coupled problem, an unconditionally stable direct solution procedure by Newmark which is defined in terms of prescribed boundary velocities is used. The following section briefly describes the Newmark scheme.

2.11.6.2 Full Newmark scheme

In the Newmark scheme it is assumed that the differential equations are satisfied at each time station and that velocity and displacement at two stations $n(t)$ and $n+1(t+\Delta t)$ are related using the finite difference form from a Taylor's series. Substituting the finite difference equation at these time stations into Eqs. (2.105) and (2.106), two non-linear equation sets are obtained as

$$C^u_{n+1} = M_{n+1}\,\Delta t\ \ddot{\bar{u}}_n + P\left(\bar{u}_{n+1}\right) - Q_{n+1}\,\theta\,\Delta t\,\Delta\dot{\bar{P}}_n - F^u_{n+1} = 0 \tag{2.107}$$

$$C^P_{n+1} = Q^T_{n+1}\beta_1\,\Delta t\,\Delta\ddot{\bar{u}}_{n+1} + \left(H_{n+1}\,\theta\,\Delta t + S_{n+1}\right)\Delta\dot{\bar{P}} - F^P_{n+1} = 0 \tag{2.108}$$

In the above:

$$F^u_{n+1} = -M_{n+1}\,\ddot{u}_n + f^u_{n+1} + Q_{n+1}\left(\bar{P} + \dot{\bar{P}}_n\,\Delta t\right) \tag{2.109}$$

$$F^P_{n+1} = f^P_{n+1} - Q^T_{n+1}\left(\dot{\bar{u}} + \ddot{\bar{u}}\,\Delta t\right) - H_{n+1}\left(\bar{P}_n + \dot{\bar{P}}_n\,\Delta t\right) - S_{n+1}\,\dot{\bar{P}}_n \tag{2.110}$$

For quasi-static condition, equation Eqs. (2.105) and 2.106 can be simplified at time station $n+1$ using reduced rank scheme.

The discretized equations Eqs. (2.107) and (2.108) must be solved by some iterative procedure at each time step. The final symmetrized equation in matrix form is given by

$$\left|\begin{array}{cc} K_T\beta\,\Delta t & -Q\theta\,\Delta t \\ -Q^T\theta\,\Delta T & -\theta\,\Delta t\left(H\theta\,\Delta t + S\right) \end{array}\right| \left|\begin{array}{c} \Delta\ddot{\bar{u}} \\ \Delta\dot{\bar{P}} \end{array}\right| = - \left|\begin{array}{c} C^u \\ -\theta\,\Delta t\,C^P \end{array}\right| \tag{2.111}$$

2.12 Summary

This chapter presents the theory on the fundamental mechanics of sugar cane crushing based on the literature review of the 1960's and the current mathematical models. The nature and fundamental properties of prepared cane are discussed from a volumetric theory. The one-dimensional theory (Murry, 1960a; Murry and Holt, 1967) of crushing the cane between the rollers is reviewed. The one-dimensional theory considered the prepared cane as a porous medium by applying Darcy's law for the determination of juice pressures on the roll, however no serious attempt was made to include the constitutive characteristics of the solid fibre.

It was only during 1990's porous media theory was applied to the crushing models, by employing the large strain nature of cane by coupling the liquid flow phenomenon through the fibrous material. Based on the experimental observations, constitutive models that represent yielding under hydrostatic pressure are identified for the fibre.

The initial attempts (Adam and Loughran, 1998; Owen et al., 1994; Zhao, 1993) of the modern computational model considered linear elasticity or non-linear elasticity with no plasticity for the fibre, and the permeability was represented by the volumetric strain or by directly measured permeabilities (Murry, 1960a). However, the complex and non-linear material properties were determined later (Downing, 1999b; Leitch, 1996; Loughran and Adam, 1998) through numerous experiments, since the existing numerical models over-simplify the complex three-dimensional grooving effects. A considerable amount of data on the frictional characteristics of bagasse (Bullock, 1957; Cullen, 1965; Loughran and Adam, 1998) is also available.

The following chapters (Chapter 3-5) discuss the elasto-plastic nature of the fibrous prepared cane material, and determine its properties from fundamental cane compression tests. This research applies the currently determined material properties in the model that had undergone the actual mill testing.

Chapter 3

Quasi-static uniaxial experiments

3.1 Introduction

The compression of prepared cane and the associated expression of juice is a flow through deformable porous media problem. The force applied to a sample of prepared cane subjected to a compression test is resisted by both pore fluid pressure and fibrous skeleton. The stress or total stress acts over the entire area of the skeleton and the fluid. The pore pressure acts over the area where there is pore fluid in contact with the total area. This area is the total area minus the fibre skeleton contact area. The establishment of the stress-strain relationship for the solid material is one of the essential formulations of the numerical simulation. To study the response of solid fibrous behaviour under stress it is necessary to isolate pore pressure effect on the fibres. A quasi-static compression test when conducted using porous boundary conditions, the pore pressures result in fibre stresses which are independent of pore effects. Hence it is possible to measure the constitutive behaviour of the fibrous solid matrix in isolation.

3.2 Scope of quasi-static uniaxial experiments

There are a considerable quantity of data available from prepared cane compression experiments (Leitch et al., 1997; Loughran, 1990; Murry, 1960a), however only limited constitutive relations exist across preparation levels. In order to analyse prepared cane under compression, the basic constitutive relationship can be obtained from a confined uniaxial test. In a confined uniaxial test, the specimen is confined laterally, and the strain exists only in the applied force direction. The plastic strain hardening/softening response is determined as a function of volumetric strain from the basic experimental response. The basic uni-axial compression tests were performed for different preparations, and cane varieties (Q117 & Q124) with different fibre contents.

3.3 Testing apparatus and equipment

3.3.1 Confined uniaxial compression cell

The one-dimensional compression test apparatus is shown in Fig. 3.1 with side walls disassembled. It has a rectangular cross section of 229 x 100 mm with porous side walls as drilled holes. The drilled holes provide drainage of expressed juice. The end walls were blank and contain no holes. The dimensions of the test cell are identical to that used by Murry (1960a).

Figure 3.1: Confined uniaxial test cell with drain holes (Adam, 1997).

The matching platen for the cell has a plan area of 200 mm (across the groove) by 100 mm (along the groove), and has detachable inserts for fixing different geometries. For the present analysis, flat and 35° grooved platens were used. The shape of the groove geometry is shown in Fig. 3.2. The groove geometry is almost identical to that of the JCU two-roll mill. The minor differences are compared in Table. 3.1.

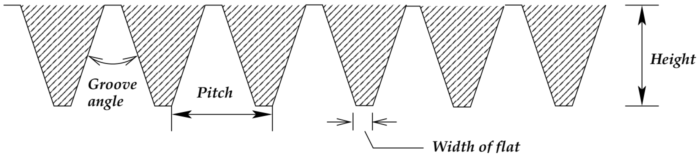

Figure 3.2: Groove geometry.

The test procedure was to apply the load vertically through the platens (Fig. 3.3) to the cane sample between the top and bottom platens with the side plates intact. The compression was continued to the desired height, and then unloaded.

Table 3.1: Dimensions of the grooved platen and the two-roll mill groove.

Dimensions	Platen	Two-roll
Groove angle (degree)	35	35
Depth (mm)	24.5	31.7
Pitch (mm)	26.1	25
Width of flat (mm)	5.2	2.5

3.3.2 Cane mass and preparation

Freshly cut cane sticks were brought to JCU after removing the tops and roots from a cane field. At JCU, the cane sticks were cut into billets and shred into loose fibrous materials using a single pass SRI shredder (Fig. 3.4). This shredder can shred about 30 kg of billets at a time. Each batch of comminuted cane was subsequently cone and quartered for homogeneity. At this stage the comminuted cane is called "prepared cane". The preparation level is designated by the rpm at which the billets were shred in a single pass. Hence, if the cane variety Q117 is shred at 1800 rpm, the preparation level is designated as Q117/1800.

For each compression test, a 2 kg cane sample mass was chosen. This sample mass was prescribed based on the test cell dimensions, the maximum stroke and the

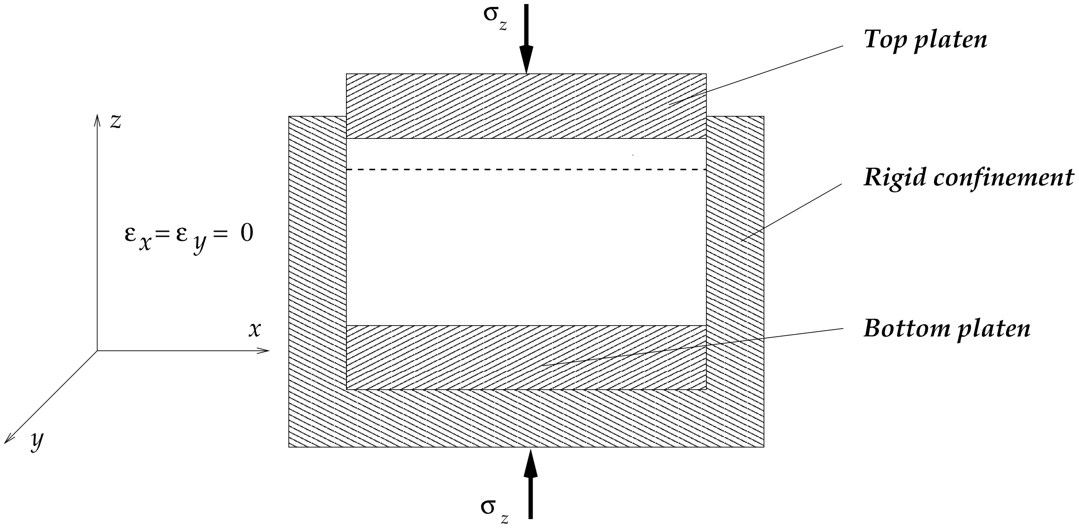

Figure 3.3: Confined uniaxial compression.

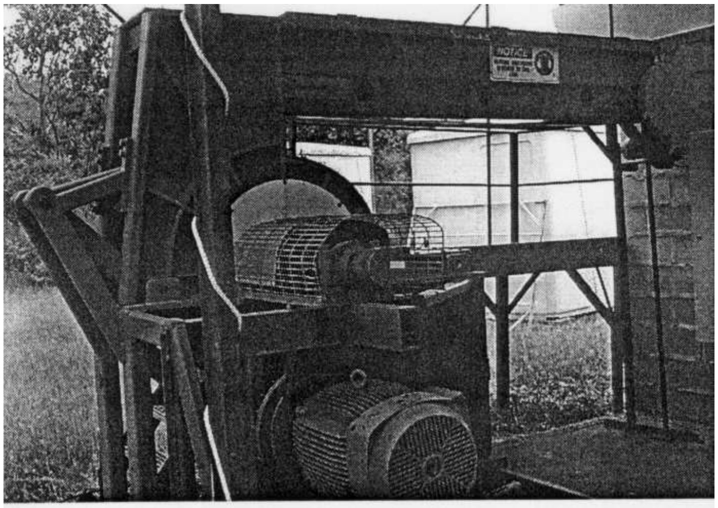

Figure 3.4: Single pass SRI shredder.

load limitation of the compression testing machine. Further, the measurement error on the compression ratio is minimum for a 2 kg mass, compared to 1 kg or 0.5 kg mass for this test cell dimensions (Adam, 1997). When filled in the test cell, a 2 kg sample initially occupies about 100 mm in height, and with a stroke of 75 mm in compression, it is possible to achieve a compression ratio close to 3.

3.3.3 Cane fibre determination

The fibre is essentially the solid component of cane. The fibre content is determined using an apparatus designed and manufactured by SRI (Fig. 3.5). The procedure is very simple in which a known mass of comminuted cane sample is placed in a container which has fine mesh at the bottom. Hot water is recirculated through the sample to form an active filter, which traps insoluble matter.

Figure 3.5: Fibre determination apparatus

Fibre determination apparatus (Leitch, 1996).

After the filter is formed, the sample is washed for a fixed period of time to remove the soluble solid. The sample is then dried by hot air until it weighs a constant mass. Now what is left is the dry mass of the solid fibre, from which the percentage of fibre is determined from the original mass of the sample. The apparatus will collect any insoluble solids including dirt in the prepared cane. Further details of the apparatus are given by Loughran et al. (1988).

3.4 Experimental scheme

Initially, the experiments were conducted on the flat platen at a steady slow speed of 2 mm/min, assuming that at this speed the juice pressure effects on the fibre are at minimum. The tests on grooved platen were carried out at a still lower speed of 1 mm/min. It is advantageous to conduct the grooved platen tests at a speed as slow as possible, since the data from these tests are used to generate the plastic strain hardening response for a two-roll mill of same groove geometry. No flat roll mill experiments were carried out using this cane, however, for a flat-roll mill experiments described in Chapter 7, the flat platen test response was conducted at 1 mm/min which was on a different cane. The effect of juice pressure may be substantial at higher compression ratios, but in the vicinity of compression ratio 2.5, this effects appears to be only marginal for the platen speeds of 1mm/min and 2mm/min as shown in Fig. 3.6. This experiment was conducted on the cane Q124 with a fibre content of 17.22%. It may be noted that all these tests are slower than Loughran's (1990) quasi-static tests, which were conducted at 2.5, 5 and 10 mm/min.

It is also worthwhile to compare the compression speed on these uniaxial tests, with the compression speed in a rolling mill. The vertical compression speed v_y over an arc of roll surface between contact angles θ_1 and θ_2 is given by Murry (1960a)

$$v_y = \frac{2S}{\theta_2 - \theta_1} (cos\theta_1 - cos\theta_2) \tag{3.1}$$

Here, θ is expressed in radians. Typically, for a surface speed (S) of 150 mm/s and for θ_2 =34° ($\simeq$ 0.60 rad), with $\theta_1 = 0$ the vertical speed is 85 mm/s which is well above the compression speed of uniaxial tests.

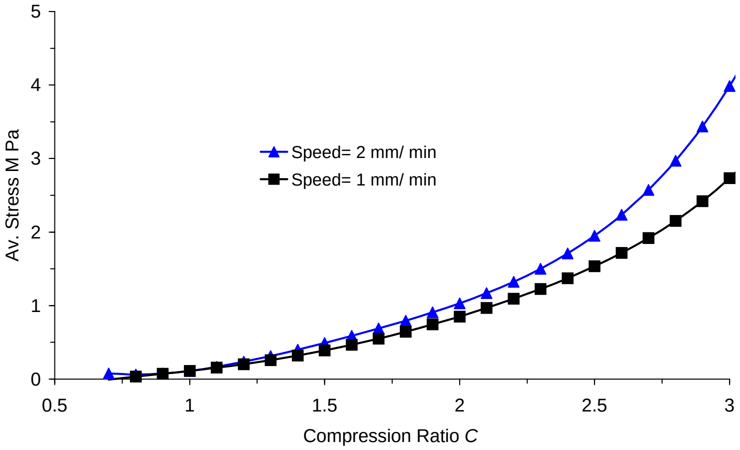

Figure 3.6: Flat platen response at 1mm/min & 2mm/min. (Cane: Q124, f=17.22%)

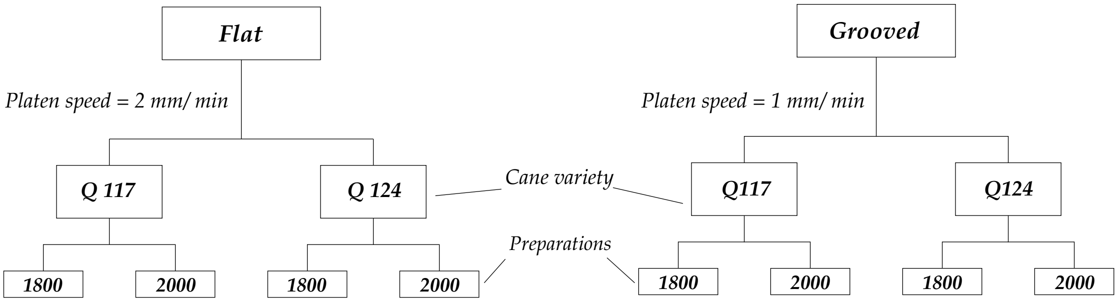

Total number of tests = (2 Platen type) x (2 Cane variety) x (2 Preparation) x (3 repeats) = 24

Figure 3.7: Experimental scheme.

For the experimental programme, tests were carried out with the flat and the grooved platens on Q117 and Q124 canes having average fibre contents of 14.7 and 13.2 percent respectively. On each of these varieties, the preparation levels 1800 and 2000 were used for the tests. Three trials were followed for each category of experiments, resulting in a total 24 tests as shown in the schematic diagram (Fig. 3.7). The order of each test was conducted at random so as to minimize the errors due to variation in material or systematic errors in the experimental technique.

Table 3.2: Experimental correlation for flat platen.
$\sigma_{av} = aC^3 + bC^2 + Cc + d$

Cane variety/ preparation	**Trial**	a	b	c	d	r^2
Q117/1800	1	0.256	-0.57	0.91	-0.47	0.98
	2	0.388	-1.11	1.73	-0.80	0.98
	3	0.355	-0.95	1.50	-0.70	0.99
Q117/2000	2	0.140	-0.25	0.68	-0.39	0.98
	3	0.140	-0.25	0.68	-0.39	0.98
Q124/1800	1	0.152	-0.15	0.46	-0.25	0.98
	2	0.160	-0.17	0.43	-0.24	0.98
	3	0.167	-0.21	0.54	0.30	0.98
Q124/2000	1	0.139	-0.15	0.44	-0.25	0.98
	2	0.204	-0.37	0.75	-0.39	0.98
	3	0.111	-0.06	0.34	-0.21	0.98

The experimental responses of Platen pressure versus Compression ratio are shown in Fig. 3.8 for the flat platen and the corresponding curve fit equations are given in Table. 3.2. Figure 3.9 shows the responses for the 35° grooved platen, and the curve fit equations are given in Table 3.3. It may be noted that the correlation coefficients, r^2 for the cubical fit are all close to unity indicating the best fit. This is due to large experimental data points are made available through data acquisition system.

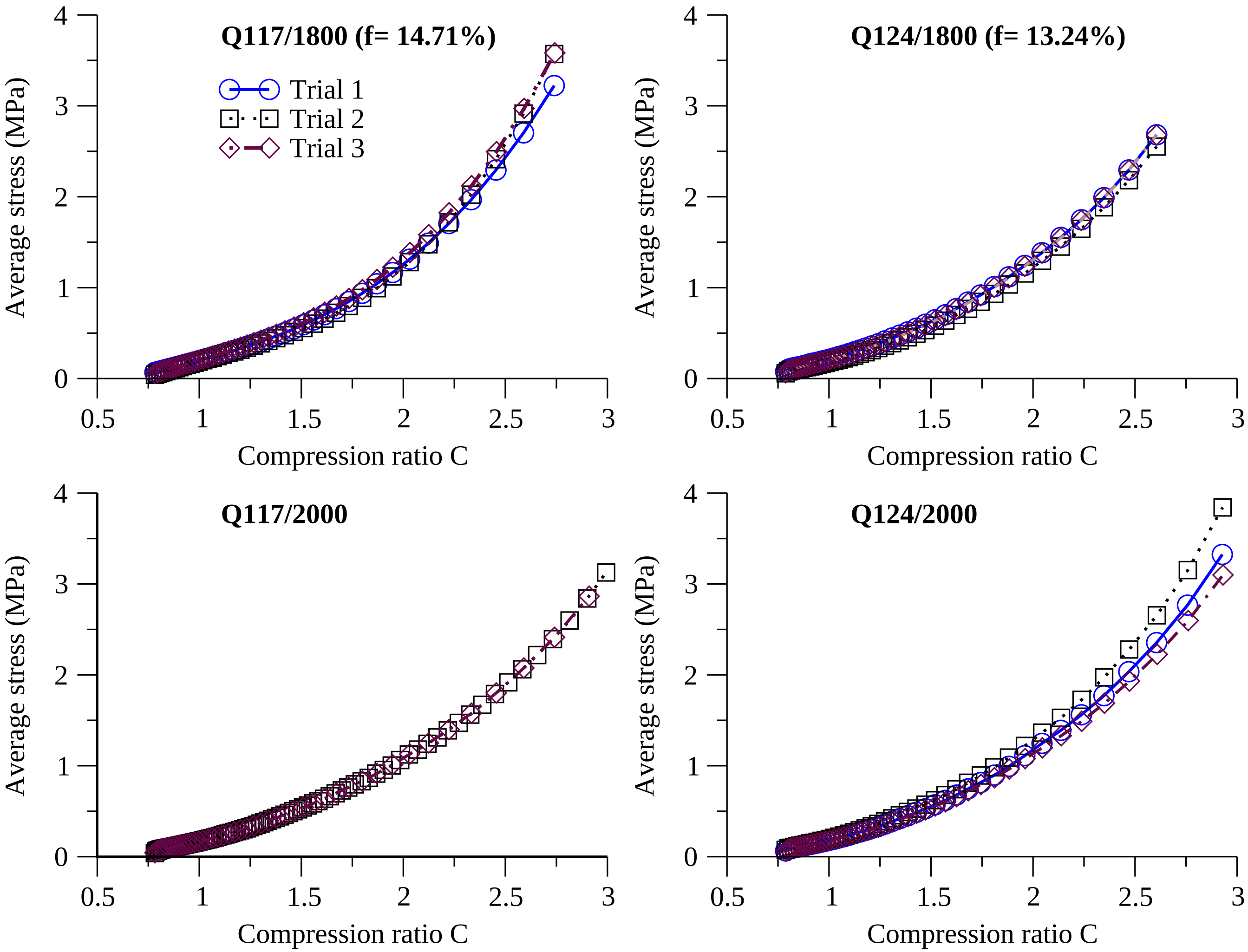

Figure 3.8: Flat platen responses at 2mm/min.

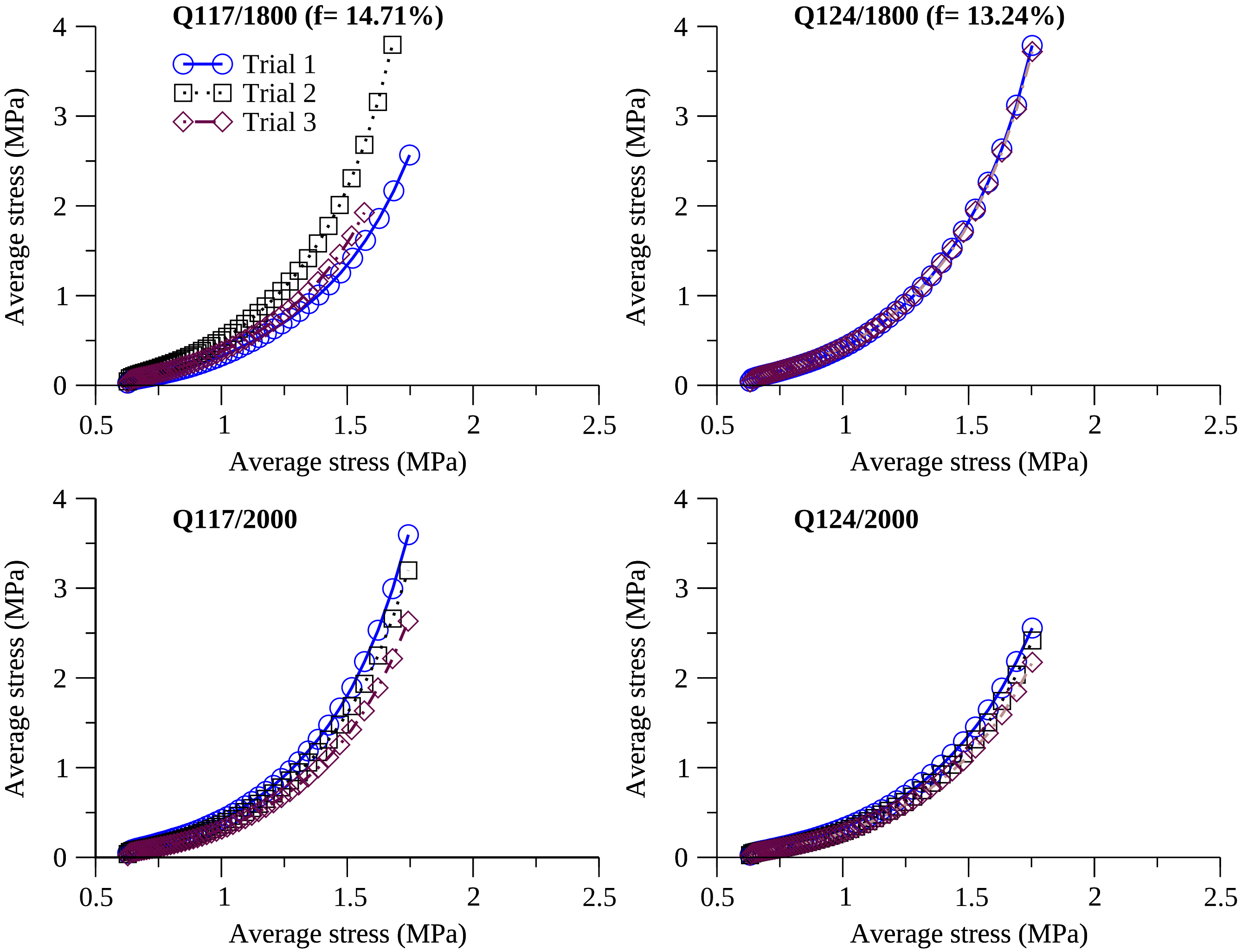

Figure 3.9: Grooved platen responses at 1mm/min.

Table 3.3: Experimental correlation for 35° platen.
$\sigma_{av} = aC^3 + bC^2 + Cc + d$

Cane variety/ preparation	**Trial**	a	b	c	d	r^2
Q117/1800	1	1.648	-3.67	3.43	-1.08	0.98
	2	3.867	-9.46	8.79	-2.70	0.98
	3	1.734	-3.62	3.25	-0.99	0.99
Q117/2000	1	2.919	-7.03	6.54	-2.01	0.98
	2	2.474	-5.82	5.35	-1.65	0.98
	3	1.919	-4.41	4.05	-1.25	0.98
Q124/1800	1	3.086	-7.51	7.00	-2.16	0.98
	3	3.062	-7.54	7.13	-2.23	0.98
Q124/2000	1	1.597	-3.51	3.28	-1.04	0.98
	2	1.727	-4.01	3.74	-1.17	0.98
	3	1.423	-3.21	3.00	-0.94	0.98

3.4.1 Uniaxial testing machine

The Instron 100 kN hydraulic testing machine normally used for testing of metals was used for the sugar cane compression tests (Fig. 3.10). The machine has a maximum stroke of 75 mm in tension or compression. The inbuilt 100 kN load cell provides force output and 150 mm LVDT provides force and displacement output respectively. The load ram velocity can be varied from zero to approximately 100 mm/s.

The Instron's hydraulic control system was interfaced with a Fast Track 8800 digital controller that provides material testing controls. The Fast Track 8800 controller in turn has been interfaced with a personal computer. An user-friendly software facilitates the operation and control of the Instron for material testing in compression or tension. The software is easily configured to suit a particular test. For example, the ram speed, stroke and sample rate of each data to be collected (in this case the load and displacement) can be selected for the test. Upon completion of the test, the data are stored in a specified directory and is retrieved for further analysis.

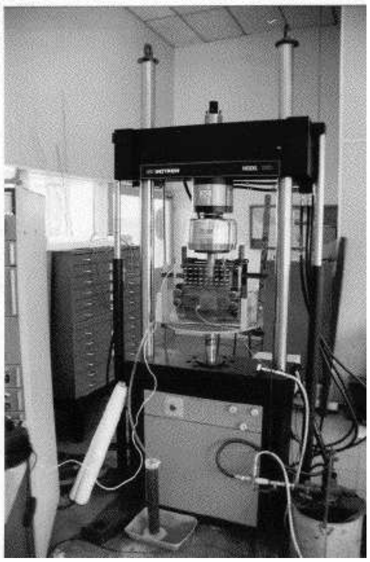

Figure 3.10: Instron uniaxial testing machine.

Prior to testing, the load cell and LVDT were calibrated to validate the measurements. The load cell was calibrated using a standard proving ring instrument supplied by CSIRO, and the LVDT was calibrated using a standard micrometer dial gauge. The maximum deviation in load from the standard instrument was 5%, however at higher loads the deviation was within 2%. The maximum error in position measurement was within 2%.

3.4.2 Testing procedure

The compression tests were carried out during a two-roll mill experimental programme. The cane sample for the compression tests were drawn from the lot used for the mill experiments. For each test, a 2 kg sample of known variety and preparation level was weighed. A known sample mass for fibre determination was also taken from the lot. The confined uniaxial test cell base was placed in the Instron, and the test cell side walls were bolted in place. On the cross head, the platen was fixed to its position. The prepared cane was placed in the test cell by hand. The no gas height h_{ng} for the test cell is estimated by

$$h_{ng} = \frac{V_{ng}}{A_p} = \frac{m_c\left(\frac{f}{\rho_f} + \frac{1-f}{\rho_j}\right)}{A_p} \tag{3.2}$$

where V_{ng} = no gas volume of cane.

A_p = cross sectional area of the cell.

m_c = mass of cane.

f = fibre content in fraction percentage.

ρ = densities (suffix f refers to the fibre, and j refers to juice.

Although it was difficult to achieve a reliable no gas height by hand filling, from the known height of filled material, the initial compression ratio C_i may be calculated from the work opening $w_o = S_o + d$.

$$C_i = \frac{h_{ng}}{w_o} \tag{3.3}$$

where w_o = work opening (Tip to tip distance for grooved platen).

S_o = set opening.

d = groove depth.

The void ratio e corresponding to the compression ratio is known from the following relation.

$$e = \frac{1}{C}\left(1 - \frac{\rho_f}{\rho_j}\right) + \frac{1}{fC}\left(\frac{\rho_f}{\rho_j}\right) - 1 \tag{3.4}$$

The Instron hydraulics and the control system was switched on and the cross head containing the platen was lowered to just touch the top layer of filled sample. At this location the cross head was locked in its position. The Fast Track software was configured to move the ram upwards at a specified speed, say 1mm/min. At this slow speed, the juice that readily comes out through the porous holes of the side walls of the test cell is collected through the tray held to the bottom of the base. Upon reaching an upward stroke of 75 mm, it was configured to unload, by moving the ram in a downward direction. The load (in kN) data and displacement (in mm) was stored in a data file. The volume of juice collected was measured using a standard measuring jar, while the density of juice was measured using a hydrometer.

3.5 Quasi-static experimental response

The non-linear characteristics of the overall stress-strain relation has been observed by several researchers (Adam, 1997; Downing, 1999a). The material essentially consists of discrete organic particles in the form of "fines" and "fibres", typically 10-20% by mass. Initially, the compressive stress causes the fibres to slide, bend and reorient perpendicular to the direction of applied stress. This causes the material to form a layered matrix. Any further increase in compressive force causes the liquid juice to express and as a result, the onset of densification causes a rapid increase in stiffness. The compression on the prepared cane causes, primarily, the rearrangement of fibres, and so the stiffness will increase from loose state (where there are plenty of voids for the fibres to move into) to dense state (where there is much less opportunity for fibres to rearrange).

The average vertical stress and the volumetric strain is calculated from the experimental response. The compression ratio may be related to volumetric strain by defining

$$\Delta V_{ng} = V_{ref} - V_{ng} \tag{3.5}$$

$$\text{and } \Delta V = V_{ref} - V \tag{3.6}$$

where V_{ng} is no gas volume, V_{ref} is the reference volume for volumetric strain, and V is the volume at any time. Therefore

$$C = \frac{V_{ng}}{V} = \frac{V_{ref} - \Delta V_{ng}}{V_{ref} - \Delta V} \tag{3.7}$$

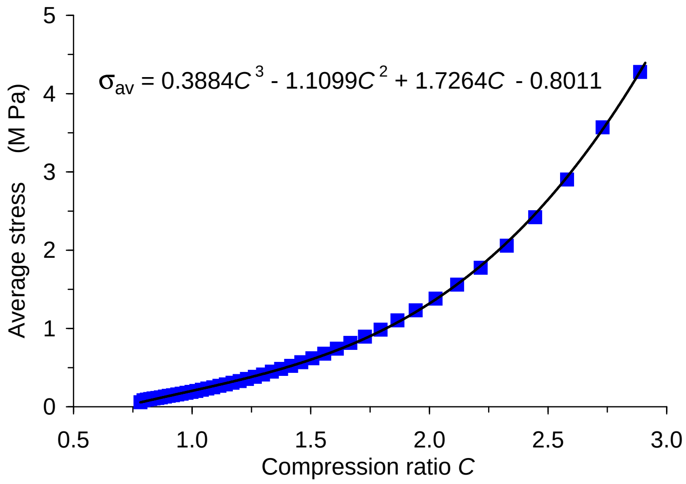

Figure 3.11: Quasi-static response for flat platen.

The above equation gives

$$C = \frac{1 - \epsilon_{vn}}{1 - \epsilon_v} \tag{3.8}$$

where ϵ_{vn} = is the volumetric strain at $C = 1$.

ϵ_v = is the volumetric strain at any position.

If the no gas volume is taken as the reference volume, then the compression may be expressed as

$$C = \frac{1}{1 - \epsilon_v} \tag{3.9}$$

Figure 3.11 shows the average stress Vs compression ratio characteristics, of a typical flat platen test for Q117/1800 (Trial 2). The non-linear characteristics of strain hardening behaviour of the fibrous solid matrix is obvious from the figure with an initial highly compressible phase, followed by the onset of densification.

A similar result is shown for 35° grooved platens in Fig. 3.12 for Q117/1800 (Trial 2) along with the equation of fitted curve to the data.

The grooving effects and the fibre plastic behaviour are essentially determined from the above responses. The details on the determination of plastic behaviour are

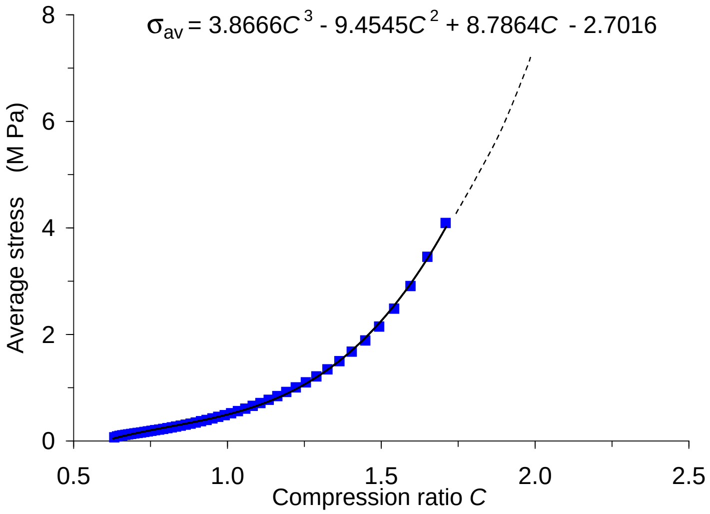

Figure 3.12: Quasi-static response for 35° platen.

explained in Chapter 5. Since no noticeable variation in the plastic behaviour was observed for any of the correlations shown in Fig. 3.9 for the canes Q117 and Q124 or for the preparation levels 1800 and 2000, the experimental correlation shown in Fig. 3.12 is utilised as a representative case for the 35°groove.

In principle, the prepared cane behaves like other solids when subjected to changes in loading, but there are significant differences, to compare with steel or concrete, in the following respects.

(1) Prepared cane is weak in tension.

(2) In compression, prepared cane will generally undergo a change in volume or an increase in pore fluid pressure.

(3) Saturated cane can only undergo a change in volume as pore liquid is expressed.

(4) Like soil, initially denser prepared cane dilates (in order to break the interlocking friction between fibres) and eventually reach a steady state shear stress, corresponding to the achievement of the critical void ratio. An initially loose sample reaches the same critical shear stress without dilation.

3.6 Uncertainty in experimental measurement

The uncertainty in the calculated experimental results is based on the uncertainties of the primary experimental measurements. The uncertainties in the calculation of compression ratio, and average vertical stress are estimated by a procedure explained by Holman (1996). According to this theory, when the experimental result R is a given function of the independent primary variables $x_1, x_2, \ldots, x_n$, and let $w_1, w_2, \ldots, w_n$, be the uncertainties in the independent primary variables, then the uncertainty w_R in the calculated result R is given by

$$w_R = \sqrt{\left(\frac{\delta R}{\delta x_1} w_1\right)^2 + \left(\frac{\delta R}{\delta x_2} w_2\right)^2 + \ldots + \left(\frac{\delta R}{\delta x_n} w_n\right)^2} \tag{3.10}$$

3.6.1 Uncertainty in compression ratio

The compression ratio for the tests is calculated from the ratio of no gas height h_{ng}, to the actual height h of the specimen in the test cell. When the specimen is around 25 mm, the compression ratio is around 3. For a no gas height of 80 mm, the compression ratio is expressed by

$$C = \frac{h_{ng}}{h} = \frac{80}{25} = 3.2 \tag{3.11}$$

The maximum error for no gas height calculation is within 2.2%, based on an estimation given in Adam (1997). The other primary measure, h has an error of 2%. The uncertainty (w_C) at maximum compression ratio based on the primary measurements h_{ng} and h is given by

$$w_c = \sqrt{\left(\frac{\delta C}{\delta h_{ng}} w_{ng}\right)^2 + \left(\frac{\delta C}{\delta h} w_h\right)^2} \tag{3.12}$$

and this works out to be within 3%. The uncertainty at lower compression ratios is also within 3%.

3.6.2 Uncertainty in vertical stress

The average vertical stress is calculated from the vertical force F_v and the cross sectional area A of the platen.

$$\sigma_a = \frac{F_v}{A} \tag{3.13}$$

The uncertainty for the force measurement is ± 5 kN as observed from the calibration procedure. For the area, the uncertainty is 0.00025 m^2 (this is arrived based on an error of ± 1 mm in length measurement). The uncertainty in the stress calculation is estimated from

$$w_{av} = \sqrt{\left(\frac{\delta\sigma_a}{\delta F_v} w_{F_v}\right)^2 + \left(\frac{\delta\sigma_a}{\delta A} w_A\right)^2} \tag{3.14}$$

Substituting the relevant values, the uncertainty in stress calculation works out to be 5.1%.

3.7 Compression and volume change

It is known that when a sample mass of prepared cane is loaded, it will be compressed, and it will swell when unloaded. In a saturated sample condition, the immediate response to loading is an increase in pore pressure, and if drainage is possible, the juice flows out of the sample as it compresses or back into it as it swells. The rate of flow and therefore of volume change is controlled by the permeability of the prepared cane. Such changes in volume are related to the effective stress. In the following sections, the prime ($'$) notation refers to effective stress states.

3.7.1 Drained conditions in uniaxial compression

When loading is applied slowly, such that the liquid drains away without any increase in pore pressure, the volume will decrease and stress-strain behaviour is defined in terms of effective stress. The principal constants are modulus of elasticity:

$$E' = \frac{\delta \sigma'}{\delta \epsilon} \tag{3.15}$$

the bulk modulus:

$$K' = \frac{\delta p'}{\delta \epsilon_v} \qquad \text{and} \tag{3.16}$$

the modulus of rigidity or shear modulus:

$$G' = \frac{\delta \tau}{\delta \gamma} \tag{3.17}$$

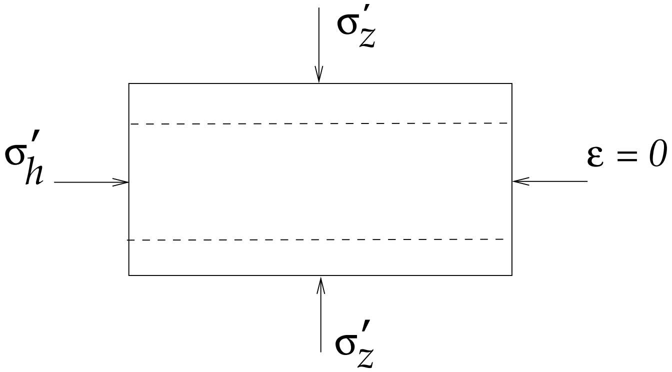

Figure 3.13: Uniaxial compression.

Although, here we are concerned with one-dimensional loading, the conditions during compression and swelling is illustrated in Fig. 3.13. Hence, by putting

$$\epsilon_x = \epsilon_y = \epsilon_h = 0 \quad \text{and} \quad \sigma'_x = \sigma'_y = \sigma'_h$$

Then

$$\epsilon_h = 0 = \frac{1}{E}\left(-\nu\sigma'_z + \sigma'_h - \nu\sigma'_h\right)$$

Therefore

$$\sigma'_h = \frac{\nu}{1-\nu}\sigma'_z \tag{3.18}$$

For an isotropic elastic material

$$\epsilon_z = \frac{1}{E'}\left(\sigma'_z - 2\nu\sigma'_h\right) \tag{3.19}$$

Substituting for σ_h from Eq. (3.18) in Eq. (3.19)

$$\epsilon_z = \frac{\sigma'_z}{E'}\left[\frac{(1+\nu)(1-2\nu)}{1-\nu}\right] \tag{3.20}$$

3.7.2 One-dimensional compression and swelling

Drained behaviour during one-dimensional compression is close to the idealized compression curve as shown in Fig. 3.14(a). The vertical strain can be expressed in terms of a change in thickness (Δh), a change in void ratio (Δe) or a change in specific volume ($\mathrm{d}v$).

$$\frac{\Delta h}{h_o} = \frac{\Delta e}{1+e_o} = \frac{\Delta v}{v_o} \quad \text{or} \quad \mathrm{d}\epsilon = \frac{\mathrm{d}h}{h} = \frac{\mathrm{d}e}{1+e} = \frac{\mathrm{d}v}{v} \tag{3.21}$$

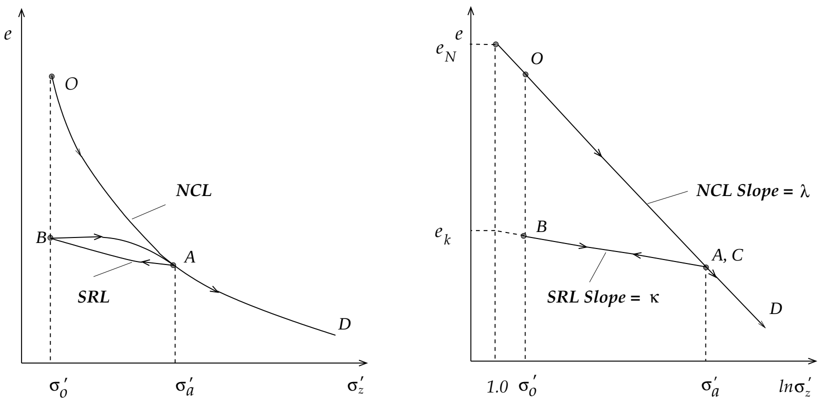

(a) Compression and swelling curve

(b) Idealized line

Figure 3.14: One-dimensional compression and swelling.

When e is plotted against $\log\sigma'_z$ (Fig. 3.14(b)), the Normal Compression Line (NCL) and Swelling Recompression Lines (SRL) are expressed as linear functions.

$$NCL: \quad e = e_N - \lambda \log\sigma'_z \tag{3.22}$$

$$SRL: \quad e = e_K - \kappa \log\sigma'_z \tag{3.23}$$

where e_N= the void ratio (e) at σ'_z= 1.0 k Pa.

λ = slope of the NCL.

e_K= the void ratio (e) at σ'_z= 1.0 l Pa (on the SRL).

κ = slope of the SRL.

The parameters e_N, λ and κ may be considered as constants for a particular cane under limited stress range. The swelling line AB meets the normal compression line at C, which is a yield point and the yield stress is σ'_a. Unlike the normal compression line, there is no unique unload/reload line. The cane sample could be unloaded from any point on the normal compression line, and there are any number of swelling lines. Note that the swelling-reloading line is flatter, indicating increased stiffness. At the intersection of the two lines, e has a common value

$$e = e_N - \lambda \log \sigma'_a = e_k - \kappa \log \sigma'_a \tag{3.24}$$

Then

$$\log \sigma'_a = \frac{e_N - e_k}{\lambda - \kappa} \tag{3.25}$$

3.7.3 Interpretation of one-dimensional test results with triaxial tests

During the increase and decrease of σ'_z in one-dimensional loading and unloading, the horizontal stress σ'_h changes, since ϵ_h is held constant and the ratio of σ'_h to σ'_z is expressed from Eq. (3.18) as

$$\frac{\sigma'_h}{\sigma'_z} = \frac{\nu}{1-\nu} = K_o \text{ (coefficient of lateral pressure)} \tag{3.26}$$

Here, the Poisson's ratio ν, cannot be easily measured however, the lateral coefficient K_o could be measured experimentally. Adam (1997) measured K_o for three preparation levels (i.e. at 810/14, 810/28, and 1440/20)[1] and noticed that it has only a small effect

---

[1] This was shredded in JCU's Waddle hammer mill. The preparation level for e.g. 810/14 refers to the shredder run at 810 rpm for 14 seconds.

on the preparation. The K_o varied from 0.12-0.22, which indicate the internal tendency of prepared cane to resist lateral expansion.

A connection can be made between one-dimensional and triaxial compression using K_o. During one-dimensional loading and unloading, σ'_z and σ'_h are generally unequal, and so there are shear stresses in the prepared cane. Any comparison between isotropic and one-dimensional compression and swelling will have to take account of the shear stress. The link between these can be developed by noting that one-dimensional loading is a special case of plane strain. From Eqs. (2.50) and (2.52) with $\sigma_x = \sigma_y = \sigma'_h$ (bi-axial symmetry), and making use of Eq. (3.26), we have

$$\text{Mean normal stress } p' = \frac{1}{3}\sigma'_z\,(1 + 2K_o) \tag{3.27}$$

$$\text{Deviatoric or shear stress } q' = \sigma'_z\,(1 - K_o) \tag{3.28}$$

Assuming a constant value of 0.22 for the lateral pressure coefficient (K_o), the loading and unloading characteristics of the flat platen is plotted in Fig. 3.15 with void ratio (e) as the ordinate. The normal consolidation line of drained triaxial test results (Leitch, 1996) is also compared with the uniaxial test results in Fig. 3.15. The uniaxial test results are in reasonable agreement with the triaxial results, and it may be noted that the triaxial results (Leitch, 1996) were generated for hand compacted cane, from high pressure isotropic drained compression tests with a preparation of 1440/20 in Waddle hammer mill.

3.7.4 Determination of logarithmic bulk moduli from loading and unloading states

Referring to Fig. 3.15, the slope of the normal compression line AB is shown typically for Q117/1800 (Trial 1).

$$\frac{\Delta e}{\Delta \ln \sigma'_z} = -2.25 \;\; (= -\lambda) \tag{3.29}$$

Similarly, the slope of the unload line BC is

$$\frac{\Delta e}{\Delta \ln \sigma'_z} = -0.21 \quad (= -\kappa) \tag{3.30}$$

The average values of λ and κ are estimated directly from the loading and unloading curves for the canes Q117 and Q124. Table 3.4 shows the range of average values estimated from all the trial tests for the flat and grooved platens. The logarithmic bulk moduli λ, and κ were estimated independently (Adam, 1997) from isotropic triaxial test results (Leitch, 1996). The estimated values of λ and κ from triaxial and uniaxial test results are compared in Table. 3.4.

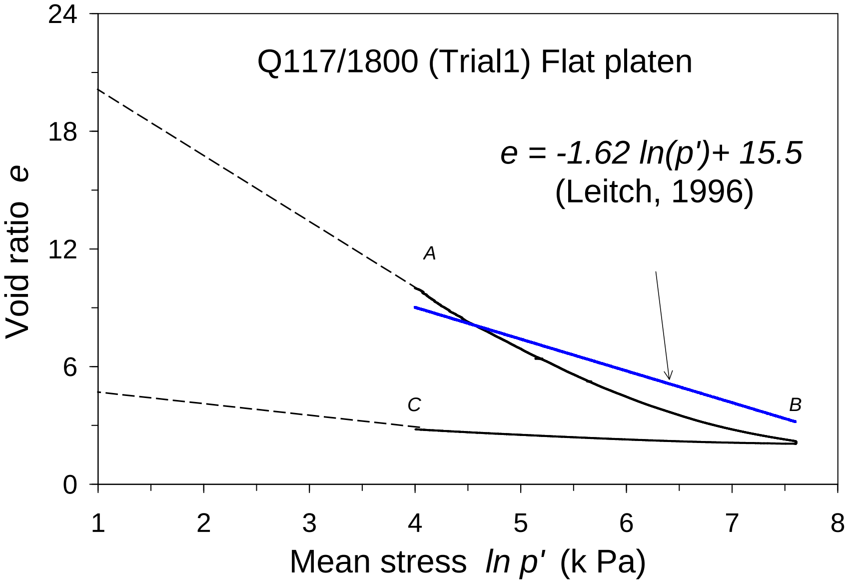

Figure 3.15: Uniaxial results with triaxial tests.

Table 3.4: The Logarithmic moduli λ and κ.

Experiments	κ	λ
Flat platen	0.19-0.31	2.08-2.82
Grooved platen (35°)	0.18-0.22	2.02-2.64
Triaxial (Adam, 1997; Leitch, 1996)	0.1-0.2	1.85-2.55

The discrepancy in κ from triaxial test results may be attributed to the elastic recovery that may have been hindered by the rubber membrane surrounding the triaxial specimen. Adam (1997) suggested a representative value for κ in the range between 0.1 and 0.2, and ultimately used $\kappa = 0.25$.

3.8 Summary

The confined uniaxial quasi-static experiments were performed, mainly to determine the constitutive behaviour of the fibrous solid matrix in the absence of any pore pressure effects. Both flat and grooved platens were used to assess their effect on the strain hardening response. The non-linear characteristics of the fundamental stress-strain relation was accounted for, and the results will be utilized for the establishment of constitutive relations for the solid matrix, mainly the plastic strain hardening relation (see Chapter 5). The plastic hardening parameters are determined through an inverse calibration of finite element simulation of the test cell. The uniaxial test results were extended for the triaxial loading situation, and the results were validated through independent data from a triaxial test. The elastic and plastic moduli were also calculated for the platens from the loading and unloading characteristics.

Chapter 4

Liquid flow through fibrous matrix

4.1 Introduction

In addition to the strength and stiffness, a third property of prepared cane of great practical importance is its permeability, a measure of the ease with which the juice may flow through the prepared cane. The porous and two-phase nature of prepared cane exhibits large resistance to juice flow especially at higher compression. The power required for expressing the juice is highly dependent on the flow properties within the fibrous solid matrix. The knowledge of the permeability response therefore will permit the calculation of pressure distribution on the rolls, and determination of the power required for crushing. In the numerical modelling, the liquid flow is coupled with the internal stress states of the fibrous matrix, hence the permeability response is a crucial factor in crushing.

Attempts were made to define permeability with reference to saturated and partially saturated canes (Adam and Loughran, 1998; Owen et al., 1995). The important aspects of partially saturated flow, namely the absorption/exsorption behaviour of prepared cane and expulsion of air from the porous media during compression are discussed in detail (Adam, 1997). However, in mill rolling, the presence of gas pressure is at atmospheric over the unsaturated domain, and hence the gas flow is assumed to be not significant. This chapter discusses the determination of the permeability response of prepared cane by various approaches. The permeability response was investigated based on a semi-theoretical approach, permeability cell experiments, and inverse-calibration methods from dynamic compression tests (Adam, 1997; Bullock, 1957; Holt, 1963).

4.2 Darcy's law and permeability

The flow channels in fibrous materials are irregular in cross-section and complex in their interconnections. The juice when flowing, follows a tortuous route through the voids which in turn are dependent on compaction. Further, this factor has been found to vary between porous media having the same void ratio and particle-size and so is likely to have a strong influence on the permeability of fibrous material such as prepared cane. Analysis of the flow through individual pores is not possible. Hence, from a practical point of view, the prepared cane as a porous medium is assumed as continuous with fluid and solid phases forming an over lapping region on a macroscopic scale.

The physical law governing flow through the porous media was expressed by Darcy's law from Eq. (2.38) as,

$$Q = kiA \tag{4.1}$$

where Q is the flow rate of liquid, i is the rate of decrease in total head with distance in the direction of flow, A is the cross sectional area of the flow-tube, and k in m/s is a material parameter known as the *"coefficient of permeability"*. The Darcy's coefficient of permeability k depends on the properties of the permeating fluid as well as the solid matrix.

$$k = K\gamma_f/\mu \tag{4.2}$$

where K (m^2) is the intrinsic permeability of the solid matrix, which does not depend on the properties of the fluid, γ_f ($\mathrm{N/m}^3$) is the unit weight of the fluid, and μ (Pa.s) is the dynamic viscosity of the fluid.

The coefficient of permeability used in Darcy's law is a measure of the ease with which the fluid can flow through the voids between the fibrous solid matrix. Darcy's coefficient of permeability depends primarily on void ratio, pore size, and viscosity of the pore fluid. Less importantly, the preparation level and material anisotropy may also affect the permeability value.

4.3 Permeability based on empirical equations

Darcy's law can be applied to both steady state, and the transient case, the main stipulation is that the flow must be laminar, rather than turbulent. The Reynolds number which defines the laminar flow regime, is based on some average characteristic dimension like the pore size. Considering the microscopic nature of material through which the juice is squeezed out, the laminar regime was confirmed through a quantitative estimate (Bullock, 1957; Downing, 1999a).

The Kozeny-Carman Equation was considered by Adam (1997), in an attempt to compare its response with the experimental results obtained by Holt (1963). The intrinsic permeability(K) was specified in terms of porosity(n) and the specific surface area (A_s) as

$$K = \frac{\left[\frac{n^3}{(1-n^2)}\right]}{5A_s^2} \tag{4.3}$$

This theory assumes that the fibrous solid matrix is comprised of uniform cylindrical particles with assumed dimensions of particle diameter and particle length. The final equation in terms of void ratio was given after accounting for the dimensions of the particle geometry.

$$K = \frac{\left[\frac{e^3}{(1+e)}\right]}{50.15X10^6} \tag{4.4}$$

The Kozeny-Carman equation, however, predicts higher permeabilities than the directly measured values, due to assumed particle geometry and the idealized theoretical basis.

When the applicability of Darcy's law is in doubt especially at higher Reynolds number, the pressure flow rate relationship was expressed in non-linear form. This has been suggested by Adam (1997) in accord with the Forchheimer equation, i.e.

$$\frac{\mathrm{D}P}{\mathrm{d}l} = \alpha v + \beta v^2 \tag{4.5}$$

where v is the superficial velocity, α, and β are constants. The parameters αv and βv^2 vary with viscous and inertia effects respectively.

4.4 Permeability response from direct experimental measurements

The first detailed fundamental approach to gain knowledge of the permeability of prepared cane was undertaken by Bullock (1957). Since the prepared sugar cane exhibits directional properties when formed into a block, Bullock attempted to measure permeability in the direction of pressure application "axial") and in direction perpendicular to the direction of pressure application ("transverse").

Holt (1963) derived from dimensional analysis and from the assumption of laminar flow, the average velocity of liquid as

$$V = \frac{K}{\mu}\frac{\mathrm{d}p}{\mathrm{d}l} \tag{4.6}$$

and described the above equation as "Darcy's law modified for viscosity". Holt went on to verify this law, considering the tortuous nature of the flow path and the size of the fibres in a sample of prepared cane.

Murry's (1960a) experimental apparatus consisted of 200 mm cube flow cell, in which a sampled cane could be compressed up to a compression ratio of three. The compression ratio was varied by using different weights of cane in the sample. Provision was made to pump liquid in both the axial and transverse directions. The liquid pressure was applied to the sample by a small plunger pump providing the required flow rate. The permeability was calculated from the rate of flow from the central section, the pressure head and the cell dimensions.

All of Murry's experimentally measured data were represented by an exponential relation of the form

$$K = aC^{-b} \tag{4.7}$$

where K is the intrinsic permeability, and C is the compression ratio. This equation may also be expressed as a function of void ratio.

$$K = a\left[f\left(e\right)\right]^{-b} \tag{4.8}$$

Holt (1963) showed from flow rate Vs pressure drop curves at different compression ratios, that Darcy's law is a fair approximation at low compression ratio and that this approximation improves as the compression ratio increases. Further, Holt observed that the permeability in the axial direction is somewhat higher than that for the transverse direction over most of the range (compression ratio). The permeability against compression ratio was shown to decrease markedly as the fineness of prepared cane decreases (Bullock, 1957; Holt, 1963)

4.5 Effective permeability

Extensive information are available on the permeability of prepared cane under various degrees of compression and fineness of preparation (Holt, 1960, 1961, 1963). However, the permeability determined in this way generally relates only to a large mat of prepared cane, and need not be applicable to the conditions encountered in the actual milling operation where only a relatively thin mat is present (Murry and Holt, 1967). Further, as the juice is extracted, it flows towards the roll and is removed along the roll surface. It encounters less resistance, particularly at the bottom of the grooves where the bagasse is not packed so tightly. It is apparent that the presence of these low resistance paths serve to reduce the pressure required to remove the juice. In an effort to overcome the difficulties allowing for these low resistance paths, a method of estimating the permeability of a sample of cane from dynamic compression tests was developed. These tests were carried out in a hydraulic press, instrumented to record continuously position of the piston (hence instantaneous volume under the ram and speed of descent) and load (hence pressure on the sample). The effective permeability K_e was derived as

$$K_e = \mu S \frac{b^2}{12 t p_m} \tag{4.9}$$

where μ = dynamic viscosity.

S = speed of descent of piston.

b = length of compression box used in test.

t = instantaneous thickness of the sample.

p_m = mean load per unit area on the piston.

The effective permeability K_e is a value calculated from the actual resistance offered by the cane sample to compression, and this term includes the effect of any low resistance paths.

4.6 Permeability response from dynamic compression tests

The permeability response determined by direct experiments (Holt, 1963; Murry, 1960a) do not account for seepage induced consolidation and underestimate the permeability by 2.4 times at compression ratios below 1.6 (Adam, 1997). Hence an alternative method of calibration of permeability response by the simulation of dynamic compression tests was attempted by Adam (1997). Unlike the quasi-static compression tests, in dynamic compression tests, the juice pressure may comprise almost all of the overall force response. In this method, the permeability response was adjusted to match experimental platen force (or juice pressure) to the finite element simulation of dynamic compression test. For dynamic compression, the juice pressure developed is generally dependent on the flow path length. However, the permeability response was inverse-calibrated by comparing with juice pressure at the center of the cell as this is considered a more fundamental process than comparison with overall platen force. The inverse-calibration was performed by comparing simulation results with measured juice pressures. The permeability Vs void ratio response is determined from the compression ratio response using Eq. (4.8). The response for the flat platen experiments with 1440/20 preparation and fibre content 11.0% was determined as

$$K = a\left(\frac{12.46}{1+e}\right)^{-b} \tag{4.10}$$

The coefficients a and b are functions of compression speed. Similarly the permeability relation for 750/15 preparation with 55° grooved platen and fibre content 14.9% was determined as

$$K = a\left(\frac{9.09}{1+e}\right)^{-b} \tag{4.11}$$

Figure 4.1: Comparison of permeability responses (Adam, 1997).

The inverse-calibrated permeability response for grooved platens implicitly account for grooving effects. These responses are appropriate for simulation of mills with grooved rolls of same geometry.

It was found that the inverse calibrated permeabilities were higher at lower void ratios and lower at higher void ratios than the directly measured permeability response. However, considering the differences in preparation level, surface type, seepage velocities and apparatus between inverse-calibration and direct measurement techniques, the two approaches provide reasonable agreement. The comparison of inverse calibrated and directly measured permeability responses are given in Fig. 4.1 as compiled by Adam (1997)

4.7 Permeability tests

The apparatus used to determine the permeability had a feeder compartment with a plan area of 150 x 150 mm. The sample specimen is placed in this area by hand, and the specimen was compacted through a baffle plate held over this sample as shown in Fig. 4.2. The compaction was achieved using a flat platen, fixed to the cross head of the Instron testing machine.

The description of the apparatus and experimental setup are described in detail by Downing (1999a). For brevity, only the relevant features to the experimental programme are explained. The factorial experiment carried out for the permeability response was

Total no. of tests = (2 cane variety) X (2 preparations) X (3 repeats)= 12 test

Recalling the Darcy's law for the porous material $Q = kA\frac{\mathrm{d}h}{\mathrm{d}l}$, the coefficient of permeability k which is a function of compression ratio (or void ratio) is determined by the direct measurement of the variables in this relation. The volume flow rate (Q), the differential pressure across the specimen $\mathrm{d}h$, and the thickness of the specimen $\mathrm{d}l$ are the measured parameters for each compression ratio.

In the experimental apparatus, for the known sample thickness, the flow rate was measured only through the centre section of the specimen over an area of 80 x 80 cm to avoid the side effects of the cell. This flow is indicated in the Fig. 4.2 as "Darcy Flow".

Figure 4.2: Permeability cell apparatus (Downing, 1999b).

The Darcy's flow rate was collected in a standard measuring jar by noting the time required to fill the known volume. The pressure drop with reference to the atmosphere was measured from the dial gauge fixed at the inlet to the flow. Different compression ratios were achieved by changing the sample height, that is by placing suitable spacers between the top baffle plate and the sample cane.

Once a set of readings of all the parameters were taken, the sample height was reduced further to the next compression ratio using appropriate spacers. The lowest void ratio achieved was around 3.0 from an initial void ratio of about 10.0. At the lowest void ratio, a differential pressure of the order of 1200 kPa was required to drive the flow. This was achieved using a high pressure/low volume diaphragm pump.

4.7.1 Uncertainty in permeability

The permeability k was calculated from $k = \frac{Q}{A}\frac{\mathrm{d}l}{\mathrm{d}h}$ by rearranging the Darcy's equation. The uncertainties for the flow rate, length, area, and pressure were estimated based on the resolution of different instruments used. They are given in Table 4.1. The uncertainty in the permeability calculation was estimated from the following equation based from the principles explained in Section 3.6.

$$w_k = \sqrt{\left(\frac{\delta k}{\delta Q} w_Q\right)^2 + \left(\frac{\delta k}{\delta l} w_l\right)^2 + \left(\frac{\delta k}{\delta A} w_A\right)^2 + \left(\frac{\delta k}{\delta h} w_{\mathrm{d}h}\right)^2} \tag{4.12}$$

Upon substituting the uncertainty values, the calculation estimates a maximum of 6% in uncertainty for the permeability.

Table 4.1: Uncertainty in the measured variables.

Measured variable	**Uncertainty**
Flow rate (Q)	$\pm 10 \text{ x } 10^{-3}\ \mathrm{m}^3/s$ (w_Q)
Length (l)	$\pm 0.5 \text{ x } 10^{-3}$ m (w_l)
Area (A)	$\pm 0.25 \text{ x } 10^{-3}\ \mathrm{m}^2$ (w_A)
Pressure (dh)	$\pm 25 kPa^{\dagger}$ ($w_{\mathrm{d}h}$)

† Expressed as equivalent water column in m.

4.7.2 Permeability results

The results of the permeability response for two cane varieties Q117 and Q124 are shown in Fig. 4.3. The general trend of increasing permeability with increasing void ratio and the non-linearity is observed for all the cases tested. The permeability response in general could not be conducted at void ratio less than 4, due to practical limitation of the Instron machine which was used to compress the cane. Sometimes, the flow rates at this level were also inconsistent with different trials. However, for Q124 few data could be measured in this region.

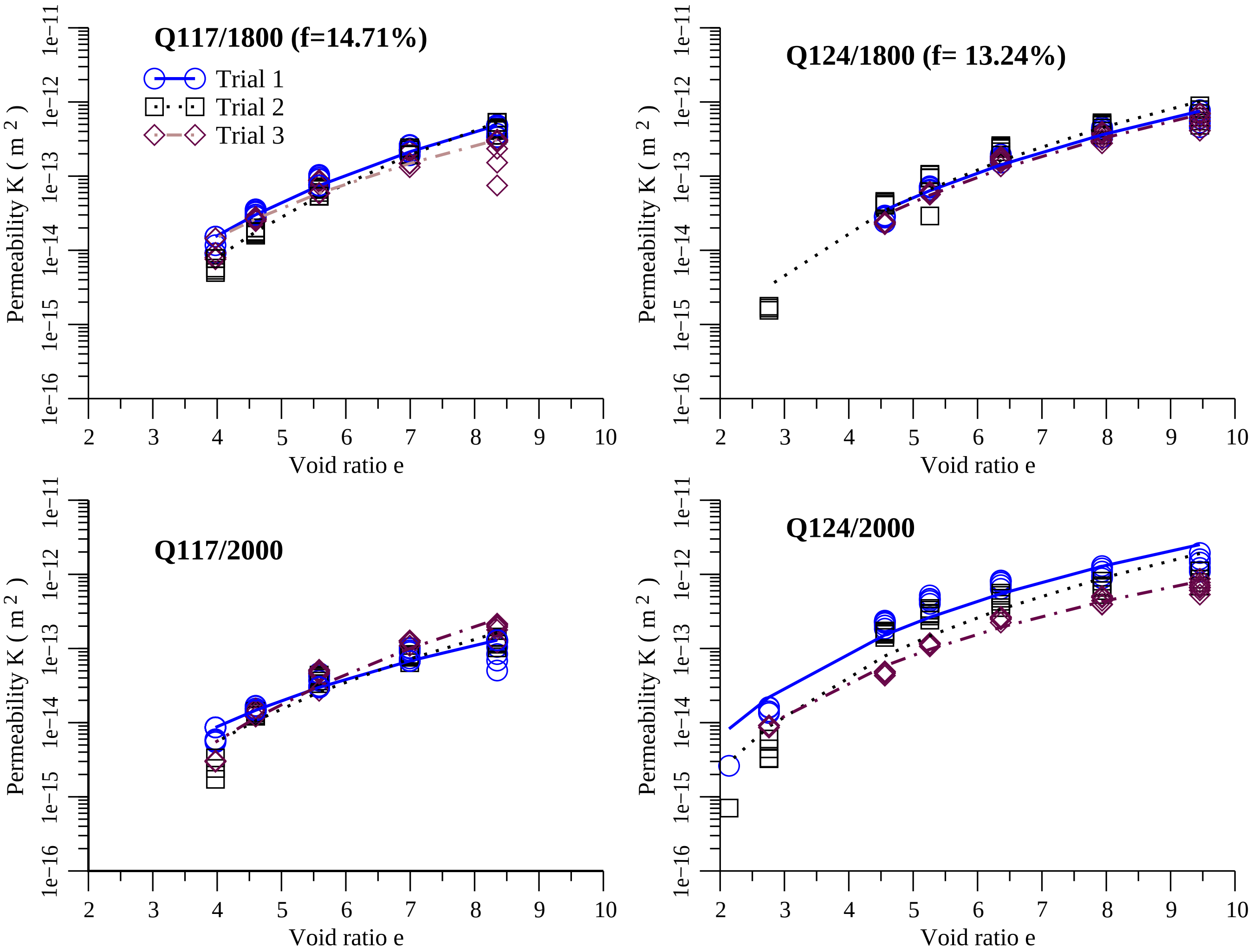

Figure 4.3: Measured permeability responses.

The experimentally determined permeability values K, have been fitted to trend line using the power equation $K = ae^b$, where e is the void ratio. The fitted equations and the associated constants are given in Table 4.2. The reliability of the trend lines are also indicated by correlation co-efficients r^2.

Table 4.2: Experimental correlation of permeability responses $K = a(e)^b$.

Cane variety/ preparation	**Trial**	a	b	r^2
Q117/1800	1	2.46 x 10^{-17}	4.66	0.98
	2	2.97 x 10^{-18}	5.70	0.98
	3	4.93 x 10^{-17}	4.12	0.92
Q117/2000	1	5.61 x 10^{-17}	3.65	0.93
	2	9.59 x 10^{-18}	4.59	0.95
	3	4.54 x 10^{-18}	5.14	0.97
Q124/1800	1	5.86 x 10^{-17}	4.21	0.98
	2	2.93 x 10^{-17}	4.66	0.97
	3	4.60 x 10^{-17}	4.28	0.98
Q124/2000	1	4.42 x 10^{-16}	3.85	0.95
	2	1.06 x 10^{-16}	4.36	0.93
	3	2.45 x 10^{-16}	3.61	0.98

Attempts were made to compare the permeability responses (based on average trial values) for the two different preparations, but no clear distinction for the preparations could be observed. This may be mainly due to overlapping of permeability values with experimental uncertainties.

Figure 4.4 compares the permeability response with the other available data (Adam, 1997; Loughran, 1990; Murry, 1960a). At low void ratios (or high compression ratios), there is generally a fair agreement among all the data presented, except Murry's (1960a). At higher void ratios due to low compaction and measurement difficulties, there is widespread variation among the data. The modified permeability of Adam (1997) is also compared in Fig. 4.4 with other experimental data.

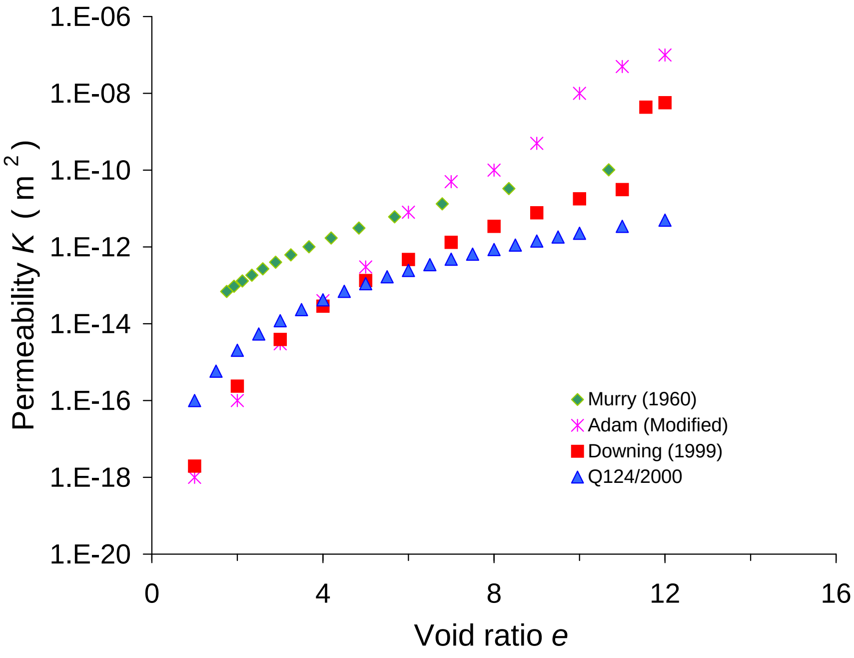

Figure 4.4: Comparison of permeability test results with known data.

4.8 Discussion of results

The permeability response in saturated conditions which is relevant to crushing was analyzed by different approaches (Adam, 1997). For the experiments conducted in this thesis, Darcy's law was directly applied for the determination of permeability response. The permeability response of canes with different fibre contents and preparation levels are measured. Regression trend lines using power law have been fitted to experimental data. The experimentally determined permeability responses are also compared with other available experimental data.

At low compression ratios (or higher void ratios) there is some wide spread variations in the permeability responses among the data. At low compression ratios, the permeability values are affected by partial saturation and seepage induced consolidation. Hence a modified permeability response (Adam and Loughran, 1998) is used to account for the effects of partial saturation, air expulsion and seepage induced consolidation.

It was explained that the seepage induced consolidation of the material is caused by a combination of highly compressible solid matrix behaviour and low permeability, and it is very difficult to avoid seepage induced consolidation at low compression ratios.

Chapter 5

Constitutive formulations for the fibre

5.1 Introduction

The roll load and torque are the fundamental mechanical quantities, and their importance must be considered in the performance and design of crushing units. They are "external" quantities arising from the "internal" compression of cane and the expression of juice. An earlier investigation (Murry, 1960a) using the experimental mill demonstrated the effects of compression ratio, preparation, speed and feed depth on roll load and roll torque. The basic mechanics of the forces on the roll was applied to estimate the pressure distribution from permeability considerations. Solomon (1968) demonstrated a more advanced model by formulating and solving a two-dimensional juice flow model using finite difference methods. Loughran (1990) solved Solomon's model using finite element methods and obtained a close agreement to the Solomon's solution. However, neither of these two-dimensional models achieved good agreement with experiment. Their approach assumed the total pressure at the roll surface was solely due to the pore pressure generated by the juice flow, and neglected the constitutive response of the solid fibrous phase. This chapter discusses elasto-plastic characteristics of the fibre from experimental and conceptual models. The established constitutive laws for the fibre closely couple with the permeability response for the crushing simulation.

5.2 Experimentally observed material responses

From a general point of view, the prediction from one-dimensional theory above are fairly satisfactory. The major deficiency in the earlier coupled models (De Souza Neta et al., 1997; Zhao, 1993) failed to account for the experimentally observed constitutive behaviour of the material. From a microstructural point of view, the matrix of prepared cane is made up of fines, fibres and juice interspersed in a random fashion. Application of a compressive stress results in frictional sliding, reorientation and bending of the fibres orthogonal to the applied stress, forming a network of interwoven fibres.

The material exhibits large elastic and plastic volume changes with little lateral strain during compression. The yielding commences immediately with no pronounced elastic zone prior to yielding, which is in contrast to other elasto-plastic materials. The loading and unloading response is non-linear (Fig. 3.14). The important features of experimentally observed material responses (Adam et al., 1997) of prepared cane under compression are summarised below:

(1) Highly compressible, yields under hydrostatic stress.

(2) Large elastic and plastic volumetric strains.

(3) Non-linear plastic strain hardening, non-linear elastic recovery.

(4) Uniaxial plastic strain co-directional with applied stress.

(5) Anisotropic behaviour due to layering of fibres.

(6) No shear failure in uniaxial or triaxial tests.

5.2.1 Approach to modelling

The features listed previously and the triaxial tests (Leitch, 1996) suggest that the solid fibres of prepared sugar cane behave anisotropically. The anisotropic properties are complex to determine because the direction of anisotropy i.e. the direction of layering of fibres is affected by the applied load. The fibres tend to adopt a preferred but random orientation normal to the major applied stress. However, realistic isotropic plasticity models together with porous or linear elasticity models have been considered adequate so far (Adam et al., 1997). The constitutive models that are required for the crushing are for the skeletal phase, liquid flow phase and contact between the skeleton and boundary surfaces.

The elastic material parameters for the solid skeleton are determined from experimental unloading data. For the isotropic plastic material behaviour, constitutive models that represent yielding under hydrostatic pressure are the most suitable. When shearing, the prepared cane should eventually reach a critical state in which further deformation takes place at constant volume, normal effective and shear stresses. Crushable foam plasticity, modified Cam-clay and capped Drucker-Prager models are considered suitable models.

The liquid movement in the model is adequately modelled by applying Darcy's law as explained in Chapter 4 over the range of conditions encountered during crushing. For the friction between the bagasse and the metal surfaces, a considerable amount of data have been measured (Braddock, 1963; Bullock, 1957; Cullen, 1965; Murry, 1960a) and these data have been reviewed (Loughran and Adam, 1998) and expressed in the form of non-linear regression equation. The friction coefficient between freshly prepared cane and metal surfaces is described as a function of normal stress, and relative rubbing speed across roll/blanket interface, and included angle of circumferential roll grooves.

Multiphase cane crushing is a highly complex phenomenon involving strong interaction between the liquid and solid phases of the material, large strain and frictional contact. Hence the numerical simulation of crushing between rolls, emphasizes modelling of the highly non-linear behaviour of the solid skeleton, coupling between the liquid and solid phases of the material behaviour, and the frictional contact at the rolls.

The elasto-plastic nature of the fibrous material properties needs to be adequately represented in the numerical model. The identification and determination of the porous material constitutive properties are mostly borrowed from geomechanic principles.

5.3 Simple constitutive equations

During general loading on the prepared cane, normal and shear stresses are likely to change simultaneously so there will be shearing and volumetric straining together. It turns out that shearing and volumetric effects are coupled so that shearing stresses cause volumetric strains and normal stresses cause shearing strains. A simple constitutive equation relating shearing and volumetric stress-strain behaviour can be written as:

$$\left\{ \begin{array}{c} \delta q' \\ \delta p' \end{array} \right\} = \left[\begin{array}{cc} S_{11} & S_{12} \\ S_{21} & S_{22} \end{array} \right] \left\{ \begin{array}{c} \delta \epsilon_s \\ \delta \epsilon_v \end{array} \right\} \tag{5.1}$$

where $[S]$ is a stiffness matrix containing stiffness moduli. The components of $[S]$ are

$$S_{11} = \frac{\delta q'}{\delta \epsilon_s} = 3G' \quad ; \quad S_{12} = \frac{\delta q'}{\delta \epsilon_v} = J_1' \tag{5.2}$$

$$S_{21} = \frac{\delta p'}{\delta \epsilon_s} = J_2' \quad ; \quad S_{22} = \frac{\delta p'}{\delta \epsilon_v} = K' \tag{5.3}$$

Alternatively, a constitutive equation can be written as

$$\left\{ \begin{array}{c} \delta \epsilon_s \\ \delta \epsilon_v \end{array} \right\} = \left[\begin{array}{cc} C_{11} & C_{12} \\ C_{21} & C_{22} \end{array} \right] \left\{ \begin{array}{c} \delta q' \\ \delta p' \end{array} \right\} \tag{5.4}$$

where C is a compliance matrix containing compliance parameters. Since the stress-strain behaviour of porous materials is largely non-linear, the stiffness and compliance parameters in Eqs. (5.1) and (5.4) will not be constants, but will vary with strain. They also depend on the current stresses and on the history of loading and unloading.

5.4 Elasticity

Materials that are subjected to stresses within their elastic limits are conservative so that all of the work done by the external stresses during an increment of deformation is stored and is recovered on unloading. This means that all of the elastic strains that occur during an increment of loading are recovered if the increment is removed. An important feature of isotropic elastic materials is that shear and volumetric effects are decoupled so that the stiffness parameters J_1' and J_2' are both zero. Eq. (5.1) becomes

$$\left\{ \begin{array}{c} \delta q' \\ \\ \delta p' \end{array} \right\} = \left[\begin{array}{cc} 3G' & 0 \\ \\ 0 & K' \end{array} \right] \left\{ \begin{array}{c} \delta \epsilon_s^e \\ \\ \delta \epsilon_v^e \end{array} \right\} \tag{5.5}$$

where the subscripts e denotes elastic strains. The complete behaviour is shown in Fig. 5.1.

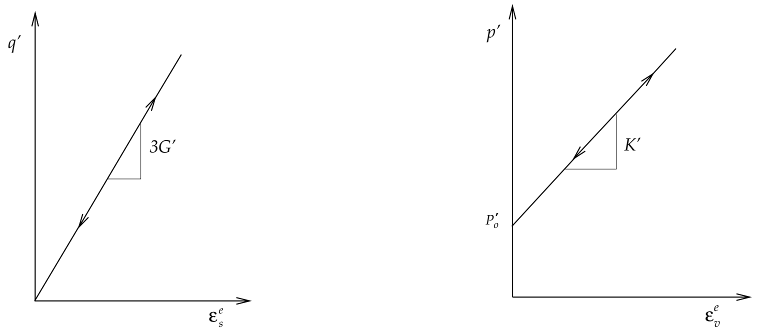

(a) Shearing **(b)** Compression and swelling

Figure 5.1: Behaviour of ideal linear elastic material.

5.4.1 Linear elasticity

The usual elastic parameters are the Young's modulus E and the Poisson's ratio ν. They are obtained directly from the results of uniaxial compression or extension tests with the radial stress held constant (or zero). The basic relationships among the various elastic parameters and for isotropic materials are:

$$G' = \frac{E}{2(1+\nu)} \tag{5.6}$$

$$K' = \frac{E}{3(1-2\nu)} \tag{5.7}$$

The shear and bulk moduli, G' and K', are preferable to Young's modulus E and Poisson's ratio ν because it is important to consider shearing or change of shape separately, or decoupled, from compression or change of size.

5.4.2 Porous elasticity

For a porous material, during elastic(recoverable) straining, the change in void ratio is related to equivalent pressure stress p as

$$\mathrm{d}e = -\kappa d\ \left(ln\left(p\right)\right) \tag{5.8}$$

The equivalent relation for material having tensile strength p_t^e is

$$\mathrm{d}e^e = -kd\ \left(ln\left(p + p_t^e\right)\right) \tag{5.9}$$

Integrating Eq. (5.9) with known initial void ratio e_o and initial pressure p_o, the volumetric elasticity relationship ϵ_v^e is written

$$\frac{k}{1+e_o} \ln\left(\frac{p+p_t^e}{p_o+p_t^e}\right) = 1 - \exp\left(\epsilon_v^e\right) \tag{5.10}$$

Eq. (5.10) can be inverted to express the equivalent pressures stress required to yield the volumetric stress ϵ_v^e.

$$p = -p_t^e + \left(p_o + p_t^e\right)\exp\left[\frac{1+e_o}{\kappa}\left(1 - \exp\epsilon_v^e\right)\right] \tag{5.11}$$

5.4.3 Elastic strains

The idealized behaviour of porous material during isotropic compression and swelling is illustrated in Fig. 5.2 with a sequence of loading and unloading from A

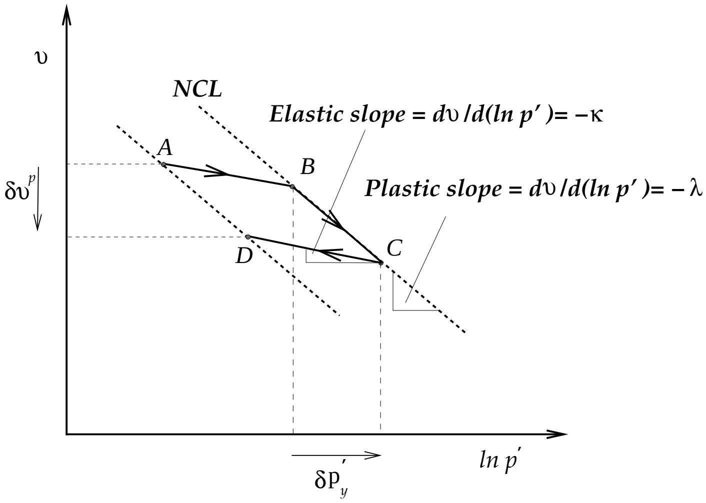

Figure 5.2: Elastic and plastic compression.

to D. Between B and C the state was on the Normal Compression Line (NCL) i.e. on the state boundary surface and the material yielded and hardened as the yield stress increased by $\delta p'_y$ with an irrecoverable plastic volume change δv^p. Along AB and CD the state was inside the boundary surfaces and the behaviour is taken to be elastic.

The stress-strain behaviour of an isotropic elastic material is decoupled and from Eq. (5.5)

$$\delta\epsilon_s^e = \frac{1}{3G'}\,\delta q' \tag{5.12}$$

$$\delta\epsilon_v^e = \frac{1}{K'}\,\delta p' \tag{5.13}$$

Another expression for the elastic volumetric strains can be obtained from the equation for swelling and recompression (Section 3.7.2)

$$v = v_\kappa - \kappa\,\ln p' \tag{5.14}$$

Differentiating the above equation with respect to p' and dividing by v we have

$$-\frac{\mathrm{d}v}{v} = \delta\epsilon_v^e = \frac{\kappa}{vp'}\,\delta p' \tag{5.15}$$

A similar equation for shearing can be written as

$$\delta\epsilon_s = \frac{g}{3vp'}\,\delta q' \tag{5.16}$$

where g is a material parameter, based on the assumption that $\frac{G'}{K'} = \frac{\kappa}{g}$ = constant, which implies that Poisson's ratio is a constant.

5.4.4 Elastic material parameters (As determined by Adam (1997))

Poisson's ratio (ν)

In quasi-static cycle tests, the stresses normal to the applied stress were measured (Adam, 1997). The side wall stress values were used to determination of Poisson's ratio. The Poisson's ratio ν, may be estimated from the following relationship (from Eq. (3.26))

$$\frac{\sigma_x}{\sigma_z} = K_o = \frac{\nu}{1-\nu} \tag{3.26$'$}$$

The lateral pressure co-efficient $K_o = \frac{\sigma_x}{\sigma_z}$ was measured from quasi-static unload cycles for 1400/20, 810/28 and 810/14 (Section 3.7.3). The range of Poisson's ratio estimated is 0.1-0.18. Adam (1997) estimated ν in the applied stress range 0-3 MPa by first expressing (Eq. (3.26$'$)) in rate form as

$$\nu = \frac{\frac{\mathrm{d}\sigma_x}{\mathrm{d}\sigma_z}}{\left[1 + \frac{\mathrm{d}\sigma_x}{\mathrm{d}\sigma_z}\right]} = \frac{\frac{\mathrm{d}\sigma_y}{\mathrm{d}\sigma_z}}{\left[1 + \frac{\mathrm{d}\sigma_y}{\mathrm{d}\sigma_z}\right]} \tag{5.17}$$

The K_o values from his quasi-static unload cycle tests were then utilized to calculate ν from the above equation for the stress range. The estimated values for ν range from 0-0.3 with a considerable degree of scatter, and no clear preparation effect was observed. A value of 0.15 for Poisson's ratio is generally considered in the absence of more reliable data.

Bulk modulus K and Young's modulus E

The volumetric strain as a function of void ratio may be expressed as

$$\epsilon_v = ln\left(\frac{1+e}{1+e_o}\right)$$

The elastic volumetric strain ϵ_v^{el} may be expressed from the virgin consolidation and elastic recovery characteristics (λ, κ)

$$\epsilon_v^{el} = \ln\left[\frac{v_f}{v_f + \frac{\kappa}{\lambda}\left(v_o - v_f\right)}\right] \tag{5.18}$$

where v_o and v_f are the initial and final specific volumes respectively. The volumetric stiffness modulus is termed the bulk modulus. For linear elasticity it is defined as

$$K = \frac{\Delta P}{\mathrm{d}\epsilon_v^e} \tag{5.19}$$

and it increases with applied isotropic stress for compressible materials like prepared cane. The bulk modulus was evaluated based on the κ and λ values estimated in Section 3.7.4. The K value was found to be in the range 5.2-9.14 MPa, which is close to 8.3 MPa estimated for the hand compacted or precompacted cane (Adam, 1997).

The Young's modulus E was estimated directly using a value of 0.15 for the Poisson's ratio using the linear elastic relation $E = 3K\left(1 - 2\nu\right)$. The E value was found to be in the range $11 - 19$ MPa. The value of E for hand compacted cane (Leitch, 1996) with $\kappa = 0.094$ and $\lambda = 1.99$ was estimated to be 41.8 MPa. Based on these results, the Young's modulus varies from 10 to 40 MPa. A value of 20 MPa is generally recommended as the property value for E.

5.5 Plasticity

The plastic behaviour of metals is an useful feature for its ability to deform plastically under high stress. This is the basis of many manufacturing processes such as rolling, drawing, machining or pressing in dies. The behaviour of porous materials is more complex, however it allows complete description of the stress-strain behaviour so that the material deformation can be predicted right up to failure. The porous material behaviour may be expressed mathematically using the framework of elasto-plasticity.

5.5.1 Plastic flow

With reference to an idealised relationship between stress and strain beyond the yield point A (Fig. 2.16), simultaneous elastic and plastic strains occur and the stiffness decreases. During an increment of plastic deformation, the work is dissipated and so plastic strains are not recovered on unloading. At the ultimate state there are no further changes of stress and so all the strains at failure are irrecoverable. Furthermore, the plastic strains at failure are indeterminate, for materials like soil they can go on more or less forever and so we can talk about plastic flow. Although it is impossible to determine the magnitudes of the plastic strains at failure, it is possible to say something about the relative rates of different strains such as shear and volumetric strains. In this context, the particulate nature of porous materials gives rise to shear and volumetric coupling.

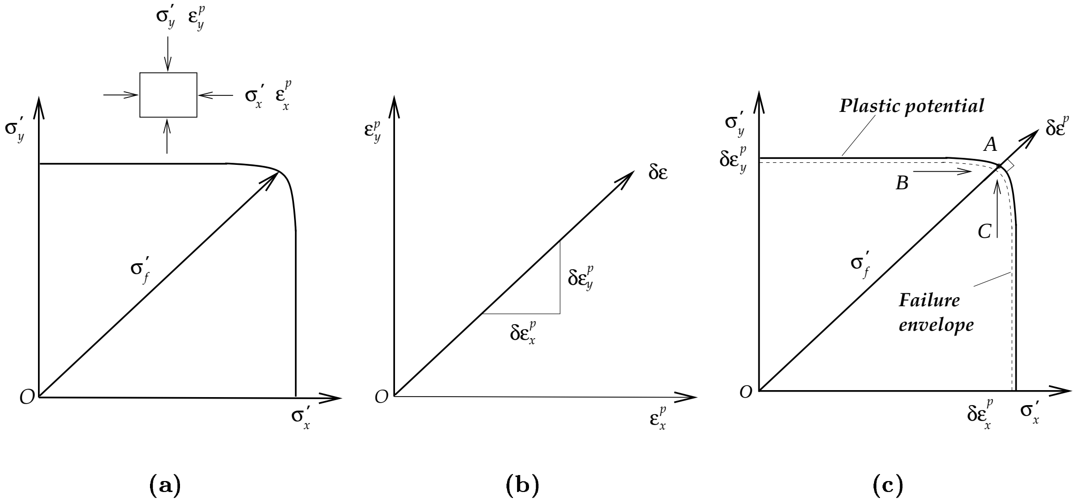

Figure 5.3: Behaviour of ideal perfectly plastic materials.

Figure 5.3(a) illustrates some arbitrary combinations of stresses σ'_x and σ'_y on an element of material loaded to failure. The combinations of stress that cause failure and plastic flow are illustrated and are represented by a failure envelope. At any point on the envelope, the vector of the failure stress is σ'_f, and the corresponding plastic strain direction is given by $\frac{\delta\epsilon^p_y}{\delta\epsilon^p_x}$ in Fig. 5.3(b). The relationship between the failure envelope and the direction of the vector of plastic strain is called a *flow rule*.

Figure 5.3(c) illustrates the same information as in Fig. 5.3(a) and 5.3(b), with axes superimposed and the origin for plastic strain placed at the end of the appropriate vector of failure stress. Since the stresses remain constant the strains accumulate with time and so the origin is arbitrary. For a perfectly plastic material, the vector of plastic strain is normal to the failure envelope and the flow rule which defines a plastic potential envelope is orthogonal to all vectors of plastic straining. This is called as *associated flow* rule as the plastic potential is associated with the failure envelope.

An important feature of plastic straining is that the strains depend on the state of stress and do not depend on the small change of stress that causes failure. This is illustrated in Fig. 5.3(c). For two different loadings $B \rightarrow A$ and $C \rightarrow A$, the plastic strains are the same. Plastic strains are governed by the gradient of the failure envelope at A and not by the loading path. This is in contrast to elastic straining where the strain depends on the increments of stress as given by Eq. (5.5).

5.5.2 Hardening law

Yielding and plastic straining may cause hardening, i.e. an increase in yield stress as shown in Fig. 5.4. Therefore the principal consequences of straining from A to B are to cause irrecoverable plastic strains and to raise the yield point from σ'_{x_1} to σ'_{x_2}.

The relationship between the increase in yield stress $\delta\sigma'_x$ and plastic straining $\delta\epsilon^p_x$ is known as a *hardening law*. A feature that is commonly found in the behaviour of soils (and in prepared cane) is "softening" i.e. a decrease in yield stress as shown in Fig. 5.4(b). In this case the state has reached, and passed, a peak in the stress-strain curve. It may be noted that in Fig. 5.4, there is a broken line to the left of the first yield point which suggests that there could be even lower yield points for previous loading.

Yielding under combined stresses may be represented by a set of yield curves which are similar to the failure envelope, as illustrated in Fig. 5.5(a). This shows a yield curve for the first yield, another yield curve for subsequent yielding and a failure

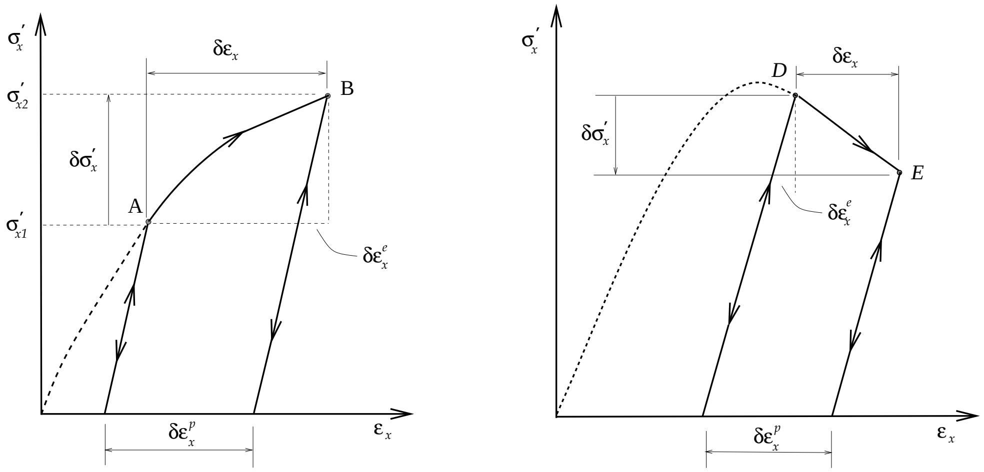

(a) Strain hardening **(b)** Strain softening

Figure 5.4: Yielding and plastic straining.

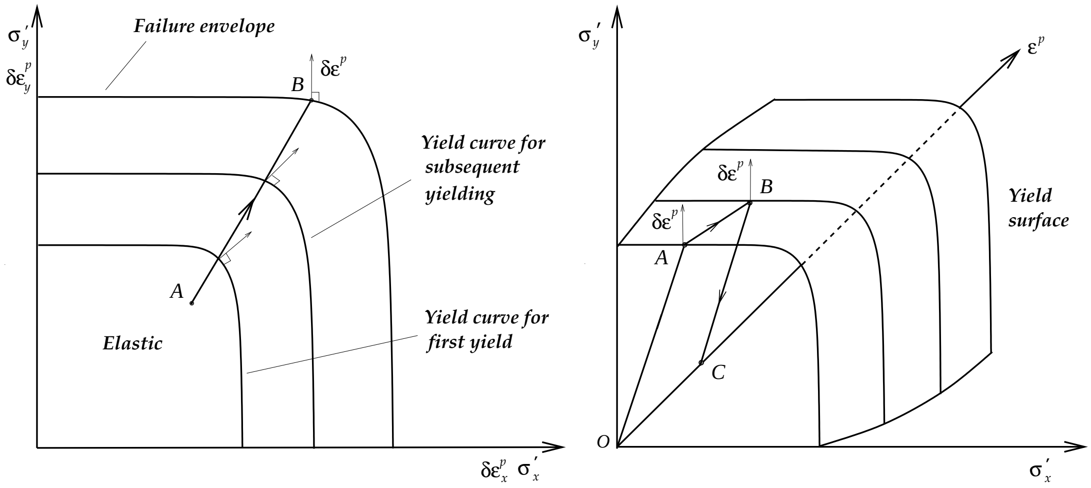

(a) **(b)**

Figure 5.5: Behaviour during a cycle of loading on and under the yield.

envelope. For the loading path AB, which crosses successive yield surfaces, the vectors of plastic strain are normal to the yield surfaces. Since each yield surface in Fig. 5.5(a) is associated with a particular strain we can use the plastic strain as a third axis to develop a yield surface as shown in Fig. 5.5(b). For any state on the yield surface there are plastic strains that are normal to the appropriate yield curve and are given by the movement of the stress point across the surface. For the loading and unloading $O \to A \to B \to C$ in Fig. 5.5, the behaviour is elastic for the path $O \to A$ and $B \to C$. For the path $A \to B$ there are simultaneous elastic and plastic strains.

It is now possible to assemble the flow rule, the hardening law and the elastic stress-strain equations in to an explicit constitutive equation for the complete range of loading up to failure.

5.5.3 Calculation of plastic strains for Cam-clay

As the state moves on the state boundary surface (as described in Section 2.10.1) from one yield curve to another there will be yielding and hardening (or softening). In a Cam-clay constitutive model, the change of the yield stress is related to the plastic volume change.

Figure 5.6 shows an increment of loading $A \to B$ on the wet side[1] of critical, and the state moves from one yield curve to a larger one with an increase in yield stress and a reduction in volume. The increment of loading $C \to D$ on the dry side is associated with a decrease in yield stress and an increase in volume. The yield curve is taken to be a plastic potential so that the vector plastic strain increment $\delta\epsilon_p$ is normal to the curve, that is

$$\frac{\mathrm{D}q'}{\mathrm{D}p'} \cdot \frac{\mathrm{d}\epsilon_s^p}{\mathrm{d}\epsilon_v^p} = -1 \tag{5.20}$$

---

[1] At a given stress, the specific volume v on the wet side is higher than at the critical state, while the specific volume on the dry side is lower than at the critical state.

and, from Eq. (2.90), the plastic strain increments are given by

$$\frac{\delta\epsilon_v^p}{\delta\epsilon_s^p} = M - \frac{q'}{p'} \tag{5.21}$$

Eq. (2.89) can now be rewritten as

$$v = \Gamma + \lambda - \kappa - \lambda \,\ln p' - \frac{(\lambda - \kappa)\, q'}{Mp'} \tag{5.22}$$

Figure 5.6: Hardening and softening of Cam-clay (Atkinson, 1993).

The volumetric strain $\delta\epsilon_v = -\frac{\delta v}{v}$ is evaluated by differentiating, and dividing by v on Eq. (5.22), and substituting $\eta' = \frac{q'}{p'}$

$$\delta\epsilon_v = \left(\frac{\lambda - \kappa}{vp'M}\right)\delta q' + \left[\frac{\lambda}{vp'} - \frac{(\lambda - \kappa)\,\eta'}{vp'M}\right]\delta p' \tag{5.23}$$

By subtracting the elastic volumetric stress from Eq. (5.15), the plastic volumetric strains are expressed as

$$\delta\epsilon_v^p = \left(\frac{\lambda - \kappa}{vp'M}\right)\left[\delta q' + \left(M - \eta'\right)\delta p'\right] \tag{5.24}$$

and from Eq. (5.21), the plastic shear strains are

$$\delta\epsilon_s^p = \left(\frac{\lambda - \kappa}{vp'M}\right)\left(\frac{\delta q'}{M - \eta'} + \delta p'\right) \tag{5.25}$$

5.5.4 Complete constitutive equation for simple Cam-clay

The complete constitutive equations for Cam-clay are obtained by simply adding the elastic strains from Eqs. (5.15) and (5.16) to the plastic strains from Eqs. (5.24) and (5.25).

$$\delta\epsilon_s = \frac{1}{vp'}\left\{\left[\frac{\lambda - \kappa}{M\left(M - \eta'\right)} + \frac{g}{3}\right]\delta q' + \left[\frac{\lambda - \kappa}{M}\right]\delta p'\right\} \tag{5.26}$$

$$\delta\epsilon_v = \frac{1}{vp'}\left\{\left[\frac{\lambda - \kappa}{M}\right]\delta q' + \left[\frac{\lambda - \kappa}{M}\left(M - \eta'\right) + \kappa\right]\delta p'\right\} \tag{5.27}$$

These constitutive equations apply to states that are on the state boundary. For states inside the boundary surface the elastic strains given by Eqs. (5.15) and (5.16) can be recovered by putting $\lambda = \kappa$ into Eqs. (5.26) and (5.27).

Equations (5.26) and (5.27) are constitutive equations like Eq. (5.4) and the components of the compliance matrix are

$$C_{11} = \frac{1}{vp'}\left[\frac{\lambda - \kappa}{M\left(M - \eta'\right)} + \frac{g}{3}\right] \tag{5.28}$$

$$C_{22} = \frac{1}{vp'}\left[\frac{\lambda - \kappa}{M}\left(M - \eta'\right) + \kappa\right] \tag{5.29}$$

$$C_{12} = C_{21} = \frac{1}{vp'}\left[\frac{\lambda - \kappa}{M}\right] \tag{5.30}$$

It may be noted that the compliances contain the intrinsic material parameters M, λ, κ and g and in Cam-clay, the behaviour is non-linear since, in general, v, p' and q' change during a loading path. It is interesting to note that towards failure at the critical state when $\eta' \to M$ one has $C_{11} \to \infty$ and $C_{22} \to 0$. Thus, near ultimate failure, the shear strains become very large while the volumetric strains become very small. This makes numerical convergence challenging.

The modified Cam-clay model is based on yield curves that are an ellipse and is described in detail by Wood (1991). The finite element implementation of Cam-clay model is described by Britto and Gunn (1987) and Zienkiewicz and Naylor (1971).

5.5.5 Capped Drucker-Prager plasticity model

The capped Drucker-Prager model for a pressure dependent yield material was explained in Section 2.9.5 and its suitability to prepared cane was discussed in Section 5.2. Unlike the Cam-clay models, the Drucker-Prager model has a yield surface which includes a shear failure surface, and a cap which intersects the equivalent pressure stress axis p. Otherwise, by appropriate choice of material parameters, the two models can be made almost identical. The cap yield surface has an elliptical shape with constant eccentricity in the $p-t$ plane (Fig. 5.7).

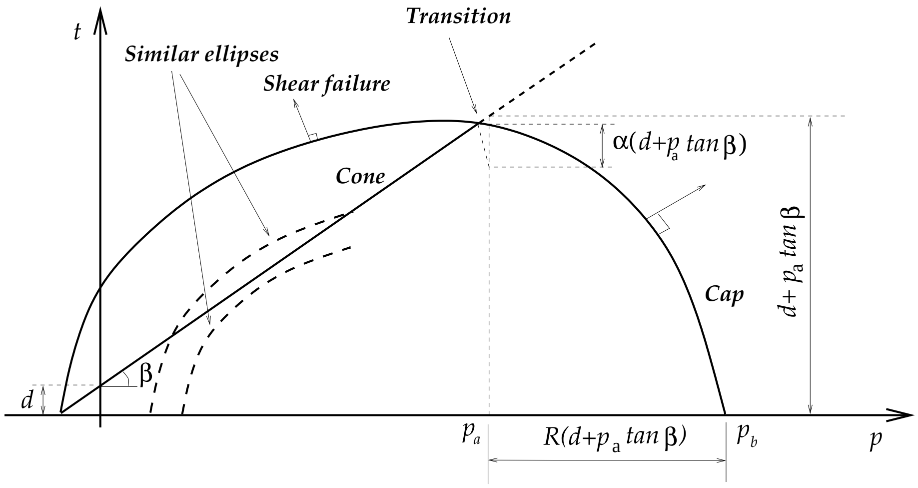

Figure 5.7: Capped Drucker-Prager model.

The cap surface hardens or softens as a function of the volumetric strain. When yielding on the cap, volumetric plastic compaction causes hardening, while yielding on the shear failure surface, volumetric plastic dilation causes softening. Associated plastic flow is assumed on the cap and non-associated flow in the cone and transition regions.

The transition yield surface joins smoothly the cone and cap yield surfaces. The yield surface equations for the cone, cap and transition regions are expressed respectively as follows (ABAQUS theory manual).

cone surface:

$$t = p \tan\beta + d \tag{5.31}$$

cap yield surface:

$$t^2 = (1+\alpha-\alpha/\beta)^2 \left[(\alpha + p_a \tan\beta)^2 - \left(\frac{p-p_a}{R}\right)^2\right] \tag{5.32}$$

transition surface:

$$\left[t - (1-\alpha/\cos\beta)\,(d + p_a\tan\beta)\right]^2 = \alpha^2\,(d + p_a\tan\beta)^2 - (p-p_a)^2 \tag{5.33}$$

Where β = material's angle of friction.

d = cohesion for the material.

t = deviatoric stress measure [2] .

R = material parameter which controls the shape of cap.

α = is a small number (typically $0.01 - 0.05$) defining a smooth transition region between cone and cap.

p_a = evolution parameter which describes the size of the yield surface.

Here $p_a = \frac{P_b - Rd}{(1+R\tan\beta)}$ is an evolution parameter in terms of hydrostatic compressive yield stress, p_b.

5.5.6 Determination of plastic material parameters

Slope of the normal consolidation line (λ)

The normal consolidation slope, λ in the $\ln p' : v$ plane is one of the important parameters of the Cam-clay critical state model. Other than the source of determination

---

[2] $t = \frac{q}{2}\left[1 + \frac{1}{K} - \left(1 - \frac{1}{K}\right)\left(\frac{r}{q}\right)^3\right]$. K is a material parameter which provides a smooth approximation to Mohr-Coulomb surface. If $K = 1.0$ then $t = q$.

from uniaxial and triaxial tests discussed in Section 3.7.4, Schembri et al. (1998) derived λ in the range 1.43-5.55 from Loughran's (1990) uniaxial compression test results. The lower value being associated with the higher applied stress. The simulated results of modified Cam-clay model for triaxial and shear box tests reproduced the trends to a limited extent, but generally under-estimated the measured results. It is clear from the experimental data that λ is not a constant but decreases with increasing mean stress.

Slope of the critical state line (M)

The ultimate or critical state is the state reached after strains of at least 10 per cent are reached and is associated with relative movements and rotations of the material (Atkinson, 1993). At the critical state there is a unique relationship between the shear stress, the normal stress and the void ratio. In other words, the end points of the shear test represent critical state, where the material continues to deform at constant stress ratio q/p' and constant specific volume. The line joining critical states referred to as the critical state line(CSL) has equations $q = Mp'$ and $v = \Gamma - \lambda \ln p'$. The deviatoric stress q is a measure of the shear stress acting on the porous material, which is characterised in the shearbox tests by the shear stress τ. The average effective stress p' is analogous to the effective stress σ' on the central horizontal plane of the shear box. The critical state lies on a straight line of gradient ($\tan \phi'_{crit}$) in (τ, σ') space. The critical state parameter M is a measure of the ratio of shear to normal effective stresses at failure, and is therefore related to the soil friction angle ϕ'_{crit}.

The critical state line has important implications together with the yield surfaces of Cam-clay or capped Drucker-Prager models on the material responses. The stress paths which intercept the yield surface below the critical state line will cause the material to strain harden, while the stress path intercept yield surface above the critical state line will result in strain softening with plastic volume increase and eventual failure at constant volume.

To represent an appropriate M value for the rolling process, attempts were made to estimate the value from confined and unconfined uniaxial tests, triaxial and shear box tests (Adam, 1997; Plaza et al., 2001; Schembri et al., 1998). In unconfined uniaxial compression tests, no radial plastic strains were observed (Adam, 1997). Using this condition, the slope of critical state line M may be determined from the gradient normal to the yield surface i.e. the gradient normal to the yield surface from Eq. (2.90) is substituted into Eq. (5.20) to evaluate M. A critical state value of M of approximately 4.2 was estimated with the Cam-clay and cap Drucker-Prager associated flow plasticity models. Results generated from a simulated partially confined and unconfined uniaxial compression revealed this M value for no lateral expansion. M value greater than 4.2 cause negative plastic radial strain, while smaller values show rapid increase in plastic lateral expansion. In a confined uniaxial compression, no lateral expansion is allowed, however, the lateral stress (K_o) will be strongly dependent on the choice of M value.

As the rolling process is more complex than a simple uniaxial compression, Schembri et al. (1998) estimated M in terms of mean stress p' and deviatoric stress q and specific volume v. Treating the triaxial test results of Leitch (1996) and considering the end points of the tests as being close to critical state, M values were estimated in the range 0.08-2.0. However, Leitch's (1996) results showed no evidence of critical state.

The M value was also evaluated from shear box tests, from the frictional angle ϕ by $M = 2\sin\phi$ (Schembri et al., 1998). For normal stresses up to 4 MPa, the friction angle ϕ falls in the range 23.8°-32.7°, resulting in M values 0.81-1.08 (Plaza and Kent, 1997). It may be noted that the friction angle ϕ measured in a shear box text is not the same as the true interparticle or material angle of friction. The layering of fibre in the prepared cane during packing tended to become preferentially but randomly oriented in a plane perpendicular to the applied stress. Hence, the friction angle to shear across fibres would be greater than that along the fibre alignment plane.

Besides the above relation, there are few other trigonometric functions of ϕ for M (Adam, 1997). The M from these trigonometric relations however fall in the lower range 0.8-1.32. The M value for the final bagasse from shear box tests in the pressure range 100- 20000 kPa is reported to be 1.1 (Plaza et al., 2001).

It is apparent that the lower M values($\sim$1.32) from shear box and triaxial tests predict approximately correct levels of shear stresses, but will severely over-predict the lateral expansion. On the other hand, a higher M value of 4.2 determined from unconfined and partially confined uniaxial stress paths will correctly predict the small lateral expansion during compression, but over-predict the shear stresses during shear box tests. It may be noted that the rolling process is an example of partially confined compression with more complex stress states and an intermediate value of $M = 3.8$ is considered to be reasonable in comparison with lateral expansion (Adam, 1997).

Plastic strain hardening

The general concept of using a hardening plasticity model is to describe the stress-strain behaviour of prepared cane. The hardening relation developed for Cam-clay and capped Drucker-Prager models using confined uniaxial compression gave identical results for all regions below the critical state line (Adam, 1997). Hence, further discussion on strain hardening is restricted to the capped Drucker-Prager plasticity model. Hardening a material can result in the yield surface either being enlarged or translated in stress space. The former is normally called "isotropic hardening" and is more often used because it is simpler to describe mathematically, although the assumption of isotropic hardening is less realistic for many materials. The hardening law generalizes the concept of the uniaxial yield stress being increased by strain-hardening to more general stress states. The strain hardening or softening is governed by plastic volumetric strain. The hardening law is incorporated into the yield surface equation by writing

$$P_b = f\left(\epsilon_v^p\right) \tag{5.34}$$

where ϵ_v^p is the volumetric strain parameter which defines the size of the yield locus, P_b. One particular value of ϵ_v^p will be relevant for a yield locus of a certain size, and after strain-hardening there will be a larger yield locus associated with a larger value of ϵ_v^p. That is when the volumetric plastic strain is compressive the yield surface grows in size. While under tensile stress the yield locus will shrink through dilation (strain softening).

There are two approaches which can be used to define the strain hardening relation quantitatively. The first approach is by direct determination from experimental data, and the second approach is through the inverse-calibration using finite element analysis (Adam, 1997). The stress path in triaxial experiments for example allows the direct estimation of plastic strain hardening curve. The uncertainty in experimental approach is, the assumption of constant plastic logarithmic bulk modulus λ, while experiments shows a non-linear trend (Loughran and Adam, 1998). The inverse-calibration approach using confined uniaxial test cell experiments, for example, provides a close fit to experimental data since the plastic strain hardening curve compensates for discrepancies between true underlying elastic behaviour of yield surface shape, and the assumed parameter (Adam, 1997). Further, this approach allows capture of grooving or other geometry effects and also preparation effects into the constitutive relations, and can be transferred directly to two-dimensional plane strain rolling simulations.

The first step in inverse-calibration is to define the initial yield surface position for the cap surface. A precompressor was used to lightly over consolidate the prepared cane prior to feeding into the experimental mill. Precompression pressure of about 50 kPa is normally applied using a confined uniaxial compression apparatus as shown in Fig. 5.8. The cross sectional dimension of the precompressor used is 900 mm x 200 mm, and for a cane blanket height of 80 mm, the initial void ratio may be around 15.0 depending upon the fibre content.

The cap position or initial yield P_b at precompressor loading is shown in Fig. 5.9. As the precompressor is following a confined uniaxial stress state, the lateral pressure

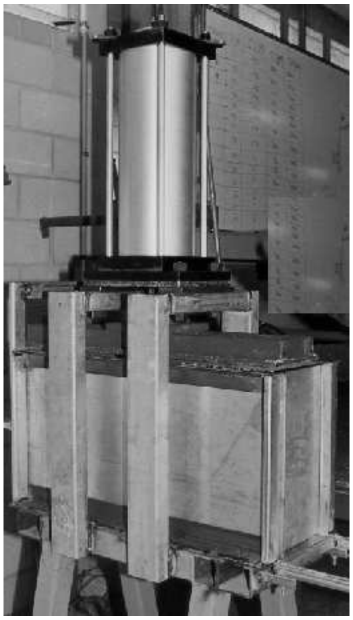

Figure 5.8: Precompression apparatus.

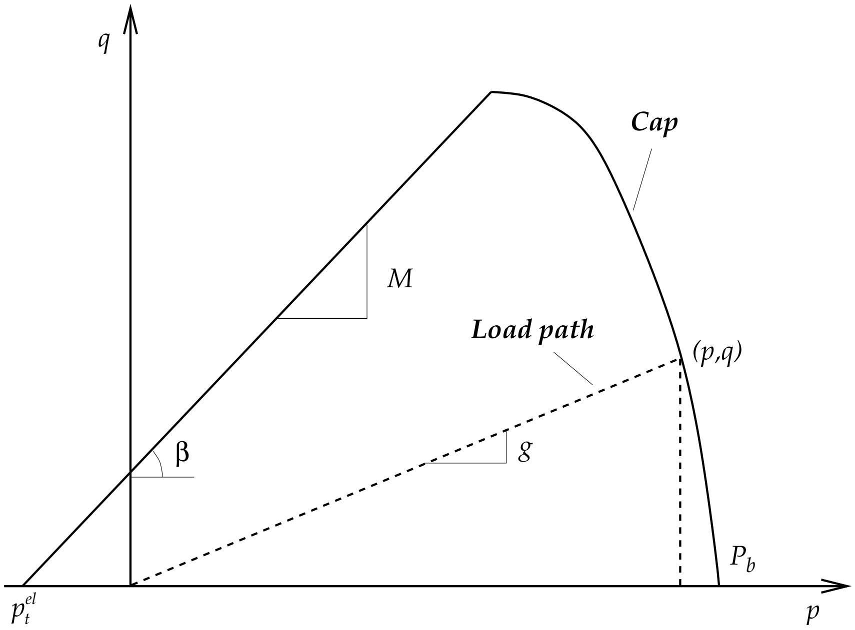

Figure 5.9: Stress path for the initial yield.

coefficient K_o may be approximated to 0.12 and the corresponding p and q values are determined by multiplying the vertical stress (σ_v) with $(1+2K_o)/3$ and $(1-K_o)$ respectively. For a small fixed value of tensile stress p_t and for a designated value of M, the cap position is defined from the cap geometry as

$$P_b = p + \frac{q^2}{M^2\left(p+p_t^e\right)} \tag{5.35}$$

For the inverse calibration, the quasi-static confined compression test response in Fig. 3.11 and 3.12 was used for flat and groove geometry. The first approximation for the strain hardening relationship is estimated by locating the cap position for each increment of a total strain. This is evaluated as piece-wise data from Eq. (5.35), using the quasi-static experimental response σ_v Vs compression ratio (or void ratio), starting with an initial compression ratio to the final value in increments. The plastic strain component corresponding to the cap position is evaluated by removing the elastic strain component. A step by step procedure of estimating plastic strain hardening data is presented in ref (Downing, 1999a).

The finite element simulation was modelled with one quarter symmetry of cane specimen in the confined uniaxial test cell as shown in Fig. 5.10. The third dimension is the larger length dimension of the specimen from plane strain consideration. The finite element simulation of the confined uniaxial compression test is carried out with an initial void ratio of 12.1 and a first approximation strain hardening curve.

Linear elasticity rather than porous elasticity was used as the former has very little effect on model performance at compression stresses up to about 5 MPa (Adam, 1997). However, porous elasticity causes a much stiffer overall material response at higher stresses. Hence if desired, porous elasticity may be used within the limits of stresses in experimental data. In the inverse-calibration, the first approximation strain hardening curve (P_b Vs ϵ_v^p) is recursively adjusted until the finite element test cell simulation matches the experimental response of average stress Vs void ratio. The use of void ratio provides consistency with the finite element specification of the material parameters, and accounts for variation in fibre content.

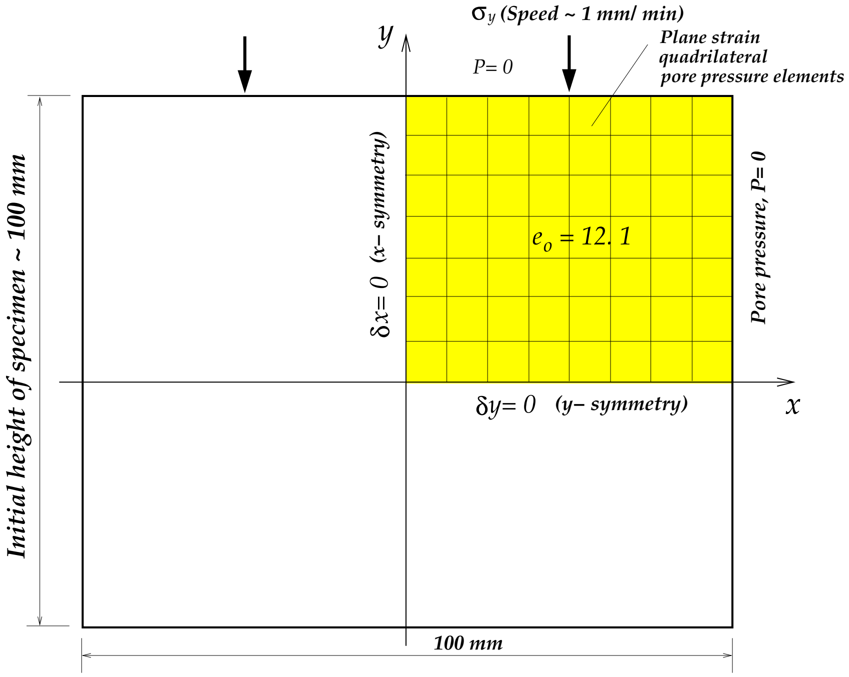

Figure 5.10: Quarter cell symmetry for inverse-calibration of strain hardening.

5.5.7 Strain hardening results from quasi-static experiments

Any comparison of plastic volumetric strain to determine the yield surface shape must be performed at the same values of volumetric strain. In addition, a reference point for zero volumetric strain is set to a corresponding reference void ratio (e_o) of 12.1, with $C_o = 0.8$ and $f_o = 13\%$ (fibre content) (Adam, 1997). This reference void ratio is maintained for all fibre contents, so that the corresponding reference compression ratio C for any fibre content f is

$$C = \frac{f_o}{f} C_o \tag{5.36}$$

The following platen force relationship is from the quasi-static compression test conducted on Q96 (750/15) with 55° groove platen (Loughran, 1990).

$$F = (C - 0.5)^2 (-10.3 + 75.1\hat{a} - 6.95S + 11.96\hat{a}S) - 17.4\hat{a} - 1.4S \qquad (5.37)$$

The zero-speed relationship for the platen force was obtained from the quasi-static experimental conditions by setting the speed component S to zero. The other available quasi-static expression for 55°groove is for Q96 (810/14) (Adam, 1997). These two quasi-static responses are compared in Fig. 5.11 along with the results of Q117/1800 and Q124/1800. The latter experiments were conducted on 35° groove platen. The experimental parameters of these different quasi-static experiments are summarised in Table 5.1.

Table 5.1: Quasi-static experimental parameters.

Cane variety	**Preparation level**	**Fibre content** (per cent)	**Groove angle**	**Compression speed**
Q96	750/15	14.9	55°	5-10 mm/min*
Q96	810/14	11.2	55°	Nominally zero†
Q117	1800 (rpm)	14.7	35°	2 mm/min
Q124	1800 (rpm)	13.2	35°	2 mm/min

* zero speed refers to substituting zero for the speed component S in the original empirical Eq. (5.37) which is $f(C, S, \hat{a})$.

† stepwise compression (Adam, 1997).

The platen pressure Vs compression ratio response in Fig. 5.11 shows a substantial difference among these experimental results. If we account for the variation in fibre content and observe the same results with void ratio, less variation in the results are noticed (Fig. 5.11(b)). These experiments were conducted with different groove angles, and preparation levels. The extrapolation to zero speed component from quasi-static response and the assumption of treatment number $\hat{a} = 0.70$ in the empirical relation may attribute to some minor variations.

The results of Q117/1800 and Q124/1800 in Fig. 5.11 are not extrapolated to beyond the measured compression ratio of around 2.0, as uncertainty in the platen pressures is expected to be higher. It is better to depend on the actual measured values.

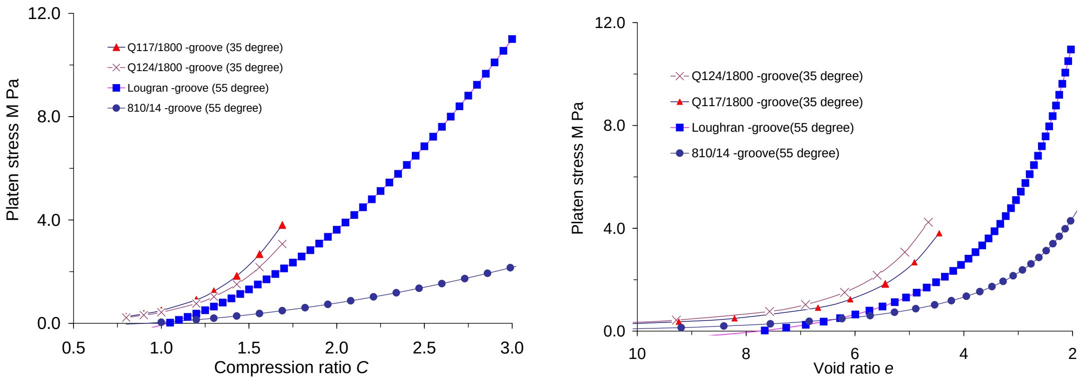

(a) Compression ratio Vs Platen stress

(b) Void ratio Vs Platen stress

Figure 5.11: Quasi-static experimental responses.

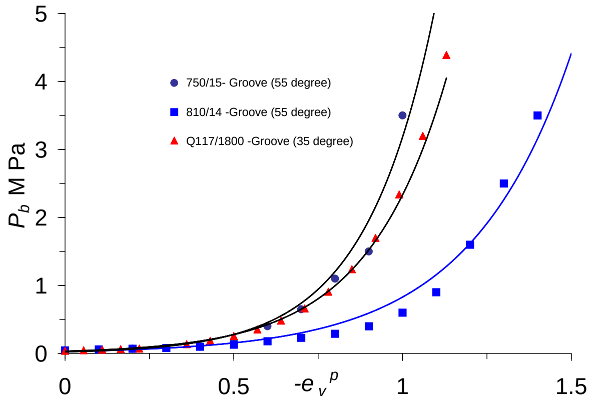

Figure 5.12: Strain hardening responses.

The inverse calibrated strain hardening relations are now compared in Fig. 5.12 for the different quasi-static experiments. The response for Q117/1800 compares well in the lower compression ratios, however the discrepancy in the higher compression ratio is mainly due to different groove angle. As the groove angle approaches towards say to a flat surface, the strain hardening response will eventually approach to that of a flat platen. Hence, the 35° groove response is expected to be stiffer than the 55° groove. The Q117/1800 experiment was limited to a compression ratio of around 2.0. The exponential curve fit for this response is $P_b = 0.033(\exp)^{4.248e}$ for which the correlation co-efficient r^2 is 0.98.

Fig. 5.13 compares the inverse calibrated strain hardening responses for the flat and 55°grooved platens. The range of elasto-plastic properties compiled from different sources for the fibrous material are given in Table 5.2.

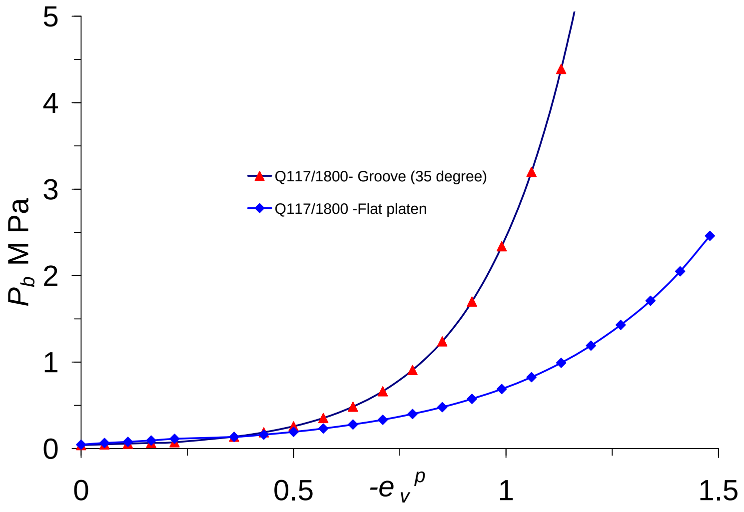

Figure 5.13: Strain hardening responses for the flat and grooved platens.

Table 5.2: Elasto-plastic properties of fibrous material.

Parameter	Range of values	Source[†]
Poisson's ratio ν	0.15 (Average)	Confined uniaxial experiment
Young's modulus E	10-40 MPa	Triaxial experiment
Log. elastic modulus κ	0.1-0.2	Confined uniaxial experiment
Log. plastic modulus λ	1.43-5.55	Confined uniaxial experiment
Critical state slope M	0.80-3.8	Uni,triaxial and shear box experiments
Initial yield	25-50 kPa	Precompressor test
Tensile stress	10 kPa	Small nominal value

[†] (Leitch, 1996; Loughran and Adam, 1998; Plaza et al., 2001; Schembri et al., 1998)

5.6 Conclusions

Though the prediction from one-dimensional theory was found satisfactory from a general point of view, it did not take into account the elasto-plastic characteristics of the solid skeleton. The elasto-plastic properties of the solid skeleton was estimated mainly from experimental observations and from suitable conceptual models where the yield stress intercepts the hydrostatic pressure axis. The modified Cam-clay and capped Drucker-Prager associative plasticity models are the suitable candidates for the fibre like material. Experimental results from quasi-static uniaxial and triaxial tests were analysed to estimate the material properties. The constitutive skeleton properties of the material are used in the numerical simulation of rolling of multi-phase material, where a strong coupling between liquid solid phases of the material exists. The following observations were deduced while evaluating the elasto-plastic characteristics of the fibrous solid material by isolating the pore pressure effects.

(1) A simple basic constitutive relation for the solid material was derived based on Cam-clay approach. The shear and volumetric strains were expressed in the p and q plane in terms of material properties λ, κ, M and v.

(2) Elastic behaviour may be represented by either linear or porous elasticity. Elastic material parameters for e.g. the Poisson's ratio ν, the bulk modulus K and Young's modulus E were estimated by Adam (1997) and have been used in this thesis.

(3) The critical state line M that was analysed from unconfined and partially confined uniaxial stress paths, as well as from shear box and triaxial test results (Leitch, 1996; Loughran and Adam, 1998; Plaza et al., 2001) has also been utilised in this research.

(4) Estimation of isotropic plastic strain hardening response by inverse-calibration from finite element simulation of confined uniaxial test cell is more appropriate than direct analysis. The strain hardening responses from different quasi-static experiments were compared.

Chapter 6

Finite element implementation of coupled model in ABAQUS

6.1 Introduction

The early research during 1960's that delivered a one-dimensional model for cane crushing basically ignored the constitutive characteristics of the skeleton. The model employed a smeared dynamic permeability determined experimentally from a specially constructed test cell of the experimental roll nip region. It was only during 1990's that porous media mechanics was applied to crushing by employing large strain coupled flow through the material. The governing equations that describe the porous material characteristics were solved using the finite element method. This modern approach produced interesting trends, however it came under close scrutiny with reference to the physical model of the fibrous skeleton (Adam et al., 1997). Recent advances in characterizing material properties of the fibre skeleton subjected to normal and shear load states, along with powerful numerical tools have paved a way forward. This chapter discusses important aspects of the coupled model with regard to its implementation in a finite element framework. Attention is also paid to implementation in the general purpose finite element computational code, ABAQUS. Some of the numerical issues like optimum mesh density, element selection and rezoning procedure for large strain problems associated with rolling of sugar cane are discussed. A mesh generating algorithm is also introduced for rezoning.

6.2 Coupled porous and elasto-plastic approach

The prepared cane is composed of a solid fibrous skeleton and the spaces are separated mostly by the liquid juice. The assumed continuum nature of fibrous skeleton is highly compressible but individual fibrovascular bundles are considered incompressible. Hence suitable constitutive models to represent the stress-strain behaviour of the fibrous material are formulated from a porous material point of view (Chapter 5).

The comprehensive finite element analysis of rolling and extrusion of sugar cane material by Zhao (1993) coupled the problem of flow through porous media with elasto-plastic consolidation of the solid fibres. Zhao's model considered linear elasticity with isotropic Mises plasticity or non-linear elasticity for the fibre. The liquid flow was expressed through a permeability relation as a function of volumetric strain ϵ_v, since ϵ_v is calculated spatially throughout the material domain. Following the generalized Biot formulation, a system of equations were written to describe the coupled behaviour of prepared cane. The coupled, highly non-linear set of partial differential equations were solved using a transient analysis code as referred to in Section (2.11) by discretizing the material domain into finite elements.

The fundamental transient solution outputs from the finite element simulations are, liquid pressure and skeleton displacement. The external quantities such as roll loads, torques, and extractions are derived from these fundamental quantities besides stresses, strains, and liquid flows within the blanket. The finite element solution demonstrated the ability to solve this class of coupled problem, for confined uniaxial and two-roll mill simulations. Since the behaviour of the fibrous skeleton is complex, the correct representation of real material behaviour was not adequately incorporated in Zhao's model. Zhao's theoretical approach was later improved by including material properties from experimental observations (Loughran and Adam, 1998), that are considered important from a constitutive material behaviour point of view.

6.3 Fundamental methodology of finite element analysis

Equations governing engineering phenomena are usually derived from a balance equation and a constitutive relation. Exact solution of the resulting equations, usually a differential equation (linear or nonlinear) with boundary conditions is available only for simple problems of regular geometry. For problems of complex geometries and general boundary and loading conditions, obtaining closed form solutions is an impossible task. The finite element method represents an approximate numerical solution of a boundary-value problem described by a differential equation. The historical review (Cook, 1974) of finite elements suggests that R. Courant in 1943 proposed the idea of breaking a continuum problem into triangular regions and replacing the fields with piecewise approximations within triangles. In this method of analysis, a complex region defining a continuum is discretized into simple geometric shapes called *finite elements.* The material properties and the governing relationships are considered over these elements and expressed in terms of unknown values at element corners. An assembly process, duly considering the loading and constraints, results in a set of equations. Solution of these equations gives us the approximate behaviour of the continuum. With the advances on computer technology and CAD systems, complex problems can now be modelled with relative ease. Developments have been taking place in the computational aspects of the finite element method through the application of basic theory, and modelling techniques. The two most commonly used finite element solution procedures are:

(1) The Rayleigh-Ritz method, which uses the energy or functional associated with the differential equation.

(2) The Galerkin method based on a weighted residual method in “weak form” applied directly to the differential equations.

The principle of virtual work is used as the basic equilibrium statement for the finite element formulation in "weak form". The weak form is a weighted-integral statement of a differential equation in which the differentiation is distributed among the dependent variable and the weight function and includes the natural boundary conditions of the problem. The "weak formulation" is a preliminary step towards both the Rayleigh-Ritz and Galerkin approaches for generating the finite element model. The advantage of weak formulation is that it is a statement of equilibrium cast in the form of an integral over the volume of the body.

6.4 ABAQUS general purpose finite element programme

ABAQUS is a powerful general purpose engineering simulation programme, based on the finite element method. ABAQUS can solve a wide range of linear and nonlinear problems involving static, dynamic and thermal response of components. It can simulate problems including soil mechanics with coupled pore fluid-stress analyses.

An input file for ABAQUS contains *model data*, and *history data*. Model data define a finite element model, which consists of nodal coordinates, elements, element connectivity, element section properties and material properties. Model data can be organized into parts, which are assembled together to create a meaningful model. *History data* defines what happens to the model- the sequence of events or loadings for which the model's response is sought. In ABAQUS the user divides this history into a sequence of steps. Each step is a period of response for a particular type - static loading, dynamic response, soils consolidation transient, etc.

In a nonlinear analysis ABAQUS automatically chooses appropriate load increments and convergence tolerances. Not only does it choose the value for these parameters, it also continually adjusts them during the analysis to ensure efficiency in obtaining an accurate solution.

6.4.1 Components of an ABAQUS model

An ABAQUS model is composed of different components that together describe the physical problem to be analyzed. The essential components required to build an ABAQUS model are not much different from the building blocks used to generate a finite element model. An ABAQUS model includes information on geometry, element section properties, material data, initial conditions, loads and boundary conditions, analysis type, and output requests. These are discussed below from the perspective of their application in porous media.

6.4.1.1 Geometry

The first step of any finite element simulation is discretization of the actual geometry. This basic geometry of the physical domain is defined using a collection of finite elements. In a discretized domain, elements are connected to one another by shared nodes. The model geometry is comprised of the coordinates of the node and the connectivity of the elements. The collection of all the elements and nodes in a model is called the mesh.

The type, shape, location and overall number of elements used in the mesh affect the results obtained. The greater the mesh density, the more accurate the results. The analysis results usually converge to a unique solution as the mesh density increases, but computer time required for the analysis also increases. The extent of the approximations made in the model's geometry, material behaviour, boundary conditions, and loading determines how well the numerical simulation matches the physical problem.

ABAQUS has an extensive element library which provides a powerful set of tools for solving many different problems. The pore pressure elements are best suited for materials like prepared cane. They allow modelling of fully or partially saturated fluid flow through a deforming porous medium. Pore pressure elements have both displacement and pore pressure degrees of freedom. Pore pressure elements in ABAQUS can be used as a continuum element for linear analysis or for complex nonlinear analysis involving contact, plasticity and large deformation. The choice on this continuum element includes first-order (linear) interpolation elements and second order (quadratic) interpolation elements in one, two, or three dimensions. Four noded and eight node quadrilateral elements are available respectively with linear and biquadratic displacement options. The pore pressure however has only linear interpolation.

For the purposes of this study, the pore pressure at the mid side nodes of second-order elements is determined by linear interpolation from the corner nodes in ABAQUS. The reduced integration element option for pore pressure elements enhances the computational efficiency. The quadrilateral elements are four sided polygon, the four nodes are located at the vertices and are bilinear. Other commonly used configurations are eight noded quadratic, nine noded biquadratic, and twelve noded cubic approximations. Some typical 4,8 noded pore pressure elements are depicted in Fig. 6.1.

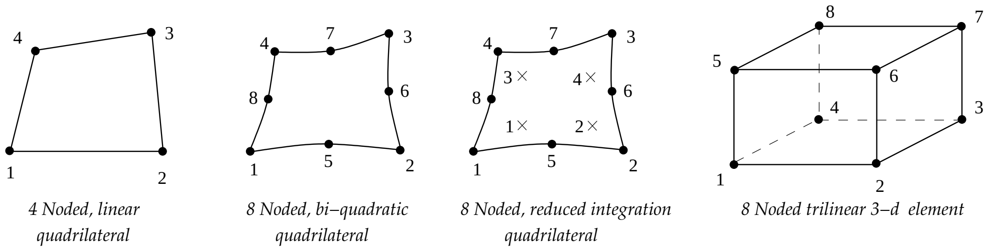

Figure 6.1: Some typical displacement pore pressure elements.

In four noded bilinear elements, the gradients are linear functions of the coordinate directions, compared to the gradients being constant in linear triangular elements. For higher order elements, more complex representations are achieved that are increasingly more accurate from an approximation point of view. In nearly all instances, a mesh consisting of a quadrilateral element is sufficient and usually more accurate than a mesh consisting of triangular elements. Although an additional node is required to define the quadrilateral element, the number of elements are reduced to half that of a mesh consisting of triangular elements for the same number of nodal points. The quadrilateral mesh more closely resembles the standard two dimensional finite difference mesh, however the finite difference mesh must be orthogonal. In the finite element quadrilateral, each element is unique and each face of the element can have a different slope. Extension of quadrilateral mesh to three dimensions is easily achieved.

In the case of two roll simulation, the geometry of the roll is defined as rigid surface. Rigid surface geometries can not deform but can translate or rotate as rigid bodies. They are much stiffer than the porous blanket material in the simulation. Rigid bodies with a single node are known as the *rigid body reference node.* The (***RIGID SURFACE**) option specifies the geometrical shape by a segmented circular rigid surface. Forces and moments are applied to the rigid body reference node to the rigid surface which is the entire roll. The position of the rigid roll reference node is important, as rotations apply to the surface where reactions are expected and moments apply. The node is placed such that it lies on the desired axis through the surface (Fig. 6.4).

6.4.1.2 Element section properties

The wide range of elements available have well defined coordinates, but additional geometric data are defined as physical properties of the element and are necessary to define the model geometry completely. Each element is characterized by the following:

(1) Family (continuum elements).

(2) Degrees of freedom.

(3) Number of nodes, order of interpolation.

(4) Formulation.

(5) Integration.

Continuum elements simply model small blocks of material in a component. As they can be connected to other elements on any of their faces, like bricks in a building or tiles in a mosaic, they can be used to build models of nearly any shape.

The degrees of freedom are the primary variable calculated during the analysis. For the pore pressure elements, the degrees of freedom are the translations, rotations and the pore pressures at the nodes. The degrees of freedom are calculated only at the nodes. At any other points in the element, they are obtained by interpolating from the nodal values. The order of the interpolation is usually determined by the number of nodes used in the element.

All of the stress/displacement elements in ABAQUS are based on the *Lagrangian* or *material* description of behaviour. Hence the material associated with an element remains associated with the element throughout the analysis, and can not move among elements. On the other hand in *Eulerian* or *a spatial* description, the elements are fixed in space and the material flows through them, typically this is used in fluid mechanics simulations.

The stresses in the quadrilateral element are not constant and vary spatially throughout the element. In practice, the stresses are evaluated at the Gauss points. To evaluate the material response in each element, numerical integration is carried out for various quantities over the volume of each element.

6.4.1.3 Material data

Material properties for all elements are specified in ABAQUS programming. The elastic properties are designated by ***ELASTIC** procedure. For isotropic behaviour, Young's modulus E, and Poisson's ratio ν are the input parameters. These two elastic properties are essentially substituted in the generalized Hooke's law equation for estimating the elastic strains.

The ***POROUS ELASTICITY** option, on the other hand, can be used to define the elastic parameters for porous materials. The instantaneous shear modulus is defined from the input parameters, logarithmic bulk modulus κ, Poisson's ratio ν, and elastic tensile limit p_t^{el}. The porous elastic model is a nonlinear, isotropic model in which the pressure stress varies as an exponential function of volumetric strain (Fig. 6.2). The corresponding volumetric elasticity relation ϵ_v^e is given in Eq. (5.11). The porous elastic material model is normally valid for small elastic strains (less than 5 %) (ABAQUS/Standard user's manual).

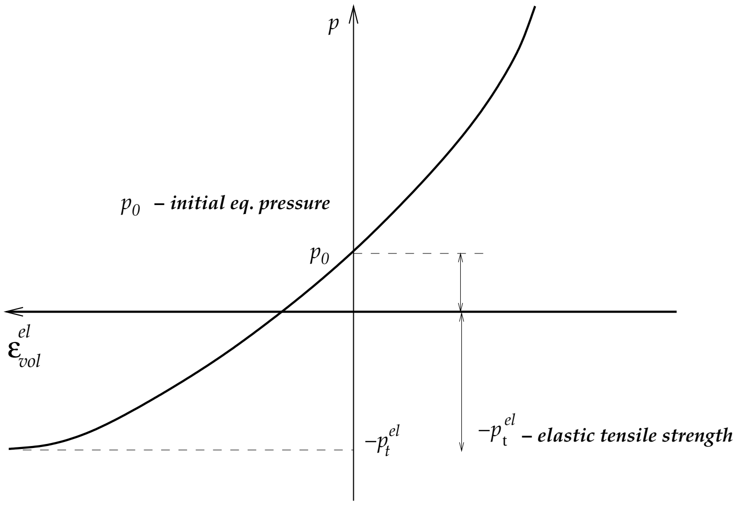

Figure 6.2: Porous elastic volumetric behaviour.

It was explained that when the stress in the material exceeds the yield stress, permanent plastic deformation occurs. Hence, the plastic behaviour of a material is described by its yield point and its post-yield hardening. It may be noted that as the material deforms in the post-yield region, both elastic and plastic strains accumulate. The ***CAP PLASTICITY** option defines the post-yield behaviour for elasto-plastic material. The modified Drucker-Prager/Cap plasticity model is used by this option to define the yield surface parameters, together with ***CAP HARDENING** option which specifies the hardening/softening behaviour. The yield surface parameters are the material cohesion d and material angle of friction in the $p - t$ plane (Fig. 5.7), cap eccentricity parameter R, initial cap yield surface position ϵ_{vol}^{pl}, and transition surface radius parameter α (Section 5.5.5, and Fig. 5.7). The total strain in the model must be decomposed into elastic and plastic strain components. The plastic strain is obtained by subtracting the elastic strain.

$$\epsilon^{pl} = \epsilon^{t} - \epsilon^{el} \tag{6.1}$$

The elastic strain is obtained from Eq. (2.59). The ***CAP HARDENING** option is used to specify the hardening part of the material model in conjunction with the cap Drucker-Prager yield surface. Hence the input for this strain hardening is the volumetric plastic strain and the corresponding hydrostatic pressure yield stress. However, the actual values of this strain hardening data are obtained by inverse-calibration of uniaxial test cell experiment as explained in Sections 5.5.6 & 5.5.7.

The relationship between the volumetric flow rate per unit area of the wetting liquid through the porous medium and the gradient of the effective fluid pressure is defined by the permeability. For the present analysis, permeability is assumed isotropic, and given as a function of void ratio. However, the permeability can also be expressed as a function compression ratio or saturation. Obviously, the permeability can only be used in elements that allow for pore pressure.

According to Forchheimer's law, high fluid velocities have the effect of reducing the effective permeability and, therefore "choking" pore fluid flow. As the fluid velocity reduces, Forchcheimer's law approximates the well known Darcy's law. Therefore, Darcy's law, was used directly in ABAQUS by omitting the velocity-dependent term in Forchcheimer's law. The fully saturated permeability k is typically obtained from experiments under low fluid velocity conditions (Chapter 4). The input for the ***PERMEABILITY** option is the permeability k in (m/s) and the void ratio e.

6.4.1.4 Initial conditions

For the prepared cane blanket, the initial pore pressures are assumed zero, and the mesh is assumed to be stress free at time zero. The void ratio for the nodes have a specified value of initial void ratio which is dependent on the cane mass and volume. The void ratio derived from compression ratio, is also a function of fibre, and juice density. Hence, through the initial void ratio, the density properties of the material are indirectly accounted for.

6.4.1.5 Boundary conditions

Loading causes displacement or deformation of the material. Loading distorts the physical structure and thus create stresses in it. The most common forms of loading for simulation of porous material consolidation include, point loads, pressure loads on surfaces and the body forces such as gravity. Normally the body force due to weight is small and may be neglected for the uniaxial test cell and two-roll mill simulations. A small load of 100 N is applied to the blanket to initiate feeding and to represent the feed pressure actually present. Though point load simulations are not used for the present investigation, it can, however, be easily implemented.

Boundary conditions are applied to those parts of the model where the displacements are known. They are used to constrain portions of the model to remain fixed (zero displacements) or to move by a prescribed amount. In either simulation, the constraints are applied directly to the nodes. In some situations a node may be constrained completely, or a node is constrained in some directions but is free to move in others.

Figure 6.3, for example, shows the boundary conditions separately for the fibre and liquid (juice) in a uniaxial test cell. The displacement and velocity boundary conditions are also shown in Fig 6.3. The top platen has a vertical speed S. The pore pressure is zero on all boundaries, since the test cell has grooved platens (top

Figure 6.3: Boundary conditions for the fibre and liquid in a test cell (Owen et al., 1994).

and bottom). There is sufficient experimental evidence (Murry, 1960a) to suggest that grooves restrict the fibre from becoming lodged at their root and therefore there ought to be minimal resistance to juice flow in this region. Boundary conditions corresponding to a typical two roll-mill simulation are shown in Fig. 6.4 both for the fibre and liquid.

Figure 6.4: Boundary conditions for the fibre and liquid in a roll mill (Owen et al., 1994).

6.4.1.6 Analysis type

A coupled pore fluid diffusion/stress analysis is carried out for the rolling of prepared cane as a fully saturated flow through porous media problem. Pore pressure elements with associated pore fluid flow properties are used in this analysis. The porous medium is modelled by attaching a finite element mesh to the solid phase, through which fluid can flow. The mechanical part of the model is based on the effective stress principle. A continuity equation is therefore required for the liquid. This equates the rate of increase in liquid mass stored at a point to the rate of mass of liquid flowing into the point within the time increment. The simulation is performed by advancing through time in small increments. The ***SOILS, CONSOLIDATION** procedure performs the transient consolidation analysis to model coupled pore diffusion/stress analysis problems involving partially and/or fully saturated fluid flow. Implicit integration scheme is performed throughout the time step in the ***SOILS** procedure, to solve the non-linear constitutive equations. The data line for time increment analysis in the ***SOILS** procedure is the initial time increment, total time period for the analysis, minimum time increment allowed, and maximum time increment allowed. At each time step an iteration process checks for a convergence. The time increment may be adjusted for an optimum computational time, without having convergence difficulties.

The uniaxial test cell simulation in ABAQUS was carried out as a quasi-static analysis, in which the top platen (Fig. 6.3) is moved down with a very slow speed, of the order of few mm/min. This was to avoid excessive juice pressure build up, since the objective of the experiment was to estimate the constitutive properties of the fibre. The solution progresses until steady state values for roll load, torque, and liquid pressure distribution within the blanket are achieved.

Interaction between surfaces The interaction between the contacting rigid roll and the cane blanket consists of two components. One normal to the surface and the second is tangential. The tangential component consists of the relative sliding motion of the surfaces, and frictional shear stresses. The distance separating two surfaces is known as the clearance. The contact constraint is applied when the clearance between two surfaces becomes zero. There is no limit in the contact formulation on the magnitude of contact pressure that can be transmitted between the surfaces. When there is no contact, no constraint or pressure is applied to the blanket. This surface behaviour is illustrated in Fig. 6.5. This default contact pressure-clearance however can be modified to include known pressure-clearance characteristics (see Chapter 7).

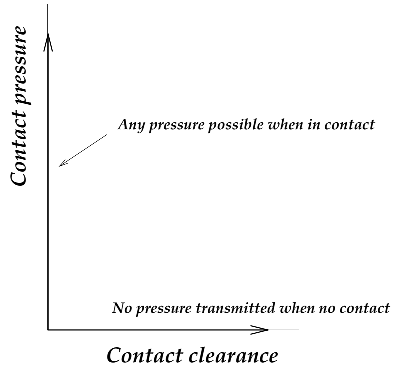

Figure 6.5: Contact pressure-clearance relationships.

Contact analysis As the blanket is fed, between the rolls, the interacting surfaces are the rigid roll surface and the blanket material. The ***CONTACT PAIR** option defines the contact deformable blanket surfaces. The friction properties are introduced into the mechanical surface interaction model governing the interaction of contact surfaces. The coefficient of friction between freshly prepared cane and machined metal surfaces decreases with increasing normal pressure and rubbing speed, and increases for small included grooving angles. Adam (1997) expressed the friction factor as a function of these parameters through a subroutine to be used in ABAQUS. Simulation results of this subroutine, and for a constant friction coefficient $\mu= 0.5$ shows the roll load response was almost constant with the roll surface speed, however the constant value friction factor response was closer to Loughran's (1990) empirical roll loads. This thesis considers the constant value analogy, in which the friction factor was given a value of 0.5.

6.4.1.7 Output requests

An ABAQUS simulation can generate a vast amount of results other than the primary solution parameters which are the nodal degrees of freedom. The secondary outputs are basically derived from the solved primary variables. These solution outputs (both primary and secondary) can be displayed in graphical form as model plotting, contour plotting, vector plotting, etc.

6.5 Mesh and element dependent study

It is important to use a sufficiently refined mesh to ensure that the results from the numerical simulations are adequate. A coarse mesh can yield inaccurate results. The numerical solution provided by the model will tend towards a unique value as the mesh density is increased. The computer resources required to run the numerical simulation also increase as the mesh is refined. The mesh is said to be converged when further mesh refinement produces a negligible change in the solution.

6.5.1 Effect of mesh density

A mesh convergence study was performed for a rolling simulation at compression ratio 1.5, using different mesh densities. The results are compared for convergence. The confidence of producing a mathematically accurate solution is assumed when two meshes give essentially the same result.

The two roll simulation was analyzed using five different mesh densities as shown in Fig. 6.6. The mesh dependent study was performed by varying mesh densities along the length of the blanket and across the blanket. The (2 x 45) mesh is coarse, and (8 x 45) is the finest mesh selected.

It is often advantageous to use a finer mesh in the area of high stress gradients and use a coarser mesh in the areas of low stress gradients or where the magnitude of the stresses is not of interest. For the rolling simulation, a sufficiently finer mesh was considered everywhere to take care of any stress gradients.

6.5.2 Effect of element type

Besides mesh density, the correct choice of element for a particular simulation is vital if accurate results are to be obtained. For example, choosing a fine mesh of linear, reduced integration continuum elements may be used to begin with for large strain analysis. The choice of pore pressure elements is limited, however three different element types were utilized to obtain a suitable element type for the simulation.

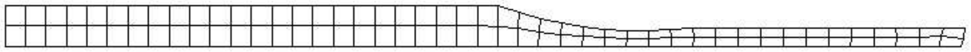

2 x 45 (Elements= 90)

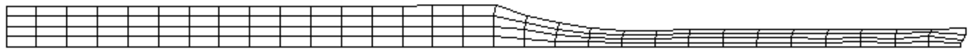

4 x 30 (Elements= 120)

4 x 45 (Elements= 180)

4 x 75 (Elements= 300)

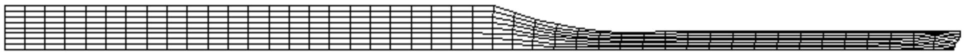

8 x 45 (Elements= 360)

Figure 6.6: Meshes of varying desity that were studied.

The different continuum element types tried were linear, quadratic and quadratic elements with reduced integration on the meshes shown in Fig. 6.6. This is to determine the effects of both the order of element and the mesh density, on the accuracy of the results. Reduced integration elements use fewer integration point in each direction than the fully integrated elements. They are computationally more efficient than the full integration elements.

The results of roll load at compression ratio 1.5 for the different meshes and the element types are presented in Table 6.1. The roll load was compared in all cases since it is influenced by the various physical parameters of the problem. As the results indicate, no major discrepancy in the results are noticed, and for subsequent analysis, element CPS8RP which is plane strain, 8 noded, biquadratic with reduced integration with (4 x 45) mesh size is chosen for the simulation.

Table 6.1: Roll loads in kN at C= 1.5 for different elements and mesh densities.

Element	**Mesh size (Depth x Length)**				
	2 x 45	**4 x 30**	**4 x 45**	**4 x 75**	**8 x 45**
CPE4P*	30.0	28.0	28.0	30.0	29.0
CPE8P†	32.0	32.0	31.5	31.0	31.5
CPE8RP‡	32.0	31.0	31.0	31.0	31.0

* 4 Node, bilinear.
† 8 Node, biquadratic.
‡ 8 Node, biquadratic, reduced integration.

6.5.3 Mesh refinement results

Displacements or any other degrees of freedom are calculated only at the nodes. At any other point in the element, the displacements are obtained by interpolating from the nodal displacements. The interpolation order is usually determined by the number of nodes used in the element.

To evaluate the material response in each element, numerical integration is carried out for various quantities over the volume of each element. For the chosen 8 noded, biquadratic reduced integration element type, the influence of mesh density on two particular results was studied for the rolling model. The two results chosen are the Mises stress at minimum work opening and the common displacement of the top right corner node of these meshes. Invariably, the maximum Mises stress occurs at the minimum work opening in all the meshes, hence, it becomes easier to compare the influence. The Mises stress and the designated displacement is almost the same for all meshes (Table 6.2). For an average mesh density of (4 x 45), the maximum deviation in Mises stress from the coarser mesh (2 x 45) is within 3%, while the specified displacement for theses meshes lies within 0.5%.

Table 6.2: Mesh refinement results for CPE8RP elements.

Mesh size	Mises stress at min. work opening (MPa)	Displacement of top right corner node (m)
2 x 45	1.56	0.4522
4 x 30	1.50	0.4530
4 x 45	1.52	0.4526
4 x 75	1.50	0.4540
8 x 45	1.49	0.4545

Since the uniaxial test cell simulation was used for estimating the plastic strain hardening response, the numerical simulation of this cell was also studied for the mesh dependency. For the numerical simulation, the optimum mesh size was found to be (10 x 10) for the quarter cell symmetry size 50 mm x 50 mm (Fig. 5.10). As in two-roll model, the 8 noded, biquadratic, reduced integration element CPE8RP was favoured.

6.6 Adaptive mesh refinement or rezoning

The major difficulty in numerical simulations using both finite difference and finite element techniques is that they generate computational errors near sharp gradients. It is the growth of the numerical dispersion errors which gives rise to computational difficulties (Pepper and Stephenson, 1995). Besides these computational difficulties, in a simulation like sugar cane rolling, the magnitude of strain and complex deformation causes severe element distortion and convergence difficulties. In an effort to eliminate these difficulties, meshes with adaptation or remeshing have been proved very successful.

Adaptive meshing schemes are well developed through mesh enrichment and automatic mesh generation techniques (Nithiarasu and Zienkiewicz, 2000; Roels et al., 1999). An adaptive mesh refinement strategy was used for mesh generation and subsequent mesh adaptation (De Souza Neta et al., 1997). In transient problems, the mesh is adapted as needed to properly correct the mesh distortion as they evolve in time. The important aspects of the transferred operation originally reported in (Perić and Owen, 1996) are given by deSouza Neta et al (De Souza Neta et al., 1997) as:

(1) Consistency with the constitutive equations.

(2) Requirement of equilibrium (fundamental for implicit finite element simulations).

(3) Compatibility of the history dependent internal variables transfer with the displacement field on the new mesh.

(4) Compatibility with evolving boundary condition.

In ABAQUS/Standard adaptive schemes are not implemented, however, a rezoning procedure is available in which a new mesh is created in substitution for the distorted mesh. The approach in rezoning meshing is to apply the solution to the new mesh from the old mesh after an initial computation for a fraction of time from a total intended duration. The solution from the old mesh is interpolated (transferred) to the new mesh, and the finite element solution procedure begun again.

6.6.1 Grid or mesh generation

When the strains become large in geometrically nonlinear analysis, the element often become so severely distorted that they no longer provide a good discretization. When this occurs, it is necessary to “rezone” or to map the solution onto a new mesh that is better designed to continue the analysis.

The procedure is to monitor the distortion of the mesh, by observing deformed plots, and decide when the mesh needs to be rezoned. At that point, a new mesh must be generated. ABAQUS has a mesh generation option for rezoning purpose, however the mesh could also be generated externally. Irrespective of the method of mesh generation, the analysis continues by beginning a new problem using the solution from the old mesh at the point of rezoning as initial conditions. ABAQUS interpolates the solution from the old mesh onto the new mesh to begin the new problem.

This technique provides considerable generality. For example, the new mesh might be more dense in regions of high strain gradients and have fewer elements in regions that are distorting rigidly. Also, there is no restriction that the number of elements be the same or that element types agree between the old and new meshes. In a typical rolling analysis at high compression ratios or at low work openings, rezoning may have to be carried out several times because of the large element distortion associated with such a process.

The interpolation technique used in rezoning is a two step process. First, values of all solution variables are obtained at the nodes of the old mesh. This is done by extrapolation of the values from the integration points to the nodes of each element and averaging those values over all elements adjoining each node. The second step is to locate each integration point in the new mesh with respect to the old mesh. The variables are then interpolated from the nodes of the element in the old mesh to the location in the new mesh. All solution variables are interpolated automatically so that the solution can proceed on the new mesh.

Whenever a model is rezoned, it can be expected that there will be some discontinuity in the solution because of the change in the mesh. If the discontinuity is significant, it is an indication that the meshes are too coarse or that the rezoning should have been done at an earlier stage before too much distortion occurred.

6.6.2 Mesh generation procedure in ABAQUS for rezoning

The first step in rezoning is to create a new undistorted mesh after an initial computation. The procedure that is followed in ABAQUS for rezoning are

1) The ABAQUS programme is run up to the specified length of time where mesh distortion requires refining. Figure 6.7(a) indicates a rolling process stopped prior to rezoning. [1]

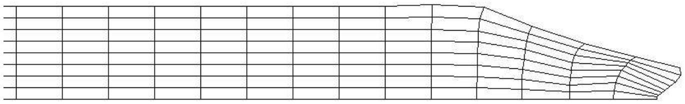

(a) Before rezoning

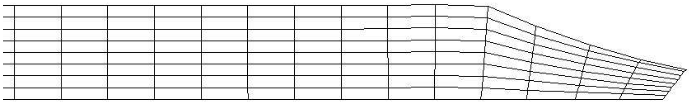

(b) Rezoning by ABAQUS

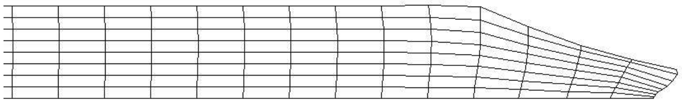

(c) Rezoning by calculation (Without grid control)

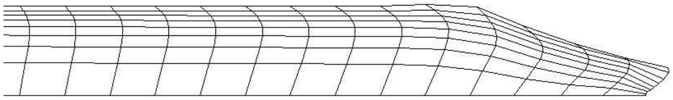

(d) Rezoning by calculation (With grid control)

Figure 6.7: Mesh for rezoning.

2) A Fortran programme was used to access the results file of step 1. Execution of this Fortran file generates a file containing the nodal coordinates of the boundaries at the end of step 1. The skeleton Fortran programme (ABAQUS example problems manual-Volume I) can be tailor made to suit a specific application.

3) An identical programme used in step 1 is followed for the continuation of the analysis except that it reads the nodal coordinates, and the solution results from the

---

[1] The mesh near the minimum opening is distorted due to the effect of juice pressures on uncompacted material. This inhibits feeding of the centre of the cane blanket into the nip and the blanket in this region undergoes plastic shear (Adam, 1997). This is obvious from the vertical lines in the nip region undergoes relative shear, as they don't travel with the same velocity as the edges.

old mesh. The nodal coordinates are read from the file generated in step 2, and the solution results are read by including ***INITIAL CONDITIONS, TYPE=OLD MESH** option. The step number and increment number at which the solution is to be read are also included in this option. A typical mesh generated by this procedure is shown in Fig. 6.7(b), which is a new mesh. The old mesh corresponding to this new mesh is at Fig. 6.7(a).

4) The solution procedure is now continued with the new mesh, and this procedure of rezoning can be repeated further if required during a roll simulation.

6.6.3 External mesh generation

The advantage of mesh refinement is that steep concentration gradients can be accurately calculated, even though one begins with a coarse mesh. Adaptation is the process by which the computational mesh changes in response to an evolving solution. Complex stress or strain regions are often regions with larger gradients and large numerical errors. The basic approach behind mesh refinement is to increase the number of elements in regions of high gradients, and to reduce the number of elements where the gradients are smooth, thereby increasing both the solution accuracy and speed of convergence. ABAQUS has limited options in this regard, hence the mesh generation procedure which is part of the solution method used in Body Fitted Coordinate techniques (Knupp and Steinberg, 1994; Thompson et al., 1985) was attempted. The basic principle in this approach is to transfer the distorted or irregular mesh in physical space (say in x, y coordinate) to rectangular mesh in terms of ξ and η in such a manner that the boundary of the rectangle corresponds to the boundary of the physical space. There is one-to-one correspondence between this mesh and the distorted mesh.

The distorted mesh shown in Fig. 6.8(a) is called the physical domain and the rectangular mesh in Fig. 6.8(b) is the computational domain. The transformation relation for mapping from x, y to the ξ, η plane are determined from the numerical solution of two elliptic partial differential equations of the Laplace or Poisson type. Parabolic and hyperbolic type differential equations have also been used for numerical grid generations, but elliptic equations are preferred because of their smoothing effect in spreading out the boundaries (Özisik, 1994).

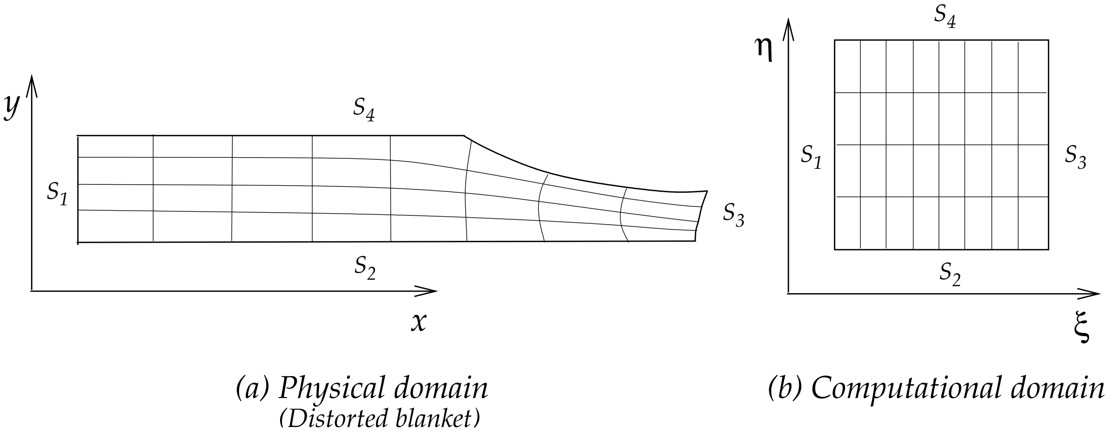

Figure 6.8: Physical and computational domain.

The transformation from the physical plane in the x, y region to computational region is expressed as

$$\xi \equiv \xi\,(x, y) \quad \text{and} \quad \eta \equiv \eta\,(x, y)$$

The correspondence between x, y and ξ, η coordinates are known at every boundary segment of the region in the physical and computational planes. To establish the coordinate transformation, the coordinates ξ, η satisfy the following two Poisson's equations over the interior region of the physical domain.

$$\frac{\delta^2 \xi}{\delta x^2} + \frac{\delta^2 \xi}{\delta y^2} = P\,(\xi, \eta) \tag{6.2a}$$

$$\frac{\delta^2 \eta}{\delta x^2} + \frac{\delta^2 \eta}{\delta y^2} = Q\,(\xi, \eta) \tag{6.2b}$$

where $P(\xi, \eta)$, and $Q(\xi, \eta)$ are mesh control functions. The boundary conditions needed to solve these equations are determined from the fact that at every boundary segment of the physical domain, the values of ξ and η are specified. The problem now becomes one of seeking the (x, y) values of the physical domain corresponding to the known (ξ, η) grid locations of the computational domain. For this reason Eq. (6.2a) & (6.2b) should be transformed to the computational domain by interchanging the roles of dependent and the independent variables. This yields the following two elliptic equations (Özisik, 1994) to be solved in the computational domain for the determination of unknown interior points x and y.

$$\alpha\frac{\delta^2 x}{\delta\xi^2} - 2\beta\frac{\delta^2 x}{\delta\xi\delta\eta} + \gamma\frac{\delta^2 x}{\delta\eta^2} + J^2\left(P\frac{\delta x}{\delta\xi} + Q\frac{\delta x}{\delta\eta}\right) = 0 \tag{6.3a}$$

$$\alpha\frac{\delta^2 y}{\delta\xi^2} - 2\beta\frac{\delta^2 y}{\delta\xi\delta\eta} + \gamma\frac{\delta^2 y}{\delta\eta^2} + J^2\left(P\frac{\delta y}{\delta\xi} + Q\frac{\delta y}{\delta\eta}\right) = 0 \tag{6.3b}$$

where the geometrical coefficients α, β, γ and the Jacobian J are given by

$$\alpha = \left(\frac{\delta x}{\delta\eta}\right)^2 + \left(\frac{\delta y}{\delta\eta}\right)^2 \tag{6.4a}$$

$$\beta = \frac{\delta x}{\delta\xi}\frac{\delta x}{\delta\eta} + \frac{\delta y}{\delta\xi}\frac{\delta y}{\delta\eta} \tag{6.4b}$$

$$\gamma = \left(\frac{\delta x}{\delta\xi}\right)^2 + \left(\frac{\delta y}{\delta\xi}\right)^2 \tag{6.4c}$$

$$J = \frac{\delta x}{\delta\xi}\frac{\delta y}{\delta\eta} - \frac{\delta x}{\delta\eta}\frac{\delta y}{\delta\xi} \tag{6.4d}$$

The coupled expressions in finite difference form are solved for $x_{i,j}$ and $y_{i,j}$ at each ξ, η grid point using successive over relaxation methods. The finite difference expression is introduced into Eqs. (6.3), and the following successive substitution formula is obtained for the determination of x, y :

$$\begin{aligned} f_{i,j} = & \frac{1}{2(\alpha+\gamma)}\Big[\alpha\left(f_{i+1,j} + f_{i-1,j}\right) - \frac{\beta}{2}\left(f_{i+1,j+1} - f_{i-1,j+1} - f_{i+1,j-1} + f_{i-1,j-1}\right) + \\ & \gamma\left(f_{i,j+1} + f_{i,j-1}\right) + \frac{J^2 P}{2}\left(f_{i+1,j} - f_{i-1,j}\right) + \frac{J^2 Q}{2}\left(f_{i,j+1} - f_{i,j-1}\right)\Big] \end{aligned} \tag{6.5}$$

where $f \equiv x$ or y. A Matlab programme was written to solve these equations. The programme is included in Appendix B.

The mesh obtained by solving Eqs. (6.3) is depicted in Fig. 6.7(c) for a typical distorted rolling problem after an initial computation. The functions P and Q are used to concentrate the mesh in the regions where large gradients occur. When P and Q are zero, no mesh control was applied (Fig. 6.7(c)). The mesh control functions P and Q can be suitably specified (Thompson, 1982) to concentrate mesh towards a boundary or a point. If the solution of the hosted equations varies rapidly in some part of the physical plane, then it is reasonable to choose a finer grid in that part of the region to reduce error in the numerical solution. Figure 6.7(d) illustrates the concentration of higher mesh densities towards the top boundary, and in the region of minimum work opening. These are the regions where the stress and strain gradients are expected to be higher. For a given mesh spacing, smooth, orthogonal grids usually result in the smallest error in simple problems.

6.6.4 Summary

The constituent properties and characteristics of liquid flow through the fibrous matter, and the elasto-plastic nature of the fibre discussed in Chapter 4 and 5 are applied together in the finite element simulation of crushing problems. The concept of finite element methods and its implementation for the porous material coupled with liquid flow are explained in this chapter. The coupled model takes into account the recent developments in material modelling and property determination. Recent studies have demonstrated the finite element simulations of uniaxial test cell compression and two-roll crushing. Further modelling on three-roll and six-roll mills crushing has also been investigated. These simulations are the basic guidelines for the present investigation, especially to validate the two roll experimental data to be discussed in Chapter 7.

The optimum mesh density and appropriate element type were assessed in the finite element simulations based on convergence/consistency trend in the results. The element distortion associated with large strain is the likely cause of convergence difficulties in the numerical computation. The inevitable mesh distortion requires intermittent rezoning or remeshing of the blanket, for the computations to proceed. The rezoning capability in ABAQUS was implemented for rolling simulations, and the required procedure for rezoning is explained. To extend its applicability, an external mesh generation technique was also demonstrated.

Chapter 7

Two-roll mill experiments and validation

7.1 Introduction

This chapter mainly presents the results of finite element simulation of a two-roll mill. The results of finite element simulation are assessed by comparing with two-roll mill experiments exclusively conducted on the C.R. Murry Advanced Experimental Milling Facility at JCU. The one-dimensional theory of the 1960's basic mill geometry and juice flow behaviour are recalled. The simple one-dimensional frictional theory to calculate roll loads and torques was also used for comparison purposes.

Two-roll mill experiments were conducted initially on grooved rolls at two speeds for three compression ratios. At a later stage, experiments were also conducted on flat rolls to give an opportunity to compare with the finite element model for both grooved and flat roll millings. The experimental schemes (for grooved and flat rolls), milling facility, and the main features of the computational model relevant to two-roll simulation are explained.

From the two-roll experimental measurements, mainly the roll loads and roll torques are compared with the predicted results. Another key parameter, namely the feeding of the material is also assessed based on the measurement of feeding velocity conducted during flat roll experiments. The sensitivity of the model output to parameter values are assessed and the results presented.

7.2 Two-roll (Grooved) experimental programme

7.2.1 Advanced experimental two-roll milling facility

This facility was established for the researchers to gain a more in depth understanding of crushing mechanisms and in particular to validate computational models. Details on the description and the capability of this experimental two-roll mill are given in (Loughran and Kauppila, 1999). This crushing facility has been designed to conduct experiments to measure the effects of the following variables:

(1) Mill compaction or filling ratio.

(2) Roll surface speed.

(3) Blanket thickness.

(4) Groove geometry or surface roughness.

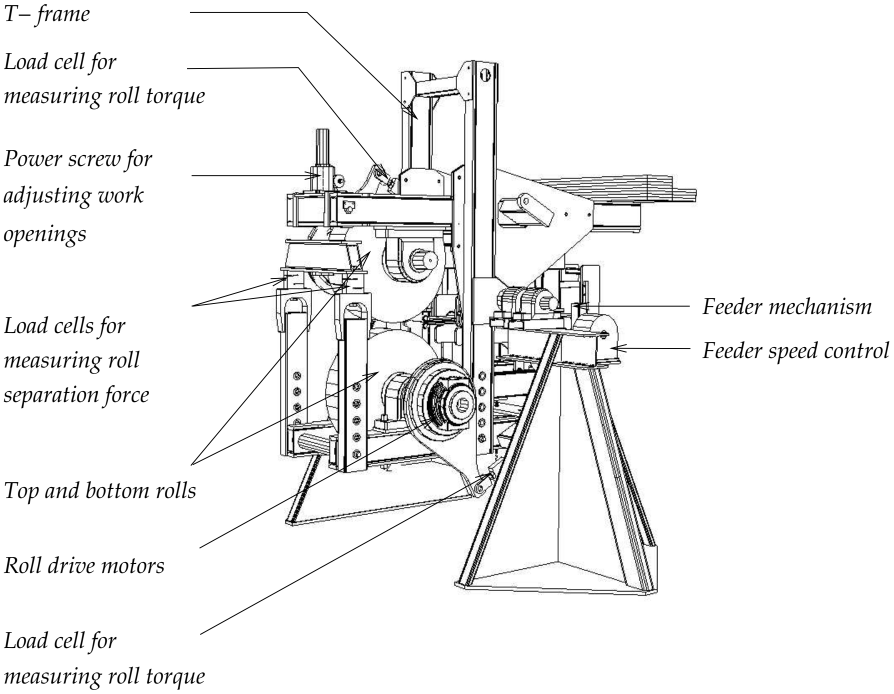

Figure 7.1: Advanced milling facility.

The two-roll experimental mill shown in Fig. 7.1 has a rigid T-shaped frame that forms the basic frame of the machine. The rolls normally circumferentially grooved are supported in bearings through the main T-frame. Each roll is powered by a hydraulic motor. To the right of T-frame, is the feeder mechanism that feeds the blanket to the mouth of the rolls. The feeder mechanism has adjustable feeder work opening. This flexible milling facility can be rotated, and thus the feeding can occur from any desired direction, to study further on the effects of gravity on juice extraction.

7.2.2 Mill control, instrumentation and measurements

During the test, the roll separating force, roll torques, roll speed, feeding force and feeder speed are measured as primary variables. The roll loads and torques are measured by load cells. The main supporting frame in which the rolls are mounted is configured with a pair of load cells placed symmetrically to measure the roll separating force. These two load cells together measure one half of the roll separating force. The torque measurement is provided individually for each roll. For the upper roll, the load cell is supported by the main T-frame, and for the lower roll, the cell is supported by a bracket attached to a pivot beam. During the operation of the mill, the roll speed is set first, and the feeder speed is set and controlled through a variable frequency controller. All transducer signals are amplified and acquired at 200 Hz, and stored in a PC.

7.2.3 Experimental scheme

The experimental roll load and roll torque response indicate no noticeable variation with cane varieties or preparation levels. This may be due to:

(1) The difference in the fibre contents of the cane handled are in the narrow region (Q124, f=13.24%; Q117, f= 14.72%).

(2) The statistical performance of the small blanket in the experimental facility,

may not match with the factory milling performance where the quantity being handled is very large.

(3) Overlapping of the experimental values, due uncertainties in the measurement.

In this regard, no distinction was made in presenting the experimental data except for the roller surface speeds. All the tests were carried out with a 10 kg sample mass with a precompressed sample height of 80 mm. Tests were conducted at three work openings that correspond to three compression ratios (Table 7.1).

Table 7.1: Work openings for the two roll experiment.

Work opening (mm)	**Compression ratio (Nominal)**
28.50	1.5
16.85	2.5
11.95	3.5

It is be noted that for all the compression ratios the grooves (Table 3.1) were in mesh. The scheme for two-roll experimental programme is shown in Fig. 7.2. The mill tests were carried out at roll surface speeds of 150 and 300 mm/s. Each compression ratio in Fig. 7.2 is shown with the successful number of tests from the originally planned tests. All these experiments were conducted at random to minimize experimental uncertainties. The other experimental parameters are given in Table 7.2.

7.3 Pressure distribution due to juice flow

The distribution of pressure on the roll surface is of prime importance to the mechanics of crushing sugar cane between rolls. It was presumed that the pressure distribution depends largely on the flow of juice in the mill (Murry and Holt, 1967). As the pressure depends on the permeability of the material, the pressure differential on a

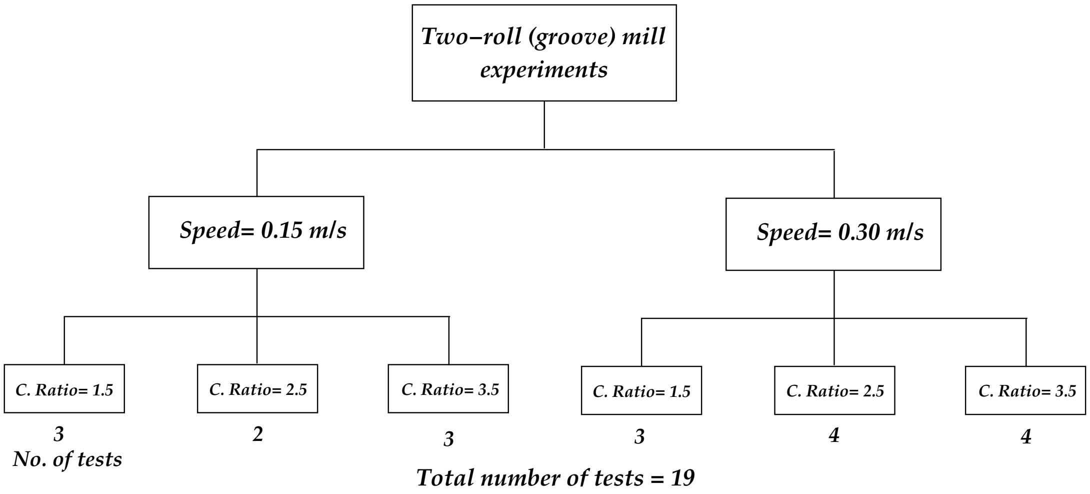

Figure 7.2: Two-roll (groove) experimental mill scheme.

Table 7.2: Parameters for the two roll experiment.

Parameter	**Value**
Cane varieties	Q117 & Q124
Preparations (RPM) (on each varieties)	1800 & 2000
Fibre contents	Q117 - 14.71% Q124 - 13.24%
Mass of cane	10 kg
Roll outer diameter	781.7 mm
Roll length	225 mm
Roll surface speed	150 & 300 mm/s
Groove geometry	(Refer Table 3.1)

segment of the roll can be deduced from Darcy's law as

$$\mathrm{d}p = -\frac{\eta S D}{2}\frac{1}{K}\cos^2\theta \; \mathrm{d}\theta \tag{7.1}$$

The shape of the pressure distribution p as a function of θ was obtained by integrating the Eq. (7.1).

$$p = \frac{\eta S D}{2}\int_{\alpha}^{\phi}\frac{1}{K}\cos^2\theta \; \mathrm{d}\theta \tag{7.2}$$

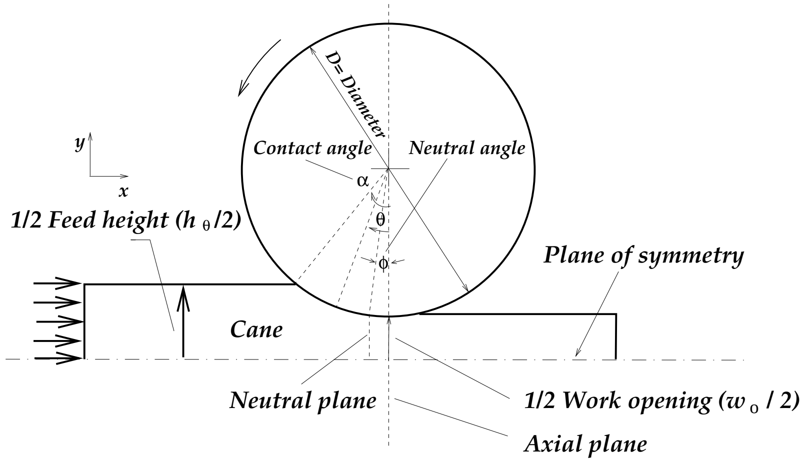

Figure 7.3: Two-roll geometry.

At the neutral plane, the volume escribed by the rolls is equal to the no-void volume of the bagasse on the delivery side of the roll, and no free juice is present beyond the neutral plane. Experiments show that juice is extracted, and hence pressures built up well before this stage of compression is reached. In fact, juice appears at compression ratio of the order of 0.6 to 0.7. Compression ratios of this order correspond fairly closely with those existing at entry angle α. Hence the integration limits are assumed between α and ϕ (Fig. 7.3) for prepared canes with an initial compression ratio close to unity.

Equation 7.2 is not valid beyond the neutral plane. However, the pressure between neutral and axial plane appears to be constant, and beyond the axial plane the pressures decays linearly (Ref. Fig. 2.4), hence a small correction may be applied to the numerical procedure. To perform this integration it is necessary to know the permeability (K), the height of solid ($h_{s\theta}$) as a function of θ and the height of cane sample (h_θ). The variation of total height between the rolls (h_θ) with θ is a matter of mill geometry. It was postulated (Murry and Holt, 1967) that the height of solid material ($h_{s\theta}$) varies inversely as the permeability, and it is expressed as a power function of compression ratio in the range α to ϕ.

For the permeability function in Eq. (7.2), when used with the directly determined response, the predicted pressures were far too high although the general form of the pressure distribution was fairly satisfactory. It was therefore felt that the resistance to flow of juice relative to the fibre must be less than the resistance indicated by the permeability tests. The most likely low resistance paths are along the roll surfaces. Hence, the effective permeability K_e, was estimated from dynamic compression tests. The dynamic compression tests depend upon the speed of compression. The effective permeability for a cane with a bulk density[1] 640 kg/m^3 was represented empirically by the following equation (Murry, 1960a)

$$K_e = 8.0X10^{-11}C^{-3.0} \tag{7.3}$$

where as the directly determined permeability for the above cane was expressed as

$$K = 9.33X10^{-11}C^{-8.52} \tag{7.4}$$

For the determination of K_e, the compression speed in the press test was conducted at 84 mm/s, while the mean speed of compression in the mill was 55 mm/s. However, the juice speed in the compression test was lower than in the mill, perhaps these differences tend to cancel, as the pressure curves predicted from these compression tests gave a good agreement on roll loads and torques (Murry, 1960a). Substituting mill parameters

---

[1] bulk density of a sample of prepared cane is a measure of fineness at arbitrary test conditions i.e. at a pressure of $7\frac{1}{2}$ psi ($\simeq$ 50 kPa) held for 20 seconds (Murry and Holt, 1967).

for h_θ from Eq.(2.23) and combining Equations 7.2 and 7.3

$$p = \frac{\eta S D}{2} \int_{\alpha}^{\phi} 1.25X10^{10} C_\theta^3 \cos^2\theta \, \mathrm{d}\theta \tag{7.5}$$

By solving Eq.(7.5), the pressure distribution is obtained.

The permeability response K_e is compared with the directly measured permeability K in Fig. 7.4, together with the directly measured permeability for the cane Q124/2000 which has the following relation.

$$K_{Q124} = 2.0X10^{-12} C^{-5.35} \tag{7.6}$$

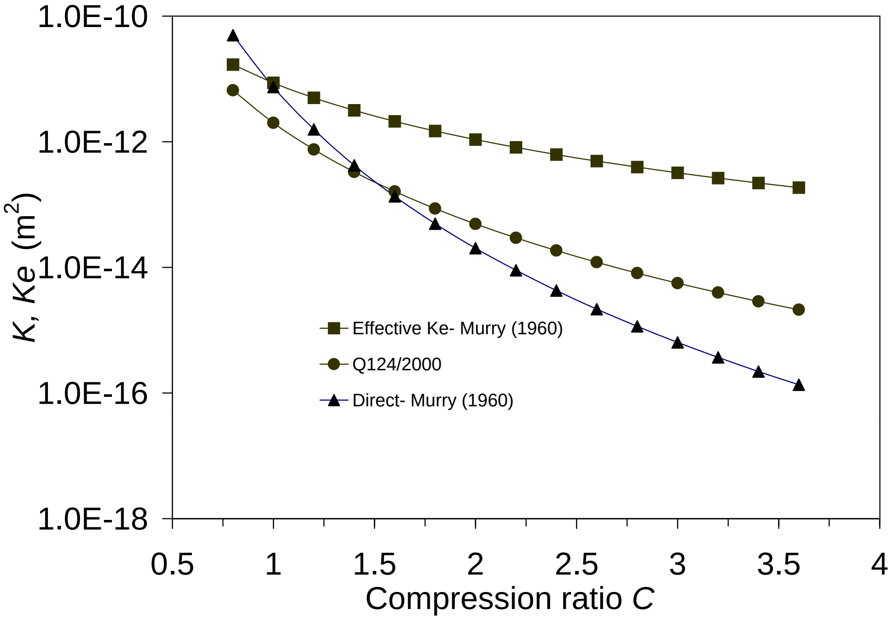

Figure 7.4: Directly measured and effective permeabilities.

7.3.1 Roll load and roll torque estimation (1-D Approach)

The accuracy of a pressure trace was tested by comparing the roll load estimated from the trace with that actually measured. From the frictional theory, the roll separating force and roll torque were expressed from Eqs. (2.29) and (2.31) as

$$R = \frac{LD}{2} \int p\,(\cos\theta + \mu\sin\theta)\,\mathrm{d}\theta \tag{7.7}$$

$$T = L\frac{D^2}{4} \int p\mu\;\mathrm{d}\theta \tag{7.8}$$

The integral limit is between entry and exit angles of the cane blanket. The variation of p as a function of θ can be established from Eq. (7.5). As a first approximation, the coefficient of friction μ between the material and the roll surface was $\mu = \tan\theta$ in the following regions.

$\mu = \tan\theta \quad \alpha \leq \theta \leq 0 \rightarrow$ For roll load estimation in Eq. (7.7)

$\mu = \tan\theta \quad \alpha \leq \theta \leq \phi \rightarrow$ For roll torque estimation in Eq. (7.8)

μ will have little effect on the vertical load beyond ϕ, and μ may still be put equal to $\tan\theta$ when considering the vertical load. Beyond the neutral plane, the material is moving forward with respect to the rolls and hence the effect of μ on torque in this region is negligible.

7.3.2 One-dimensional frictional theory results

From one dimensional frictional theory, the equation for roll separating force R between the rolls was simplified by approximating the coefficient of friction $\mu = \tan\theta$ (Section 7.3.1). Thus the roll separating force is expressed as

$$R = \frac{LD}{2} \int_0^{\alpha} p\;\sec\theta\;\mathrm{d}\theta \tag{7.9}$$

The torque (T) equation (7.8) becomes

$$T = \frac{LD^2}{4} \int_{\phi}^{\alpha} p\;\tan\theta\;\mathrm{d}\theta \tag{7.10}$$

In the part between β (the particular value of θ at which no free juice moves into the mill) and ϕ, The pressure at any angle θ is expressed by Eq. (7.2)

$$p = \frac{\eta SD}{2} \int_{\beta}^{\phi} \frac{1}{K_e} \cos^2\theta\;\mathrm{d}\theta \tag{7.11}$$

K_e may be thought of as an "effective" permeability since it is a value calculated from the actual resistance offered by the cane sample to compression. The following material properties are considered for estimating the roll load and torque from the frictional theory.

Parameters for one-dimensional frictional theory

Permeability relation (as used by Murry (1960a))
$K_e = 5.57\ \exp^{-12} C_\theta^{-2.32}$
Dynamic viscosity $\eta = 2.25\text{X}10^{-3}$ Pa.s
Roller mean diameter $D = 750$ mm
Roller surface speed $S = 0.15$ m/s
Work openings w_o= 11.95 mm, 16.85 mm & 28.5 mm
Reabsorption factor $K(C_o, S) = 0.5644{+}0.1763C_o{+}0.4075S$ (Kauppila, 1999)

Equation 7.11 is to be solved first to get the pressure distribution before substituting into Eqs. 7.9 & 7.10 to estimate roll load and roll torque. These equations are solved by numerical integration using Simpson's rule, with the above material parameters (A Fortran programme to solve to this effect is included in the Appendix A). Roll loads and roll torques are estimated at three compression ratios namely at 1.5, 2.5 and at 3.5.

Figure 7.5 compares the roll load with compression ratio together with the experimental data, and the results from frictional theory. The one dimensional model is very sensitive to the reabsorption factor K, permeability response and the roller speed. Comparison of experimental values was undertaken only for the roller speed $S = 0.15$ m/s as an exercise, and no practical importance on the applicability of this theory is emphasised at this stage. However, the experimental values at $S = 0.15$ and 0.30 m/s are compared in detail in Section 7.6 with the results of finite element simulation of a two-roll mill. The weakness of frictional theory in modelling the porous material for rolling processes is expected, since it neglects the behaviour of solid fibrous stresses.

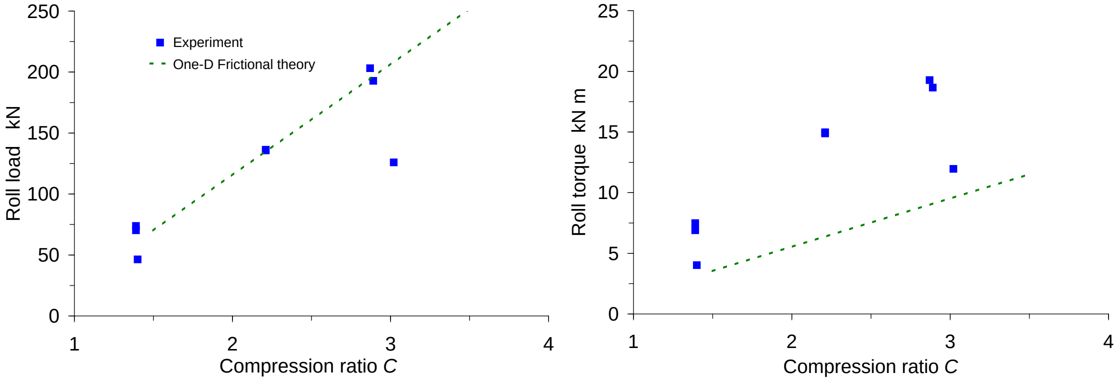

Figure 7.5: Roll load and torque for roller speed S= 0.15 m/s.

7.4 Modelling considerations

The finite element simulation of two-roll experimental mill is based on the following approaches:

(1) The two roll model is assumed as symmetric at the half groove depth of the rolls (Fig. 7.6).

(2) The symmetric model is assumed as plane strain, and hence the strain in the z-direction is confined. The z-direction corresponds to the axial direction of the rolls.

(3) The blanket is modelled as fully saturated both initially and throughout the crushing process. For the partially saturated state, the analysis is performed by increasing the permeability over the partially saturated region to prevent premature liquid pressure generation. The fully saturated mill simulation showed negligible difference on roll load and torque in comparison with partially saturated flow model (Adam, 1997). (Further discussion in Section 7.4.2).

(4) The material behaviour under stress is considered to be isotropic. Any anisotropic properties due to the direction of layering of fibres are too complex to determine. The realistic isotropic representation of the experimentally observed

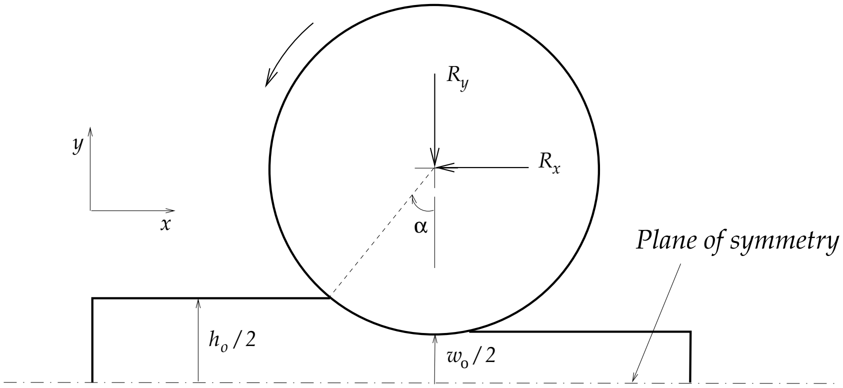

Figure 7.6: Two-roll symmetry at half groove depth.

behaviour of the material is modelled using linear elasticity and capped Drucker-Prager plasticity models. The effect of porous elasticity from uniaxial/unload cycle results in greater final material volume than the initial volume which is unrealistic (Adam, 1997). Porous elasticity was not attempted in this analysis, however porous elastic material properties have been determined from experimental unload data (Section 5.4).

(5) The rolls are modelled as circular, 2-dimensional rigid surfaces. The grooving effect is however built in through the plastic strain hardening relation (measured on grooved platens) and therefore a $p = 0$ boundary condition is justified.

(6) The frictional behaviour between the rolls and blanket is specified by a contact friction coefficient. More elegant representation of friction models is available when modelling two-dimensional rolls (Adam, 1997). By and large the model produces similar results to that where the coefficient of friction μ is set to about 0.5.

(7) The finite element solution is performed with Lagrangian formulation in which the mesh moves and is attached to the solid material, however the fluid can flow through the mesh relative to the solid. The solution progresses until steady state values for roll load and torque within the blanket is reached.

7.4.1 Initial compression ratio of the blanket

The reference point for zero volumetric strain was already defined at void ratio $e = 12.1$, corresponding to a compression ratio of 0.8 at 13% fibre content. This reference void ratio of 12.1 is maintained as the strain hardening material is strongly dependent on the void space. Based on this acceptance, the constitutive properties were developed in Chapter 5. It is also essential that two-roll mill simulation must begin at this initial void ratio. There are two approaches, that may be followed when the initial void ratio of the mill blanket is different from 12.1 (Adam, 1997).

Simulation by adjusting the blanket height

For a mill blanket initial void ratio higher than 12.1, the blanket height is reduced such that the initial void ratio is 12.1, and then the finite element simulation is followed. This reduces the contact angle α for finite element simulation. This alteration has little effect on simulation results. It was further suggested that calculation involving the contact angle of material on the roll should be performed using the experimental feed blanket contact angle rather than the lower simulation contact angle.

Simulation by shifting the yield surface

The other approach is to shift the yield surface for higher initial void ratios (or lower compression ratios), providing the elastic material properties are assumed constant across the full range of compression. The yield surface parameter (ϵ_v^p) is shifted by the following relation to represent a higher void ratio by neglecting any elastic strain since stresses are small.

$$\epsilon_v^{p*} = \ln\left(\frac{1+e}{1+e_o}\right) \tag{7.12}$$

where e = 12.1 (reference void ratio).

e_o = initial void ratio of the blanket.

The additional strain hardening curve may be determined from low pressure experimental data, or may be extrapolated from the existing value as shown in Fig. 7.7(b).

This procedure allows the simulation at higher initial void ratio, and maintains the original constitutive behaviour beyond the compression ratio corresponding to void ratio 12.1. Both of the previous methods were tried for the initial void ratios higher than 12.1, and no noticeable difference in the results of roll load or torque was observed.

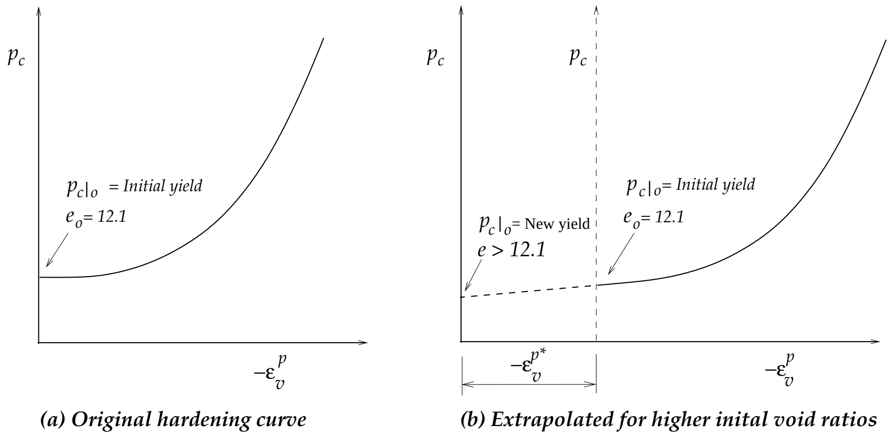

(a) Original hardening curve *(b) Extrapolated for higher inital void ratios*

Figure 7.7: Modification of yield surface for initial void ratios higher than e= 12.1.

7.4.2 Appropriate form of permeability response

The experimentally determined axial permeability responses from different investigators (Downing, 1999a; Murry, 1960a) and from the present investigation agree generally in the tested range of compression ratios (Fig. 4.4). Any variation in the permeability may be due to material properties, preparation levels and other factors. It is appropriate to consider permeability only in the axial direction which is the direction of juice flow. For a two-roll crushing process, the initial condition of the blanket may be in partial saturation under low compression ratios. The likely effects of partial saturation are absorption, exsorption and air expulsion. Under low compression regimes in a saturated condition, seepage induced consolidation is in effect.

The capillary effects present in a partially saturated flow medium correspond to negative pore pressure in the wetting liquid. Zero or positive pore pressure corresponds to a fully saturated condition. In the case of partially saturated flow, the permeability of the medium to liquid flow is dependent on the degree of liquid saturation as well as the porosity of the material. The expulsion of air under partial saturation is a relatively minor factor that affects the crushing process. However in the volume reduction process, for any air entrapped at high pressures some liquid must be expressed in preference to air.

Seepage is the process of liquid flowing through the fibrous solid matrix caused by a combination of a highly compressible solid matrix and low permeability. Under seepage flow the matter undergoes consolidation and hence the apparent measured permeability values are affected. The finite element simulation study on a permeability cell model (Adam, 1997) suggests that Murry and Holt's permeability values at lower compression ratios could be lower than the true value.

Hence to account for the likely effects of partial saturation, air expulsion, and seepage-induced consolidation the permeability response was modified. The modification essentially refers to an increase in permeability at low compression ratios to prevent juice pressure being built up in the feeding region of roll nip. The juice pressure response at higher compression ratios is unaffected by the permeability modifications.

The experimental evidence suggests that the feed velocities in a mill should be approximately equal to $S\cos\alpha$ where S is the roll surface speed. The low permeabilities in the loosely compacted material under high void ratios causes relatively high juice pressure gradients, and is responsible for the irrecoverable plastic strains on the fibres. This inhibits the required feeding at $S\cos\alpha$. Another observed factor was that maximum juice pressure occurs in the compacted area or at the minimum work opening. It was noticed that the mill is able to feed correctly for higher maximum juice pressure (at the compacted area of the mill) where the degree of strain hardening is sufficient to sustain the seepage flow. Hence, it is apparent that at low compression regions juice pressure generation is avoided by increasing the permeability, and in the compacted area, seepage induced flows are accounted for.

Figure 7.8: Recommended modifications for the permeability (Adam, 1997).

The specific modification in permeability adopted by Adam (1997) affects the partially saturated ($C < 1.0$) region and in low compression regions ($1.0 < C < 1.5$). There are no permeability data for partially saturated prepared cane. For the partially saturated region the permeabilities are increased by two orders of magnitude to prevent premature juice pressure generation. For the low compression regions, the permeabilities are increased by a factor of four for seepage flow (Fig. 7.8). The corrective measures on the apparent permeability was arrived at based on all these factors for a fully saturated analysis. The modified permeability response gives better feeding characteristics that leads to better roll loads and roll torque responses.

7.4.3 Boundary conditions

In the actual groove, there exists two boundary conditions for the juice pressure. The drainage consideration suggests that at the base of the grooves the juice pressures are close to zero, while the inter-facial flow along the flanks may require significant driving juice pressure. Maximum pressure will occur at the tip of the groove and be almost zero pressure at the root (Fig. 7.9). The computational model geometry assumes a flat roll, and in the absence of a suitable method to implement a moving boundary condition during crushing, juice pressures are assumed zero for the blanket roll interface during two-dimensional plane strain modelling.

Figure 7.9: Pressure distribution along flank of tooth (Murry, 1960b).

A small feed pressure of around 10kPa is applied at the rear edge of the blanket, to prevent breakage of the cane blanket prior to nip entry and to simulate the feeding. The body force of the blanket due to weight is small and can be neglected.

7.4.4 Friction factor

The coefficient of friction between freshly prepared cane and the machined steel surface decreases with increasing normal pressure and rubbing speed and increases for smaller included angle. The overall regression equation for the friction coefficient between fresh prepared cane and non-rusted, machined, iron or steel surfaces was developed (Loughran and Adam, 1998) using the experimental data (Bullock, 1957; Cullen, 1965; Murry, 1960a) as

$$\begin{aligned}\mu =&1.0 - 8.65X10^{-2}\ln(\sigma_n) - 2.21X10^{-3}S_r - 1.27X10^{-3}G_\alpha + \\ &8.01X10^{-5}\ln(\sigma_n)\,G_\alpha + 2.47X10^{-4}\ln(\sigma_n)\,S_r \qquad (7.13)\end{aligned}$$

where μ = friction coefficient.

σ_n = normal pressure across the interface (kPa).

S_r = relative rubbing speed between the surfaces (mm/s).

G_α= included angle of the grooving(degrees), with $G_\alpha = 180°$ for flat surfaces.

In a typical milling situation, the juice flow under high pressure in the groove tip region may serve to lubricate the contact interface, thus reducing the friction coefficient. The coefficient of friction $\mu = 0.5$ served as a reasonable value for all practical two-roll simulations.

7.5 Mesh distortion and feeding

While the blanket close to the roll is pulled mainly due to the frictional effects, the centre of the blanket undergoes plastic shear with respect to the edge. In this situation, high distortion of finite element grids are noticeable in the nip region. The modified permeability response discussed in Section 7.4.2, gives favourable feeding conditions and the mesh distortion due to poor feeding is unlikely at compression ratios less than 3.5.

The default hard contact relationship in the mechanical interaction normal to the surface, allows no penetration of the slave nodes into the master surface and no transfer of tensile stress across the interface. Here the slave nodes are referring to the blanket and the master surface is the rigid roll. In this arrangement, the computational model predicted the roll loads and torques much lower than the experimental values. The maximum deviation was found the torque values which were nearly 80% lower. The reason for this was probed in the feeding behaviour of the material. The computed feeding velocities have been found lower than the required feed velocities especially for compression ratios higher than 1.5.

A softened contact relation was tried by allowing the blanket material to penetrate to a small value at zero contact pressure and also a nominal pressure was designated at zero clearance. This was tried to improve feeding. The assumed softened contact relationship is that the contact pressure is an exponential function of the clearance between the surfaces i.e. this option is to define an exponential (soft) contact-overclosure relationship. In this relationship, the surfaces begin to transmit contact pressure once the clearance between them reduces to c, measured in the normal contact direction. The contact pressure transmitted between the surfaces then increases exponentially as the clearance continues to diminish as shown in Fig. 7.10.

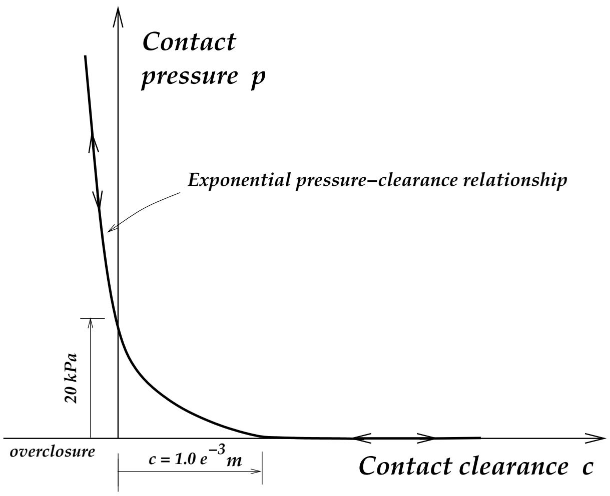

Figure 7.10: Softened pressure-overclosure relationship.

For a value of c = 1mm, and the contact pressure at zero clearance = 20kPa, the finite element solution has resulted in improved feeding, and improved load and torque responses. However, the torque response was still much lower than the experimental values by 60%.

The examination of vertical lines formed by the initial finite element mesh shows that, it almost remains vertical when it goes through the nip region as seen in Fig. 7.11. Even at higher compression ratio ($C = 3.5$), the mesh distortion is minimal. The finite element results of feeding velocities at steady state are given in Table 7.3 for two roll surface speeds.

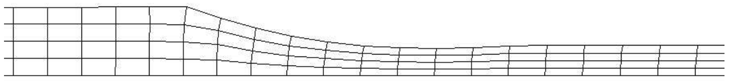

Compression ratio= 1.5

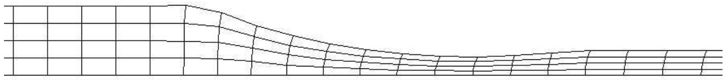

Compression ratio= 2.5

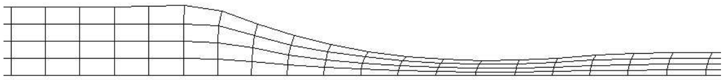

Compression ratio= 3.5

Figure 7.11: Displaced mesh at different compression ratios.

Table 7.3: Feeding velocities at different compression ratio.

Compression ratio	**Feed velocities at roller surface speed**	
	0.15 m/s	**0.30 m/s**
1.5	0.140	0.28
2.5	0.136	0.28
3.5	0.135	0.27

7.6 Two-roll experimental results and predictions

As per the experimental programme discussed in Section 7.2.3 the two-roll mill experiment was exercised at three compression ratios (1.5, 2.5 and 3.5). All the relevant experimental data was acquired and stored during the experiments. The finite element simulation was carried out corresponding to the experimental settings for each compression ratio. The work openings and the roller speed are the only variables to be changed for each compression ratio in the numerical simulation, while all the other parameters and properties were kept constant.

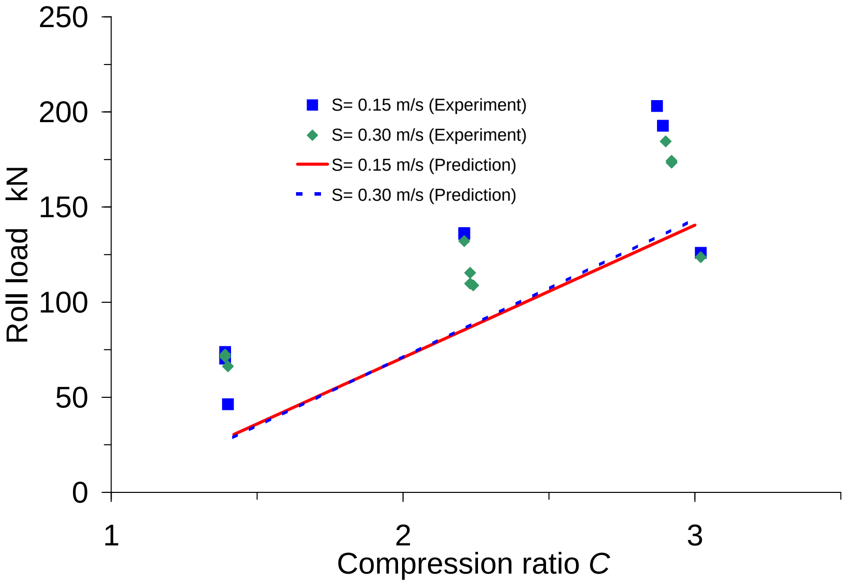

Figure 7.12: Comparative response of roll load to nip compression ratio for increasing roll surface speed.

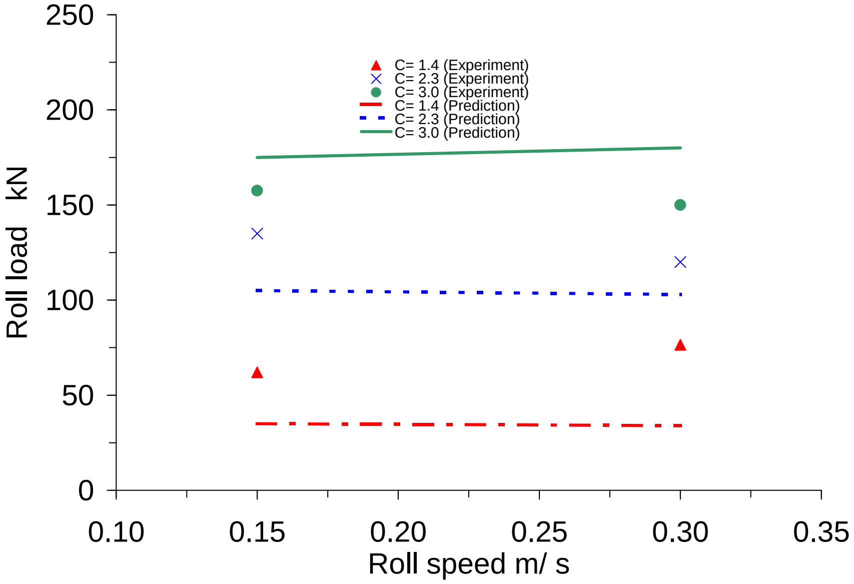

Figure 7.13: Comparative response of roll load to surface speed.

The experimental observations and the simulation results of roll load indicate the roll load is proportional to the compression ratio. The roll load is almost constant with the tested speed. Figure 7.12 shows the plot of roll load Vs compression ratio at two speeds. The predicted trend and level of response for roll load is much closer to experimental data between compression ratio 1.5 and 3.0. Figure 7.13 displays the response of roll load to roll surface speed at a set compression ratio. The model displays the nominal flat response that is a characteristic of crushing experiments. For a compression ratio of 1.5 the level of response is low.

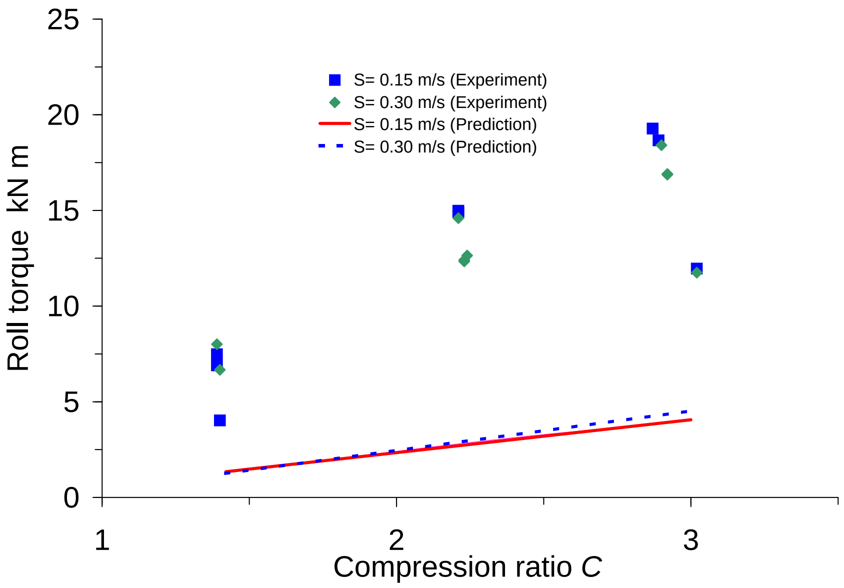

Figure 7.14: Comparative response of roll torque to nip compression ratio.

Figure 7.14 and 7.15 shows the comparative responses for roll torque. Here, the trends are roughly consistent with experiment but the level of response is unsatisfactory. Several points are worth noting. Firstly, the two dimensional model ignores side-wall friction and the moment required to peel compressed bagasse out of the grooves. These factors will not influence roll load because they are vertically balanced but will affect roll torque to some degree. Perhaps of more importance is the fact that the two dimensional representation ignores the stress concentration of fibre (very low void ratios) around the

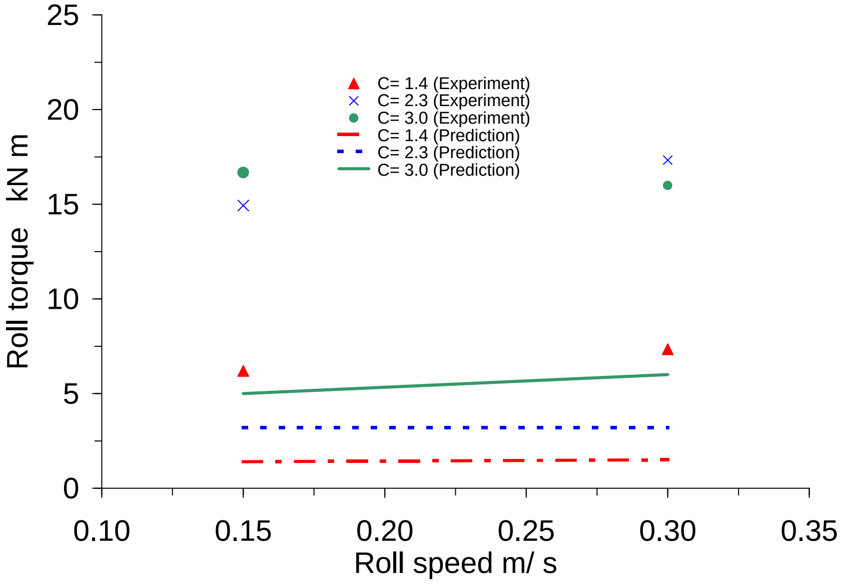

Figure 7.15: Comparative response of roll torque to surface speed.

tip region of teeth. The predicted torque will be strongly influenced by the stress state adjacent to the tooth boundary. It is not surprising that the two-dimensional model does a poor job of predicting absolute torque values at high nip compression ratios. A three-dimensional model which captures the penetration of bagasse into the tooth root region may provide a better prediction.

7.6.1 Comparison of results with other experiments

The predicted results and this thesis current experimental values are now compared with the other available data. The thesis results are plotted together with the results of similar comparison (Adam, 1997) for Pindar cane of 750/15 preparation (fibre content 12.8%). The roll load and torque values are presented in per metre length of roller in Figs. 7.16 & 7.17. The roll data presented by Adam consists of Murry's experimental data (Murry, 1960a), Loughran's empirical roll load equation (Eq.2.32) result, and his finite element simulation results. For the roll torque values, Murry's torque load number (Murry, 1960a) was used to represent Loughran's formula.

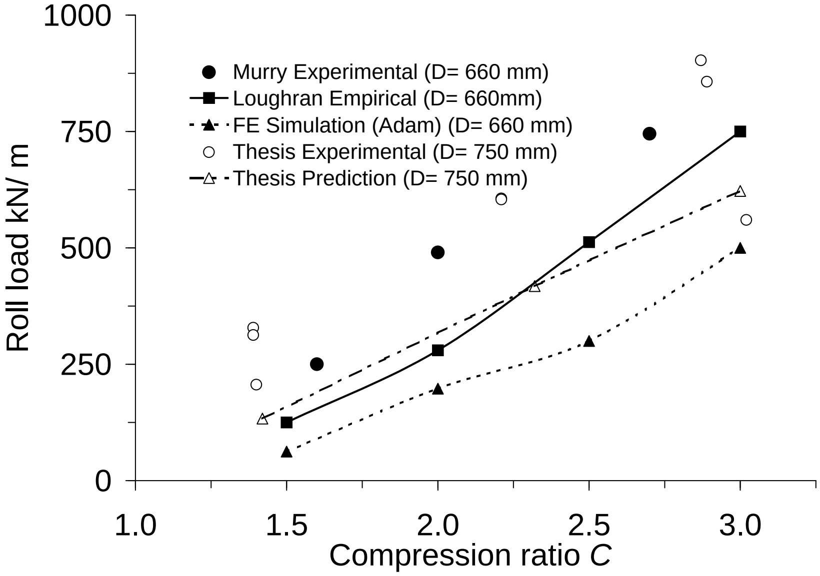

Figure 7.16: Comparative responses of roll load with other data at roll surface speed $S = 0.15$ m/s.

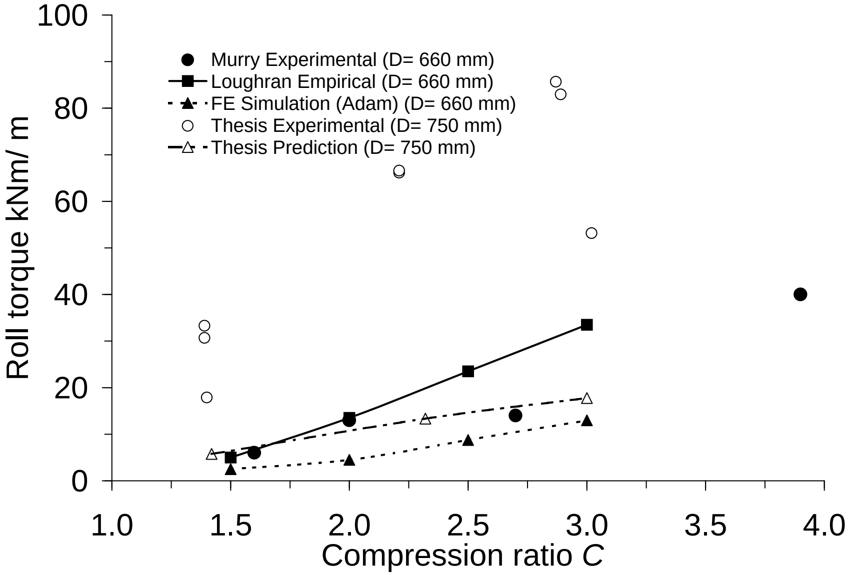

Figure 7.17: Comparative responses of roll torque with other data at roll surface speed $S = 0.15$ m/s.

It may be noted that all of Adam's comparisons are made for a roller diameter of 660mm with 55°groove, where as the current thesis results are for a 750mm roller with 35°groove. The roll load increases almost in linear with roll diameter. Hence to compare with the 750mm diameter roller data, the 660mm diameter values in Fig. 7.17, may be increased by about 10-15% at compression ratio 2.5. The extrapolation of this result is based on the results provided by Adam for different roller diameters, and similar trend is expected at other compression ratios. When comparing the results, the effects of different canes and groove geometries may also have to be considered. Though the data compared here are not in identical conditions, comparison at the same compression ratio gives some insight on these variables.

7.6.2 Other predicted output parameters

Other than predicting the overall gross effects, namely the roll loads and roll torques, the shape of juice pressure distribution, pressure distribution on the roll surface, juice extraction and reabsorption factor K can also be estimated. A blanket internal parameter can be assessed to study its effects on the specific aspect of the milling performance. Figures (7.18 - 7.20) depicts some of the vital parameters of internal blanket conditions at the lowest and the highest compression ratios conducted. The three-dimensional stress and strain effects are shown in Fig. 7.18 through Mises stress and volumetric strain. The volumetric strain for example is compared at two compression ratios that gives the overall reduction in the volume of the blanket. This reduction in volume of the porous material is responsible for the void ratio reduction. The juice extraction may be estimated quantitatively from the void ratio reduction across the nip region (Fig. 7.19). These qualitative plots are very useful in determining the milling characteristics as a function of nip compression ratio, roller diameter and roller speed.

The reabsorption factor, K may be calculated by estimating the velocities of the fibre material at the axial plane of the rolls. Since the reabsorption is caused by the

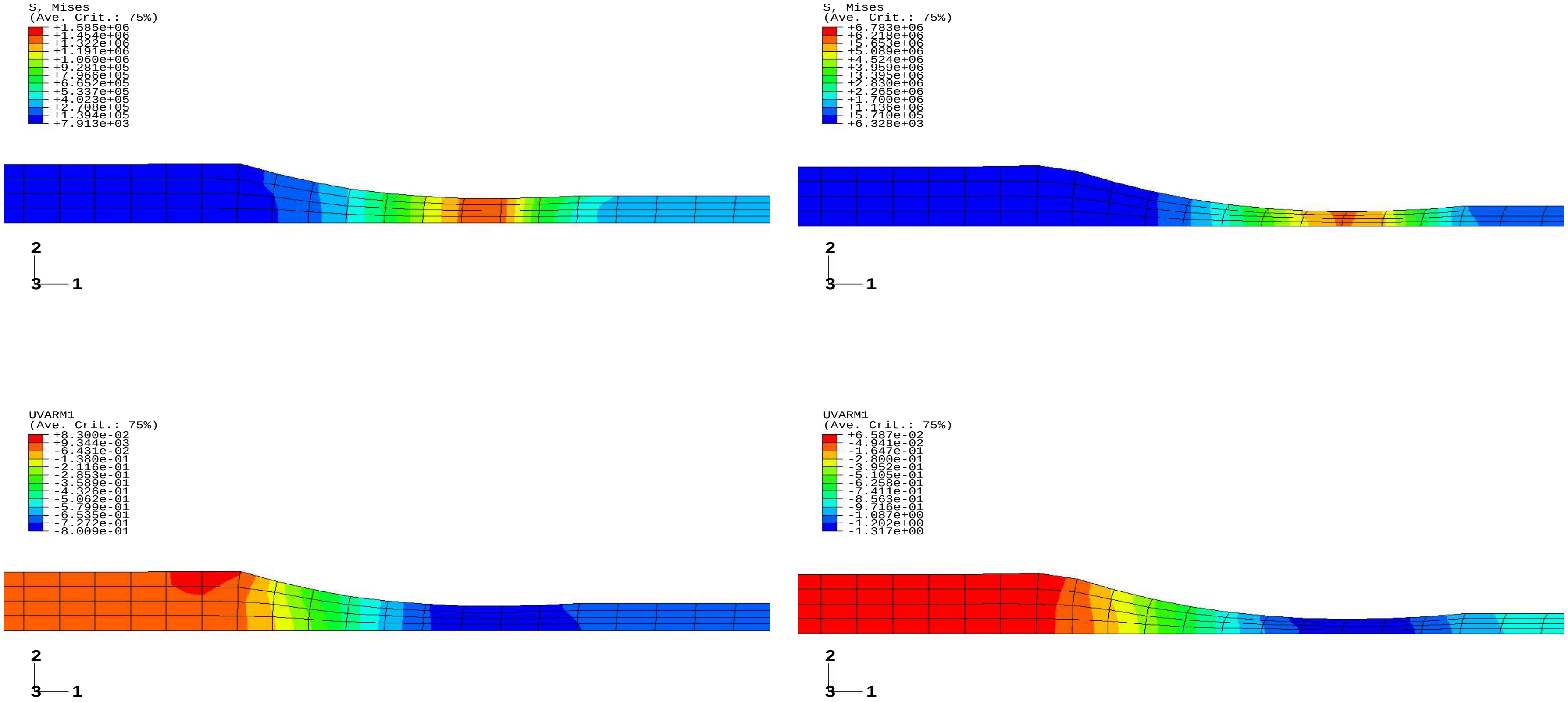

Compression ratio= 1.42

Compression ratio= 3.0

Figure 7.18: Predicted Mises stress (top row) and volumetric strain (bottom row).

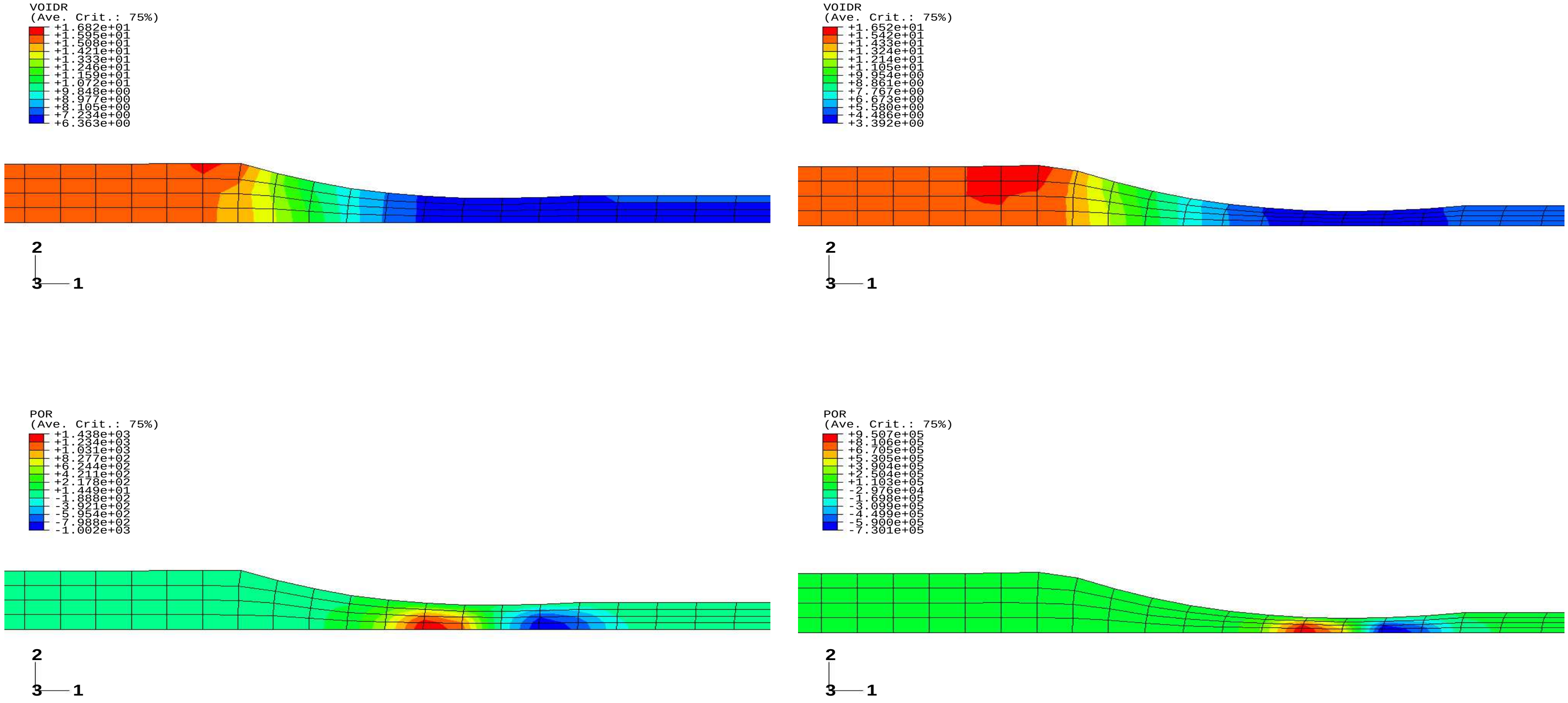

Compression ratio= 1.42

Compression ratio= 3.0

Figure 7.19: Predicted void ratio (top row) and pore pressure (bottom row).

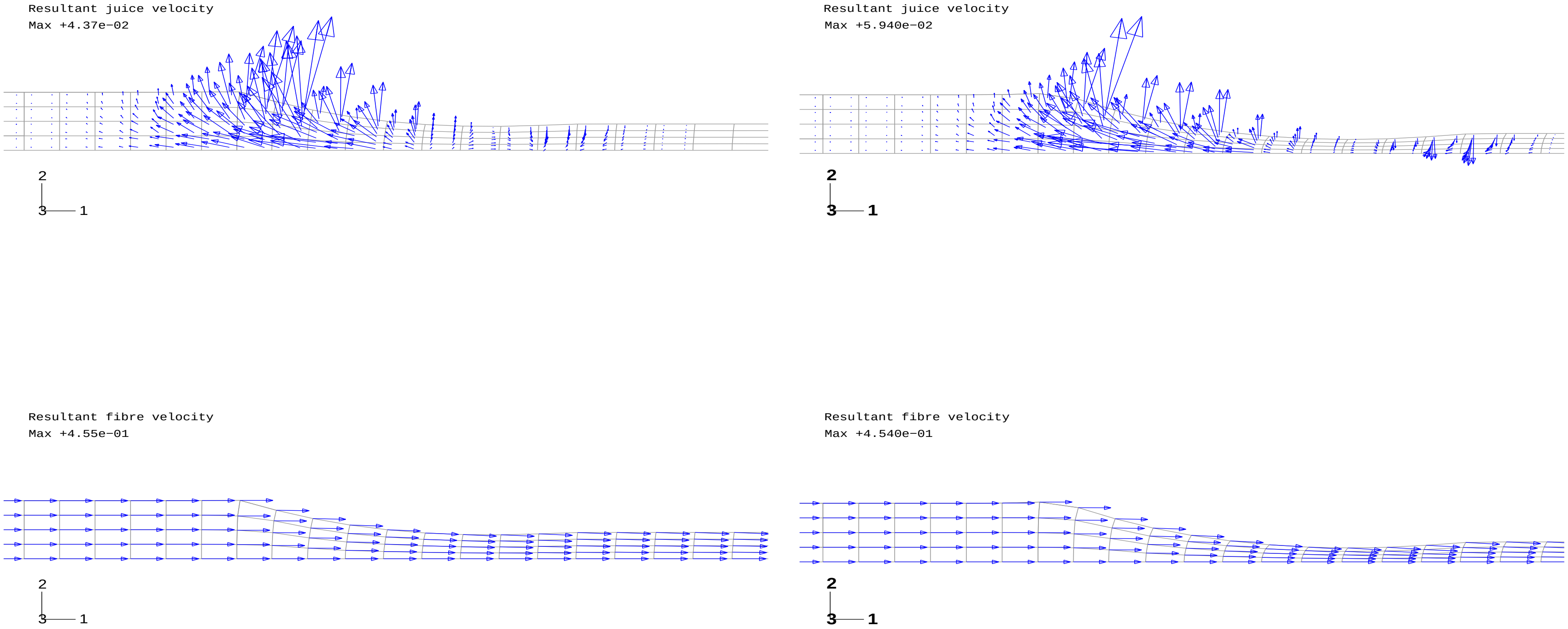

Compression ratio= 1.42

Compression ratio= 3.0

Figure 7.20: Juice velocity vectors (top row) and fibre velocity vectors (bottom row).

combination of forward slip, forward extrusion, and forward flow of liquid relative to the solid phases, the knowledge of juice and fibre velocities are useful. The juice velocities relative to the fibre is shown in Fig. 7.20. The forward juice flow at the roll boundary near the contact point of the roll, and the backward juice flow in the nip entry region are some of the characteristics of juice flow behaviour.

7.7 Parameter sensitivity of elasto-plastic property responses

The effectiveness of computation of porous elasto-plastic response also depend on the accuracy of the property values. Some of the parameters are determined experimentally, and some are assumed to be based on the general characteristic nature of the material. A numerical experiment was conducted by varying key parameters, to observe overall response on roll load, roll torque and feeding of the material.

Table 7.4: Parameters varied for the numerical experiment.

Parameter	**Range of values**
Blanket height	60 - 100 mm
Feed pressure	1.11 - 11.1 kPa
Young's modulus	20 - 40 MPa
Tensile stress	0.1 - 10 kPa
Critical state slope M	1.0 - 4.5

Five parameters of interest were chosen for the study namely, the blanket height, feed pressure, Young's modulus, tensile stress and the critical state slope M (Table 7.4). In the numerical experiment, the effect of a particular parameter was studied by keeping all other parameter values as given in Table 5.2. The tensile stress and M value combination is studied to simulate different cohesiveness of the material. The numerical experiment on the effect of blanket height and feed pressure is straight forward because these parameter are independent of the plastic strain response. For other parameters, recalibration of plastic strain response is required.

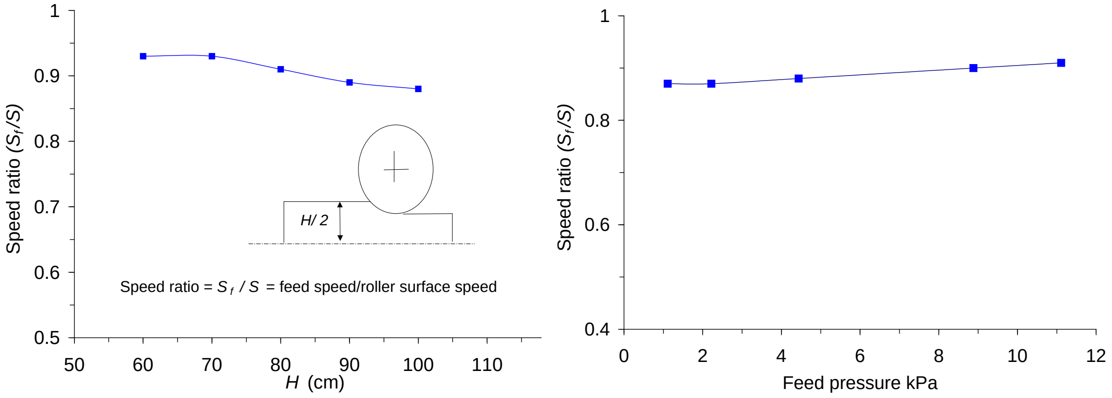

Figure 7.21: Effect of blanket height and feed pressure on feed velocity.

The effect of blanket height, and feed pressure on feeding is shown in Fig. 7.21. Any increase in blanket height reduces feeding, while the feed pressures pushes feeding to a slightly higher value. Feed pressure may be assumed due to the self weight acting on the moving blanket in a typical hopper mill arrangement. Feed pressure beyond 10kPa was not attempted in this study.

The experimentally determined property values of Young's modulus on different prepared canes indicate that its value lies in the range 20-40MPa. The effect on the rolling performance due to a small variation in Young's modulus is not significant (evident from the back calibrated plastic strain).

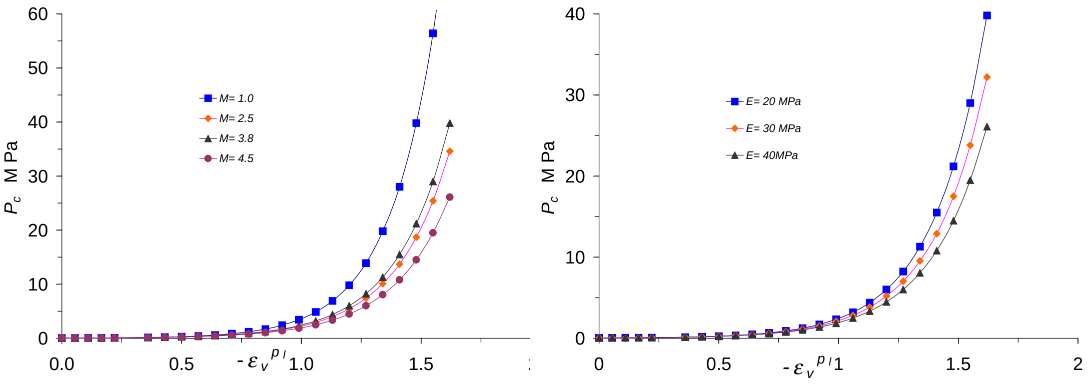

Figure 7.22: Strain hardening responses for different M (critical state slope) and E (Young's modulus).

The effect of M in the range 1.0-4.5 was studied. No noticeable difference was observed for the different tensile stresses in the back calibrated strain hardening responses (Fig. 7.22). However, in the two-roll simulation, increase in tensile stress and M value increases the level in feeding response, but the increasing trend is small as shown in Fig. 7.23. For M values lower than 3.0, the expansion of the material was too severe and the results are not practical.

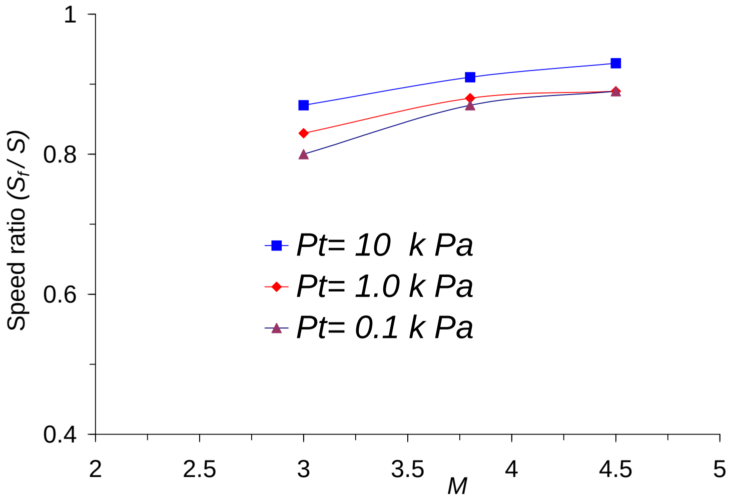

Figure 7.23: Effect of M on speed ratio.

Table 7.5: Summary of numerical experiment for an increase in parameter value.

Parameter	Load	Torque	Speed ratio
Blanket height	Increase (225%)	Increase (275%)	Decrease
Feed force	Increase (14%)	No change	Increase
Young's modulus	No change	No change	No change
Tensile stress	Increase (16%)	Increase (25%)	Increase
Critical state slope	Increase (12%)	Increase (20%)	Increase

Table 7.5 summarizes the sensitivity analysis on the effect of increasing the influencing parameter. Overall, the maximum change in speed ratio was within 5%, while

the corresponding change in roll load and torques was substantial as seen in the Table. The quantitative estimates in the above table should be read carefully, for e.g., when the blanket height is increased say from 60 mm to 100 mm, the corresponding increase in load and torque vaues are more than 200%. Similarly, the other parameter effects are for the range indicated in Table 7.4. The comparison for M value is restricted in the range $3.8 < M < 4.5$. As the above changes in load and torque are observed only in the selected range of parameter values, it can not be extrapolated beyond this range.

7.8 Flat roll mill experiments

The comparisons of numerical prediction of roll loads and torques of two-roll grooved surfaces with experimental values, are better by within 40% at low compression ratios, but at higher compression ratios the predictions are poor. One of the reasons for this may be due to the over simplification of groove effects that affects largely at higher compression ratios. To understand this effect, an experiment was conducted using two circumferentially flat rolls.

7.8.1 Flat roll mill experimental plan and input conditions

Mill experiments using flat rolls were carried out similar to the grooved roll experiments, but for the flat roll experiments the initial blanket condition was varied for each compression ratio. Different initial conditions were achieved by having different combinations of feed height, and cane mass. These combinations minimise experimental errors compared to using a few fixed settings. For the flat roll experiments, prepared cane was sourced from a local sugar mill. The different combinations of feed height, and cane mass were adapted for the compression ratios 1.5, 1.25 and 3.0. Due to this, every experiment was unique for the numerical analysis. Two trials were repeated to get reasonable average estimates. Other experimental parameters used are given in Table 7.6.

The experimental plan, and the mill input parameters are indicated in Fig. 7.24, and in Table 7.7 respectively. For the flat roll simulation, elastic and frictional properties and the permeability response were retained from two-roll grooved simulations. As the initial conditions for each compression ratio for the selected roller speed is unique, the numerical simulation should also account for these initial conditions. Two trials were repeated to get reasonable average estimates.

Table 7.6: Parameters for the two roll (flat) mill experiments.

Parameters	Value
Cane source	From CSR Invicta Sugar Mill
Cane variety	Q124
Preparations	Mill preparation
Fibre content	17.22 % (Average)
Mass of cane	8.30-21.55 kg
Roll diameter	750 mm
Roll length	225 mm
Roll surface speed	150 & 300 mm/s

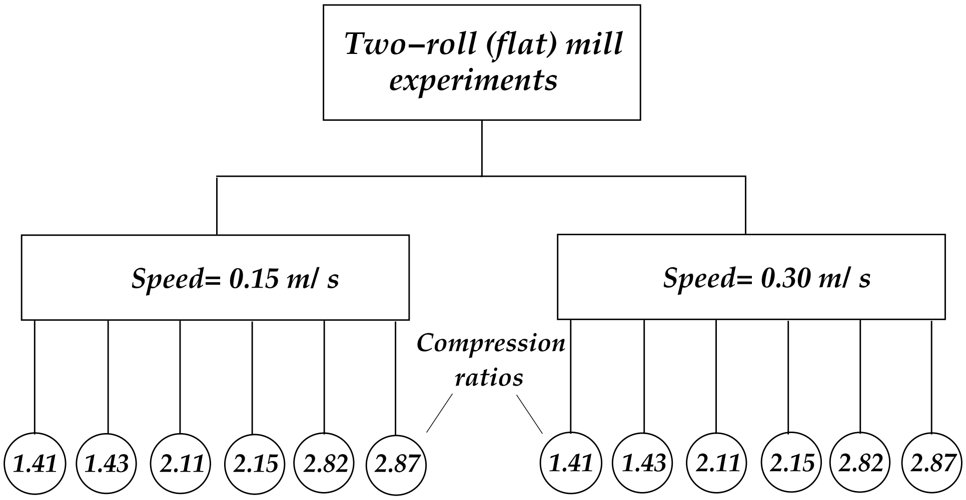

Total number of tests = (2 speed) x (6 compression ratios) x (2 repeat) = 24

Figure 7.24: Two-roll (flat) mill experimental scheme.

Table 7.7: Two-roll (flat) mill operating parameters.

Roll	diameter	750	mm
Fibre	density	1530	kg/cu.m
Trial 1	& Trial 2		

S. No	Ju. Den kg/cum	Ca. den kg/cum	Fib.ratio %	Cane Ma kg	No gas ht mm	Wo.Op mm	Mill C. Ratio	Cont,ang degree	Feed Ht. mm	Initial C. Ratio	Initial V. Ratio	Speed m/s
1	1090	1147	17.13	8.30	35.73	25	1.41	9.70	80	0.45	16.45	0.15
2	1072	1130	17.22	10.00	43.68	30	1.43	10.96	80	0.55	13.40	
3	1090	1147	17.13	10.14	43.67	20	2.11	14.43	80	0.55	13.27	
4	1072	1130	17.22	15.53	67.88	30	2.15	18.29	110	0.62	11.74	
5	1090	1147	17.13	13.85	59.63	20	2.82	18.71	100	0.60	12.06	
6	1072	1130	17.22	21.55	94.18	30	2.87	23.88	155	0.61	11.94	
7	1090	1147	17.13	8.30	35.73	25	1.41	9.70	80	0.45	16.45	0.30
8	1072	1130	17.22	10.00	43.68	30	1.43	10.96	80	0.55	13.40	
9	1090	1147	17.13	10.14	43.67	20	2.11	14.43	80	0.55	13.27	
10	1072	1130	17.22	15.53	67.88	30	2.15	18.29	110	0.62	11.74	
11	1090	1147	17.13	13.85	59.63	20	2.82	18.71	100	0.60	12.06	
12	1072	1130	17.22	21.55	94.18	30	2.87	23.88	155	0.61	11.94	

7.8.2 Issues in the numerical modelling of flat-roll milling

For the finite element simulation, the pore pressure boundary condition on the outer blanket is assumed to be zero. The assumption of zero pressure condition for the grooved roll simulation may be a reasonable judgement due to the drainage of juice at groove roots. For a flat roll numerical simulation, it is difficult to impose a non-drainage boundary condition at the roll surface-blanket interface. This may affect the feeding of the material numerically, but in the experiment the actual feeding may be affected by poor frictional contact.

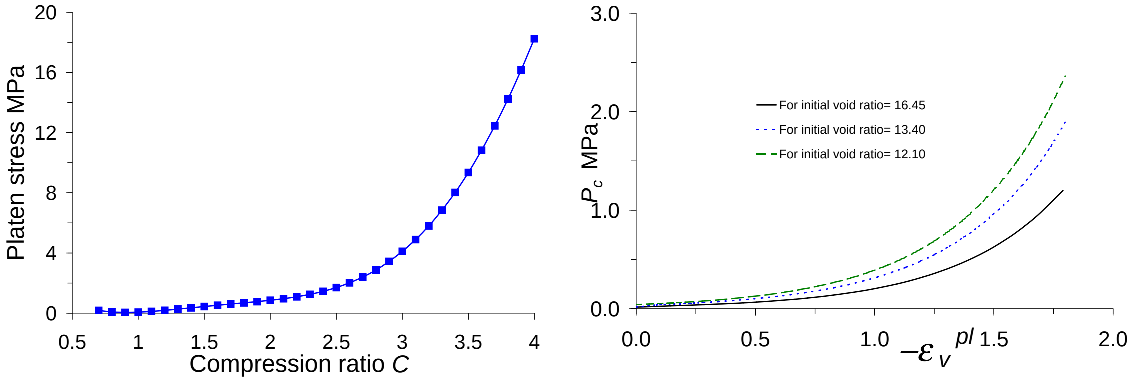

Figure 7.25: Flat platen response, and strain hardening responses for different initial conditions.

The plastic strain hardening relation for the flat roll was estimated from the flat platen's quasi-static response conducted at 1 mm/min (Fig. 7.25). For different initial void ratios of the blanket, the appropriate form of hardening relation was to be used in the mill simulation. The calibrated hardening relation was adjusted to different initial void ratios as per the relation given in Eq. (7.12).

7.8.3 Numerical modelling results

A pair of counter rotating rolls has been simulated assuming 2-D plane strain was carried out for the twelve different cases (Table 7.7) at two roll speeds namely at

0.15 m/s and at 0.30 m/s. The predicted results are compared in Fig. 7.26 with the experimental values. The experimental flat roll mill loads and torques are much lower than the grooved roll mill experimental values at all compression ratios. This is mostly due to insufficient friction encountered by the blanket with the flat rolls, resulting in poor feeding. Interestingly, the flat roll load and torque predictions match well with the experimental values at all compression ratios. For friction factor values below 0.5, the numerical simulations has shown non-feeding or slipping of the blanket with the roller.

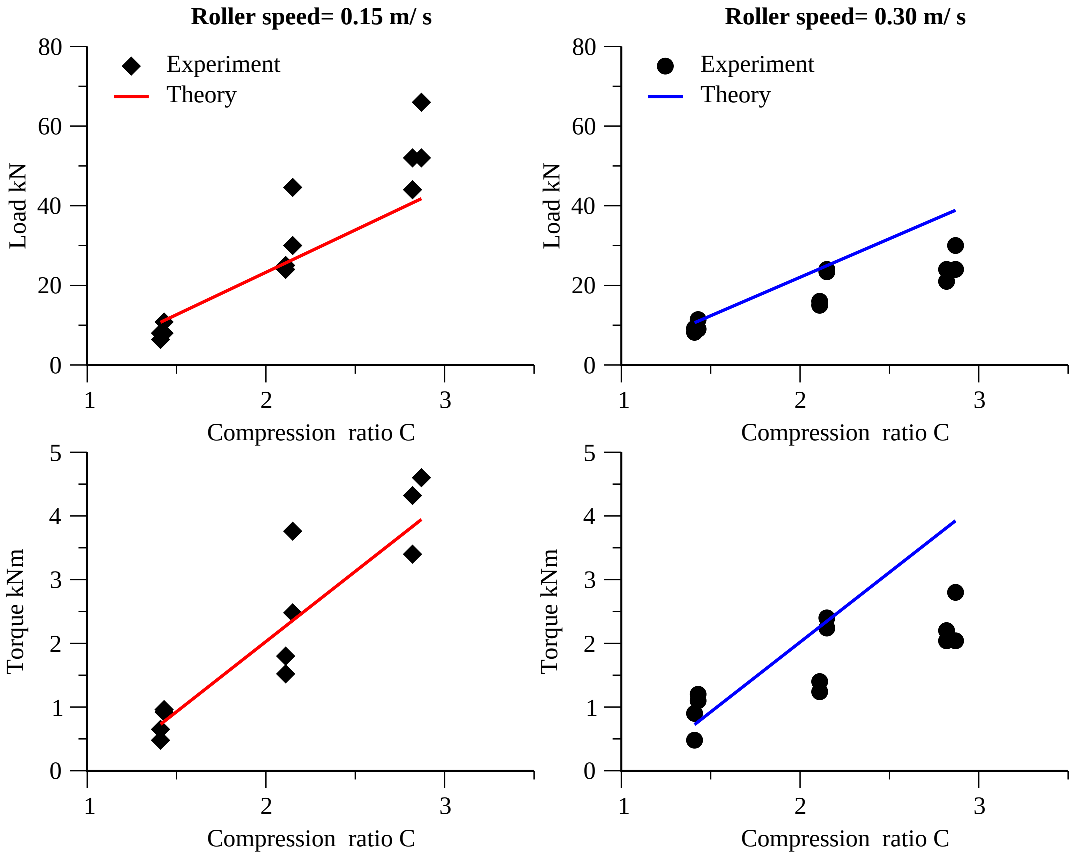

Figure 7.26: Comparison of roll load and torque at speeds 0.15 & 0.30 m/s.

For the flat-roll tests, the cane with relatively a higher fibre content, namely at 17.22% was used. Higher fibre cane is likely to cause much stiffer platen load response for both flat and groove profiles. However, the bagasse penetration for a grooved platen is likely to be less for a higher fibre cane than for a low fibre. This may result in a much harder plastic strain response for a grooved platen. In this regard, had this cane been simulated for a grooved roll-mill, the numerical simulation is likely to predict higher roll loads and torques than for a flat-roll mill at the same compression ratio.

In this experiment, other than measuring the vital milling outputs, the feeding velocities of the blanket were also measured using a technique known as Image Tensor Analysis (ITA). ITA is an imagery technique that can track the motion of a body through space and time.

The ITA procedure (Britton, 2001) involves taking video footage of the moving blanket through a transparent window slot. The video footage is decomposed into a series of adjacent images, separated by known time intervals. A particle-tracking algorithm is employed to track particles in the cane and store the location of each particle spatially at all available times i.e. the location of each particle in each frame of the video.

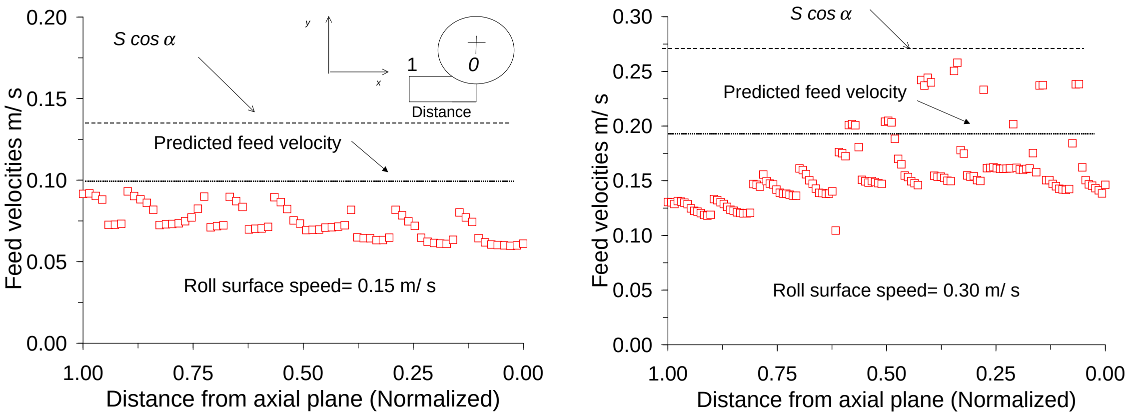

Figure 7.27: Measured x-velocities at $C=$ 2.82 for roller speed 0.15 & 0.30 m/s.

The experimentally measured feeding of the material shows that the material was not feeding at $S \cos \alpha$ as shown in Fig. 7.27. The predicted feeding velocities shown in Fig. 7.28 are also not up to $S \cos \alpha$. Different reasons are attributed to poor feeding velocities in the numerical prediction and in the measurement. This has previously been explained in Section 7.8.2.

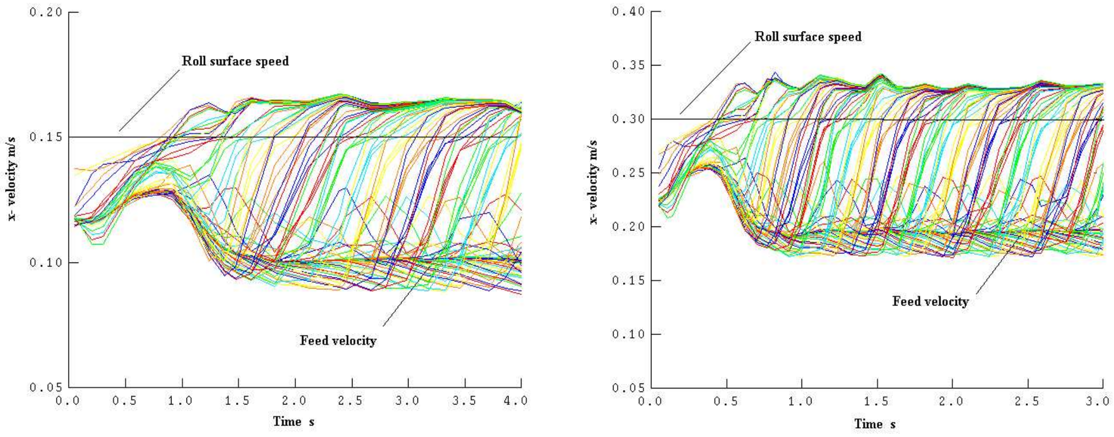

Figure 7.28: Predicted feed velocities at $C= 2.82$ for roll speed 0.15 & 0.30 m/s.

7.9 Conclusions

A pair of counter rotating rolls has been simulated assuming two-dimensional plane strain. Experiments on both grooved and flat roll surfaces have been conducted and the results are compared from appropriate numerical simulations. Both the grooved roll and flat roll experimental programme uses the experimentally determined material properties and a proper form of permeability response. A parametric study on the sensitivity of the numerical model was also conducted and the results are presented.

The initial prediction of roll loads and torques in grooved roll programme was far from satisfactory especially at higher compression ratios (above $C = 1.5$). Material feeding behaviour was suspected for this, and a soft contact relation at roll surface-blanket interface gave the required feeding. However, the roll torque was still at unsatisfactory level. This has been assigned largely due to oversimplification of groove details. Hence, a flat roll experimental programme was carried out to verify this.

A detailed experimental programme on a flat roll surface was carried out in the compression ratio range $1.4 \sim 3.0$. The numerical model and the measurements gave the feeding much less than the required $S\cos\alpha$. Different reasons are attributed in the prediction and measurements. However, the prediction of roll loads and torques matched well, as the stress levels associated with grooves are irrelevant to the flat roll surface. It is apparent that the stress levels that exist between the groove tips and roots might have been largely responsible for the poor prediction of torque level in the two-dimensional plane strain grooved model. This has been further probed in the following chapter through a three-dimensional model.

Chapter 8

Three-dimensional simulation of rolling

8.1 Introduction

The two-roll computational model explained in Chapter 7 depicts the roll surfaces as circumferentially flat rolls with symmetry about the centre of blanket. However, when it comes to modelling roll surface with grooves, the top and bottom rolls are aligned tip to base and base to tip, hence the symmetry of single roll assumption is lost especially at smaller blanket thickness. This non-symmetry is much more significant at negative set-openings. This chapter explains the application of coupled porous media theory, to capture grooving effects through three-dimensional modelling. The experimental mill's 35° groove geometry was modelled by three-dimensional surfaces of revolution.

8.2 Three-dimensional surfaces of revolution

To define a rigid surface of revolution in a model, two points A and B shown in Fig. 8.1 are specified along the axis of rolls that define the local coordinate system. The coordinates of these points (X_A, Y_A, Z_A) and (X_B, Y_B, Z_B) are defined in the default global coordinate system. Point A defines the origin of the local system and the vector from A to B defines the local y-axis, which is the axis of a cylindrical coordinate system. The line segments forming the profile of the surface of revolution (groove geometry in this case) are defined in the local x-y plane, where the local x-axis aligns with the radial axis of the cylindrical coordinate system. The three-dimensional surface is formed by revolving a half symmetry 35°groove profile about the axis of the cylindrical system, i.e. the local y-axis.

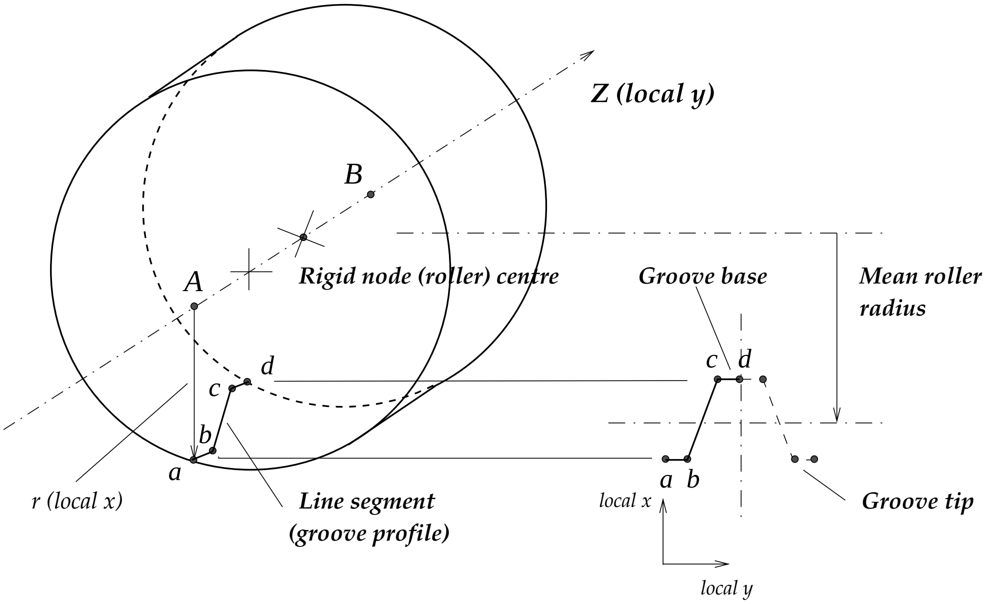

Figure 8.1: Three-dimensional formation.

8.3 Input parameters in three-dimensional simulation

It may be recalled that even at the minimum compression ratio used in the two-roll mill experiments, the set opening was a negative value. Numerical modelling with negative set opening in three-dimensions is more complicated from a mesh distortion point of view. Further, ABAQUS has no rezoning facility for three dimensional pore pressure elements.

Theoretically, positive set openings may be assumed to achieve the same compression ratios that prevail at negative set openings, by suitably increasing blanket heights. Increase in blanket thickness causes the contact angle to increase and hence the increased contact frictional area may result in an increase in the feed. However, it was noticed from the parametric sensitive study, for an increased blanket height the feeding velocity was found to be slightly lower (Fig.7.5). The quantitative feeding assessment in this case is difficult to estimate.

Table 8.1 shows the input parameters that were used in the numerical simulation for positive set openings. The initial void ratio for three-dimensional modelling was kept same as in the two-dimensional model. While modelling the true groove geometry in the three-dimensional simulation, the inverse-calibrated strain hardening response of compression between flat platens is used. The results from three-dimensional simulation generally produced higher loads and torques compared to flat roll simulation where the groove effects are "built into" the plastic strain hardening.

Table 8.1: Blanket parameters used for 3-D simulation.

Mass of cane (kg)	**No gas height** (mm)	**Blanket height** (mm)	**Work opening** (mm)	**Compression ratio** (C)
17.8	80.8	141.7	45.0	1.5
22.5	102.1	179.2	40.0	2.0
27.5	125.0	219.0	30.0	3.0

The three-dimensional roll torques were found to be higher than the two-dimensional values by a greater margin similar to the observation made by Adam (1997). The reason for this as given by Adam is that the confined compression tests used for inverse-calibration only consists of compression normal to the grooved surface, with no tangential component. This implies that the effect of grooves on roll torque may be more significant than the effect on roll load.

8.4 Results from three-dimensional analysis

Figure 8.2 shows the deformed mesh for typical three dimensional roll groove accounting for existing non-symmetry between top and bottom rolls. The rolls are not shown for clarity. The differential compression of top roll groove tip on the blanket is clearly visible. In the corresponding plane, the bottom roll's groove base produced lesser penetration and hence lesser compression. An ABAQUS programme for three-dimensional roll groove simulation is given in Appendix D.

The vertical compressive stress is shown in Fig. 8.3(a) at compression ratio $C =$ 3.0, and for the corresponding input parameters, the void ratio contours are shown

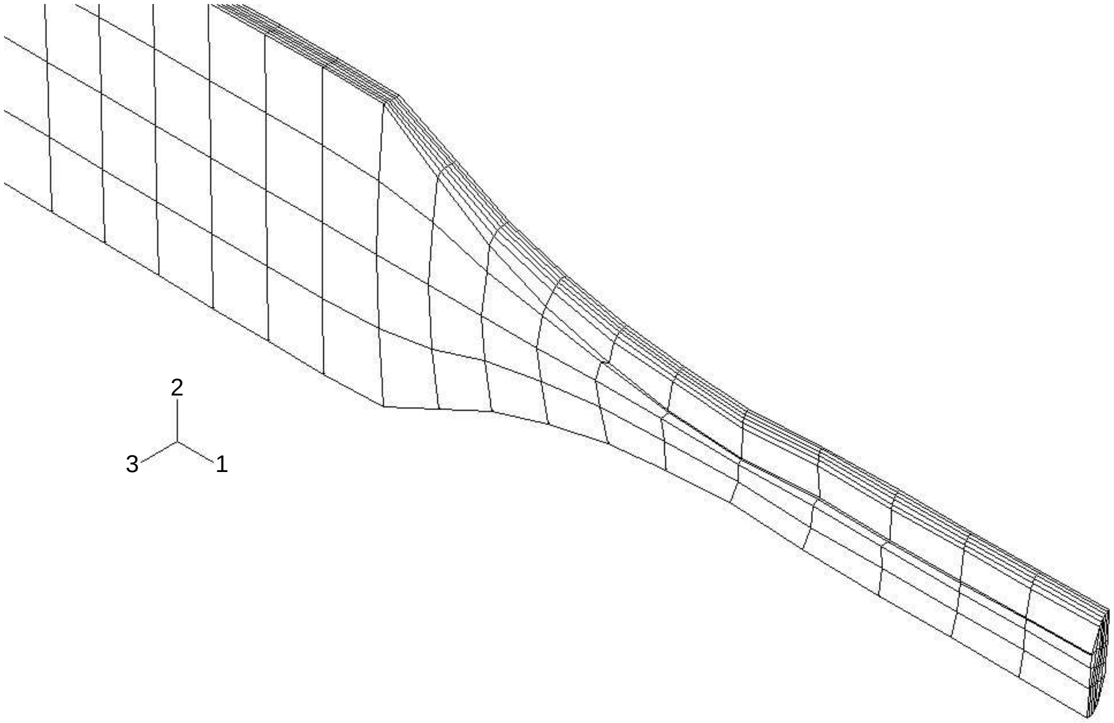

Figure 8.2: Blanket in 3-dimensions (25 x 4 x 6= 600 elements).

in Fig. 8.3(b). The uncompacted and compacted material region is evident around the tip region of grooves. The penetrated material to the groove base is at relatively high void ratio.

The advantage of three-dimensional simulation is that the interior blanket condition can also be assessed from sectional views. Figure 8.4(a) for example, exposes void ratio contours in the middle plane of the blanket. In this middle plane, the groove has produced a lesser impact on void ratio. Visible changes occur only on material close to the groove profile. The extent of high pore pressure concentration area at the blanket core is shown in Fig. 8.4(b).

The velocity vectors of the liquid juice and solid fibres are seen separately in Fig. 8.5. The higher void ratio region that prevails at the entry to the mouth of the mill is relatively uncompacted, hence the juice flows more easily in this region, but inhibits the feeding of incoming fibre.

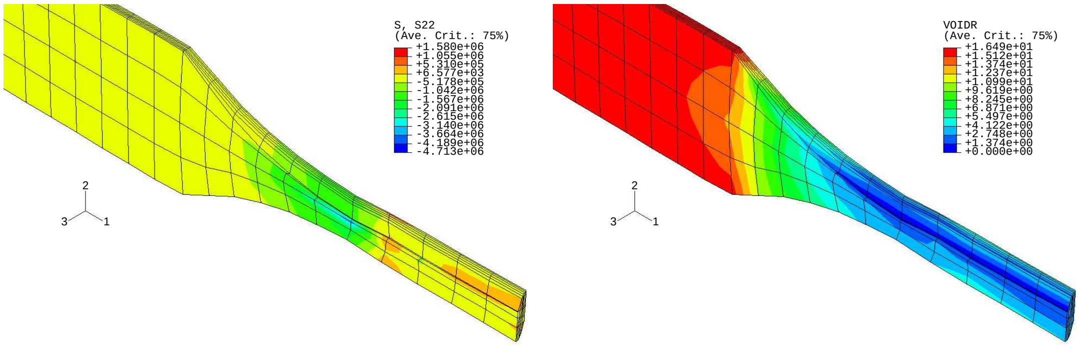

(a) Vertical stress (b) Void ratio

Figure 8.3: Stress and void ratio at C= 3.0.

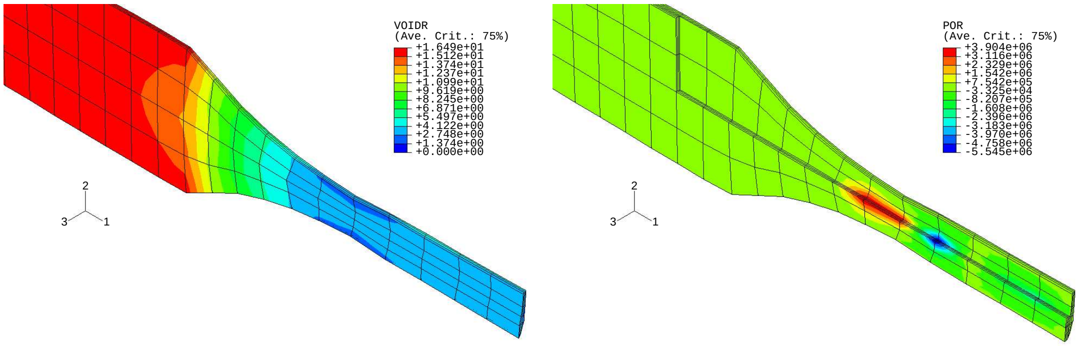

(a) Void ratio in the middle plane (b) Pore pressure in the core

Figure 8.4: Void ratio and pore pressure in inner blanket at C= 3.0.

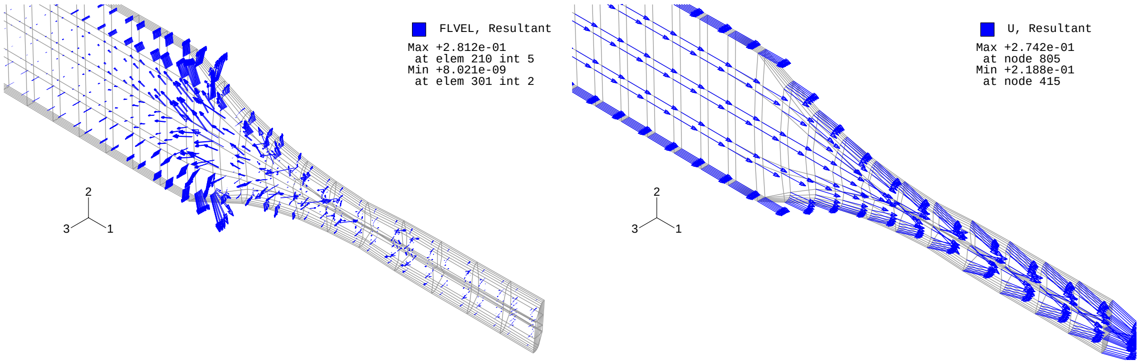

(a) Juice velocity vectors (b) Fibre velocity vectors

Figure 8.5: Juice and fibre velocity vectors for a 3-D blanket.

8.4.1 Roll load and roll torque in a three-dimensional modelling

It was pointed out while presenting the two-dimensional results (Loughran and Kannapiran, 2002) that the two-dimensional model ignores side wall friction and the moment required to peel compressed bagasse out of the grooves. These factors will not influence roll load because they are vertically balanced but will affect roll torque. Perhaps of more importance is the fact that the two-dimensional representation ignores the stress concentration of fibre (very low void ratios) around the tip region of grooves (Fig. 8.6).

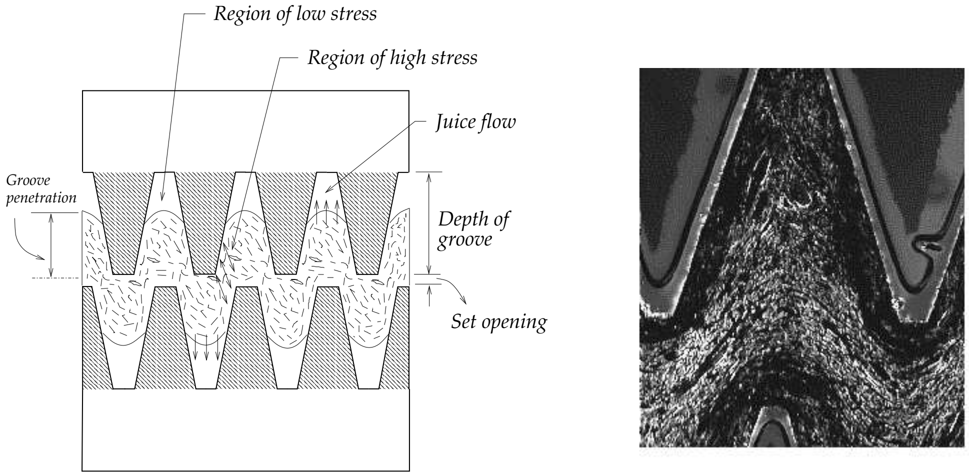

Figure 8.6: Groove penetration and stress variation (Leitch et al., 1997; Vas, 1999).

The predicted torque is strongly influenced by the stress state adjacent to the groove boundary and in hind-sight the two-dimensional model does a poor job of predicting absolute values at high nip compression ratios. It was further suggested that a three-dimensional model which captures the penetration of bagasse into the groove base region may provide better predictions.

Results from controlled uniaxial laboratory experiments (Leitch et al., 1997) suggest that bagasse does not penetrate to the base of the groove under typical milling conditions (Fig. 8.6). The groove penetration is a function of groove geometries and speed of compression. Hence, the actual compression ratio C_c, is higher than the compression ratio C based on mill settings. This has been quantitatively estimated by

Leitch et al. (1997), i.e.

$$C_c = 1.348C - 0.158 \tag{8.1}$$

for 35° grooves across all platen speeds.

The three-dimensional simulation result of roll load is compared with the experimental data of corrected compression ratio (shown by the broken line) in Fig. 8.7. The experimental data were averaged at each compression ratio.

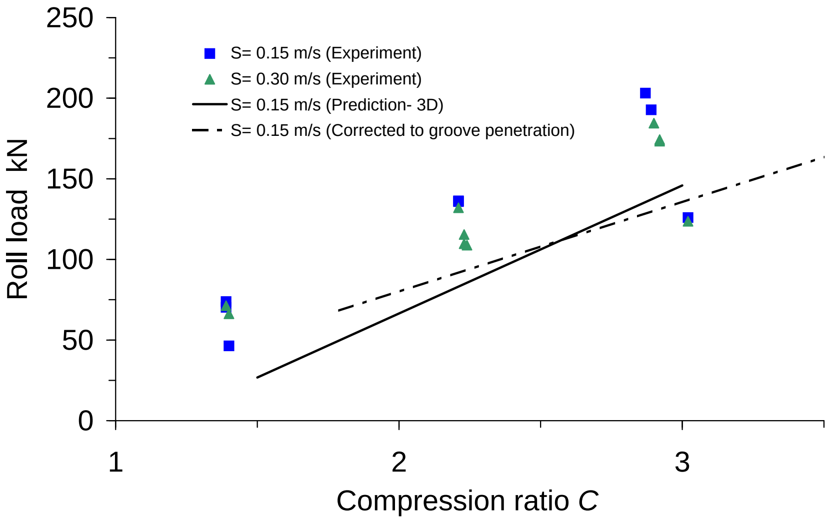

Figure 8.7: Roll loads from 3-D simulation.

As the three-dimensional simulation was carried out with increased set openings but with the same nip compression ratio, the effect of increasing (w_o/D) is to increase crushing rate and corresponding increase roll torque (Murry, 1960a). It was shown theoretically that torque load number N is proportional to the square root of the work opening diameter ratio (w_o/D) and a function of the mill compression ratio C_o. This function was found empirically from experimental mill results (Murry, 1960a) as

$$N = \rho C_o^{\frac{3}{4}} \sqrt{\frac{w_o}{D}} \tag{8.2}$$

where ρ depends on the preparation and roll diameter. The torque-load number N is defined by

$$N = \frac{T_{tot}}{RD} \tag{8.3}$$

and T_{tot} is the total torque for the rolls and R is the roll load. Roll load is simply a function of the average nip compression ratio, and hence is unaffected by increased capacity.

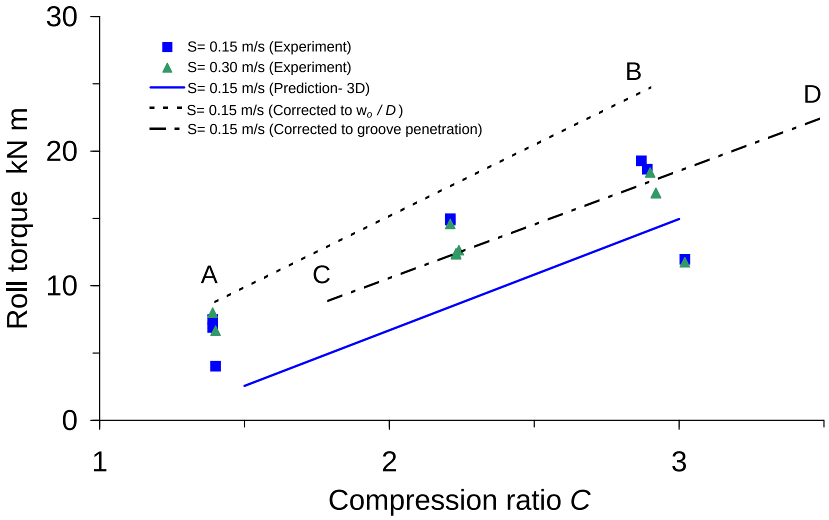

Figure 8.8: Roll torques from 3-D simulation.

The groove penetration and (w_o/D) effects are applied to the torque values of the measured experimental data from Eq. (8.1) and (8.2) respectively. The corrected experimental data for the (w_o/D) effect is shown in Fig. 8.8 as line AB, and to this line, the groove penetration effect was adjusted to line CD. The manipulated experimental data are compared with the simulation result in Fig. 8.8 for roll surface speed of 0.15 m/s. The three-dimensional simulation results compare much better with the experimental values than the two-dimensional response. However, the predicted values are still lower than the experimental values. The actual pore pressure distribution on the roll surface has a maximum and minimum value (Fig. 7.9) which is difficult to impose in the present numerical code. The correction for the (w_o/D) effect may be avoided, if the three-dimensional numerical simulation was carried out with actual work openings.

The effect of mesh density on the predicted response was studied using different numbers of elements, namely at 600, 1200 and 2400 for a nip compression ratio of 1.5. The difference in the steady state values of roll load or roll torque are within 5% for these mesh discretizations. However, this study could not be conducted at higher compression ratios due to convergence problems associated with severe element mesh distortion. Further work in three-dimensional simulation requires adaptive mesh refinement strategies.

It may be noted that the experimental mill had side plates at the minimum opening area. In the numerical simulation, this end effect was not considered. The end boundary condition introduces additional frictional torque in the numerical simulation. The prediction in roll torque values is expected to improve further, if this end effect is accounted for.

8.5 Conclusions

Computational models that assume the rolls as flat with “built in” groove effects (strain hardening response), failed to adequately capture the tangential component of compression. The compression ratios at negative set openings of the experiments were modelled in three-dimensions, as equivalent compression ratios through increased set openings. However, the effect of (w_o/D) on the increased set openings and groove penetration effects were taken into account while comparing experimental data with the numerical results. The three-dimensional model with the flat platen’s strain hardening response, captured high and low compression regions in groove tip and groove base respectively. The roll load as well as roll torque matched much closer with experimental values than the plane strain two-dimensional model. The three-dimensional model results may be used to assess interior blanket characteristics.

Chapter 9

Advanced milling simulations

9.1 Introduction

Sugar mills crush prepared sugar cane, using crushing trains consisting of multi-rolls. For efficient operation of mills, optimum mill settings are the crucial factors. Given the allowable mill roll load and torque, information on mill geometry, limits of work openings and the lowest allowable speed are selected to achieve the given crushing rate. The lowest possible speed is selected since it is well known that juice extraction decreases with increasing roll surface speed. The mill is said to be operating efficiently, if the ratio of work opening at feed to delivery nip is as high as possible, since the maximum amount of power is being used in the delivery pair of rolls. This allows the highest possible operating filling ratio to achieve higher crushing rate (Russell and Murry, 1968). From this perspective, a robust and efficient numerical simulation of multi-roll systems would be useful for optimization purposes. Multi-roll simulations have been demonstrated previously by Adam (1997) and Kent and Edwards (1994). This chapter extends the application of coupled porous media theory explained in Chapter 6 to a multi-roll system.

9.2 Geometry of a three-roll mill

A schematic diagram of a three-roll pressure feeder is shown in Fig. 9.1, and the configured dimensions are given below.

Pertinent nomenclature in Figure. 9.1 are

D = mean roll diameter

L = roll length

h_f = height of feed chute at feed rolls

α_a = angle of contact between feed chute and rolls

w_f = work opening at feed nip

w_d = work opening at delivery nip

S = roll surface speed

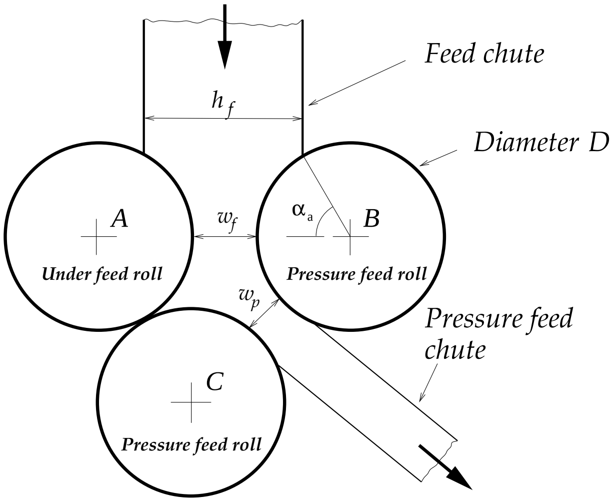

Figure 9.1: Geometry of a three-roll mill pressure feeder.

The above figure shows the precompressing stage of a six-roll mill. The compression ratio (C) at the feed entry is described similar to a two-roll mill,

$$C = \frac{h_{ng}\ \cos \alpha_a}{w_f} \tag{9.1}$$

If the fibre rate Q_f is known, the filling ratio (F_r) for the feed nip is given by

$$F_r = \frac{Q_f}{w_f S L \rho_f} \tag{9.2}$$

where ρ_f is the density of fibre. A similar relationship applies to the delivery nip. The crushing rate ($\dot{q}$) in a mill test with a block length l_b is expressed by the following relationship.

$$\dot{q} = \frac{\text{Cane weight x } S \cos \alpha_a}{l_b} \tag{9.3}$$

The location of rolls may be fixed based on the dimensions of roll diameters and work openings. The centre to centre distance of rollers is calculated by the following relationships.

$$a = w_d + \frac{1}{2}\left(D_2 + D_3\right) \tag{9.4}$$

$$b = \frac{1}{2}\left(D_2 + D_3\right) \tag{9.5}$$

$$c = w_f + \frac{1}{2}\left(D_1 + D_2\right) \tag{9.6}$$

In the above, no effective work opening between under feed and bottom pressure feed roll is assumed. The angle α (Fig. 9.2) for example is known from the following relationship :

$$\alpha = \cos^{-1}\left(\frac{b^2 + c^2 - a^2}{2bc}\right) \tag{9.7}$$

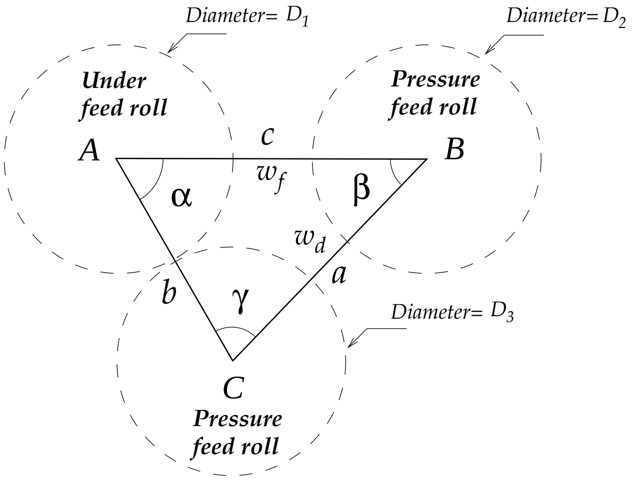

Figure 9.2: Geometrical relationship.

9.3 Three-roll mill crushing simulation and results

A three-roll crushing system was modelled as a demonstrative example using typical input parameters. A six-roll simulation is much more complicated, however it can be modelled based on the steps followed for a three-roll by adding another set of three rolls (similar in configuration) which takes the output from the first set of three rolls. The parameters used for a three-roll simulation are shown in Table 9.1.

Table 9.1: Parameters used for three-roll simulation.

Parameter	Values
Roll diameters	Feed rolls= 950 mm Bottom Pr. feed roll= 920 mm
Groove profile	From two-roll mill (Table 3.1)
Work openings	Feed nip= 375 mm Pressure feed nip= 175 mm
Roller speed	300 mm/s
Initial compaction	90 kg/m^3 (Void ratio= 16.0)
Height of feed chute	680 mm (Fig. 9.1)
Fibre ratio	13%
Crushing rate	350 tonne/hr

Unlike a two-roll system, no symmetry exists for modelling the three-roll system (Fig. 9.1), hence the entire geometry must be considered in the simulation. The three roll model assumes the rolls as flat cylindrical surfaces and the work openings are estimated from groove depths and set openings (Eq. 2.19). The roll surface speed were kept the same for all rolls. The boundary conditions between the blanket and rolls are assumed similar to the two-roll case, i.e. porous boundaries on roll surfaces.

The three roll simulation was modelled as plane strain. The effect of groove geometry is accounted for through the strain hardening relationship (see Section 5.5.7). Typical roll load and roll torque traces at steady state are given in Fig. 9.3. The resultant loads of individual rolls must be calculated from horizontal and vertical components of load. The major loads are shared by the top and bottom pressure feed rolls. The loads and torques of the under feed roll are almost negligible.

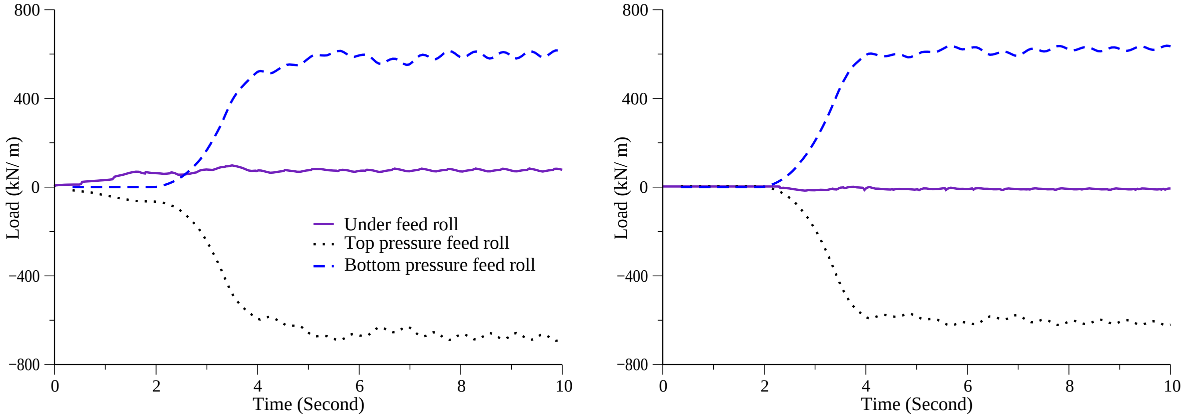

x- Component of roll loads

y- Component of roll loads

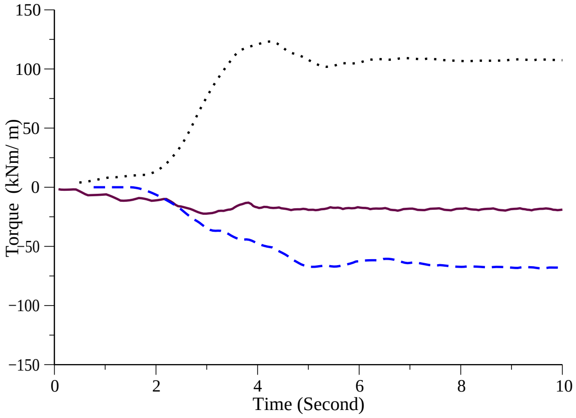

Roll torques

Figure 9.3: Roll load and torque traces for a three roll mill.

The vector plot of Fig. 9.4, shows the maximum principal stresses to be compressive and predominantly perpendicular to the direction of blanket travel. Though these compressive stresses are shared by the pressure feed rollers, the top pressure feed roll encounters more blanket contact area, and plays a more dominant roll in compressing the blanket. Consequently the top pressure feed roll torque value is found to be higher than the bottom pressure feed roll. The compaction of fibres at the pressure feeder nip is about 250 kg/m^3 (up from about 90 kg/m^3 at the base of the hopper).

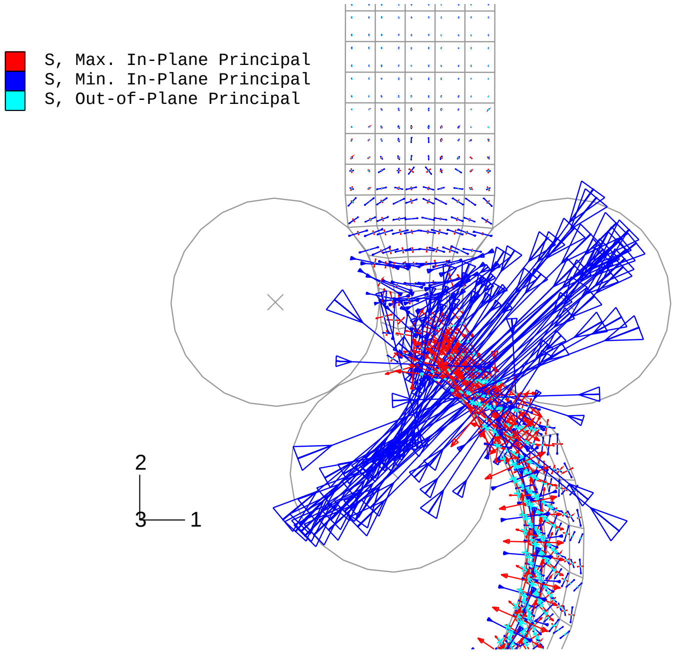

Figure 9.4: Principal stress vectors.

As in the two roll case, the juice velocities near the mouth of the mill were found to be higher than at nip as seen in Fig. 9.5(a). The juice velocities exhibit a symmetrical velocity distribution at the blanket entry, however the symmetry is lost when the fibre enters the pressure feed rollers. The moving fibre direction and its velocity vectors are shown in Fig. 9.5(b).

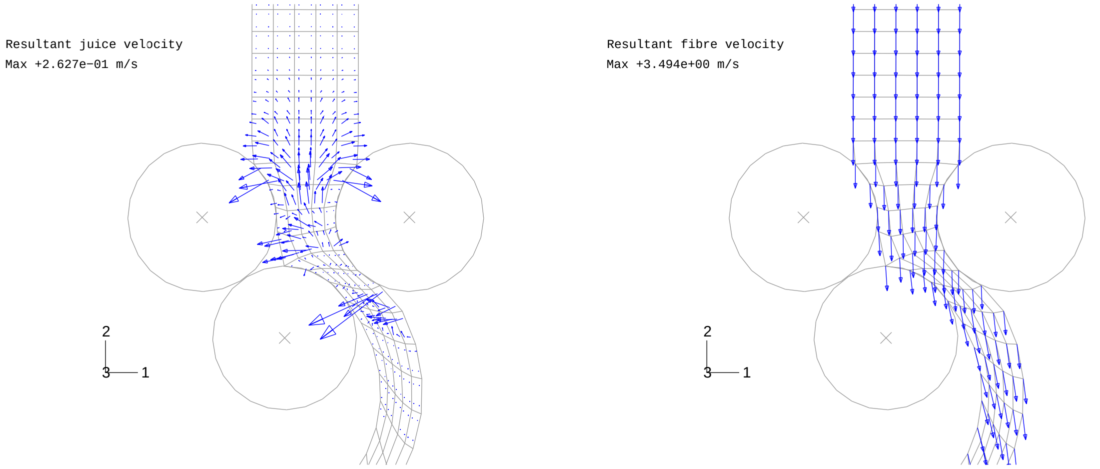

(a) Juice velocity vectors

(b) Fibre velocity vectors

Figure 9.5: Juice and fibre velocity vectors for a 3-roll.

9.3.1 Rezoning during three-roll simulation

In multi-roll modelling, more frictional contact area is involved with rolls and blanket, and the material undergoes more intense irreversible deformation. Numerically, this introduces severe mesh distortion. The frictional contact may be addressed through proper frictional characteristics, and the mesh distortion through rezoning.

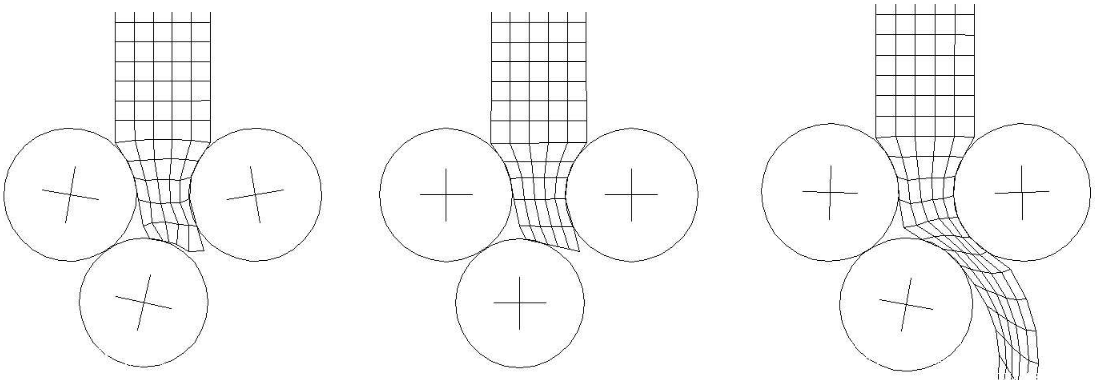

(a) Deformed mesh

(b) Rezoned mesh

(c) After rezoning

Figure 9.6: Adapted mesh for rezoning.

As a sample demonstration, a rezoning procedure was attempted similar to the procedure applied to two-rolls. Figure 9.6 shows the various stages of rezoning procedure for a three-roll simulation. Figure 9.6(a) indicates the distorted mesh that requires refinement before proceeding to further computation. The mesh is refined as shown in Fig. 9.6(b) and the computational results from the previous step is now adjusted to this new mesh. The computation continues from this point as indicated in Fig. 9.6(c). If required this procedure may be repeated further. The severe mesh distortion which is typical to three-roll modelling can be rezoned as and when the quality of the mesh is deteriorating. No attempt was made to rezone for a high pressure feed nip compression, however the same procedure is followed for such situation.

A sample programme in ABAQUS for a three roll crushing simulation is given in Appendix C. The developed program may be used to study the effect of different operating parameters. For example, the effect of different diameters, roll surface speeds, and work openings can be studied on an operating mill. The ABAQUS programme includes a subroutine that was written to view derived outputs like volumetric strain, compaction, and compression ratio in post processing.

9.4 Conclusions

The simplified two-roll computational model was extended to a multi-roll system. The multi-roll system was demonstrated mainly to explore its applicability to crushing units in actual milling trains. For the typical input parameters used in the multi-roll modelling, the roll load and roll torque values are found in the expected range. Unlike in a simplified two-roll system, no symmetry in the multi-roll geometry can be found. As the material undergoes more bending and rotation, computationally this introduces severe mesh distortion. However, for a two-dimensional plane strain approach this was handled suitably through rezoning techniques. Using appropriate inputs in the multi-roll crushing models, optimized mill operating parameters could be achieved in conventional multi-roll mills.

Chapter 10

Conclusions

10.1 Introduction

This thesis presents recent advances in modelling of crushing prepared sugar cane. The present knowledge of extracting juice from prepared cane has come through extensive experimentation and through application of modern mathematical and computational tools. Relevant theory covering sugar cane crushing is described in Chapter 2.

The guidance to the physical and finite element modelling of the crushing process is mainly based on the PhD work of Zhao (1993) who formulated the fully coupled model. Adam (1997) extended the model to include a range of isotropic critical state constitutive laws for the fibre skeleton. This thesis uses these formulations and specifically validates the numerical results with the experiments carried on a special two-roll mill, using cane that has also passed through a series of basic property tests. This thesis further addresses the numerical issues of mesh distortion at large strains, and accounts for the roll groove geometry effects in three dimensions.

10.2 Basic property tests and two-roll mill experiments

Experiments were conducted for determination of basic property data needed for computer simulation. A uniaxial test-cell with flat and grooved platens and a permeability test cell were used to conduct the experiments. Two cane varieties designated Q124 (Soft) and Q117 (Hard) at two preparation levels were used in the experiments. In addition, a series of two roll mill experiments were used to validate models.

10.2.1 Quasi-static uniaxial tests

Quasi-static compression tests (Chapter 3) were conducted at slow speed to isolate the solid matrix constitutive behaviour from juice pressure effects. The plastic strain hardening relations for the fibrous skeleton were determined by inverse calibration from finite element simulation of confined uniaxial test cell data (Chapter 5). Both flat and grooved platen responses were determined in these experiments. The other constitutive properties of the solid matrix of fibrovascular bundles were made available from reported uniaxial, triaxial and shear box tests.

10.2.2 Permeability responses

Permeability is a measure of the ease with which liquid flows through a porous material and is governed by Darcy's law. The permeability responses for the canes that were used in the experimental mill program were determined on a standard permeability test cell apparatus. Experimentally determined permeability responses are compared with other available experimental data (Chapter 4).

At the low compression regime (compression ratio less than about unity), it maybe assumed that the prepared cane blanket is partially at saturation. Between a compression ratio of unity and 1.5 the blanket is saturated and possibly dominated by "seepage induced consolidation". Reliable experimental data in these regimes is difficult to obtain. In this thesis we follow the approach mooted by Adam and Loughran (1998) where for partially saturated cane the permeability was increased over that measured by two orders of magnitude. In the "seepage induced consolidation" regime the permeability was increased four times of magnitude. For the remainder of the compression regime measured, the measured permeability was used.

10.2.3 Two-roll mill experimental results

The finite element simulation of the two-roll mill was undertaken with the ABAQUS nonlinear code using initially a plane strain approach. Three compression ratios of 1.5, 2.5 and 3.5 were used. The initial predictions of roll loads and torques were poor especially at higher compression ratios ($C > 1.5$). Close scrutiny of the numerical solution showed that the cane did not feed into the roll system at the expected feed velocity ($S \cos \alpha$), regardless of friction specification. However, the adoption of a soft contact relation at roll surface-blanket interface alleviated the problem (i.e. feed velocities were approximately $S \cos \alpha$). With soft contact, numerical prediction of roll loads matched within 30% with experimental values, but the predicted roll torque level was lower by 60%. This was regarded largely due to oversimplification of groove details.

10.3 Flat roll experiments

To further explore the grove boundary condition, an experiment was conducted using two-circumferentially flat rolls. A detailed experimental programme on a flat roll surface was carried out over the compression ratio range 1.4~3.0. Numerical simulation of this experiment was run with a strain hardening relation determined from uniaxial experiments with flat but porous platens.

Neither the numerical model nor the measured feed velocities match the $S \cos \alpha$ requirement. In the experiment, feeding was affected by poor frictional contact between the blanket and flat roll surface. In the numerical model, a non-drainage boundary condition at the roll surface-blanket interface was considered appropriate. However, it was difficult to impose a moving boundary condition in the ABAQUS code and in this instance a zero pore pressure boundary condition was assumed as in the groove model. This may have resulted in poor feeding in the prediction. However, the numerical prediction of roll loads and torques matched well, as the stress levels associated with grooves are absent for the flat roll surface. Hence, it is believed that the stress levels that exist between the groove tips and groove base (which are in the third dimension, not considered in plane strain models) might have been responsible for the poor predictions of torque levels in the two-dimensional groove model.

10.4 Rezoning studies

A limitation of the existing numerical model is that elements distort at large strains and since the modelled is implicit convergence of solution is compromised. The large strains associated with highly deformable porous material and complex milling geometry, introduce severe element distortion in the Lagrangian model where the mesh moves and is attached with the highly deformable solid material. The distorted mesh no longer provides a good discretization in the numerical calculation. The solution to this problem is to map the current solution to a revised mesh and continue the analysis. ABAQUS has a mesh generating facility for such situations. External mesh generation was also attempted by concentrating higher mesh densities in a region where steep gradients in the results were expected. Results are given for remapping in plane strain.

10.5 Three-dimensional simulation of grooves

The two-dimensional plane strain model assumes the roll surface can be modelled as a flat single roll symmetric with the centre of blanket. However, with groove geometry the top and bottom rolls are aligned tip to base and base to tip, and the symmetry employed for a single roll cannot be used. The deviation from symmetry is more severe for smaller blanket thicknesses and at negative set openings. Modelling the actual mill settings with anticipated severe element distortion in three dimensions is a difficult task from a convergence and computational point of view. However, if the conditions are scaled to have a positive set opening with an equal compression ratio, element distortion is minimized around the groove tip and a solution can be achieved. The effect of (w_o/D)

on the increased set openings and groove penetration effects were taken into account while comparing experimental data with the numerical results. The three-dimensional model with the flat platen's strain hardening response, captured the high and low compression regimes in and around the groove tip and groove base respectively. The roll loads and torque of the three-dimensional computer model matched well with the experimental values. The steady state feeding velocities in three-dimensional modelling was at the required feed velocity at all compression ratios conducted (up to $C = 3.0$). An advantage of three-dimensional modelling is that interior blanket characteristics can be scrutinised. However, the solution time for three-dimensional computation took nearly two hours, where as the corresponding problem in plane strain simulation was solved in 10 - 15 minutes.

10.6 Demonstration of three-roll mill simulation

The plane strain two-roll numerical simulation was extended to a multi-roll system to demonstrate its applicability in actual mills. The complexity involved in three-roll modelling is discussed, and the mesh distortion associated with multi-roll simulation is successfully handled through a rezoning or remeshing procedure.

References

C. J. Adam. Application of computational porous media mechanics to the rolling of prepared cane. PhD thesis, James Cook University, 1997.

C. J. Adam and J. G. Loughran. Application of computational mechanics to rolling of a saturated porous material. In Proc. of the sixth international conference on Numerical Methods in Industrial Forming Processes, Enschede (Netherlands). Numiform '98, 1998.

C. J. Adam, J. G. Loughran, and D.R.J. Owen. Large strain analysis of a porous elasto-plastic material. In S. Valliappan and N. Khalili, editors, Proc. of the second China-Australia symposium on computational mechanics. Australian association for computational mechanics, 1997.

John Atkinson. The mechanics of soils and foundations. McGraw-Hill Book Company, 1993.

T. E. Braddock. The coefficient of friction between prepared cane and metal surfaces. B. Eng thesis, University of Queensland, 1963.

A. M. Britto and M. J. Gunn. Critical state soil mechanics via finite elements. Ellis Horwood Limited, 1987.

Paul Britton. Image tensor analysis (Personal communication). On going PhD studies, James Cook University, 2001.

K. J. Bullock. An investigation into the crushing and physical properties of sugar cane and bagasse. PhD thesis, University of Queensland, 1957.

R. D. Cook. Concepts and applications of finite element analysis. John Wiley & Sons, 1974.

W. R. Crawford. Reabsorption- A limiting factor in mill performance. In Proc. of I.S.S.C.T, 10, 1959.

R. N. Cullen. An investigation of the shear strength of bagasse. Master's thesis, University of Queensland, 1965.

E. A. De Souza Neta, S. Y. Zhao, D.R.J. Owen, D. Peric, and J. G. Loughran. Finite element simulation of the rolling and extrusion of multi-phase materials. In Proc. of the fifth International Conference on Computational Plasticity, Barcelona, 1997.

C. M. Downing. Investigation of effect of soil contamination on the crushing of comminuted sugar cane. PhD thesis, James Cook University, 1999a.

C. M. Downing. Rate dependence of permeability in clean and soil contaminated prepared cane. In *Proc. of Australian Soc. of sugar cane technologists*, 21. ASSCT, 1999b.

D. C. Drucker and W. Prager. Soil mechanics and plastic analysis or limit design. *Quart. Appl. Math.*, 10(2):157–165, 1952.

ABAQUS theory manual. *ABAQUS*. Hibbit, Karlsson & Sorensen, Inc, Pawtucker, RI, USA, version 6.1 edition, 2000.

ABAQUS/Standard user's manual. *ABAQUS/Standard Version 6.1*. Hibbit, Karlsson & Sorensen, Inc, Pawtucker, RI, USA, version 6.1 edition, 2000.

ABAQUS example problems manual-Volume I. *ABAQUS Version 6.1*. Hibbitt, Karlsson & Sorensen, Inc, Pawtucker, RI, USA, version 6.1 edition, 2000.

J. P. Holman. *Experimental methods for engineers*. McGraw-Hill Book Company, 1996.

J. E. Holt. Permeability of prepared cane. In *Proc. of Queensland Soc. of sugar cane technologists*, 27. QSSCT, 1960.

J. E. Holt. The effect of fineness on the permeability of prepared cane. In *Proc. of Queensland Soc. of sugar cane technologists*, 28. QSSCT, 1961.

J. E. Holt. The prediction of roll loads in the crushing of prepared sugar cane. Master's thesis, University of Queensland, 1963.

E. Hugot. *Handbook of cane sugar engineering*. Elsevier, 1986.

G. H. Jenkins. A basis for assessing power requirements in cane milling. In *Proc. of Inst.Soc. of sugar cane technol. conf*, pages 154–165, 1956.

David Kauppila. Empirical modelling of the reabsorption phenomenon, 1999. SRDC, Final report, Project No: JUO24.

G. A. Kent and B. P. Edwards. A model of mill feeding without juice expression. In *Proc. of Australian Soc. of sugar cane technologists*, 18. ASSCT, 1994.

Patrick Knupp and Stanly Steinberg. *Fundamentals of grid generation*. CRC Press, 1994.

T. W. Lambe and R. V. Whitman. *Soil mechanics*. John Wiley and Sons Inc., 1969.

C. J. Leitch. An experimental investigation into the constitutive behaviour of prepared sugar cane. Master's thesis, James Cook University, 1996.

C. J. Leitch, C. J. Adam, and J. G. Loughran. On the capacity of prepared cane to penetrate grooved surfaces. In *Proc. of Australian Soc. of sugar cane technologists*, 19. ASSCT, 1997.

J. G. Loughran. *Mathematical and experimental modelling of the crushing of prepared sugar cane*. PhD thesis, University of Queensland, 1990.

J. G. Loughran and C. J. Adam. Properties of prepared cane for computational crushing models. In *Proc. of Australian Soc. of sugar cane technologists*, 20. ASSCT, 1998.

J. G. Loughran, P. C. Ivin, W. N. MacCarthy, and T. L. Vidler. A new method and apparatus for determination of fibre in cane. In Proc. of Australian Soc. of sugar cane technologists, 10. ASSCT, 1988.

J. G. Loughran and A. Kannapiran. Finite element modelling of the cursing of prepared cane and bagasse. In Proc. of Australian Soc. of sugar cane technologists, 24. ASSCT, 2002.

J. G. Loughran and D. Kauppila. Development of an advanced experimental crushing facility. In Proc. of Australian Soc. of sugar cane technologists, 21. ASSCT, 1999.

J. G. Loughran and C. R. Murry. A new model for the uniaxial compression of prepared cane. In Proc. of Australian Soc. of sugar cane technologists, 10. ASSCT, 1988.

B. M. Munro. An investigation into crushing of bagasse and the influence of imbibition on extraction. PhD thesis, University of Queensland, 1964.

C. R. Murry. The mechanics of crushing prepared sugar cane. PhD thesis, University of Queensland, 1960a.

C. R. Murry. Milling studies. In Proc. of Queensland Soc. of sugar cane technologists, 27. QSSCT, 1960b.

C. R. Murry and J. E. Holt. The mechanics of crushing sugar cane. Elsevier, 1967.

P. Nithiarasu and O. C. Zienkiewicz. Adaptive mesh generation for fluid mechanics problems. Int. J. Numer. Meth. Engng., 47:629–662, 2000.

D. R. J. Owen and E. Hinton. Finite elements in plasticity: Theory and practice. Pineridge Press, Swansea, 1980.

D. R. J. Owen, Zhao S. Y, and J. G. Loughran. Application of porous media mechanics to the numerical simulation of the rolling of sugar cane. Engineering Computations, 12: 281–302, 1995.

D. R. J. Owen, S. Y. Zhao, and J. G. Loughran. An overview of crushing theory investigations at Swansea Part-1 & Part-2. In Proc. of Australian Soc. of sugar cane technologists, 16. ASSCT, 1994.

M. Necati Özisik. Finite difference methods in heat transfer. CRC Press, 1994.

J. H. Payne. Sugar series 5, *Noël Deerr* - Classic papers of a sugar cane technologist. Elsevier, 1983.

D. W. Pepper and D. E. Stephenson. An adaptive finite-element model for calculating subsurface transport of contaminant. Ground Water, 33:486–496, 1995.

D. Perić and D. R. J. Owen. Transfer operators for evolving meshes in small strain elasto-plasticity. Comp. Meth. Appl. Mech. Engg., 137:331–344, 1996.

J. Pidduck. Physical properties of bagasse. In Proc. of Queensland Soc. of sugar cane technologists, 22. QSSCT, 1955.

F. Plaza, H. D. Harris, and J. M. Kirby. Modelling the compression shear and volume behaviour of final bagasse. In Proc. of Australian Soc. of sugar cane technologists, 21. ASSCT, 2001.

F. Plaza and G. A. Kent. Using soil shear tests to investigate mill feeding. In Proc. of Australian Soc. of sugar cane technologists, 19. ASSCT, 1997.

William Powrie. Soil mechanics: Concepts and applications. E & FN SPON, 1997.

Staff Roels, Jan Carmeliet, and Hugo Hens. Mesh adaptive finite element formulation for moisture transfer in materials with a critical moisture content. Int. J. Numer. Meth. Engng, 46:1001–1016, 1999.

K. H. Roscoe, A. N. Schofield, and C. P. Wroth. On the yielding of soils. In Géotechnique, 8, pages 22–53, 1958.

G. E. Russell. The extraction performance of sugar cane crushing trains. PhD thesis, University of Queensland, 1968.

G. E. Russell and C. R. Murry. A method of determination of settings for three-roll mills. In Proc. of Queensland Soc. of sugar cane technologists, 35. QSSCT, 1968.

M. Schembri, J. M. Kirby, and G. A. Kent. Describing the mechanical behaviour of prepared cane using critical state theory. In Proc. of Australian Soc. of sugar cane technologists, 20. ASSCT, 1998.

A. Schofield and P. Wroth. Critical state soil mechanics. McGraw-Hill, 1968.

J. E. Shigley. Mechanical engineering design. McGraw-Hill Book Company, 1963.

B. D. Sockhill. Fibre properties as related to milling quality of cane. In Proc. of Queensland Soc. of sugar cane technologists, 25. QSSCT, 1958.

T. J. Solomon. Theoretical and experimental studies in the mechanics of crushing sugar cane. PhD thesis, University of Queensland, 1968.

K. Terzaghi. Theoretical soil mechanics. Wiley, 1943.

Joe F. Thompson. Elliptic grid generation. Elsevier Publishing Co., Inc., 1982.

Joe F. Thompson, Z. U. A. Warsi, and C. Wayne Mastin. Numerical grid generation: Foundation and application. North-Holland: Elsevier Science Pub. Co., 1985.

Noelene Vas. Experimental and numerical investigation of bagasse compression between grooved surfaces. B. Eng thesis, James Cook University, 1999.

D. M. Muir Wood. Soil behaviour and critical state soil mechanics. Cambridge University Press, Cambridge, 1991.

S. Y. Zhao. Finite element solution of saturated-unsaturated porous materials with application to the rolling of prepared sugar cane. PhD thesis, University College of Swansea, 1993.

O. C. Zienkiewicz and D. J. Naylor. The adaptation of critical state soil mechanics theory for use in finite elements. In Stress-strain behaviour of soils, pages 537–547. Proceedings of the Roscoe memorial symposium, Cambridge University, 1971.

Appendix A

Fortran programme for roll load and roll torque estimation (One-dimensional approach)

```
      open(15,file='robassi.out',STATUS= 'UNKNOWN')
c
c     wo= work opening, d=diameter, ek=reabsorption factor
c     n=  no. of points is an even number
c     co= comp. ratio, s= speed (m/s), dvis= dynamic viscosity
c     a = initial contact angle (in degrees)
c     simps-  integration by Simpson's rule for pressure
c     calcn-  calculates intermediate values of pressure
c             and roll load and roll torque.
c
      wo= 0.01184
      d= 0.6604
      ek= 1.14
      cosphi= ((1.0+ wo/d)/ 2.0)+ sqrt(((1.0+wo/d)**2.0/ 4.0)-
     1        (ek*wo/d))
      phi= (180.0/3.1416)*acos(cosphi)
      b= phi
      a= 16.1
      n= 24
      h= abs(b- a)/n
      co= 3.0
      s= 0.1524
      dvis= 2.25e-3
      const= dvis*s*d/2.0/57.3
      write(15,10) phi
 10   format(/'Neutral Plane is at =',f8.2,' degree')
      call simps(a,b,n,h,d,s,co,wo)
      call calcn(a,b,n,h,d,s,co,wo,const)
      stop
      end
c
c     Subroutine uses Simpson's rule
c
      subroutine simps(a,b,n,h,d,s,co,wo)
      value= fun(a,d,s,co,wo)+ fun(b,d,s,co,wo)
```

```
      do 11 i= 1,n,2
      value= value+ 4.0* fun(real(a- i*h),d,s,co,wo)
 11   continue
      do 12 i= 2,n-1,2
      value= value+ 2.0* fun(real(a- i*h),d,s,co,wo)
 12   continue
      value= value*h/3.0
      write(15,31) value
 31   format('Integrated value    =',e10.3/)
      return
      end
c
c     Calculates intermediate values & Roll Load and Torque
c
      subroutine calcn(a,b,n,h,d,s,co,wo,const)
      common y(100),v(100),pr(100)
      y(1)= a
      v(1)= fun(a,d,s,co,wo)/2.0
      pr(1)= const* v(1)
      write(15,5) y(1),v(1),pr(1)
      va=0
      n2= n-1
      do 4 j= 1,n2,2
      i= j- 1
      jb2= j/2+ 2
      va = va+ h*(fun(real(a- i*h),d,s,co,wo)
     1       + fun(real(a- (i+2)*h),d,s,co,wo)
     2    +4.0*fun(real(a- (i+1)*h),d,s,co,wo))/3.0
      y(jb2)= a- (i+2)*h
      v(jb2)= va
      pr(jb2)= const*v(jb2)
      write(15,5) y(jb2),v(jb2),pr(jb2)
 4    continue
 5    format('y=',f10.1,5x,'v=',e10.4,5x,'pr=',e10.4)
c
c     loadato- Calculates roll load and roll torque
c              uses Simpson's rule
c
      call loadato(a,b,d,n)
      return
      end
c
c     Calculation of Roll load & Torque
c
      subroutine loadato(a,b,d,n)
      common y(100),v(100),pr(100)
      a1= a
```

```
      b1= b
      n1= n/2
      h1= abs(b1-a1)/n1
      xtha=3.1416*a1/180.0
      xthb=3.1416*b1/180.0
      valo= 0.0
      valo= (pr(1)/cos(xtha))+ (pr(n1+1)/cos(xthb))
      vato= (pr(1)*tan(xtha))+ (pr(n1+1)*tan(xthb))
      do 11 i= 2,n1,2
      xth=3.1416*y(i)/180.0
      valo= valo+ 4.0* pr(i)/cos(xth)
      vato= vato+ 4.0* pr(i)*tan(xth)
 11   continue
      do 12 i= 3,n1-1,2
      xth=3.1416*y(i)/180.0
      valo= valo+ 2.0* pr(i)/cos(xth)
      vato= vato+ 2.0* pr(i)*tan(xth)
 12   continue
      valo= (((valo*h1/3.0)+ (pr(n1+1)*b))/57.3)*d/2.0
      vato= ((vato*h1/3.0)/57.3)*(d**2/4.0)
      write(15,31) valo,vato
 31   format(//'Roll load per unit length=',f12.3//
     1         'Roll Torque per unit length=',f12.3)
      return
      end
c
c     Function subprogram
c
      real function fun(x,d,s,co,wo)
      common y(100),v(100),pr(100)
      xth= 3.1416*x/180.0
      cthet= (co* wo/d)/ ((1.0+ wo/d- cos(xth))* cos(xth))
c
c     cos(theta)**2/K (K= aC**(-b), K is in m**2 or ft**2
c
      fun=cos(xth)**2/(5.574e-12*cthet**(-2.32))
      return
      end
```

Appendix B

Matlab programme to generate mesh for rezoning

```
% This programme is with grid control
clear;
load top.out; load bot.out;
load left.out; load right.out;
m=46; n= 9;
for i= 1:m
   x(i,1)= top(i,2);
   x(i,n)= bot(i,2);
   y(i,1)= top(i,3);
   y(i,n)= bot(i,3);
end
for j= 1:n
   x(1,j)= left(j,2);
   x(m,j)= right(j,2);
   y(1,j)= left(j,3);
   y(m,j)= right(j,3);
end
ap(1)= 25;ap(2)= 25;bp(1)=0;bp(2)=0;
aq(1)= 50000;aq(2)= 50000;bq(1)=0;bq(2)=0;
cp(1)=.5;cp(2)=.5;dp(1)=5;dp(2)=5;
cq(1)=.5;cq(2)=0.5;dq(1)=5;dq(2)=5;
cei(1)=m;cei(2)=m-3;eti(1)=1;eti(2)=3;
%SOR applied below
w= 1.2;
for it=1:100
errorx=0; errory=0;
for i= 2:m-1
for j= 2:n-1
ix= x(i,j);
iy= y(i,j);
   p=0.0;q=0;
   for k=1:2
   dc= (i-cei(k));de= (j-eti(k));
   p=p+(-(ap(k)*sign(dc)*exp(-cp(k)* abs(dc)))- ...
         (bp(k)*exp(-dp(k)*sqrt(dc^2+de^2))));
   q=q+(-(aq(k)*sign(de)*exp(-cq(k)* abs(de)))- ...
```

```
        (bq(k)*exp(-dq(k)*sqrt(dc^2+de^2))));
   end
xc= diff_fo(x(i+1,j),x(i-1,j));
xe= diff_fo(x(i,j+1),x(i,j-1));
yc= diff_fo(y(i+1,j),y(i-1,j));
ye= diff_fo(y(i,j+1),y(i,j-1));
al= xe ^2+ ye ^2; alp(i,j)=al;
ga= xc ^2+ yc ^2; gam(i,j)=ga;
be= xc* xe+ yc* ye; bet(i,j)=be;
ja= xc* ye- xe* yc; jay(i,j)=ja;
a=(0.5/(al+ga))*(al*(x(i+1,j)+ x(i-1,j))- ...
  (0.5* be*(x(i+1,j+1)- x(i-1,j+1)- x(i+1,j-1)+ x(i-1,j-1)))+ ...
  (ga*(x(i,j+1)+ x(i,j-1)))+ (0.5*(ja ^2)*p*(x(i+1,j)- x(i-1,j)))+ ...
                           (0.5*(ja ^2)*q*(x(i,j+1)- x(i,j-1))));
b=(0.5/(al+ga))*(al*(y(i+1,j)+ y(i-1,j))- ...
  (0.5* be*(y(i+1,j+1)- y(i-1,j+1)- y(i+1,j-1)+ y(i-1,j-1)))+ ...
  (ga*(y(i,j+1)+ y(i,j-1)))+ (0.5*(ja ^2)*p*(y(i+1,j)- y(i-1,j)))+ ...
                           (0.5*(ja ^2)*q*(y(i,j+1)- y(i,j-1))));
x(i,j)=(w*a)+ ((1-w)* x(i,j));
y(i,j)=(w*b)+ ((1-w)* y(i,j));
x(i,j)=(w*a)+ ((1-w)* x(i,j));
y(i,j)=(w*b)+ ((1-w)* y(i,j));
errorx= errorx+ abs(x(i,j)- ix); errory= errory+ abs(y(i,j)- iy);
end
end
   if errorx <1.0e-3 & errory <1.0e-3
     save x.tmp x -ascii;save y.tmp y -ascii
     save m.tmp m -ascii;save n.tmp n -ascii
     break
   else
   end
home
it,errorx%,x
end
for j=1:n
plot(x(:,j),y(:,j));hold on
end
for i=1:m
plot(x(i,:),y(i,:))
end
```

Appendix C

ABAQUS programme for three-roll crushing simulation

```
*HEADING
**********************************************************
  THREE ROLL CRUSHING SIMULATION (USES 4 NODED ELEMENTS)
**********************************************************
*NODE,NSET=NODES
1,  0.34000000,  7.34873867
1001, -0.34000000,  7.34873867
51,  0.34000000,  0.34873879
1051, -0.34000000,  0.34873879
*NODE,NSET=N1
10000, -0.66250002,  0.00000000
*NODE,NSET=N2
20000,  0.66250002,  0.00000000
*NODE,NSET=N3
30000, -0.13504720, -0.77202237
******************************
*NGEN,NSET=R1
1,51,1
*NGEN,NSET=L1
1001,1051,1
*NFILL,NSET=NODES
R1,L1,5,200
************************
*NSET,NSET=RWAL2,GENERATE
1,51,1
*NSET,NSET=LWAL2,GENERATE
1001,1051,1
*NSET,NSET=TOP2,GENERATE
1,1001,200
*NSET,NSET=TIP2,GENERATE
51,1051,200
*NSET,NSET=DRAIN
RWAL2,LWAL2,TIP2,TOP2
************************
*ELEMENT,TYPE=CPE4P
101,1,201,202,2
```

```
*ELGEN,ELSET=BAGASSE
101,5,200,200,50,1,1
*********************************************************
*RIGID SURFACE,NAME=UF,REF NODE=10000,TYPE=SEG
START, -0.66250002,  0.47499999
CIRCL, -0.18750000,  0.00000000, -0.66250002,  0.00000000
CIRCL, -0.66250002, -0.47499999, -0.66250002,  0.00000000
CIRCL, -1.13750005,  0.00000000, -0.66250002,  0.00000000
CIRCL, -0.66250002,  0.47499999, -0.66250002,  0.00000000
*RIGID SURFACE,NAME=TPF,REF NODE=20000,TYPE=SEG
START,  0.66250002,  0.47499999
CIRCL,  1.13750005,  0.00000000,  0.66250002,  0.00000000
CIRCL,  0.66250002, -0.47499999,  0.66250002,  0.00000000
CIRCL,  0.18750000,  0.00000000,  0.66250002,  0.00000000
CIRCL,  0.66250002,  0.47499999,  0.66250002,  0.00000000
*RIGID SURFACE,NAME=BPF,REF NODE=30000,TYPE=SEG
START, -0.13504720, -0.31202236
CIRCL,  0.32495281, -0.77202237, -0.13504720, -0.77202237
CIRCL, -0.13504720, -1.23202240, -0.13504720, -0.77202237
CIRCL, -0.59504724, -0.77202237, -0.13504720, -0.77202237
CIRCL, -0.13504720, -0.31202236, -0.13504720, -0.77202237
*********************************************************
*SURFACE DEFINITION,NAME=MAT
BAGASSE
*SURFACE INTERACTION,NAME=FRICUF
*SURFACE BEHAVIOR,SOFTENED
0.001,5e6
*********
*FRICTION
0.8
*********
*SURFACE INTERACTION,NAME=FRICPF
*SURFACE BEHAVIOR,SOFTENED
0.001,5e6
*FRICTION
0.8
*********
*CONTACT PAIR,INTERACTION=FRICUF
MAT,UF
*CONTACT PAIR,INTERACTION=FRICPF
MAT,TPF
*CONTACT PAIR,INTERACTION=FRICPF
MAT,BPF
*SOLID SECTION,ELSET=BAGASSE,MATERIAL=BAGASSE
*MATERIAL,NAME=BAGASSE
*ELASTIC
20e6,0.15
```

```
*CAP PLASTICITY
38000,75.26,0.2632,0.0,0.0,1.0
***************************
*CAP HARDENING
.400E+05, 0.000
.483E+05, 0.065
.565E+05, 0.130
.648E+05, 0.195
.730E+05, 0.260
.137E+06, 0.400
.188E+06, 0.470
.258E+06, 0.540
.353E+06, 0.610
.484E+06, 0.680
.663E+06, 0.750
.908E+06, 0.820
.124E+07, 0.890
.170E+07, 0.960
.234E+07, 1.030
.320E+07, 1.100
.439E+07, 1.170
.601E+07, 1.240
***************************
*PERMEABILITY, SPECIFIC=1.0
1.23E-15, 1.0
1.23E-13, 2.0
3.69E-12, 3.0
4.92E-11, 4.0
3.69E-10, 5.0
9.85E-09, 6.0
6.16E-08, 7.0
1.23E-07, 8.0
6.16E-07, 9.0
1.23E-05, 10.0
6.16E-05, 11.0
1.23E-04, 12.0
***************************
*USER OUTPUT VARIABLES
4
******************************
*INITIAL CONDITIONS,TYPE=RATIO
NODES,16.0
******************************
*RESTART,WRITE,FREQ=6
*STEP,UNSYMM=YES,NLGEOM,INC=10000,AMP=STEP
*SOILS,CONSOLIDATION,UTOL=3e6
1.0E-04,12.0,1E-25,0.01
```

```
****************************************
*BOUNDARY
DRAIN,8,8
*BOUNDARY,TYPE=VELOCITY
TOP2,1,1,0
N1,1,2,0.0
N1,6,6,  -0.6315790
N2,1,2,0.0
N2,6,6,   0.6315790
N3,1,2,0.0
N3,6,6,  -0.6521739
*CLOAD
1,2,-600.0
201,2,-1200.0
401,2,-1200.0
601,2,-1200.0
801,2,-1200.0
1001,2,-600.0
****************************************
*CONTROLS,PARAMETERS=TIME INCREMENTATION
8,10,,,,,,15
*CONTROLS,PARAMETERS=LINE SEARCH
4
*PRINT,CONTACT=YES,PLASTICITY=YES,SOLVE=YES
*NODE PRINT,FREQ=10
U,RF,POR
*EL PRINT,FREQ=10
VOIDR,PEEQ
*output,field, freq=10
*element output, elset=bagasse
s,e,ie,voidr,por,flvel,UVARM
*node output
v,u
*contact output,slave=mat,master=uf
*contact output,slave=mat,master=tpf
*contact output,slave=mat,master=bpf
*output, history, freq=1
*node output, nset=n1
rf,rm3
*node output, nset=n2
rf,rm3
*node output, nset=n3
rf,rm3
*END STEP
**************************************************************
*USER SUBROUTINES
      SUBROUTINE UVARM(UVAR,DIRECT,T,TIME,DTIME,CMNAME,ORNAME,
```

```
     1NUVARM,NOEL,NPT,LAYER,KSPT,KSTEP,KINC,NDI,NSHR)
C
      INCLUDE 'ABA_PARAM.INC'
C
      CHARACTER*8 CMNAME,ORNAME,FLGRAY(15)
      DIMENSION UVAR(NUVARM),DIRECT(3,3),T(3,3),TIME(2)
      DIMENSION ARRAY(15),JARRAY(15)
C
      CALL GETVRM('E',ARRAY,JARRAY,FLGRAY,JRCD)
C
C     Volumetric strain
C
      UVAR(1)=ARRAY(1)+ARRAY(2)+ARRAY(3)
C
C     Void ratio
C
      UVAR(2)=(1.0+16.0)*EXP(UVAR(1))-1.0
C
C     Compaction (kg/m^3)
C
      UVAR(3)=1530.0/(1+UVAR(2))
C
C     Compression ratio
C
      uvar(4)= 10.48/(1+uvar(2))
      RETURN
      END
**************************************************************
```

Appendix D

ABAQUS programme for three-dimensional roll groove simulation

```
*HEADING
3-D ROLLING: ABAQUS/STANDARD
******************************************
*NODE
1,   0.0, -0.07100000,  0.00000000
801, 0.0,  0.07100000,  0.00000000
51, -1.11485219, -0.07100000,  0.00000000
851, -1.11485219,  0.07100000,  0.00000000
24001, 0.0, -0.07100000, -0.01250000
24801, 0.0,  0.07100000, -0.01250000
24051, -1.11485219, -0.07100000, -0.01250000
24851, -1.11485219,  0.07100000, -0.01250000
*NODE, NSET=N1
30000,  0.00000000,  0.59750003, -0.00625000
*NODE, NSET=N1
40000,  0.00000000, -0.59750003, -0.00625000
******************************************
*NGEN,NSET=BOT1
1,51,2
*NGEN,NSET=TOP1
801,851,2
*NGEN,NSET=BOT2
24001,24051,2
*NGEN,NSET=TOP2
24801,24851,2
*NGEN,NSET=FRO1
1,24001,4000
*NGEN,NSET=BACK1
51,24051,4000
*NGEN,NSET=FRO2
801,24801,4000
*NGEN,NSET=BACK2
851,24851,4000
*NGEN,NSET=MID
811,24811,4000
```

```
******************
*NFILL,NSET=NSIDE
BOT1,TOP1,4,200
*NFILL,NSET=FSIDE
BOT2,TOP2,4,200
*NFILL,NSET=NODES
NSIDE,FSIDE,6,4000
******************
*NFILL,NSET=TOP
TOP1,TOP2,6,4000
*NFILL,NSET=BOTTMOM
BOT1,BOT2,6,4000
*NFILL,NSET=FRONT
FRO1,FRO2,4,200
*NFILL,NSET=BACK
BACK1,BACK2,4,200
*NSET,NSET=DRAIN
BACK,TOP,FRONT,BOTTOM
*NSET,NSET=OUTER
FSIDE,NSIDE
*NSET, NSET=TO1,GEN
801,851,2
*********************************
*ELEMENT,TYPE=C3D8P,ELSET=BAGASSE
1,3,1,4001,4003,203,201,4201,4203
*ELGEN,ELSET=BAGASSE
1,4,200,100,25,2,1,6,4000,1000
*ELGEN,ELSET=TOPE
201,2,200,100,25,2,1,6,4000,1000
*ELGEN,ELSET=FRONTE
1,4,200,100,8,2,1,6,4000,1000
*ELGEN,ELSET=NSIDE
1,4,200,100,25,2,1,3,4000,1000
*ELGEN,ELSET=TOP1
201,2,200,100,13,2,1,3,4000,1000
*********************************************************
*RIGID SURFACE, TYPE=REVOLUTION, NAME=UP, REFNODE=30000
 0.0,  0.59750003,  0.0,   0.0,  0.59750003,  0.8
START, 0.39085, 0.00000
LINE,  0.39085,-0.00125
LINE,  0.35915,-0.01125
LINE,  0.35915,-0.01250
*RIGID SURFACE, TYPE= REVOLUTION, NAME= DOWN,REFNODE=40000
  0.0, -0.59750003,  0.0,   0.0, -0.59750003,  0.8
START, 0.35915, 0.00000
LINE,  0.35915,-0.00125
LINE,  0.39085,-0.01125
```

```
LINE,  0.39085,-0.01250
*************************************
*SURFACE DEFINITION, NAME=SSURF
BAGASSE
*CONTACT PAIR, INTERACTION=FRIC
SSURF,UP
*CONTACT PAIR, INTERACTION=FRIC
SSURF, DOWN
*SURFACE INTERACTION, NAME=FRIC
*SURFACE BEHAVIOR, SOFTENED
1.0e-3,2e4
*FRICTION
0.5
*************************************
*SOLID SECTION,ELSET=BAGASSE,MAT=CANE
*MATERIAL,NAME=CANE
*ELASTIC
20E6,0.15
*CAP PLASTICITY
38000,75.26,0.2632,0.0,0.0,1.0
*************************************
*CAP HARDENING
.160E+05, 0.000
.207E+05, 0.055
.254E+05, 0.110
.302E+05, 0.165
.349E+05, 0.220
.549E+05, 0.356
.690E+05, 0.424
.866E+05, 0.491
.109E+06, 0.559
.136E+06, 0.627
.171E+06, 0.695
.215E+06, 0.763
.270E+06, 0.831
.339E+06, 0.899
.425E+06, 0.966
.534E+06, 1.034
.670E+06, 1.102
.841E+06, 1.170
***************************
*PERMEABILITY, SPECIFIC=1.0
1.23E-15, 1.0
1.23E-13, 2.0
3.69E-12, 3.0
4.92E-11, 4.0
3.69E-10, 5.0
```

```
9.85E-09, 6.0
6.16E-08, 7.0
1.23E-07, 8.0
6.16E-07, 9.0
1.23E-05, 10.0
6.16E-05, 11.0
1.23E-04, 12.0
*INITIAL CONDITIONS,TYPE=RATIO
NODES, 15.4
*****************   step 1   ***************
*STEP,inc=500,NLGEOM
*STATIC
1,10
*BOUNDARY
DRAIN,8,8,0
OUTER,1,1,0.0
OUTER,3,3,0.0
N1,1,1,0.0
N1,3,6,0.0
N2,1,1,0.0
N2,3,6,0.0
*BOUNDARY, TYPE= VELOCITY
N1,2,,-0.02
N2,2,, 0.02
*PRINT,CONTACT=YES,PLASTICITY=YES,SOLVE=YES
*NODE PRINT, FREQ=10
RF,POR
*EL PRINT,FREQ=0
VOIDR,PEEQ
*RESTART,WRITE,FREQ=20
*END STEP
*****************   step 2   ***************
*STEP,UNSYMM=YES,NLGEOM=NO,INC=10000,AMP=STEP
*SOILS,CONSOLIDATION,UTOL=1.0e8
0.01,4.0,1.0e-10,0.1
********************************
*BOUNDARY, OP=NEW, TYPE=VELOCITY
N1,6,6,  0.38377896
N2,6,6, -0.38377896
N1,1,5,0.0
N2,1,5,0.0
DRAIN,8,8,0.0
NSIDE,3,3,0.0
FSIDE,3,3,0.0
BACK,2,2,0
*CLOAD
BACK,1,0.77
```

```
*****************************************
*CONTROLS, PARAMETERS=TIME INCREMENTATION
8,10,,,,,,15
*CONTROLS, PARAMETERS= LINE SEARCH
4
CONTROLS, ANALYSIS= DISCONTINUOUS
*PRINT,CONTACT=YES,PLASTICITY=YES,SOLVE=YES
*NODE PRINT, FREQ=10
RF,POR
*EL PRINT,FREQ=100
VOIDR,PEEQ
*output,field, freq=10
*element output, elset=bagasse
s,e,por,voidr,flvel
*node output, nset=nodes
v,u
*node output, nset=mid
u
*node output, nset=nodes
*contact output,slave=ssurf,master=msurf
*output, history, freq=1
*node output, nset=n1
rf,rm1,rm2,rm3
*node output, nset=back2
u1
*END STEP
*****************************************
```